

UNIVERSITY OF NAPOLI “FEDERICO II”
Naples, Italy

Gian Piero Lignola

**RC hollow members confined with FRP:
Experimental behavior and numerical modeling**

Ph.D. Thesis
19th Cycle



Tutor
Prof. Gaetano Manfredi

Coordinator
Prof. Paolo Gasparini

Ph.D. Programme in Seismic Risk

Index

	Pag.
Abstract	vii
Objectives	viii
Research Impact	ix
Introduction	1
Chapter 1 Background: Hollow cross sections in RC Structures and FRP Strengthening Techniques	5
1.1 Hollow Bridge Piers.	7
1.2 State of the art: Hollow Bridges Piers	14
1.2.1 Hollow Circular Piers.	15
1.2.2 Hollow Square Piers.	22
1.3 State of the art: Strengthening techniques.	26
1.3.1 Concrete encasement.	27
1.3.2 Steel plates Externally bonded.	28
1.3.3 Advanced Composites (FRP)	29
<i>Externally Bonded FRP</i>	31
<i>FRP materials (Fibers and Resins)</i>	32
<i>Durability of FRP</i>	34
1.4 State of the art: Strengthening hollow piers with FRP.	35
1.5 Upgrading index through FRP pier wrapping.	38
1.5.1 Design Procedure.	40

	Pag.
1.6 Chapter References.	44
Chapter 2 Experimental Campaign: From the design of the test matrix and test set-up to the main experimental outcomes	47
2.1 Test Matrix and Set-Up Design.	47
2.1.1 Materials Characterization.	56
2.2 Strengthening Scheme.	60
2.3 Instrumentation.	64
2.3.1 Internal Instrumentation.	64
2.3.2 External Instrumentation.	66
2.4 Test Results.	69
2.4.1 Specimen U1: test result.	70
2.4.2 Specimen U2: test result.	74
2.4.3 Specimen U3: test result.	78
2.4.4 Specimen S1: test result.	83
2.4.5 Specimen S2: test result.	91
2.4.6 Specimen S3: test result.	97
2.5 Chapter References.	102
Chapter 3 Modeling Hollow Cross Sectional Behavior: Proposed Refined Nonlinear Method	103
3.1 Brief Review of available models.	103

	Pag.	
3.1.1	Unconfined concrete behavior.	104
	<i>Cracked Concrete Behavior in tension</i>	109
3.1.2	Confined concrete behavior.	112
	<i>First Confinement models based on Mohr's Circle</i>	114
	<i>Confinement models based on reinforcement yielding: Mander</i>	117
	<i>Confinement models based on elastic reinf.: Spoelstra-Monti</i>	119
	<i>Confinement models based on elastic theory: Fam and Rizkalla</i>	121
	<i>Confinement models based on plain strain theory: Braga Laterza</i>	126
	<i>Shape factor for confinement effectiveness</i>	128
	<i>Superimposed models for internal and external confinement</i>	134
	<i>FRP strain efficiency</i>	135
3.1.3	Confined concrete eccentrically loaded.	136
3.1.4	Steel internal reinforcement.	141
	<i>Reinforcement stability and Fracture of concrete cover</i>	142
3.1.5	Wall Stability.	146
3.2	Proposed Nonlinear Refined Method.	150
3.2.1	Model Assumptions.	152
3.2.2	Cross Section Discretization.	153
3.2.3	Computation Algorithm.	157
	<i>Convergence Criteria</i>	159
3.2.4	Numerical Strategies.	165
	<i>Moment Curvature diagram</i>	165
	<i>Interaction diagram plot</i>	166
3.2.5	Taking into account second order effects.	167
3.3	Proposed Hollow Sections Confinement model.	171
3.3.1	First Part: Walls interaction and confinement.	171

	Pag.	
3.3.2	Second Part: Square hollow section confinement.	175
3.3.3	Plane Strain Conditions.	176
3.3.4	Concrete model with variable confinement pressure.	179
3.3.5	Radial Displacement Compatibility.	181
3.3.6	Non Linear Characteristics.	183
3.3.7	Iterative Procedure.	185
3.3.8	Ultimate Strain and Failure of the Confining Device.	187
3.3.9	Parametric Study.	187
	<i>Radial and Circumferential Stresses</i>	188
	<i>Effect of Confining Device Relative Stiffness</i>	190
	<i>Effect of Hole Size</i>	190
3.4	Chapter References.	193
Chapter 4	Experimental-Theoretical Comparison	197
4.1	Experimental Outcomes: Comparative Discussion.	197
4.1.1	Strength.	198
4.1.2	Failure Modes.	201
4.1.3	Ductility.	207
4.1.4	Longitudinal Strains.	212
4.1.5	FRP Strains.	214
4.1.6	Theoretical Model Restraints Validation.	218
4.2	Experimental-Theoretical Comparison.	221
4.2.1	Constitutive Laws of Materials.	222
	<i>First part: Walls interaction and confinement</i>	225

	Pag.
	227
	229
	233
	238
	244
	246
	247
4.3 Chapter References.	250
Chapter 5 Finite Elements Nonlinear Modeling of Hollow Cross Section RC piers and FRP Confinement effects	251
5.1 Finite Elements Non Linear modeling of RC members.	252
5.1.1 Solid elements.	253
5.1.2 Concrete model.	256
<i>Crack modeling</i>	259
5.1.3 Reinforcement elements	270
5.2 DIANA models of tested specimens.	272
5.2.1 Specimen U1: FEM numerical predictions.	277
5.2.2 Specimen U2: FEM numerical predictions.	280
5.2.3 Specimen U3: FEM numerical predictions.	284
5.2.4 Specimen S1: FEM numerical predictions.	288
5.2.5 Specimen S2: FEM numerical predictions.	295
5.2.6 Specimen S3: FEM numerical predictions.	301
5.2.7 Summary of FEM predictions.	307

	Pag.
5.3 Chapter References.	311
Chapter 6 Conclusions.	313
6.1 Conclusions.	314
6.2 Design Guidelines: Add-on proposal.	318
6.3 Basic Design Example.	323

Abstract

High elevation bridges with very large size columns are constructed to accommodate high moment and shear demands. In particular, bridge piers designed in accordance with old design codes may suffer severe damage during seismic events, caused by insufficient shear or flexural strength, low ductility and inadequate reinforcement anchorage. Many parameters may influence the overall hollow column response such as: the shape of the section, the amount of the longitudinal and transverse reinforcement, the cross section thickness, the axial load ratio and finally the material strength of concrete and reinforcement. This research program focuses on rectangular hollow cross sections and investigates the columns behavior under a state of compression combined with flexure. The experimental results have been compared with analytical predictions, concentrating on the behavior of the hollow column strengthened with FRP composite materials to improve the cross section performances both in terms of ductility as well as flexural strength. As the state of stress changes from pure compression to combined compression and flexure, and the flexural stresses become predominant over the compression ones, the neutral axis moves inside the section altering the failure mode and consequently the response that the cross section may have to such type of loading. FRP materials have been widely used in the form of jacketing to enhance shear and flexural strengths as well as ductility, and their effectiveness has been extensively proven in many research programs investigating solid column behavior. Although it is uncertain how these jackets may perform in the repair of rectangular hollow columns since very little research has been performed in this area and the few studies are related to circular and

rectangular hollow columns with applied low level of axial load, investigating the performance of the cross section subjected to combined shear and flexure stresses. This research investigation provides an overall view of square hollow cross section behavior subjected to several combined axial load and bending loads and strengthened with FRP jacketing.

Laboratory work has been conducted at the University of Naples and includes two parts: the first series of tests focusing on the flexural-compression behavior of un-strengthened square hollow columns and a second series of tests studying FRP strengthened hollow columns under the same loading conditions, investigating changes in failure mode, ductility and flexural strength enhancements.

Objectives

The objective of the proposed investigation is to evaluate the behavior of square hollow bridge cross sections retrofitted with FRP composites materials used as external jacketing. The influence of external loading conditions, namely pure compression and combined flexure and compression has been studied in order to determine the available ductility of unstrengthened and strengthened rectangular hollow cross sections. This evaluation consists in an experimental phase undertaken in conjunction with analytical studies to predict and to model the results of the former tests. The development of design construction specifications and a refined methodology to design and assess hollow cross section members behavior under combined axial load and bending is the final output of the program.

Research Impact

Apart from the possible human victims, severe earthquake damage on bridges results in economic losses in the form of significant repair or replacement costs and disruption of traffic and transportation. For these reasons, important bridges are required to suffer only minor, repairable damage and maintain immediate occupancy after an earthquake so as to facilitate relief and rescue operations. Most of the existing bridges worldwide were designed before their seismic response had been fully understood and modern codes had been introduced; consequently they represent a source of risk in earthquake-prone regions.

Since recent destructive earthquakes and modern studies have caused the revision of seismic maps, there is now the need to assess the seismic capacity of existing bridge structures.

Till FRP materials approached the construction market as a viable, cost and time effective solution for upgrading and retrofitting existing concrete structures, the only available answer to the aforementioned problems were either to rebuild the structure or to use standard restoring techniques (i.e. section enlargement, steel jacketing and others) that would have had a high social and economical impact as well as structural consequences such as increase in self weight consequently with a negative contribution to foundations and to seismic response of the overall structure.

The aim of this research program is to contribute the knowledge towards as-built hollow square piers and together with the information gathered from previous research works, to provide the tools for best approaching the retrofitting and strengthening of such kind of cross sections with a cost and time effective solution.

Introduction

The last occurred intense seismic events confirmed, worldwide, the need of identifying, developing and implementing measures to accomplish effective earthquake hazard risk reduction. Infrastructure's vulnerability to earthquake damage and consequently losses might be reduced by implementing preventive (mitigative) actions. This mitigation can be defined as sustained actions taken to reduce or eliminate long-term risk to people and property from hazards and their effects. Seismic risk calculations are the foundation for risk mitigation decision-making, a key step in risk management. Improvement gained from a mitigation measure is the difference between the original condition and the improved (mitigated) condition.

Earthquake loss reduction is a complex long-term commitment. It requires the continuing participation of a team of scientist from multidisciplinary fields.

The multidisciplinary of the seismic risk evaluation R is evident in its definition:

$$R = (Seismic\ Hazard) \times (Vulnerability) \times (Exposition)$$

Where the Seismic Hazard is defined as the probability that a given level of a seismic parameter is exceeded in a given period of time and the Exposition represents the estimation of the economic damage expected for the element exposed to the risk.

The Vulnerability is the probability that a given level of damage is reached as consequence of the seismic event.

These concepts express the multidimensionality of disasters by focusing attention on the totality of relationships in a given social situation which constitute a condition that, in combination with environmental forces, produces a disaster.

In the present work the mitigation measurements are evaluated in the field of vulnerability. Measures such as incorporating seismic design requirements into new structures, or accomplishing seismic rehabilitation of existing structures, will reduce the vulnerability, thus reducing the expected losses.

Bridges and viaducts are amongst all the structures, those that sustain the most damage, as clearly demonstrated in several reports of recent earthquakes. Object of this study is a significant part of the Italian, and global, highway network, whose vulnerable elements are supposed to be the Reinforced Concrete (R.C.) bridges, and in particular, their safety is limited and conditioned by pier capacities.

Several studies and works have been carried out on solid piers vulnerability and can be applied also to building structures (i.e. columns); however, for hollow piers much less research is found in the literature.

Many of these hollow section piers, especially those built in last '60s and '70s, are now in need of a seismic upgrade to improve their response under earthquake.

Bridge piers designed in accordance with old design codes may suffer severe damage during seismic events because of insufficient shear or flexural strength or low ductility. Because of its brittle nature, failure in shear of an RC bridge pier must be avoided. Accordingly, the member behavior is dominated by flexure; therefore, the flexural performance of hollow cross sections must be investigated. However, the knowledge about the behavior of hollow piers is still lacking, and their seismic performances (in flexure and shear), retrofit techniques, and numerical analyses should be investigated. Recently Fiber Reinforced Polymers (F.R.P.) has been widely used in the retrofitting and strengthening of reinforced

concrete structures, especially in regions under high seismic risk. The present work aimed at evaluating the benefits generated by an FRP wrapping on hollow section piers vulnerability.

To investigate the behavior of unstrengthened and FRP jacketed square hollow piers subjected to combined axial load and bending, a total of seven 1:5 scaled specimens has been tested at University of Naples Federico II. Tested specimens represent in reduced scale typical square hollow bridge piers. Along with test results on shear controlled/dominated tests, the present work was meant to provide a complete summary on the behavior of members having hollow non-circular cross section.

The thesis discusses the outcomes of the performed tests focusing on the analysis of cross-section curvature, member deformability, specific energy, etc...

An original refined method has been developed to predict the behavior of unstrengthened and FRP strengthened hollow square piers.

The work is exposed in the following chapters:

In *Chapter 1* are introduced the main issues of bridges with hollow cross section piers, a discussion of the typical retrofit techniques with particular attention to the FRP confinement/wrapping and to a state-of-the-art of the actual knowledge of FRP effectiveness as a strengthening technique for hollow columns.

In *Chapter 2* is described the experimental campaign with details on the design of the test matrix, the design of the equipment setup to realize the experimental campaign. The main results in terms of both global and local parameters are presented for each specimen.

In *Chapter 3* are critically described the existing available models concerning solid section assessment (concrete modeling, steel reinforcement stability, effect of confinement, etc...). Besides is described the proposed refined nonlinear methodology. An automated algorithm has been developed accounting for steel bars buckling and concrete cover spalling. The effect of concrete hollow

core confinement by FRP wrapping has been also modeled adopting two confinement models: the former is an adaptation of existing models for a solid section to a hollow one, the latter is an innovative model proposed for confinement of hollow sections.

In *Chapter 4* is presented an experimental-theoretical comparison. With reference also to the theoretical considerations, the main experimental outcomes are discussed. The refined methodology proposed to predict the behavior of square hollow section unstrengthened and wrapped with FRP has been checked on the experimental outcomes.

In *Chapter 5* is presented a Finite Elements Method (F.E.M.) modeling of the tested specimens both unstrengthened and strengthened. The nonlinear behavior of concrete in tension (cracking) and in compression, the effect of FRP wrapping have been modeled also by means of the commercial code TNO DIANA v. 9.1. The proposed methodology has been also validated with the FEM modeling in terms of both global and local deformability.

In *Chapter 6* a basic example on a real pier upgrade, not designed for seismic actions, by means of FRP wrapping to satisfy seismic ductility requirements is illustrated. The proposed refined algorithm coupled with the proposed confinement model for hollow square RC piers was adopted. Besides main conclusions are discussed and some design recommendations related to hollow cross section piers, as built assessment and FRP strengthening, are drawn to improve their response under seismic actions thus reducing their vulnerability.

Chapter 1

Background: Hollow cross sections in RC Structures and FRP Strengthening Techniques

Bridge are key elements in our society, they control the capacity of the transportation system, representing the highest cost per kilometer of an infrastructure. For example, a bridge crossing a valley may have the function of safely connecting a community with the schools and services (i.e. hospitals, first aids) of another community by avoiding dangerous journeys down and up steep and twisting roads. If the bridge fails, the system fails.

In recent years progresses in design and assessment procedures have been achieved all over the world and practices have changed.

Beautiful bridges have been built in high seismicity areas and large viaducts were severely challenged by intense seismic action; some of them sustained significant damage and had to go through complex and innovative repair and retrofit process.

Pier Section design is more critically affected by seismic considerations than other parts of the bridge. With conventional seismic design, ductility, implying potential damage, will be expected from the piers under design-level seismic response.

Single-column or multiple-column piers: circular, rectangular, oval, or special architectural section shapes: solid or hollow pier sections are the alternatives the designer can deal with. As a matter of fact, the choice between the

above alternatives is currently based on convention and tradition, rather than pure structural considerations, and hence regional differences are noticeable.

The choice between single-column and multi-column piers depends on the kind of pier/superstructure connection type. When dealing with supported superstructures, the single-column design results in a seismic response equal in orthogonal directions, since the pier responds as a simple vertical cantilever in all directions. On the other hand, a single-column vertical cantilever has a lack of redundancy that should lead to assign lower design ductility levels for this type of design relative to multi-column designs.

This latter design is more appropriate when monolithic pier/superstructure are present and also when the superstructure width is large, resulting in high eccentric load moments. However, if the superstructure is simply supported on a multi-column pier-cap, pier response is as a vertical cantilever in the longitudinal direction, and by double-bending transversely, resulting in non-uniform strength and stiffness in orthogonal directions. Multi-column piers with small section size were the rule with bridges constructed in the 50's to 70's. The general trend world-wide today appears to be the single-column piers with much larger section size. In the case of very wide bridges with multiple traffic lanes, bridge superstructure width can be reduced by supporting the two traffic directions by independent bridge structures.

Once the substructure is chosen, then the principal choice will be between circular and rectangular sections, with a secondary choice between solid and hollow section shapes. Additional more complex section shapes, principally chosen on the basis of architectural considerations, may be considered. Hollow sections are used to reduce seismic masses, based on economic considerations of the cost saving associated with reduced material and design moments compared with increased construction complexity, and hence increased labor costs.

Hollow columns are larger and taller than solid columns, as a consequence

they are more visible, and also more expensive and architectural considerations have a significant influence. For example, a single-column bridge design increases the transparency of a tall bridge. It is not sufficient to have adequate information about a bridge site and the traffic loads to have an automatic design of an efficient and aesthetically pleasing bridge. The design process is different for every engineer because it is dependant on personal experience. Aesthetics are a part of the bridge design program from the beginning. Oftentimes the function of a bridge goes beyond the simple connection of points with a given volume of traffic. Its function must be understood by the designer; given a choice, even with a modest increase in initial cost, the community will prefer the bridge that has the nicer appearance. The parts of the structure must be in agreement with each other and the whole structure must be in agreement with its surroundings.

Harmony between the elements of a bridge depends on the proportions between the span length and depth of the girders, height and size of piers, and free spaces and solid masses. Piers have features of their own that can improve the appearance of a bridge. The key is that they fit in with the superstructure and its surroundings and they express their structural process. The most successful ones are those that have some flare, taper, texture or other features that improve the visual experience of those who pass by them.

1.1 Hollow Bridges Piers

Compression column elements potentially support a variety of structures, for example bridge decks and floor slabs, and can act as piers or piles, and may do so whilst above or below water. Columns vary in physical shape depending on their application within a situation, although typically they are either circular or rectangular, solid or hollow, for ease of construction.

A number of spectacular concrete bridges incorporating hollow piers and

pylons have been constructed throughout the world particularly in Europe, United States and Japan, where high seismic actions and natural boundaries require high elevation infrastructures. In Europe, hollow columns are used for columns as low as 20m (Slovenia) or 30m (Italy), but in the United States, it is rare to use hollow columns for column heights less than 40m.

Hollow bridge piers accommodate the high moment and shear demands by reducing the self weight and the high bearing demand on pile foundations, maximizing structural efficiency of the strength-mass and stiffness-mass ratios and reducing the mass contribution of the column to seismic response.

Recent earthquakes in urban areas have repeatedly demonstrated the vulnerability of older structures to seismic actions, also those made with reinforced concrete materials, with deficient shear strength, low flexural ductility, insufficient lap splice length of the longitudinal bars and, very often, inadequate seismic detailing, as well as, in many cases, very bad original design, with insufficient flexural capacity. The most critical mode of failure in RC structures is the column shear failure. To prevent this brittle failure, the column needs to have guaranteed shear capacity both in its ends, the potential plastic hinge regions, where concrete shear capacity can degrade with increasing ductility demands and in its center portion, between flexural plastic hinges.

Bridges and viaducts are amongst all the structures, those that sustain the most damage, as clearly demonstrated in several reports of recent earthquakes. Object of the study is a significant part of the Italian highway network, whose vulnerable elements are supposed to be the bridges.

Even for “moderate magnitude” earthquakes, the consequences in these structures have been very dramatic, in many occasions causing their partial destruction, and in some cases total collapse, with corresponding heavy costs. In comparative terms, these consequences of bridge vulnerability are found greater than those observed in building structures and, in most cases, the bridge safety is

limited and conditioned by piers capacity. Several studies and works have been carried out on solid piers and can be applied to building structures; however, for hollow piers, much less research is found in the literature.

The need for strengthening the existing bridges stems from the consideration that most of the bridges built in the past in seismic zones according to now-obsolete codes are inadequate to meet the more stringent requirements imposed in the new generation of codes, as regard both strength and ductility. The deficiencies that make existing bridges, even those built until the very last few years, vulnerable to seismic action all have a single common cause: the conventionality of the seismic design approach used in the former codes (and still in some of the present ones).

It is widely known that those codes had the limitations of emphasizing the strength aspects while only making implicit reference to the concept of ductility. As a consequence, existing bridge piers built according to those codes – as observed either from original project drawings or through in-situ inspections after destructive seismic events – rather frequently, at least in Italy, are equipped with adequate amounts of longitudinal reinforcement (thus complying with the flexural strength requirements), while systematically showing insufficient transverse reinforcements (thus lacking the confinement necessary for ensuring a ductile response).

Specific column deficiencies are mainly related to:

- Inadequate transverse reinforcement volume to provide adequate confinement to concrete and anti-buckling restraint to longitudinal reinforcement.
- Inadequate transverse reinforcement to ensure reliable shear strength exceeds maximum feasible flexural strength.
- Inadequate detailing of transverse reinforcement to ensure that the required shear strength and anti-buckling roles are achieved satisfactorily.

- Premature termination of longitudinal reinforcement in columns, resulting in a propensity for flexural hinging and shear failure at column mid-height.
- Inadequate anchorage of flexural reinforcement in footings and cap beams.
- Lap-splicing of flexural reinforcement at the base of columns, thus limiting the curvature ductility capacity of column-base plastic hinges.

Another common source of inadequacy of existing bridge piers arises from the nowadays frequent re-classifications of seismic zones (based on more accurate hazard studies); in such cases, most bridge piers designed according to a previous seismic zonation do not satisfy the verifications with the new increased seismic actions.

As traffic expanded (i.e. track loading constantly increasing), highway bridges increased in number and size. In Italy, the Autostrade S.p.a. highway system has 5594 km of highways, comprising a total of less than 3000 bridges. These bridges were built basically in the 60's and in the 70's. Seismic design regulations of that time considered almost nominal horizontal forces equal to 10% of the permanent weights in the zones of highest seismicity (less in the other seismic zones), with no attention to grant ductile behavior, to check compatibility between adjacent decks, the strength of the bearings, etc.; in addition, many areas, which today are considered to be seismic, in those years were not yet classified. In low seismicity regions the column size may be affected by eccentric live-load considerations, particularly for single-column piers. In mid to high seismicity regions seismic considerations control the column size.

The reinforcement of the piers were not designed for the seismic forces, but for wind and braking forces, or more simply considering the minimum percentage code requirements. Tradition has in Italy that bridge piers should be and look rather rigid and this provides in many cases a useful extra strength. Also the foundations, in order to ensure satisfactory performances under service loads, in many cases are stronger than the superstructure, a desirable property under

seismic action.

More than one third of the total of the bridges are made up of decks which are simply supported on different piers systems. An other third of the total of the bridges are single span structures directly supported on the abutments, and the remaining bridges are variously distributed among Gerber, arch, continuous deck, cantilever construction and frame-like types and some of them have unique characteristics, like some large arch bridges built in the sixties, as well as other important bridges with large spans (in excess of 100 m).

Pinto and Monti (2000). found that in Italy, most spans are around 30 m and only the more recent ones reaching 40 m, while the ratio between the cross section dimension and the height of the pier is a widely variable parameter.

Representative hollow cross sections of the cited Italian bridges piers can be a rectangular hollow cross section with dimensions of $6.60 \times 3.80 \text{ m}^2$ and a circular shaped one with a diameter of 3.80 m. For those cross sections, the pier heights are in the range of 10 to 45 m for rectangular section and in the range 8 to 24 m for the circular one. Internal reinforcements, both longitudinal and transverse can be, on safe side, those provided by the '60s codes.

Upper limits to the longitudinal reinforcement ratio are generally specified by codes to be about 4%, but previous codes often permitted ratios as high as 8%. In the case of higher ratios, the anchorage of longitudinal reinforcement in foundations or cap beams becomes difficult because of congestion. Volumetric ratios of transverse reinforcement have a practical lower limit of 0.5%; upper limits tend to be between 1% and 2%, with spacing along the column axis between 50mm and 150mm, although spacing of transverse reinforcement was typically 300mm in the '60s and '70s.

In table 1.1 is reported a survey of pier reinforcement details courtesy of Fib TG 7.4 on Seismic Design and Assessment Procedures for Bridges.

Table 1.1 – Pier reinforcement details

	USA West	USA East	NZ	Mexico	Japan	Italy	France	Greece	Slovenia
Lap Splice	Out hinge	In hinge	Out hinge	Out hinge	Out hinge	In Hinge	Out hinge	Out hinge	Varies
ρ_l	>0.01 <0.04	>0.01 <0.04	>0.008 <0.03	>0.01 <0.05	>0.008 <0.020	>0.01 <0.04	>0.005 <0.03	>0.01 <0.03	>1% <2.5%
Long. Bar Size (mm) and Type	32-57 ASTM A706	28-44 ASTM A615	25-32	25-38 ASTM A615	29-51 JIS SD295	16-26	>10	25-32 S500 temcore	16-28 S500
ρ_v	>0.005 <0.012	>0.002 <0.10	>0.005 <0.012	>0.005 <0.020	>0.005 <0.018	>0.002	>0.005	>0.007 sp >0.009 rc	>0.3% <1.5%
Trans. Steel size and spacing (mm)	12-25 50-150	10-12 75	12-20 75-200	12 150	16-32 150	12-20 100-250	>10 <8d _b <0.5B <200	>14 75-150	10-16 100-200
f'_c f_y (MPa) f_u	30-45 420 600	26 420 600	30-45 500 700	25-30 420 630	24-30 >295 440-600	20-35 >430 >540	30-45 500 >600	25-30 500	25-30 500 >600
ALR	0.04 to 0.12	0.04 to 0.10	0.04 to 0.10	0.04 to 0.12	0.03 to 0.08	0.03 to 0.08	About 0.10	0.07 to 0.15	About 0.10
Drift Limit	None	None	None	<0.01	None	None	None	None	None
Design Ductility	3-4		<6	2-3	3-4	Varies	3.5	1.5-3.5	1.5-3.5
Seismic Demand	High	Low - Mid	Varies	Varies	High	Low-Mid	Low-Mid	Mid-High	Mid

Legend: B=section depth; $\rho_l = \frac{A_{st}}{A_g}$; $\rho_v = \frac{V_{st}}{V_{member}}$; $ALR = \frac{P}{f'_c A_g}$

Flexural behavior of these piers made up of single bents can be described by means of a bi-linear force-displacement relationship at the top of the pier where ultimate ductility is given by the ratio of ultimate curvature at the base section and yielding curvature.

Considering elastic spectrum suggested in the Eurocode 8 for intermediate

soil conditions, and shear capacity evaluated in accordance with Eurocode 2, shear failure occurs only for the shorter ($H=10$ m) rectangular pier; in all other piers collapse is governed by exhaustion of ductility. Circular piers have consistently lower values of acceleration causing collapse, due to lower available ductility with respect to the rectangular ones: this in turn is due to the shape of the section and to the higher average vertical stress.

In addition to the considered structural failure mechanisms of the piers, another type of failure, frequently observed in recent earthquakes, even for bridges of the last generation, is the possibility of collapse due to loss of support of the deck. Recent studies, analyzing recorded soil time histories obtained from strong motion arrays installed in seismic areas, clearly demonstrated that relatively close points on the soil can experience significant relative displacements. This is due both to reflection and refraction of seismic waves through underlying soil layers with different mechanical characteristics and to the presence of soils of different nature. From the structural analysis point of view, this implies that the conventionally adopted assumption of equal seismic input under all supports is only acceptable when dealing with bridges of moderate dimensions, while it is far from reality if long-span bridges are considered. In these cases different input motions experienced at adjacent supports can significantly modify the overall structural response thus making vulnerable the design concept.



Figure 1.1 – Hollow Circular Piers (Viaduct Sarsina, Italy)

1.2 State of the art: Hollow Bridges Piers

As many other concrete structures, hollow bridge piers show different level of deterioration and structural deficiencies. In particular, bridge piers designed in accordance with old design codes may suffer severe damage during seismic events, namely insufficient shear or flexural strength, low ductility and inadequate anchorage bonding.

Many formulations in codes of practice or recent research documents have been proposed and validated only for solid sections requiring a better understanding of the role played by the different resisting mechanisms and some adjustments.

The most important parameters that govern the behavior of hollow columns are:

- the shape of section: circular or rectangular,
- the amount of longitudinal and transverse reinforcement (steel ratio ρ),

- the numbers of layers of reinforcement placed near inside and outside faces of the section and tied through the wall thickness,
- the wall relative thickness (inside to outside diameter ratio D_i/D_e), and
- the axial load ratio

The main body of research conducted till now can be divided into two main categories of tests based upon the shape of the section being either circular or rectangular.

1.2.1 Hollow Circular Piers

Whittaker et al. (1987) have investigated the flexural strength and ductility available from circular hollow reinforced concrete column sections with two layers of longitudinal and transverse reinforcement placed near both the inside and outside faces of the section and tied through the wall thickness by transverse reinforcement (*see figure 1.2*). The core of the tube walls was well confined by the reinforcement, when properly detailed, and the columns performed in a ductile manner during cyclic lateral loading.

To place the longitudinal and transverse reinforcement in one layer only near the outside face of the cross section may be convenient for smaller cross-sectional size columns. Zahn et al. (1990) have investigated the flexural strength and ductility of circular hollow reinforced concrete columns with one layer of longitudinal and spiral reinforcement placed near the outside face of the section to establish the parameters that control the available flexural strength and ductility. The concrete near the inside face of the hollow section is unconfined and the flexural failure may be brittle.

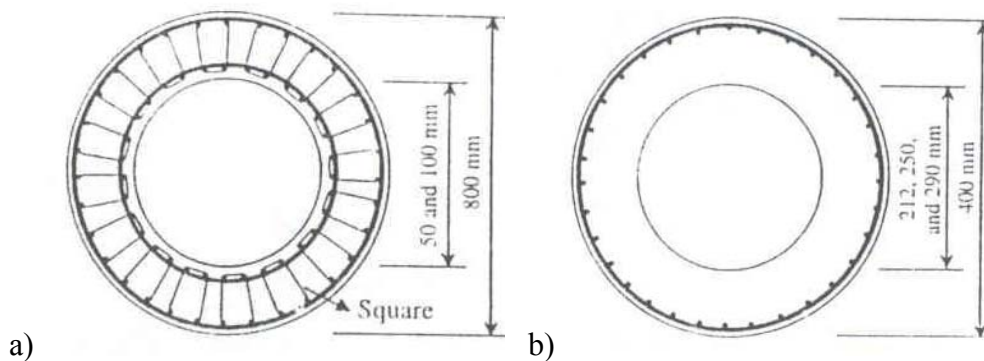


Figure 1.2 – Configuration of transverse reinforcement in hollow circular columns: (a) Whittaker et al. (1987); (b) Zahn et al. (1990).

Transverse reinforcement in columns has three roles: to provide shear resistance, to prevent premature buckling of longitudinal reinforcement, and to confine the compressed concrete.

Spiral or circular hoop reinforcement placed near the outside face of circular hollow column restrains the growth of the tube diameter caused by longitudinal compression.

The resulting spiral bar stress applies a radial pressure f_r that causes a circumferential compression stress σ_2 in the curved tubular wall. The circumferential compression stress σ_2 puts a concrete element cut out of the curved wall into biaxial compression, with the primary stress σ_1 arising from axial load and flexure (see figure 1.3). A compressive confining stress acts on the inside face of curved wall in the radial direction only in a solid confined concrete section. When concrete compressive strain arise and concrete on the inside face of the tube wall crushes, there is nothing to prevent this crushing from penetrating into the tube wall towards the outside face.

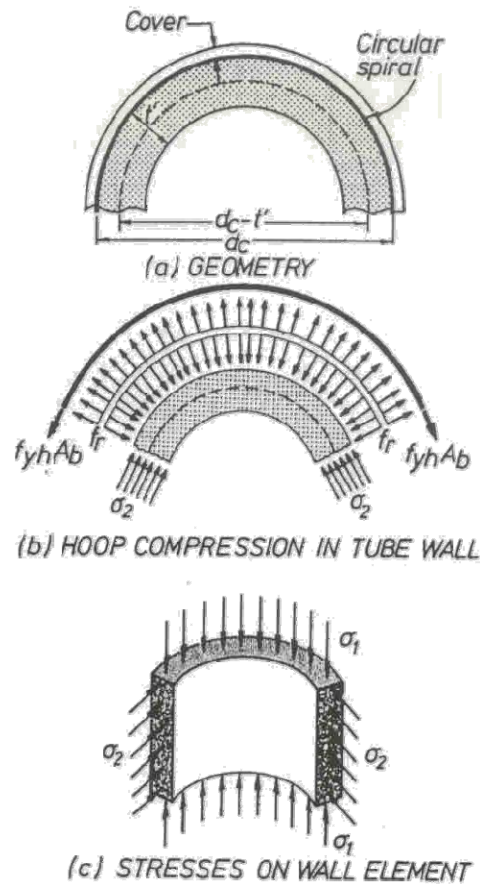


Figure 1.3 – Geometry and stresses in wall of circular hollow column.

The position of the neutral axis at the flexural strength of the section is the most important variable controlling whether a circular hollow cross-section column has available curvature ductility:

- Low axial load, moderate longitudinal steel percentage or reasonably thick wall (wall thickness of not less than 15 percent of the overall section) put the neutral axis close to the inside face of the tube wall and the column may be expected to be ductile, resulting in small longitudinal strain in the unconfined region of the concrete compression zone.

- Instead, if the neutral axis passes through the void at some distance from the inside face of the tube, the column can be expected to fail in a brittle manner as a result of rapid disintegration of the concrete in the compression zone and deterioration of the flexural strength. There is a little margin for the strain to grow with increasing curvature before failure commences because the resulting high longitudinal compressive strain on the inside face causes early vertical splitting and crushing of the concrete.

The amount of spiral steel placed near the outside face of the tube wall plays a relative minor role in the available ductility of circular hollow sections. The radial confining stress exerted by spiral reinforcement puts the compressed portion of the curved wall into circumferential compression and thus helps to delay vertical cracking. In solid members, the restraint provided by the transverse steel against concrete dilatancy generates a confining action in terms of an inward radial pressure. In contrast, in thin-wall circular hollow members the action of transverse steel generates circumferential compression stresses on the tubular wall. In this case, the radial component of the confining stress is rather low and does not contribute to the enhancement of the concrete strength.

In the absence of any confinement in the radial direction, annular cracks start to form once a critical value of the longitudinal compressive concrete strain is exceeded.

For direct design or for determining the flexural strength of circular hollow columns with a single layer of longitudinal and spiral reinforcement placed near the outside face of the section with inside to outside diameter ratio $D_i/D_e < 0.70$, it is sufficiently accurate to base the calculations on an equivalent solid circular with the same outside diameter, area of longitudinal reinforcing steel and axial load ratio based on the sectional area of the hollow column excluding the void. Using a code approach, the reinforcing ratio percentage ρ_t for the equivalent solid columns

is the area of longitudinal steel as a percentage of the gross sectional area of the hollow columns A_{tot} including the void. The axial load ratio $P/f_c \cdot A_g$ is taken as the value given P over A_g , the gross sectional area of the column excluding the void.

Zahn et al. (1990) constructed and tested six circular hollow RC columns under axial compression (applied through steel roller and held constant throughout the test) and cyclic fatigue (horizontal load applied at the mid-height of the column). The voids in the columns were formed by cardboard tubes that were left in place after the concrete had been cast, and the voids did not penetrate neither into the central stub nor into the end regions of the column units. The parameters analyzed were the wall relative thickness and the axial load ratio.

All column units failed by more or less rapid collapse of the concrete wall in the compression zone. No signs of shear failure were observed in any of the tests. The smallest measured concrete compression strains measured at first visible crushing at the extreme (outside) fiber of the cover concrete was 0.008.

They validate the suggested simplified design approach based on an equivalent solid section proposing a conservative set of curvature ductility design factor to allow the designer to read off directly the curvature ductility factor that a particular section can sustain. The obvious variables in these charts are the axial load ratio, the inside to outside diameter ratio D_i/D_e , the longitudinal steel percentage.

Yeh et al. (2001) tested three hollow circular bridge piers under a constant axial load and a pseudo static, cyclically reversed horizontal load applied at the end of the specimen. The parameter considered for the specimens were the amount of lateral reinforcement to evaluate the displacement ductility factor, and the height-diameter ratios to study the influence of flexure or shear, respectively.

All three specimen developed flexural cracks perpendicular to the column axis. The first occurred in region close to the bottom of the columns. The flexural cracks became inclined and extended into the neutral axis of the column due to the

influence of shear, typically as a stage exceeding the first yielding of longitudinal reinforcing bars.

Although each specimen developed the estimated flexural strength, the ultimate performance was different for each column. The ultimate capacity of the specimen with sufficient shear reinforcement was dominated by flexural due to the rupture of longitudinal reinforcing bars at the bottom of the column occurred after steel buckling during compression cycles (this effect can be reduced by using smaller spacing of the transverse reinforcement).

When the ultimate state was dominated by a bond failure of spliced longitudinal reinforcing bars at the plastic hinge region, fewer and wider cracks occurred (insufficient shear reinforcement and relatively large lateral reinforcement spacing). The plastic hinge did not fully develop and much lower displacement ductility was observed.

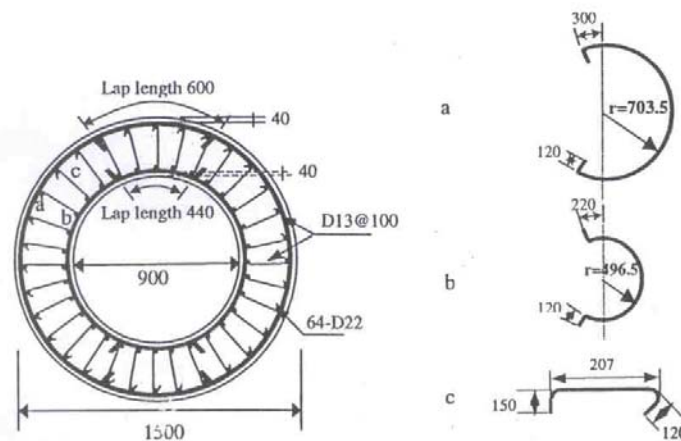


Figure 1.4 – Dimension of Yeh et al. cross section.

When the ultimate performance was dominated by shear capacity (shear reinforcement only 40% of the code required) concrete crushed at the bottom of

the specimen. The rupture of a few tensile longitudinal reinforcing bars occurred immediately before shear failure of the specimen and it developed low displacement ductility because its plastic hinge can not be fully developed.

The displacement ductility factor is defined as the displacement at 80% of the maximum lateral load in the descending portion of the horizontal load-displacement relationship divided by the yield displacement.

The yield displacement is defined according to Zahn et al. (1990) as the displacement obtained from the intersection point of the horizontal line at the ideal load capacity and the straight line from the origin passing through the point on the load-displacement plot at 75% of the ideal lateral load capacity.

The available displacement ductility factor capacity should decrease as the aspect ratio L/D or L/h of the column increases.

Ranzo and Priestley (2000) conducted experimental studies on three large size specimens, designed with only one layer of longitudinal and spiral reinforcement near the outside face, and tested with a cantilever scheme, under pseudo-static cyclic loading. The results indicated that the implosion of concrete in the inside surface, under the effect of high bending and shear forces, governs the activation of the strength degradation mechanism. For the same shear strength, members with higher flexural capacity were found to require thicker walls in order to prevent concrete spalling in the inside wall surface.

Predictions on the behavior and on the failure mode of members characterized by a small ratio of the shear span to section diameter, approached with recently developed shear strength models and with the experimental results, can be obtained and well predicted, i.e. using the shear strength model UCSD suggested by Priestley.

The nominal shear capacity is expressed as the sum of three independent components: the term V_s derived by the classical truss analogy proposed by Ritter and Mörsh and representing the shear carried by transversal steel reinforcement,

V_c and V_p derived by the concrete resisting mechanism and identifying two effects: the one provided by concrete in tension (V_c) where is recognized a reduction of the shear stress transmitted by aggregate interlock as diagonal cracks become wider and a certain extent of degradation of the strength capacity with increasing displacement ductility, and the one provided by the concrete in compression (V_p) through a compression field developed by the presence of the axial load, that is not subjected to degradation.

The shear carried by concrete in tension (V_c) is also included in some models through the longitudinal steel ratio and the transversal volumetric ratio, those parameters should be approximately accounted considering the full section, neglecting thus the presence of the hollow core, in order to avoid the paradox to have on a hollow section a better nominal crack control respect to a solid section with more concrete and the same amount of reinforcement.

1.2.2 Hollow Square Piers

Priestley, and Park (1987) have tested RC concrete columns with square hollow section shape under combined axial load and bending moment applying the compressive axial load and an horizontal load at the top of the hollow column by means of a servo-hydraulic loading jack. Bending moment, shear force, and axial load were applied to the member, with the critical section being just located above the base. These columns had longitudinal reinforcement near both the inside and outside faces of the cross section, and transverse reinforcement in the form of closed hoop around groups of four longitudinal bars, plus a peripheral hoop to confine the core concrete between the longitudinal steel layers.

The main variables were the level of axial load and the amount of transverse reinforcement in the plastic hinge.

The test indicate very stable behavior in the loops with comparatively light axial load ratio $P/f_c \cdot A_g = 0.1$ and with 74% of the transverse reinforcement required. Column which was provided with only 55% of the transverse reinforcement required and a higher axial load ($P/f_c \cdot A_g = 0.3$), due to the reduced level of confinement failed due to the fracture of some hoops in the compression flange, followed by buckling of longitudinal reinforcement.

Whenever larger spacing of transverse reinforcement is used, the ductility of the column is prematurely limited by buckling of longitudinal reinforcement.

Mander et al. (1983) tested four rectangular hollow specimens with different arrangements of confining steel in the plastic hinge zone, under constant axial load and cyclic lateral displacements, investigating shear and ductility behavior of the columns varying the level of axial load and the amount of transverse reinforcement in the plastic hinge zone to prevent buckling of the longitudinal reinforcement. Tests showed the need to reduce the stirrups spacing and to increase the length of lap splice of the longitudinal bars in columns with high levels of axial load, to avoid premature failure caused by buckling of longitudinal reinforcement. The ductility capability of RC members is achieved by providing sufficient transverse reinforcement in the form of rectangular hoops or spirals to adequately confine the concrete, to prevent buckling of the longitudinal reinforcement, and to prevent shear failure. When the axial load level is high, the secondary moments from the $P-\Delta$ effect become more significant as the displacement increases.

Yeh and Mo (2002) tested prototype and scaled model of hollow columns under a flexure dominant loading condition and discussed the size effect. The scale ratio of prototype to model was 1:3. The study showed that prototypes had greater ductility than models. The failure mode governing was rupture of longitudinal rebars for all the specimens since shear failure and buckling was prevented by an appropriate anchoring and confinement.

The crack pattern analyzed for all specimens showed flexural cracks in the flange part (in all reviewed literature, it is common to call flanges the two opposite sides of the hollow cross section perpendicular to the horizontal load and web the two parallel to it) changing into diagonal cracks drastically when the progressed into the web part of the column.

Mo et al. (2001) tested columns under a flexure dominant loading condition. The specimens were designed with the lateral reinforcement code requirements to avoid shear failure and spacing less than six times the diameter of longitudinal reinforcing bars (suggested by Priestley et al. 1996).

Specimens with higher concrete compressive strength had greater maximum lateral force than expected. Higher concrete compressive strength increased the yielding displacement, so decreasing displacement ductility factor. In fact the displacement ductility factor depends on the steel yielding.

Greater axial force produces greater maximum lateral force and less ductility factor, also the failure mode changed from flexural failure to shear failure. The shear capacity predicted by the ACI code was less than (conservative) the actual capacity (the force in the specimen when shear failure occurred)

Deformation performance around the ultimate state is deteriorated when the axial load applies. Since the concrete area to bear the axial load is small in the hollow section, the pier loses the restoring force rapidly once the concrete begins spalling not only outside, but also into the void and reinforcement buckles.

Few studies (Taylor et al. 1995) are reported on the behavior of thin walled concrete box piers. Tests results showed the validity of guidelines proposed by AASHTO Specifications on the slenderness ratios. If the slenderness ratio of the compression flange (defined in Figure 1.5) reaches the value of 15 or greater it was found that the flange would fail by buckling while for lower values the flange failed due to crushing of the concrete.

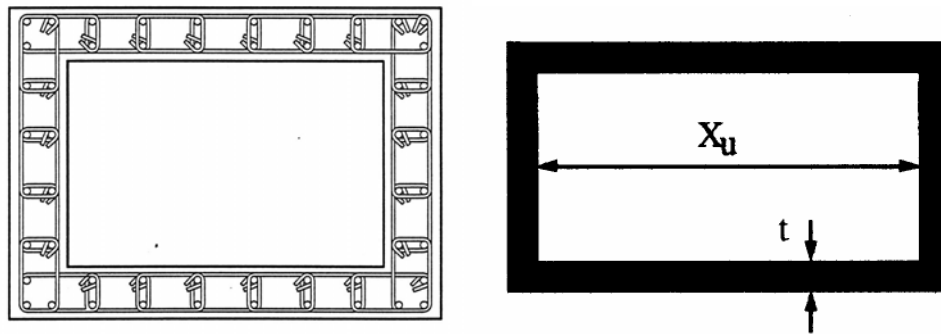


Figure 1.5 – Typical Cross Section and Definition of Wall Slenderness Ratio X_u / t

As found in circular hollow columns, local buckling reduces the capacity of the hollow column and must be avoided by appropriate detailing: when double layer of reinforcing is used, cross ties must be provided between the two layers of steel.

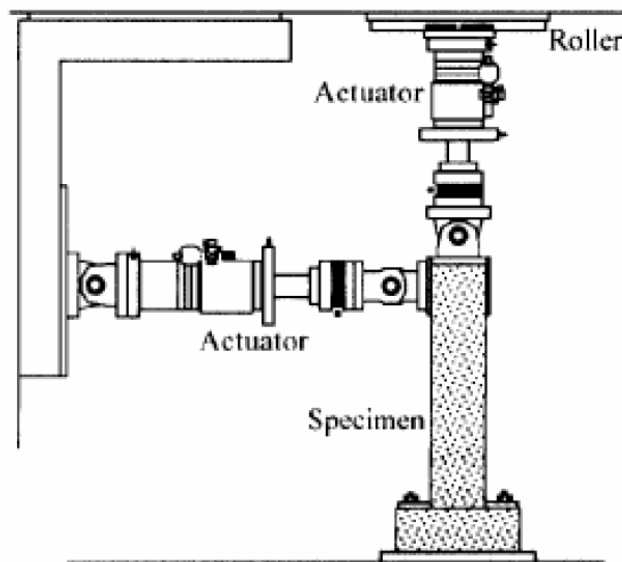


Figure 1.6 – Typical Test Setup Used for Testing Hollow Columns

Masukawa et al. (2000) analyzed the timing of spalling of concrete cover and buckling of reinforcement on the inner and outer sides of hollow sections, a key aspect to predict accurately and to understand the ductility of RC members with a hollow section. Hollow piers first suffer the spalling of concrete cover outside the compressive flange followed by the buckling of reinforcement, then the concrete cover spalls and reinforcement buckles inside the section. Finally, internal concrete crushes and the strength deteriorates substantially (Figure 1.7).

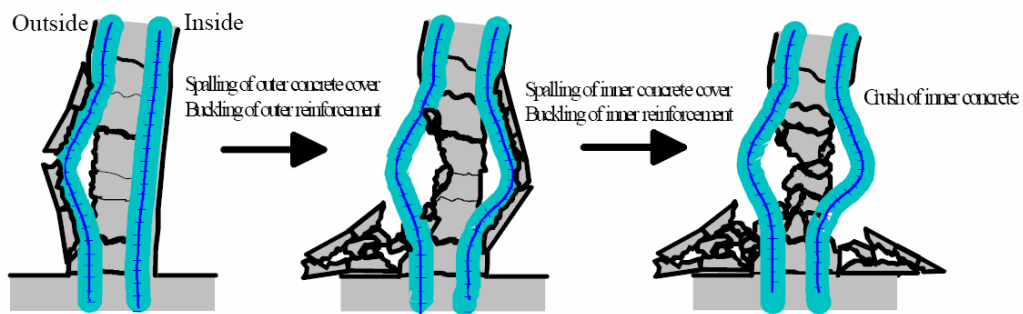


Figure 1.7 – Progress of failure at compressive flange of hollow RC member

1.3 State of the art: Strengthening techniques

During the last years the construction industry in Italy has shown a clear trend to increase the investments in the upgrade and rehabilitation of existing structures; surveys have highlighted that in 2005, for the first time in Italy, the investments on existing structures have overcome those on new construction. This is due to two main reasons. First, the high population density has reduced the availability of areas for new construction. Secondly, after the latest classification of seismic zones issued by means of OPCM 3274 in 2003 (updated by OPCM 3431 in 2005), seismic provisions are to be accounted for when building new structures or strengthening existing ones on almost the entire Italian territory; in particular, OPCM 3274 devotes a chapter (i.e., chapter 11) to the assessment of

existing structures. This chapter provides suggestions about how structures made out of different materials (i.e., reinforced concrete, masonry, steel) should be assessed and outlines also which strengthening techniques could be used. This significant upgrade of the national codes has stimulated the awareness of institutions, owners and engineers on the fact that any intervention on an existing structure should not be done without an assessment of its current conditions and of its seismic performance; the availability of design criteria and formulas for the assessment and for the design of upgrade interventions has increased the trust of owners about the reliability of engineers judgments as well as about necessary strengthening works for which they have to pay.

For RC structures, the following three techniques are allowed by OPCM 3431: concrete encasement; steel encasement; external strengthening using (FRP) materials. The first two techniques have been extensively used in the past; however, several disadvantages have been highlighted.

1.3.1 Concrete encasement

Concrete encasement implies the enlargement of existing cross-sections with loss of space and increase of structural mass; in addition, constructability issues related to time and difficulty of execution have been pointed out; seismic events have also evidenced that perfect bond and collaboration between old and new portions is not easy to ensure.

This is the oldest strengthening method. The additional concrete may be “structural” concrete reinforced with steel bars or wire mesh and designed to be a load-carrying element. Or, it could be “protective” concrete used to fireproof post-tensioning steel or FRP cables or bonded steel elements, and also to protect them from mechanical and environmental damage. Using this method, columns, beams,

slabs, and walls can be enlarged to add load-carrying capacity or to increase the stiffness. In all cases, the designer should incorporate the weight of the additional concrete overlay/jacket in the design of the enlargement. The section enlargement method is relatively easy and economically effective. The disadvantage of this method is possible corrosion of embedded reinforcing steel. These problems can be avoided by using adequate concrete cover or the use of FRP reinforcement, which is resistant to corrosion. A typical enlargement is approximately 2 to 3 inches for slabs, and 3 to 5 inches for beams and columns.

1.3.2 Steel plates externally bonded

Steel encasement implies several of the above disadvantages; with this technique the mass increase is less significant but major issues due to corrosion have been observed. Strengthening of reinforced concrete members using bonded steel plates was developed in the '60s in Switzerland and Germany. This method of strengthening consists of steel elements that are glued to the concrete surface by a two-component epoxy adhesive to create a composite system. The steel elements can be steel plates, channels, angles, or built-up members. In this technique, the bonded steel element is considered a passive reinforcement (the new steel does not become effective until the concrete deflects under additional loads). However, adequate design, specification, and execution of the job are necessary to ensure the composite action of the repair/upgrade system. Steel plates bonded to the tension face of concrete beams can increase the flexural capacity, along with increases in flexural stiffness and associated decreases in deflection and cracking. Steel elements bonded to the sides of the member can improve the shear strength of the concrete member.

A practical problem with steel plates on site is their weight and the

restriction on the length of individual plates for ease of manipulation and handling. The steel elements may need to be spliced, which complicates the design and construction operations. As with any glue, bonding the steel plates to the concrete requires pressing them together. This is achieved by using adhesive anchors. It is strongly recommended to provide some supplemental anchors, especially at the ends of the plate. This is done to ensure that the bonded steel element will still share some load in case of adhesive failure. Considerable site work is required to accurately locate the existing reinforcement to avoid damaging them while placing the anchors. In addition, elaborate and expensive falsework is required to maintain the steelwork in position during bonding.

1.3.3 Advanced Composites (FRP)

Since the end of the Cold War, many advanced military technologies and products have been transferred to the civil engineering industry. FRP applied to structure retrofitting is one of the most successfully transferred technologies. During the last decades, the use of FRP has gained increasing popularity due to several properties such as: high strength to weight ratio; corrosion resistance; ease and speed of application; minimal change of cross-sections; possibility of installation without interruption of structure functions. For these reasons, FRP has been widely used in the retrofitting and strengthening of reinforced concrete structures, especially in regions under high seismic risk.

The diffusion of the FRP technique as competitive strengthening solution has induced researchers and engineers to develop specific design guidelines; after those proposed by the American Concrete Institute (ACI), by the Federation International du Beton (fib) and by the Canadian Standard Association (CSA), a national guideline has become available in 2004 as a result of the effort of a

committee of the Italian National Research Council (CNR). The CNR DT-200 is more than a standard CNR guideline because the OPCM 3431 refers to it for the design of FRP strengthening and this reference makes CNR DT-200 the official Italian code for FRP interventions.

The applications of Carbon FRP (CFRP) and Glass FRP (GFRP) materials in Italy have grown during the last 10 years; the first cases have concerned the flexural strengthening of building slabs or beams as well as bridge girders. These types of interventions were mainly requested by durability (i.e., corrosion of internal steel reinforcement) or by lack of structural capacity under gravity loads. Then, the market has slowly started to select FRP as an alternative to the traditional techniques (i.e., concrete or steel encasement) for seismic strengthening; at present, seismic applications have become comparable if not more frequent than those related to lacks under gravity loads. Externally bonded FRP laminates with fibers in the hoop direction are often wrapped around column buildings or bridge piers to increase their confinement and/or their shear capacity. In fact, the lack of appropriate size and spacing of ties in a column or pier can induce the collapse to occur at its end, resulting in crushing of the not confined concrete, instability of the steel reinforcing bars in compression and pull out of those in tension. In addition, the lack of transverse reinforcement can cause a brittle shear failure, with formation of inclined cracks due to diagonal tension, concrete cover spalling and rupture of the transverse reinforcement. FRP wrapping is sometimes designed also to prevent the brittle failure that could be generated by insufficient length of the lap splice in the longitudinal steel reinforcement. This is a typical deficiency concerning the lower end of columns or piers; as vertical cracks initiate in the cover, concrete dilatation occurs and eventually cover spalling is generated. Along with that of columns or piers, the upgrade of beam-column joints represents another key issue for both buildings and bridges. In fact, the strengthening of columns by providing them with higher

confinement level and/or with more flexural reinforcement could cause the failure to occur in the nodal zone. In order to move up along the strength hierarchy, the joint panel should be also strengthened. The upgrade of both column and panel could allow moving from the previous intermediate level of the strength hierarchy (i.e., shear failure of the panel) to its upper bound (i.e., crisis of the beams). Inducing such failure mode would be the best result of a seismic repair/strengthening. Formation of plastic beam hinges would mean that a ductile and very effectively energy dissipating mechanism is achieved. Experimental tests on single members (i.e., columns or piers) and on sub assemblages (i.e., portions of frames including columns, joint and beam) have confirmed the effectiveness of FRP laminates as a strengthening technique. Full-scale tests on real RC frames have lately validated these results and witnessed the beneficial influence of FRP upgrade on the global seismic performance.

Externally Bonded FRP

For seismic zones, FRP may also be used to wrap columns to enhance the ductility due to the induced confinement of the concrete. FRP material selection should be based on strength, stiffness and durability required for a specific application. Resins are selected on the basis of the environment to which the FRP will be exposed, as well as the method by which the FRP is manufactured.

Externally bonded FRP systems come in a variety of forms, including wet lay-up systems and precured systems. Wet lay-up FRP systems consist of dry unidirectional or multidirectional fiber sheets or fabrics impregnated with a saturating resin on-site. Precured FRP systems consist of a wide variety of composite shapes manufactured off-site. Typically, adhesive along with the primer and putty are normally used to bond the precured shapes to the concrete surface. The primer is used to penetrate the surface of the concrete, providing an

improved adhesive bond for the saturating resin or adhesive. The putty is used to fill small surface voids in the substrate and to provide a smooth surface to which the FRP can bond. Precured FRP systems include unidirectional laminates, multi-directional grid and precured shells. In spite of the significant research being reported on their structural mechanism and performance, there are still heightened concerns regarding possible premature failure due to debonding, especially in zones of combined high flexural and shear stresses. In addition, externally bonded FRP reinforcement is relatively unprotected against wear and impact loads. The structural performance of the externally bonded FRP could also be greatly affected by harsh environmental conditions.

FRP materials (Fibers and Resins)

Fibers are the basic load-bearing component of any FRP product. Fibers are often preassembled into various forms to facilitate the fabrication of composite products. Discontinuous fibers are often used also to produce low-cost composite products such as sheet molding compounds or non-woven mats. Fiber, filaments yarns and rovings generally represent parallel bundles of continuous filaments. The fiber bundles may be used directly in composite fabrication, such as by filament winding or pultrusion process to produce bars or structural shapes, or they may be further converted to other reinforced forms such as ‘prepregs’ (preimpregnated plates), fabrics and sheets. Fibers used in modern composites can be broadly classified into three main categories:

- Polymeric fibers, including aramid fibers (i.e. Kevlar 29, Kevlar 49 and Kevlar 149 which is the highest tensile modulus aramid fiber);
- Carbon fibers, including pan-based carbon and pitch-based carbon. Polyacrylonitrile (PAN) and cellulose are the common precursors from which pan-based carbon fibers are currently made. Petroleum and

polyvinyl chloride are the common sources for the pitch used for carbon fibers. Pan-based carbon fibers have diameters of 5–7 μm while pitch-based carbon fibers have diameters of 10–12 μm .

- Inorganic fibers including E-glass, S-glass and boron fibers. Other specialty fibers such as optical fibers are currently being investigated for structural health monitoring applications.

Figure 1.8 illustrates the strength and modulus of elasticity of various FRP materials.

Bars, preregs or sheets are parallel filaments held by matrix material. The matrix could be thermoplastic resin or partially cured thermoset resin. The role of the resin in composites is vital. Resin selection controls the manufacturing process, upper use temperature, flammability characteristics, and corrosion resistance of the composite. Although loads are carried by the fiber composite, mechanical performance depends to a large extent on the resin modulus, failure strain and the bond between the resin and the fiber.

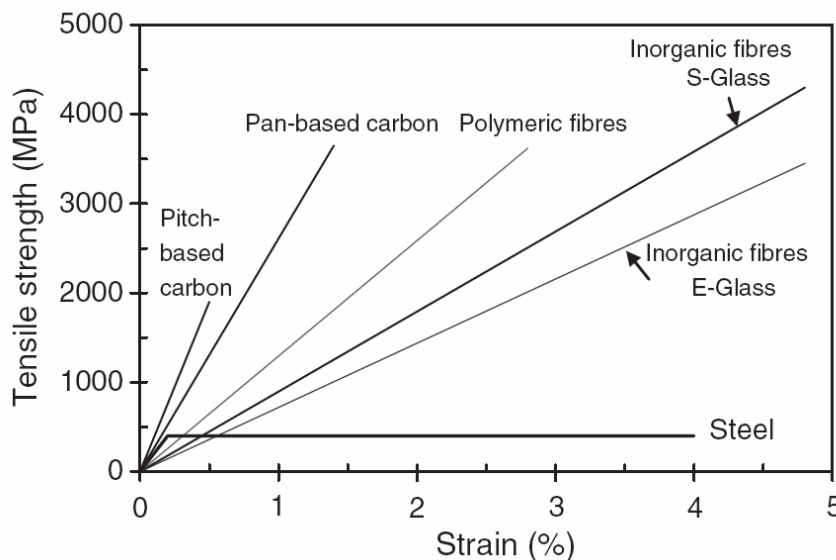


Figure 1.8 – Stress-strain relationship of FRP materials

Durability of FRP

Although FRP composites perform extremely well in practice, there are heightened concerns related to their durability in the field as related to civil infrastructure applications. In these cases, FRP composites are exposed to harsh environmental conditions, ranging from wide temperature fluctuations and humidity levels to rain and snow. There are limited theoretical and experimental studies on the durability of the bond between FRP and concrete. Investigations by different researchers are focusing on the durability of externally bonded FRP reinforcement. Further studies are still needed to establish accurate reduction factors to be used in bond strength models for design purposes. Wet–dry cyclic exposure has a significant effect on the bond length, shear stress distribution and differential strain between FRP and concrete. The shear modulus of the adhesive at the FRP–concrete interface was found to be a critical parameter for obtaining durable FRP retrofitted concrete members. Adhesives are generally sensitive to water. Deterioration of bonded joints is characterized by absorption of water by the adhesive and by moisture diffusion to the adhered interface. Voids can be created in the adhesive layer and at the interface. Presence of voids implies less area of contact. Water can also replace the adhesive by capillary transmission, and this weakens the bond between the externally bonded FRP reinforcement and concrete. The influence of freeze–thaw cycles on the structural performance of concrete beams strengthened with FRP sheets and strips was studied by several Researchers and test results showed that freeze–thaw action did not degrade the bond of FRP-strengthened beams. High temperatures showed a detrimental effect on the bond characteristics of FRP. Test results showed a reduction of 80–90% in the bond strength of FRP with different surface treatment at temperatures ranging from 20 to 250°C. In comparison, steel showed a reduction of 38%.

1.4 State of the art: Strengthening Hollow Piers with FRP

Research programs have mainly addressed the issue of solid columns with either rectangular or circular cross sections and have shown how FRP confinement can play a significant role in constraining the concrete core and consequently improving flexural strength and ductility and by adding additional reinforcement in the hoop directions, increasing also shear strength, such reducing seismic vulnerability. A critical brief review of them is in Chapter 3, where they are implemented and modified to comply with hollow core cross section.

Very little has been done about hollow columns strengthened with FRP composite materials. Only few research investigations (related to three research groups) have been found in literature dealing with hollow cross sections strengthened with FRP, with predominant shear stresses.

There are two seismic retrofit ways for reinforced concrete piers:

- the first way is to give piers enough ductility, and
- the other way is to make piers to have enough strength.

If the design seismic force is too large to adopt only the first way due to residual deformation or other reasons, we have to adopt both the ways to retrofit.

If the pier shows shear failure or failure at the cut-off section of longitudinal bars, restoration from seismic damage after earth quakes would be difficult. The pier has to fail in flexure at the bottom end.

Osada et al. (1999) carried out static and pseudo-dynamic tests investigating the seismic behavior of hollow circular RC piers having reinforcement cut-off planes and variable wall thicknesses, examining the effect of carbon fiber sheets to improve seismic performances. The specimens were created as close as possible to the actual piers as 1:20 scaled models. Tests were conducted with low level of axial load and high horizontal load applied at the top of the column, with the most solicited cross section subjected to both flexure and shear. FRP showed

good improvement of cross section properties, increasing shear strength and avoiding premature buckling of longitudinal reinforcement as experienced in section with very high confinement reinforcement.

The outermost longitudinal rebars yielded at all cut off points, the load carrying capacity decreased from the peak due to the extensive growth of diagonal cracks and suddenly decreased due to the concrete crushing at the top of the reinforced concrete column.

Flexural failure occurred near the bottom end of the CFRP zone in the specimen retrofitted mainly longitudinally (3 to 4 layers). CFRP in the hoop direction ruptured at overall height and lateral load declined markedly. It finally failed in shear representing brittle behavior.

Specimen which was retrofitted only in the hoop direction suffered no serious damage such as shear failure and buckling of longitudinal rebars even at the ultimate load, and displayed ductile behavior without any decrease of lateral load.

In view of the concentration of crack openings at the point where stiffness changed drastically at the bottom end of the CFRP, it was considered preferable to avoid a sudden decrease of CFRP used for retrofit in the longitudinal direction but to gradually reduce the volume of CFRP for retrofit at the end.

It was verified that the lateral strain in CFRP indicated almost the same level as in the hoop reinforcement at the same position until the hoop yielded. From this result, it seems possible to convert the CFRP volume into hoop volume in the calculation of shear capacity.

Mo et al. (2002) investigated the seismic behavior of eight hollow rectangular bridge columns retrofitted by FRP sheets under constant low levels of axial load ($P/f_c \cdot A_g = 0.080$ to 0.136) and cyclically reversed horizontal load. Columns had two-layers of longitudinal reinforcement. The effects of FRP sheets on ductility, dissipated energy as well as on shear strength were investigated. Test

results showed that the ductility factor increases with the number of FRP sheets as well as the shear strength of the hollow cross section, being able to eliminate all shear cracks and changing the failure mode of the specimen from shear to flexure.

Specimen without steel and FRP transverse reinforcement failed due to longitudinal bars buckling, while the specimen with only steel stirrups failed due to shear.

Specimen with only FRP transverse reinforcement failed due to concrete crushing and afterwards, the FRP sheets ruptured. No buckling of longitudinal rebars occurred.

The specimen confined both by transverse reinforcement and FRP sheets failed due to flexure with the rupture of longitudinal rebars at the bottom end of columns.

Yeh and Mo (2005) found that the confinement provided by FRP sheets in the circular piers is more effective than in rectangular ones. CFRP sheets can improve both the ductility factors (in their tests up to 5.5) and the shear capacity of the hollow bridge piers and can successfully transform the failure mode from shear (brittle) to flexure (ductile).

At the University of Pavia, Italy, two testing campaigns have been carried out recently (Pavese et al. 2004), investigating the seismic behavior of both unstrengthened and strengthened rectangular hollow piers respectively. Different FRP strengthening solutions have been considered to improve the cyclic response of bridge piers with native deficiencies due to design philosophy assumptions as in the case of structures built in Italy. The piers investigated were reduced scale square hollow bridge piers with the following characteristics: rectangular cross section $45 \times 45 \text{ cm}^2$ and 7.5 cm thickness, 1.35 m height, and longitudinal reinforcement made of 24D8 or 40D8 and transversal reinforcement made of two or four legs D3@75 mm stirrups. Tests were performed with columns subjected to low levels of axial load and increasing horizontal load investigating the most

solicited cross section at the base of the column, under a state of both shear and flexure stresses. The variables investigated were lacks in shear reinforcement and insufficient lap-splice length. FRP showed to be very efficient restoring the shear strength not accomplished in the original design. They found that under-designed structures are often unable to sustain the loads essentially for loss of detailing (insufficient confinement, loss of bonding, etc.) and incorrect proportioning of flexural and shear strength. Particularly this second aspect is due to a global lack of design strategy oriented to a hierarchical arrangement of the collapse modes expected on structural elements and on the whole structure. The best results have been obtained in piers, where the lack of shear resistance is responsible of the brittle behavior. The transversal wrapping improves the shear capacity allowing deep plastic deformations in the longitudinal bars.

When FRP are adopted also for flexural strengthening, the importance of anchorage of fibers at the base of the pier was emphasized as the crucial problem and, only after the debonding was prevented, the benefit of strengthening was fully achieved.

The aim of the cited studies is mainly the prediction of the shear strength of FRP wrapped hollow piers.

1.5 Upgrading index through FRP pier wrapping

RC pier failures during past earthquakes have often been a consequence of using elastic design (force as opposed to displacements). Strength design may be successful if the demand is estimated accurately, and the strength is frequently insufficient to guarantee the elastic response of the bridge. Hence to survive intense shaking, structures must exhibit an adequate ductility capacity.

The most common damage patterns for bridge piers are outlined below.

The lack of ductility in **flexural failure** mechanism is due to inadequate

confinement of the plastic hinge zone. Unless the concrete is well confined by closed transverse stirrups, crushing rapidly extends into the core, buckling of longitudinal reinforcement occurs and loss of strength is observed. In extreme conditions the columns become unable to sustain gravity loads. There are several examples of failure in plastic hinge zones, such as top column failure, as shown in Figure 1.9.

Another common design deficiency is highlighted by discontinuity of longitudinal reinforcement leading to weak sections. Failure may also occur without yielding of vertical reinforcement, due to an inadequate lap-splice length or failure in welded bars.



Figure 1.9 - Different damage patterns for RC piers: symmetric buckling (left) flexural failure (middle) shear failure (right).

Elastically designed structures may suffer **shear failure**, since the shear strength corresponding to the maximum (not design) flexural strength would not have been considered. Shear failure mechanisms are not usually (with a few exceptions) suitable for ductile seismic response, because of the low levels of deformation corresponding to failure. Short columns are particularly susceptible

to such effects.

Several cases of **symmetric buckling** of reinforcement and compressive failure of piers may be attributable to high vertical earthquake forces.

1.5.1 Design Procedure

The mechanical model of the pier consists in many cases of a cantilever carrying a mass at the top. If the original structure is a frame, with two or more columns, the force-displacement relationship is evaluated considering the columns with a height equal to half of the clear height between foundation and pier cap.

The design procedure stems from the definition of an upgrading index, given as the ratio of the target-to-available ductility at the pier base section, to be attained through FRP jacketing (assuming that yielding force is almost constant). The available ductility is that identified through the usual assessment procedures on the RC member to upgrade, while the target ductility is evaluated based on the expected actions on the bridge.

Ductility is the ability of a structure or a selected structural element to deform beyond elastic limits without excessive strength or stiffness degradation.

The fundamental source of ductility is, at material level, the ability to sustain plastic strains without significant reduction of stress. The most desirable source of ductility is rotations in potential plastic hinges. The curvature ductility μ_χ is, at the section level, the ratio between maximum expected and yield curvatures. In an elastoplastic or bilinear approximation the yield curvature does not necessarily coincide with the first yield of tensile reinforcement, while the equivalent slope K of the elastic portion of the response can be defined by the secant stiffness at first yield. Axial compression can greatly reduce the available curvature ductility capacity of a section, resulting in spalling of concrete cover at an early stage,

while increasing compression strength is effective for increasing section curvature ductility capacity. High strength steel produces a reduction in ductility.

Significant ductility in a structural member can be achieved only if inelastic strains can be achieved over a reasonably length of that member. At member level, the displacement ductility capacity μ_{Δ} is governed by the ability of plastic hinges at the ends to be sufficiently ductile. For vertical cantilevers, the relationship between curvature and displacement ductilities can be expressed by integrating the curvature along the height ℓ . Adopting a linear approximation and defining an equivalent plastic hinge length ℓ_p over which the plastic curvature is assumed equal to its maximum, the displacement ductility factor is:

$$\mu_{\Delta} = 1 + 3(\mu_{\chi} - 1) \frac{\ell_p}{\ell} \left(1 - \frac{\ell_p}{2\ell} \right) \quad (1)$$

Plastic hinge length is not only proportional to the length of the element because theoretical curvature distribution does not end suddenly at the base of the cantilever due to tensile yielding strain penetration (bar elongation beyond the theoretical base of the member). A detailed analysis of plastic hinge length is beyond the scope of this work and with adequate accuracy will be used a plastic hinge length equal to half the section depth.

Flexural behavior is described by means of a bi-linear force-displacement relationship at the top of the pier. The yield force is F_y , the stiffness $K = F_y/D_y$, where D_y is the top displacement at yield, the period $T = 2\pi\sqrt{M/K}$, where M is the mass of the deck inclusive of the pier cap and of a part of the pier (usually the upper half).

If the response is in the elastic range, the maximum force on the pier is:

$$F_{\max} = M \cdot S_a(T) < F_y$$

where $S_a(T)$ denotes an appropriate elastic acceleration response spectrum (depending on PGA and soil conditions), and failure can only occur if F_{\max}

exceeds the shear strength V_u .

In a ductility-based design, the spectral ordinates used for evaluating the forces acting on a structure are related to the amount of available ductility. In the inelastic range, the following equation applies:

$$F_{\max}(\mu) = \frac{M \cdot S_a(T)}{\mu} < F_y$$

where the dependence of F on the ductility actually required has been made explicit. Failure in this case can occur due to two different mechanisms: a flexural failure, if to satisfy previous equation it must be $\mu > \mu_{\Delta}$; a shear failure if F_{\max} exceeds V_u .

It is possible to define a pier upgrading index I_{pier} , to measure the increase from the available ductility μ_{Δ} of the “as built” section, to the target ultimate ductility μ (considering that the yielding point, and stiffness K , are almost constant after FRP wrapping).

$$I_{\text{pier}} = \frac{\mu}{\mu_{\Delta}} = \frac{M \cdot S_a(T)}{F_y \cdot \mu_{\Delta}} \quad (2)$$

The above formula states that a SDOF system having mass M , elastic period T , yield force F_y , under a response spectrum acceleration $S_a(T)$ is required to have pier upgrading index lower than 1 to be well-designed, or sound structure.

For insufficiently-designed or damaged structures, the upgrading index I_{pier} is greater than 1. This might occur, in practical cases, if: the mass M on top of the pier increases (e.g., enlargement of the deck to accommodate more lanes, or replacement of traffic barriers with heavier ones); the response spectrum $S_a(T)$ ordinate increases (e.g., change of the design spectrum in the seismic code, change in the conventional seismic classification); the pier available strength F_y or available ductility μ_{Δ} decreases because of damage. These two latter values can be found through usual assessment procedures.

Considering the most common case of unidirectional fibers wrapping in the

transverse direction with respect to the column axis (resulting in relevant increases of section ductility, with limited increases in flexural strength), a section upgrading index I_{sec} can be introduced analogous to that already defined in terms of displacement, and to measure the increase from the available curvature ductility $\mu_{\chi,av}$ of the “as built” section, to the target ultimate ductility $\mu_{\chi,tg}$ of the strengthened section.

$$I_{pier} = \frac{\mu}{\mu_{\Delta}} \xrightarrow{Eq.(1)} I_{sec} = \frac{\mu_{\chi,tg}}{\mu_{\chi,av}} \quad (3)$$

The section upgrading index value is a measure of upgrading requirement of the section (if needed). In the design procedure is involved also the evaluation of the plastic hinge length, that can increase after FRP wrapping. The shear failure, due to its brittle nature has to be avoided, and the shear strength can be evaluated taking into account the interaction between flexural ductility and shear strength (i.e. Priestley et al. 1994, where the strength component of concrete is reduced as flexural displacement ductility increases). Shear capacity is increased by the presence of FRP wraps with fibers oriented in the transverse (hoop) direction. Slender piers are considered, whose behavior is dominated by flexure. A detailed analysis of shear strength and plastic hinge length is beyond the scope of this work. The aim of the present work is to outline a procedure to design the upgrading jacket, through the evaluation of available curvature ductility $\mu_{\chi,av}$ and target ultimate ductility $\mu_{\chi,tg}$.

1.6 Chapter References

AASHTO, 2002: “Standard Specifications for Highway Bridges”, 17th Edition, Published by the *American Association of State Highway and Transportation Officials*, Washington D.C.

ACI 440.2R-02, 2002: “Guide for the Design and Construction of Externally Bonded FRP Systems for Strengthening Concrete Structures,” Published by the *American Concrete Institute*, Farmington Hills, MI.

American Concrete Inst. (ACI) Committee 318, 2005. “Building Code Requirements for Structural Concrete (ACI 318-05) and Commentary (ACI 318R-05)”, American Concrete Inst., Michigan, 369 pages.

CNR-DT 200, 2004, “Guide for the Design and Construction of Externally Bonded FRP Systems for Strengthening Existing Structures, Published by *National Research Council*, Roma, Italy.

Code of Practice for the Design of Concrete Structures (NZS 3101:1982), *Standards Association of New Zealand*, Wellington, 127 pages. 1982.

Kowalsky M.J., M.J.N. Priestley, (2000): “Improved Analytical Model for Shear Strength of Circular Reinforced Concrete Columns in Seismic Regions”, *ACI Structural Journal*, Vol.97, 3, pp.388-396.

Mander J.B. (1984) “Experimental behavior of ductile hollow reinforced columns”, In Proceedings, *8th World Conference on Earthquake Engineering*, Vol. 6, pp. 529-536.

Masukawa J., Suda K., Maekawa K. (2000) “Predicting post-peak behavior of high bridge pier with hollow section using a new model for spalling of cover concrete and buckling of reinforcement”, *12th World Conference on Earthquake Engineering*. CD-ROM: Paper No.1869

Mo Y.L., Jeng C.H., Perng S.F. (2001) “Seismic shear behavior of

rectangular hollow bridge columns”, *Structural Engineering and Mechanics*, Vol. 12, Issue 4, pp. 429-448.

Mo Y.L., Yeh Y.-K., Hsieh D.M. (2002) “Seismic retrofit of rectangular hollow bridge columns”, *In Proceedings, 7th National Conference on Earthquake Engineering*, Boston, ref. 373.

Ordinanza n. 3431, 2005, Ulteriori modifiche ed integrazioni all’ordinanza del Presidente del Consiglio dei Ministri n. 3274 del 20 marzo 2003, recante ‘Primi elementi in materia di criteri generali per la classificazione sismica del territorio nazionale e di normative tecniche per le costruzioni in zona sismica.

Osada K., Yamaguchi T., Ikeda S. (1999) “Seismic performance and the retrofit of hollow circular reinforced concrete piers having reinforcement cut-off planes and variable wall thickness”, *In transactions, The Japan Concrete Institute*, vol. 21.

Pavese A, Bolognini D, Peloso S. (2004). “FRP Seismic retrofit of RC square hollow section bridge piers.” *Journal of earthquake engineering*, Special issue 1;8:225-250.

Pinto P.E. and Monti G. (Eds) (2000), Vulnerability evaluation and strengthening criteria for R.C. bridges, *CNR-Gruppo Nazionale per la Difesa dai Terremoti - Roma*, 152 pp.

Pinto P.E., Giannini R. and Nuti C., (1997) “An automatic procedure for quantitative evaluation of seismic reliability of highway networks”, *Proc. of the Second Italy-Japan Workshop on Seismic design and retrofit of bridges*, Roma.

Priestley M.J.N., Park R. (1987) “Strength and ductility of concrete bridge columns under seismic loading”, *ACI Structural Journal*, Vol. 84, Issue 1, pp. 61-76.

Priestley M.J.N., R. Verma, and Y. Xiao, (1994): “Seismic shear strength of reinforced concrete columns”, *Journal of Structural Engineering*, Vol.120, 8, pp. 2310-2329.

Priestley M.J.N., Seible F., Calvi G.M. (1996) “Seismic Design and Retrofit of Bridges”, *John Wiley & Sons, Inc.*, 314 pages.

Ranzo G., Priestley M.J.N. (2000) “Seismic performance of large RC circular hollow columns”, In Proceedings, *12th World Conference on Earthquake Engineering*, ref. 0250.

Takahashi Y., Iemura H. (2000) “Inelastic seismic performance of RC tall piers with hollow section”, In Proceedings, *12th World Conference on Earthquake Engineering*, ref. 1353.

Taylor A., Rowell R.B., and Breen J. (1995), “Behavior of Thin Walled Concrete Box Piers,” *ACI Structural Journal*, Vol. 92, No. 3, pp. 319-333.

Whittaker D., Park R., Carr A.J. (1987) “Experimental tests on hollow circular Concrete columns for use in offshore concrete platforms”, In Proceedings, *Pacific Conference on Earthquake Engineering*, New Zealand, Vol. 1, pp. 213-224.

Yeh Y.-K., Mo Y.L. (2002) “Seismic Performance of rectangular hollow bridge columns”, *Journal of Structural Engineering*, Vol.128, 1, pp. 60-68.

Yeh Y.-K., Mo Y.L. (2005) “Shear Retrofit of Hollow bridge Piers with Carbon Fiber-Reinforced Polymer sheets”, *Journal of Composite for Construction*, Vol.9, 4, pp. 327-336.

Yeh Y.-K., Mo Y.L., Yang C.Y. (2001) “Seismic Performance of hollow circular bridge piers”, *ACI Structural Journal*, Vol. 98, Issue 6, pp. 862-871.

Zahn F.A., Park R., Priestley M.J.N. (1990) “Flexural Strength and ductility of circular hollow reinforced concrete columns without confinement on inside face”, *ACI Structural Journal*, Vol. 87, Issue 2, pp. 156-166.

Chapter 2

Experimental Campaign: From the design of the test matrix and test set-up to the main experimental outcomes

2.1 Test Matrix and Set-Up Design

Full-scale testing of the structures is out of the question, both for logistic and cost reasons, and also because data are needed prior to the design of the structure. Engineers thus have to rely on scale-model tests to predict the behavior of the prototypes and consequently to know how to estimate ultimate strains and stresses in the structures from the results obtained in scaled-down specimens.

The probability of finding a serious flaw in a structural member increases with its size and varies with the type of material. Tests of unidirectional FRP cylinders show, for example, greater scatter of mechanical properties than do tests of metal specimens. The question arises of whether this fact, due partially to the larger density of microdefects in the FRP, should make the design strength -or equivalent parameter- dependent on the volume of material involved.

In the state of the art review was found that only in few cases real scale models was tested, especially when retrofitted, due to the high intensity forces to be applied and to the dimensions of the testing specimens. For example, some studies showed that real scale prototypes had greater ductility than scaled models.

So, the experimental program has been planned on hollow columns in

reduced scale. Test specimens reproduce in scale typical bridge piers having section area of $1800 \times 1800 \text{ mm}^2$, wall thickness of 300 mm and height equal to 6.50 m, longitudinal reinforcement made by 44-D30 steel bars and stirrups D12@30 cm;

The selection of the scale factor has been driven by two considerations: the attempt to study specimens whose dimensions were sufficiently large to represent the behavior of real piers and the need to respect laboratory constraints.

A feasibility analysis has been conducted to determine the scale factor that satisfied the following four constraints:

- Specimens dimensions and weight compatible with the laboratory facilities (i.e. 4.2 m in height under the testing machine and maximum weight of 3 tons for the crane capability)
- The maximum axial force that is possible to apply on a specimen is 3000 kN under the Testing Machine at the Department of Structural Analysis and Design at the University of Naples “Federico II”
- To have a reasonable margin on the unstrengthened specimen load capacity to be able to test up to failure also the strengthened specimens: there are not yet reliable models to predict the capacity of FRP wrapped hollow square columns.
- Technological reasons, the wall thickness should be large enough to let the specimen contain the required (scaled) steel reinforcement both longitudinal and transversal.

Accordingly, different scale factor have been evaluated and the main results are summarized in table 2.1, where unstrengthened axial capacity have been evaluated according to conventional RC theory assuming a concrete compressing strength of 25 MPa and steel strength of 500 MPa.

Table 2.1 – Feasibility Analysis

Scale factor	Height Hollow Portion [mm]	Weight Hollow Portion [ton]	Square Side [mm]	Wall Thickness [mm]	Ultimate capacity [kN]
1:1	6500	29.250	1800	300	58424
1:2	3250	3.656	900	150	14606
<u>1:5</u>	<u>1300</u>	<u>0.234</u>	<u>360</u>	<u>60</u>	<u>2337</u>
1:10	650	0.029	180	30	584
1:20	325	0.004	90	15	146

With reference to the adopted reduction scale factor 1:5, all the dimensions involved in the experimental campaign has to be scaled according to the following scale factors (table 2.2).

Table 2.2 – Scale factors

Physical Parameter	Scale Factor
Length	1:5
Area	1:25
Volume	1:125
Force	1:25
Strain	1:1
Stress	1:1

The scale factor 1:5 has then been chosen and tested specimens had hollow section external dimensions of $360 \times 360 \text{ mm}^2$ and walls thickness of 60 mm. The internal reinforcement was given by 16-D10 longitudinal bars with 25 mm

concrete cover and D4 stirrups at 80 mm on center.

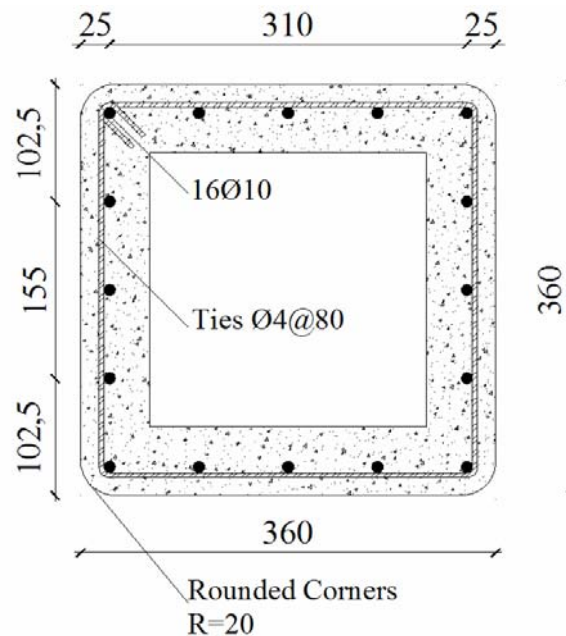


Figure 2.1 – Specimen Section Geometry

The hollow portion of the column had a height of 1.30 m and was made by foam-polystyrene.

The test matrix was designed in order to assess the FRP wrapping effectiveness in correspondence of three P/M ratios, which are three different neutral axis positions. The parameters used to assess the FRP benefits were flexural strength increases (interpreting the modifications to the P-M diagram) and ductility (analyzing load-deflection and moment-curvature curves). Accordingly three specimens have been tested un-strengthened (Series U = Unstrengthened), while other three have been strengthened with CFRP laminates (Series S = Strengthened). A simply axially loaded unstrengthened specimen (U0) was

also tested.

The three eccentricities of 50 mm, 200 mm and 300 mm have been selected to study the behavior of the hollow members under P-M combinations carrying the neutral axis at ultimate load external to the cross section ($e = 50$ mm, fully compressed), at mid-height ($e = 200$ mm), and close to the compressed flange ($e = 300$ mm). The matrix of tests done is reported in Table 2.3, where e is the load eccentricity kept constant during each test. Note that a construction issue did not allow testing of both specimens U1 and S1 with eccentricity of 50 mm; the actual eccentricity was 52 mm and 80 mm.

Table 2.3 – Test Matrix

Specimen Code	Loading Condition	Eccentricity e (mm)
U0 – ...	Pure Compression	0
U1 – S1	Combined Compression and Flexure	50* (52-80)
U2 – S2	Combined Compression and Flexure	200
U3 – S3	Combined Compression and Flexure	300

In the U-series and S-series the two ends have been designed with corbels to allow the application of the axial load with the desired eccentricity as showed in Figure 2.6b of the test set-up, whereas the heads had solid sections in order to distribute the load and avoid local failures.

In Figures 2.2 to 2.5 are shown the specimen details: concrete geometry, steel reinforcement cages, construction details, etc...

The load is applied in cycles through hydraulic actuators in force control at the first stage with 2kN/sec rate, then in displacement control up to failure at 0.002 mm/sec. Some cycles at low load levels (up to about 30 percent of theoretical ultimate load) were performed only to check the test and to verify that no anomalous effects occurred in the elastic range.

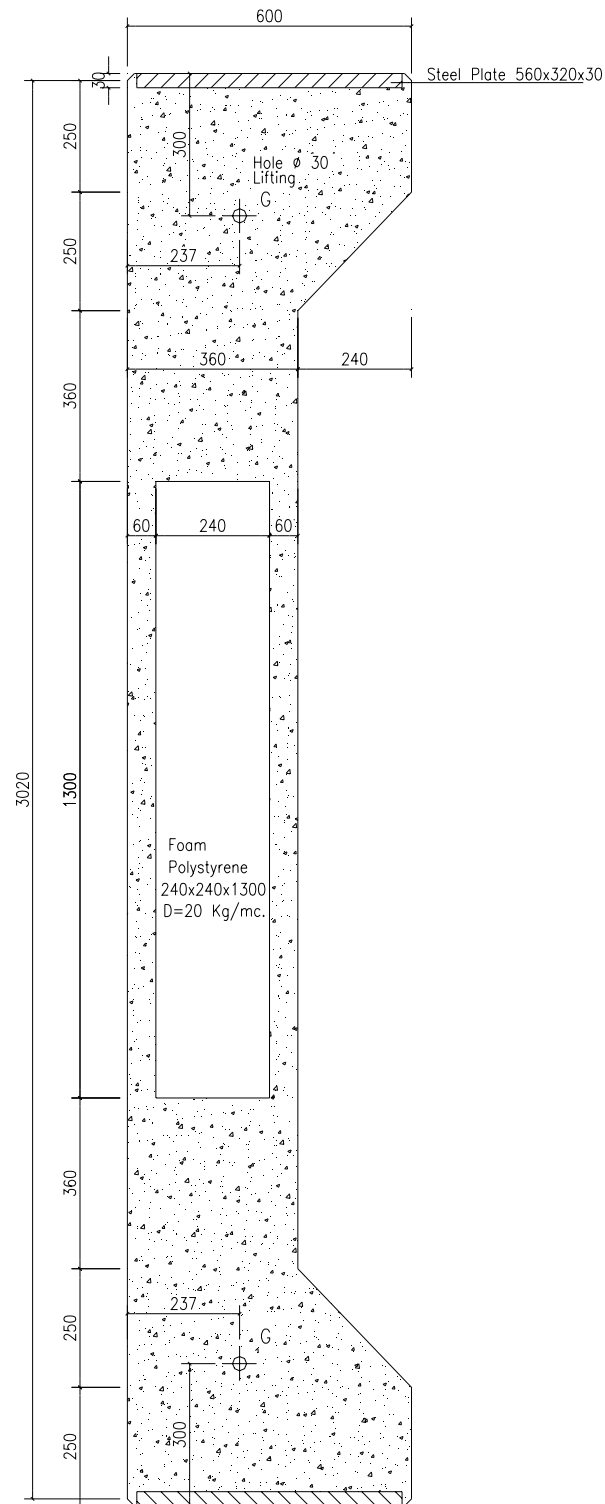


Figure 2.2 – Specimen Geometry

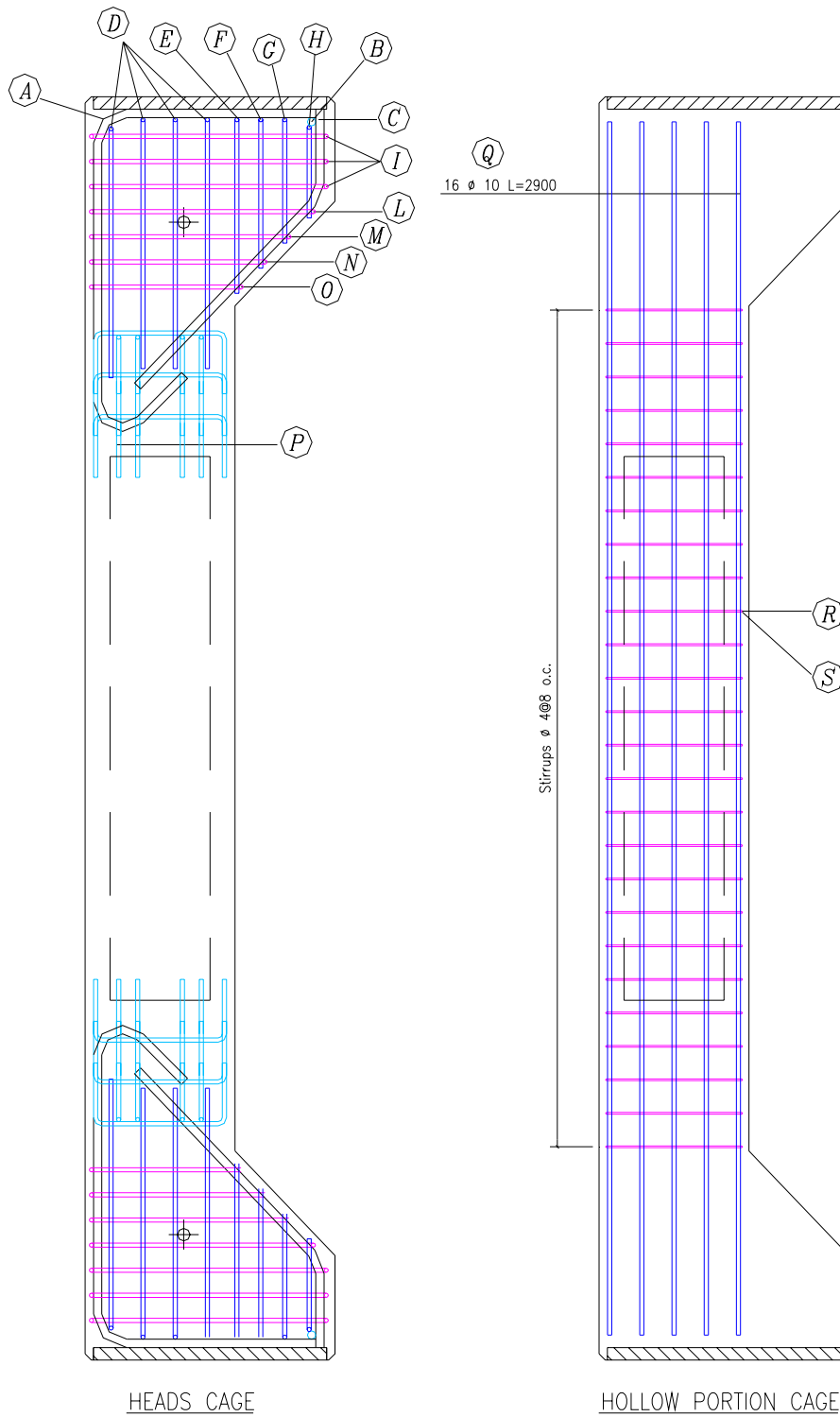


Figure 2.3 – Specimen Steel Reinforcement cages

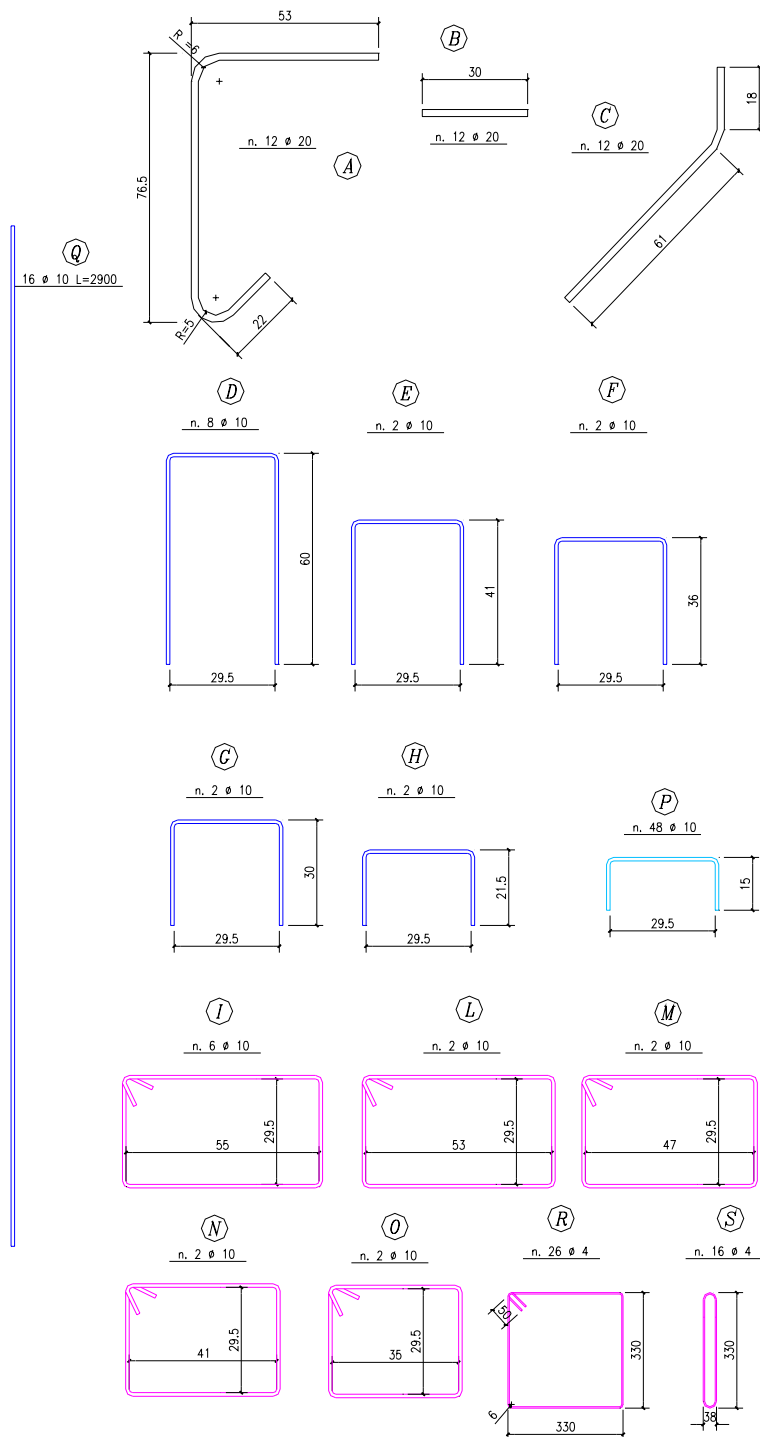


Figure 2.4 – Steel Reinforcement details



Figure 2.5 – Specimen: cage ready for concrete pouring and after concrete curing

In order to apply the axial load with the desired eccentricity, two open hinges have been designed (fig. 2.6a) to facilitate the centering of the specimen under the testing machine and to apply an eccentric axial load without shear and having free rotations at the two specimen ends.

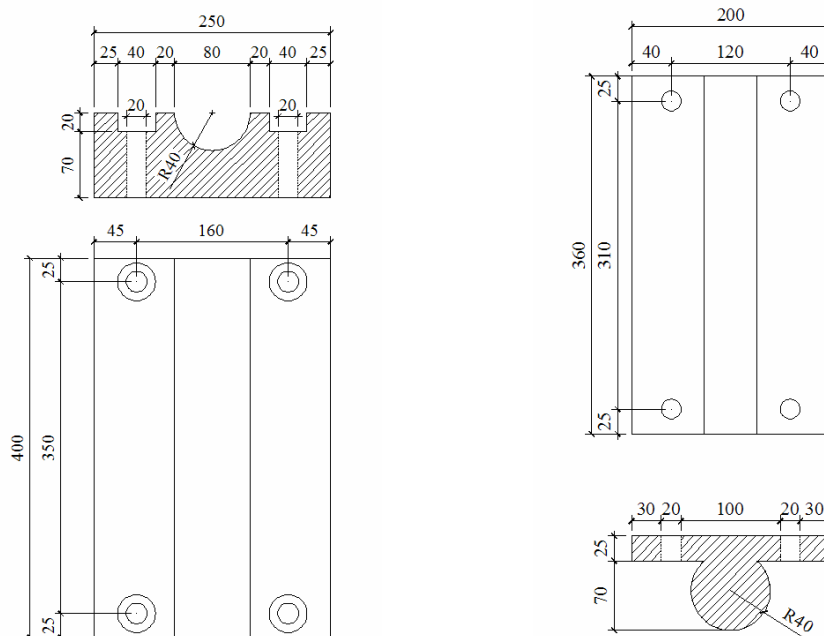


Figure 2.6a – Open Hinges designed to apply eccentric loads up to 3000 kN

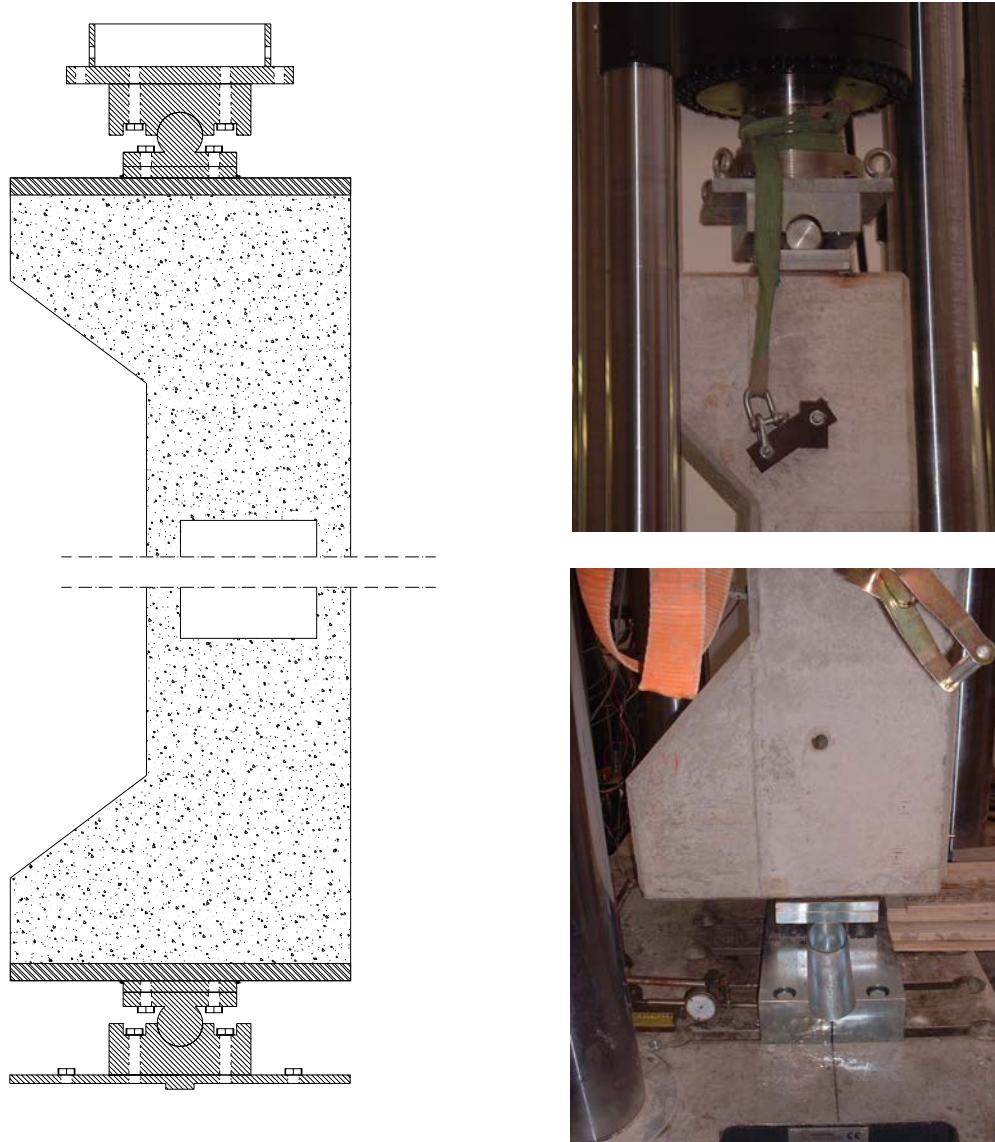


Figure 2.6b – Specimen on the testing machine under eccentric loading

2.1.1 Materials Characterization

Some tests have been executed on concrete and steel bars: during concrete pouring five specimens of plain concrete have been taken and nine pieces of steel

longitudinal bars (D10) picked up. Concrete specimens have been crushed and test results (tab. 2.4) show a mean compressive strength of 32 MPa.

Table 2.4 – Test results on plain concrete specimens

Specimen #	Weight [kg]	Volume [m ³]	γ [kg/m ³]	Ultimate Load [kN]	Strength [MPa]
1	7.660	0.0034	2269.63	866.50	38.51
2	7.650	0.0034	2266.67	767.00	34.09
3	7.655	0.0034	2268.15	669.80	29.76
4	7.680	0.0034	2275.56	720.20	32.00
5	7.715	0.0034	2285.93	613.40	27.30
Mean	7.672	0.0034	2273.18	727.38	32.33

Three series of steel bars have been also tested. The first one have been tested under tension, while the other two under compression with a Length to Diameter L/D ratio of 8 and 16 (to simulate the different free length of the compressed bar). Depending on the stirrup stiffness, the compressed longitudinal bar between two stirrups has different free length: the distance of the two testing grips have to be one or two times the stirrup spacing to simulate stirrups that are relative stiff or weak, respectively. A completely different behavior can be observed (fig. 2.7) in the three cases: the instability in the compression case (buckling) have been extensively described and accounted for in the following chapters. Test results show a mean tensile strength of 600 MPa and a yield stress of 506 MPa (that in compression roughly correspond to buckling stress in the case of L/D = 16).

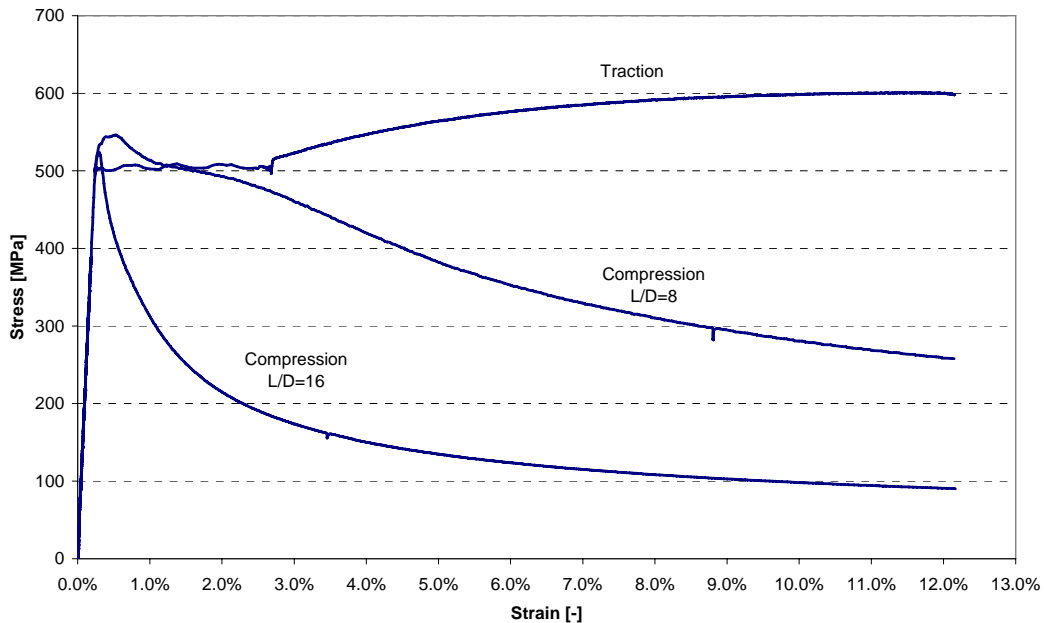


Figure 2.7 – Experimental Stress-Strain behavior for longitudinal steel reinforcement

The theoretical P-M interaction diagram of the reinforced square hollow section is plotted in figure 2.9 based upon conventional RC theory (not taking into account premature failure modes such as reinforcement buckling) and 3 points at selected eccentricities shown in test matrix are highlighted in order to evaluate the neutral axis depth. The procedure adopted to draw the interaction diagram is fully explained in the next Chapter 3.

In Figure 2.9 is also represented the interaction diagram of a solid column with the same external dimensions of the hollow section and the same internal longitudinal steel reinforcement. Both diagrams are equal until the neutral axis pass through the hollow portion of the section

The U0 specimen column have the same hollow portion length and shorter heads 400 mm of solid cross section without corbels and proper reinforcement to avoid localized failures during the loading. Ties spacing was constant throughout the overall length of the specimen (in figure 2.8 is specimen U0 at failure). The

capacity of this specimen (axial load $P_{\max} = 2929$ kN) was very close to the predicted value (see table 4.1)



Figure 2.8 – Column U0 at failure

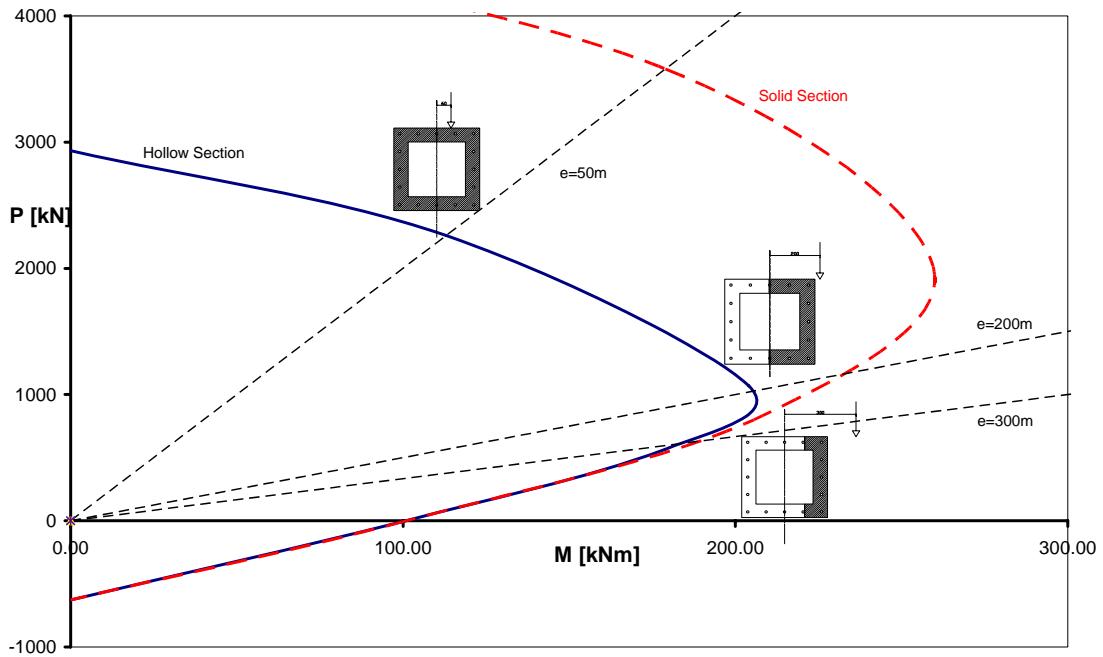


Figure 2.9 – Interaction PM Diagram (not taking into account premature failure modes)

2.2 Strengthening scheme

Two plies of CFRP unidirectional fabric with density of 600 gr/m^2 have been applied in all S specimens for the entire specimen height. Tensile modulus of elasticity of the CFRP (Figure 2.10) material is 230 GPa and ultimate tensile strength is 3450 MPa. The fabrics have a nominal width of 400 mm and nominal thickness (dry) of $333 \text{ }\mu\text{m}$.

The solid parts have been further reinforced with a third layer of CFRP in order to avoid the occurrence of failure in zones not of interest for the tests but subjected to high compressive stress concentrations.

The CFRP laminates were applied by manual lay-up in the transverse

direction. Corners were rounded with a radius of 20 mm as prescribed in many codes and the two plies have been overlapped by 200 mm. The number of installed plies was considered an upper limit that could be derived from an economical and technical analysis, also accounting for the scale reduction. On this scheme the CFRP reinforcement ratio is four times bigger than the stirrups reinforcement ratio. Nevertheless it has been observed that the influence of the number of layers of FRP on the solid section specimen under eccentric loading is not so pronounced as that of the specimen under concentric loading (*Li et Hadi 2003*). The choice of carbon fibers over glass and aramid has been made since the former have not only better mechanical properties with respect to glass and aramid both in terms of ultimate strength and elastic modulus but also have the best durability performance in exposed environments, guaranteeing the longest life of the intervention.

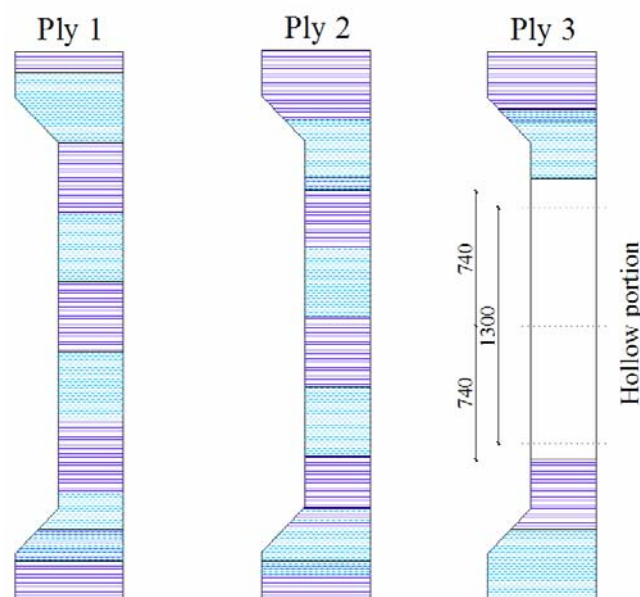


Figure 2.10 – CFRP Strengthening Scheme

Surface Preparation: the concrete surfaces have been freshly exposed and freed of loose or unsound materials. The corners have been rounded to a minimum 20 mm radius to prevent stress concentrations in the FRP system and voids between the FRP system and the concrete. All laitance, dust, dirt and any other thing that could interfere with the bond of the FRP system to the concrete have been removed. Bug holes and other small surface voids have been completely exposed during surface profiling.

Primer application (fig. 2.11a): primer has been applied to all areas on the concrete surface where the FRP system is to be placed. The primer has been placed uniformly on the prepared surface. Primer is wet before applying putty, which is used to ensure concrete surface evenness.

Putty Application (fig. 2.11b): putty has been used in an appropriate thickness and after the primer as recommended by the FRP manufacturer. The system-compatible putty is a thickened epoxy paste used to fill voids and smooth surface discontinuities before the application of other materials. Prior to applying the saturating resin, the primer and putty partially cured as specified by the FRP system manufacturer.

CFRP wet lay-up application (fig. 2.11c-d): fabrics have been kept free from any contamination and checked for possible damage. Wet lay-up FRP is installed by hand using dry fiber sheets and a saturating resin. The saturating resin has been applied uniformly to prepared surfaces. The fibers were impregnated before placement on the concrete surface. The reinforcing fibers have been gently pressed into the uncured saturating resin. Entrapped air between layers has been rolled out before the resin set. Sufficient saturating resin has been applied to achieve full saturation of the fibers. Successive layers of saturating resin and fiber materials have been placed before the complete cure of the previous layer of resin. The application has been completed within the pot life of the resins.



Figure 2.11 –Strengthening Application: (a) Primer application, (b) putty application, (c) saturating resin application, (d) fabrics application

FRP System materials have been supplied by MAPEI. In table 2.5 trade names of the materials adopted are reported.

Table 2.5 – Adopted FRP system materials

Fabric	MapeWrapC Uni-Ax 600/40
Primer	MapeWrap Primer1 A+B
Putty	MapeWrap12 A+B
Resin	MapeWrap31 A+B

2.3 Instrumentation

All columns have been monitored with strain gauges placed on the internal steel longitudinal reinforcement. Linear Variable Differential Transformers (LVDTs) have been used to monitor deflections and end rotations and then derive cross section deformations. LVDTs on the opposite faces in the bending plan gain a medium behavior of the concrete that can be compared to strain gauges data. These data from LVDTs, strain gauges and load cell are collected continuously by a data acquisition system.

2.3.1 Internal Instrumentation

All columns have been monitored with at least four strain gauges placed at mid span of the column on the internal steel longitudinal reinforcement on opposite sides of the section, two on tension side and two on compression side. Specimens U3 and S1 had eight more strain gauges. The same layout has been

used to measure strains at about 600 mm above and below the mid span section.

In figure 2.12 is a strain gauge placed on smoothed bar before the application of the protective coating and after.



Figure 2.12 –Strain Gauge on the internal steel reinforcement

In figure 2.13 is reported the layout of the four strain gauges placed on reinforcement to measure section strains.

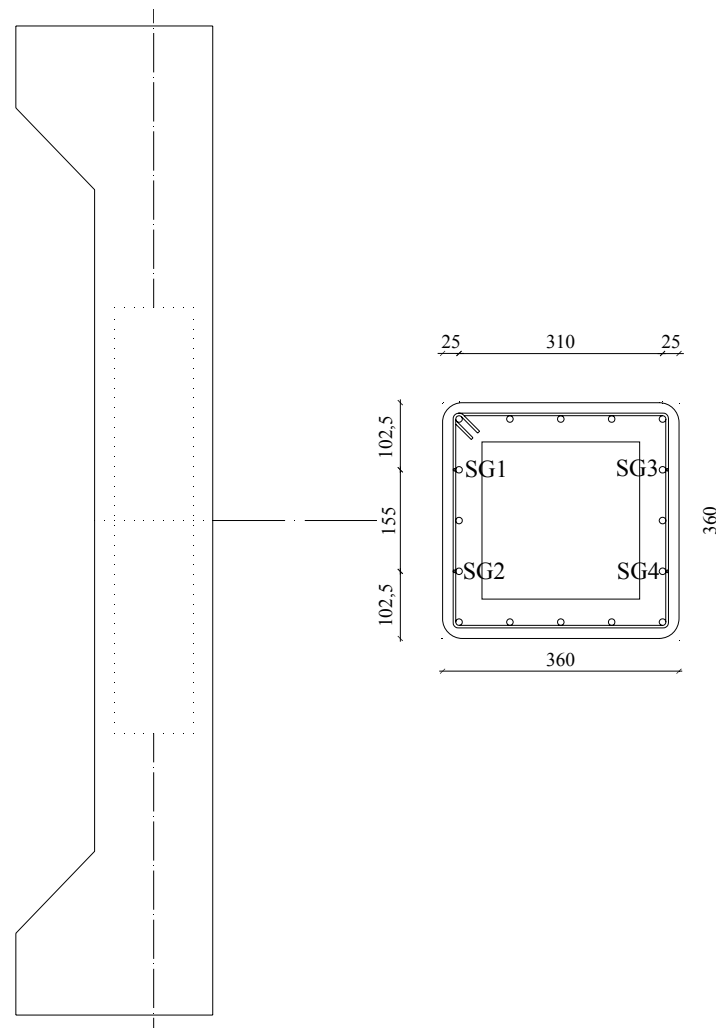


Figure 2.13 –Strain Gauge layout

2.3.2 External Instrumentation

Two vertical LVDTs (with a gauge length of 400 mm) have been applied on the opposite faces in the bending plan to measure (relative) medium behavior of the concrete in the hollow portion in compression and tension.

Two vertical LVDTs have been applied on the opposite faces of the lower

steel plate to measure (absolute) the displacement of the lower end and to estimate the average rotation of the base relative to the hinge.

Two horizontal LVDTs have been applied on the lateral and back side respectively of the column at mid span, in order to measure the absolute displacement (deflection) in the plane of the deflection and on the normal plane. The first measure was relevant for the safety of the test, because it gave a rough measure of the out of plane, spurious, load.

Only on the strengthened specimens were applied nine Strain Gauges on FRP wrapping parallel to the fiber direction to measure lateral strains in the jacket. Along the mid span section have been applied five of them on the front, most compressed, wall, other two further on 120 mm on the other side of the corner and other two on the middle of the front wall 400 mm above and below the mid span section.

In figure 2.15 is reported the layout of the LVDTs placed on the specimens, and the external Strain Gauges on the FRP jacket (in the case of specimen S2).



Figure 2.14 –LVDTs on the hollow portion

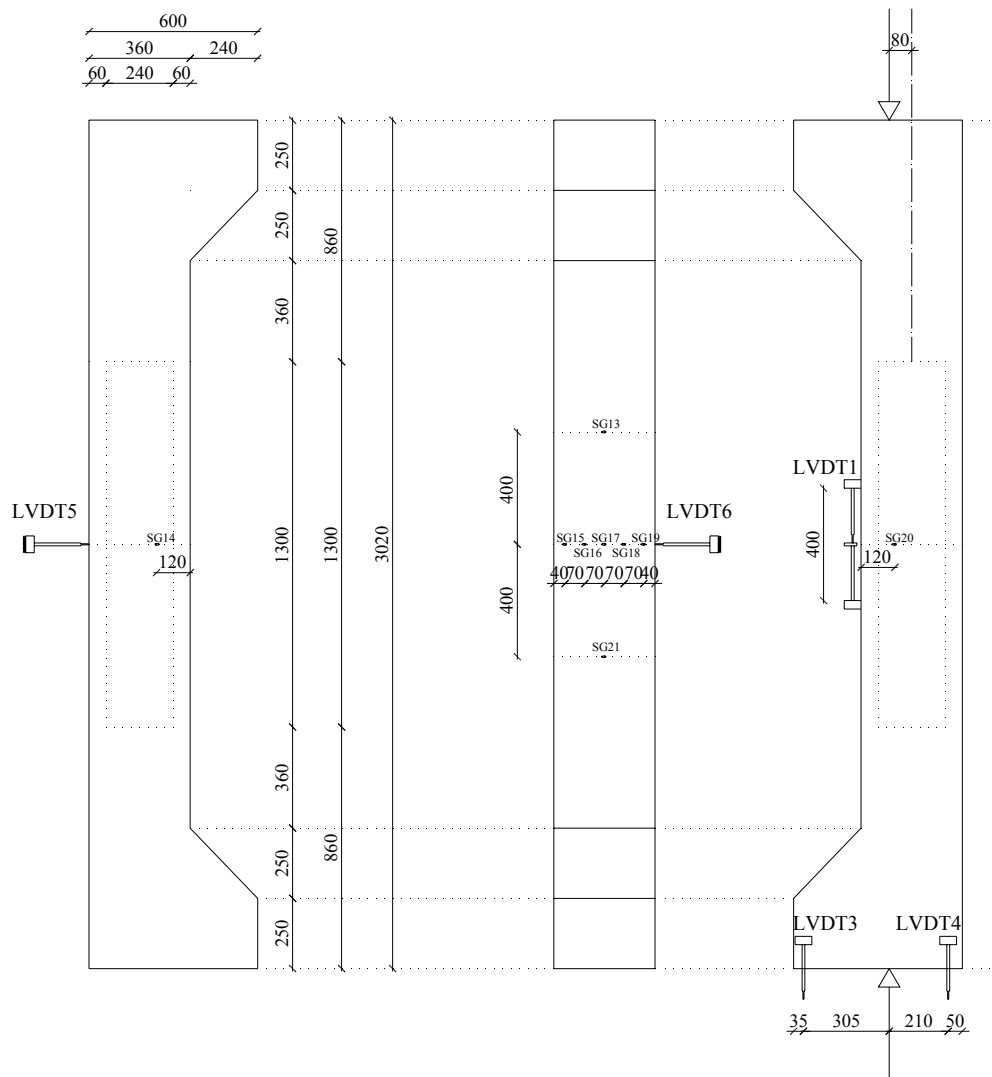


Figure 2.15 –LVDTs layout (specimen S2)



Figure 2.16 –LVDTs to measure hinge rotations

2.4 Test Results

In the next paragraphs a report is described in terms of local and global behavior of the specimens with and without FRP reinforcement: to underline the different behavior, results and graphs for each specimen are reported.



In Chapter 4 with reference also to the theoretical considerations, the main experimental outcomes are methodically and comparatively discussed and FRP effectiveness is assessed.

2.4.1 Specimen U1: test results

The failure of this column has occurred at the basis of the hollow column, in correspondence with discontinuity due to the change from the solid section of the ends to the hollow section. The failure was particularly brittle with sudden crush of the concrete in compression and concrete cover spalling (Fig. 2.17).

Buckling of the compressed steel bars occurred in the crushing zone: the buckling was outward.

The axial load eccentricity was small enough to allow the hollow section to be fully compressed. The neutral axis was outside the section, close to the rear wall: strain diagram was almost triangular, with higher strains on the crushed wall.

The deflection (not measured in this case) was very small so that the flexural moment was almost constant along the length of the hollow column ($P\Delta$ effects are negligible).



Figure 2.17 –Crushed wall and steel reinforcement buckling (U1)

In Figure 2.18 is reported the strain versus axial force P diagram. Strain diagrams are obtained from data of vertical LVDTs on a gauge length of 400 mm placed on the exterior wall, and good agreement was generally found with strain gage measurements on steel bars. The ultimate axial capacity was 2264 kN.

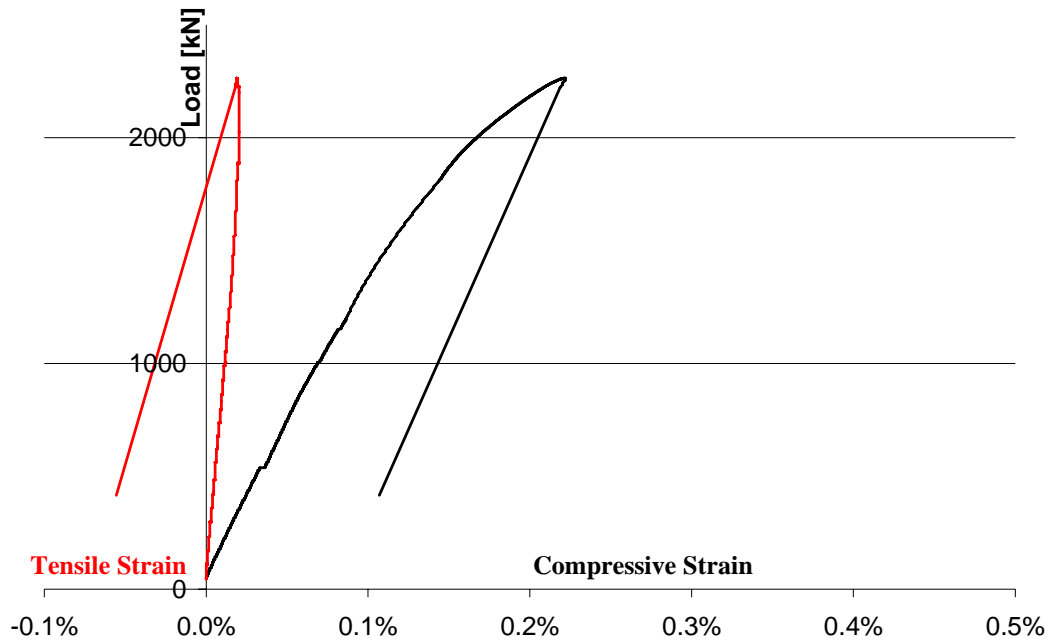


Figure 2.18 –Strains vs. Axial Load Diagram (U1)

It is clearly shown the brittle failure, the loss of load carrying capacity of the specimen when the concrete strains were as small as 2‰ and when steel compressed bars did not reach the yielding strain. This gives evidence of the brittle failure due to steel reinforcement buckling and concrete cover spalling.

Starting from axial load and LVDTs readings it is possible to plot also the moment-curvature diagram (Figure 2.19). The experimental curvature was computed connecting 3 data points, 1 on compressive concrete fiber and 2 on

internal steel reinforcement bars (compressive strains are positive). Moments M are based on the equations $M = P \cdot e$ where P and e are axial force and eccentricity respectively.

Initial diagram slope is matching the theoretical initial gross hollow cross section flexural stiffness EI . In the first linear elastic phase before concrete cracking and neutral axis migration it is possible to refer to the well known relationship: $\chi = M/EI$, then, due to the cracking process, the effective moment of inertia reduces and tension stiffening effects take place. Due to the sudden bearing capacity drop there is no curvature increment after-peak.

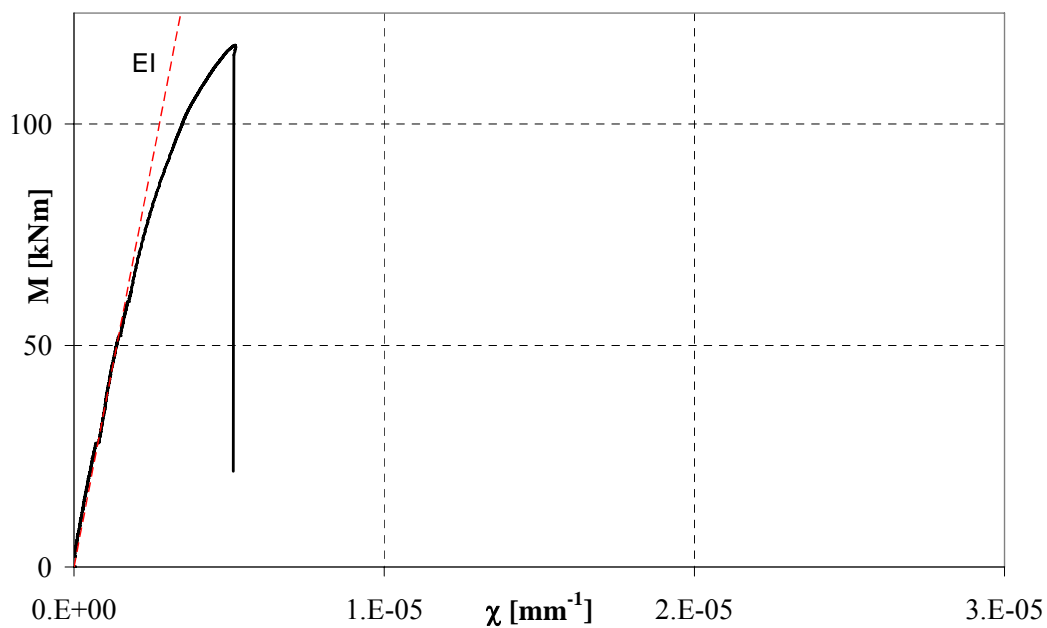


Figure 2.19 –Moment Curvature Diagram (UI)

2.4.2 Specimen U2: test results

The failure of this column has occurred at mid-span, where the $P-\Delta$ effects mostly impact flexural moment. The failure was brittle (less than before) with sudden crush of the concrete in compression and concrete cover spalling (Fig. 2.21). In this case, the buckling of the compressed steel bars occurred in the crushing zone, but it was both inward and outward.

The axial load eccentricity (in this case 200 mm) put the hollow section both in tension and compression. The neutral axis was inside the section, close to the middle of the section: strain diagram was bitriangular.

In Figure 2.20 is reported the strain versus axial force P diagram. Strain diagrams are obtained from data of vertical LVDTs and good agreement was generally found with strain gage measurements on steel bars.

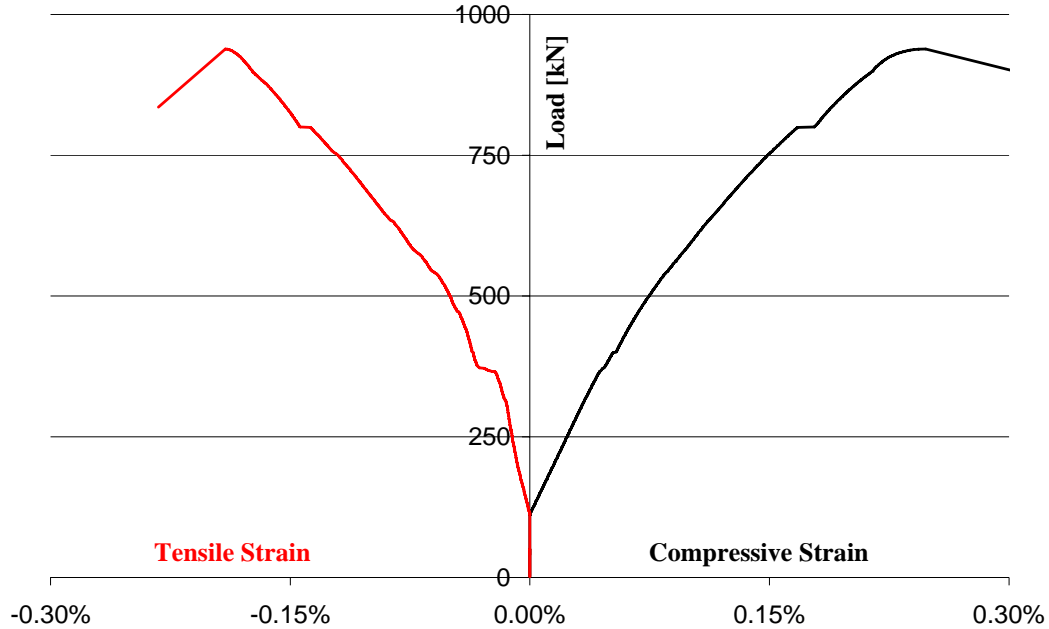


Figure 2.20 – Strains vs. Axial Load Diagram (U2)



Figure 2.21 –Crushed wall and steel reinforcement buckling (U2)

It is clearly shown (Figure 2.20) the brittle failure, the loss of load carrying capacity of the specimen when the concrete strains were as small as 2.5‰. This gives evidence of the brittle failure due to steel reinforcement buckling and concrete cover spalling. The ultimate axial capacity was 939 kN. Tension reinforcement did not reach yielding strains.

The deflection has been measured. In Figure 2.22 is the mid span deflection vs. axial load diagram: at peak load it was 11.51 mm, with respect to the imposed eccentricity it causes a small $P\Delta$ effect of less than 6%.

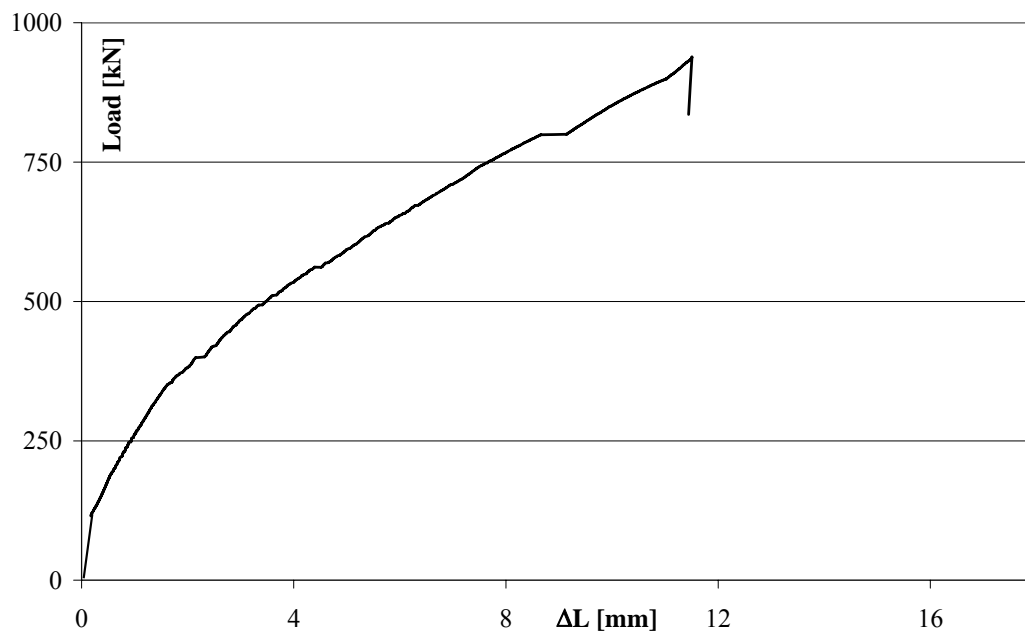


Figure 2.22 – Mid Span Deflection Diagram (U2)

In Figure 2.23 is plotted also the moment-curvature diagram: the brittle behavior of the U2 specimen is clear reading this diagram. Due to the sudden bearing capacity drop there are no curvature increments after-peak.

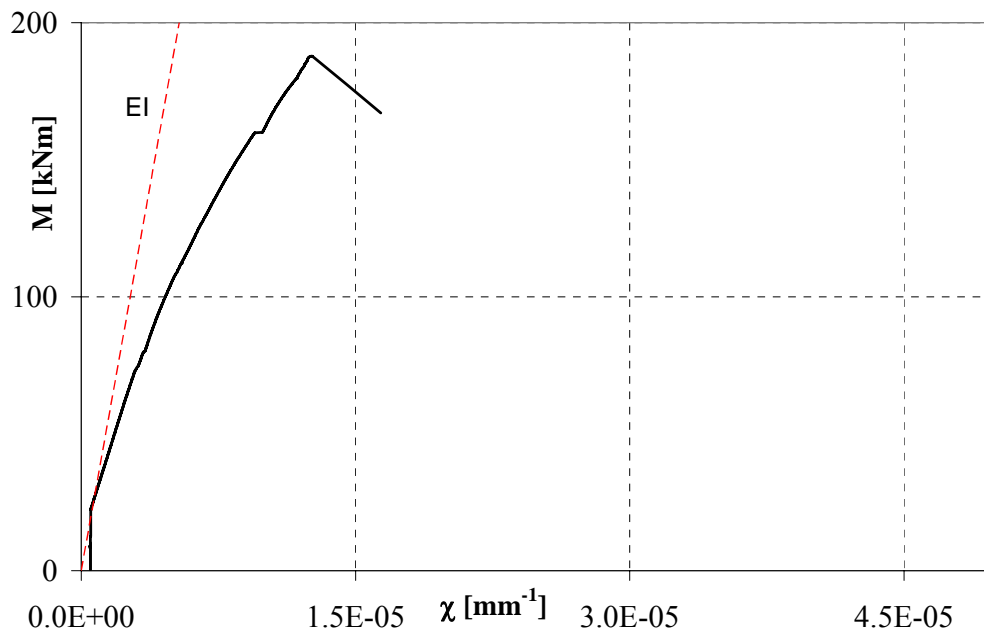


Figure 2.23 – Moment Curvature Diagram (U2)

As explained later in the theoretical analysis Chapter: hinge rotation is assumed to be due to the *constant* curvature of the hollow portion of the column (constant moment hypothesis and curvature evaluated from the experimental data).

Hinge rotations have been recorded by two LVDTs placed on the steel plate at the lower end of the column. Calculated hinge rotations can be compared with estimated rotations (Figure 2.24). Symmetry considerations allow evaluating rotations by multiplying constant mid-span curvature by length of half column (only the hollow portion, because in order to evaluate rotations, solid portions are supposed rigid).

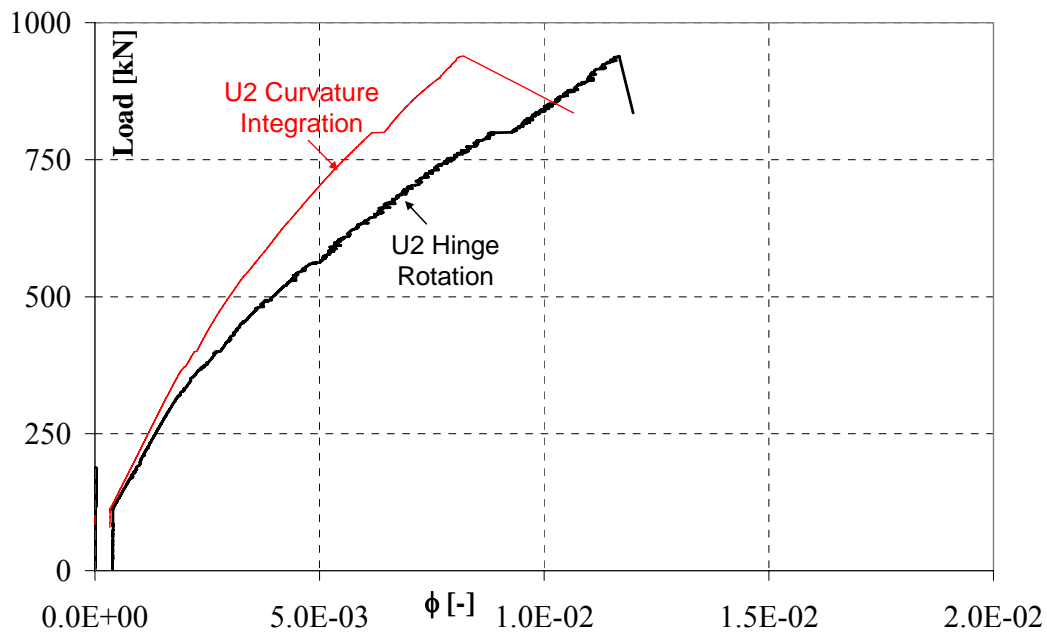


Figure 2.24 – Hinge rotations and estimated rotations Diagram (U2)

The two obtained curves (figure 2.24) are almost matching up before the peak load, validating the hypothesis on different stiffness of hollow and solid portions. Instead the different slope in the post-peak phase can be easily explained. The global rotation evaluated numerically by integration is due to the cracked section curvature, and does not take into account well known tension stiffening effects. Besides the curvature is not really constant along the column and mid-span evaluated curvature overestimates average curvature.

2.4.3 Specimen U3: test results

The failure of this column has occurred at the basis of the hollow column, in correspondence with discontinuity due to the change from the solid section of the ends to the hollow section. The failure was brittle with crush of the concrete in

compression and concrete cover spalling also inside the hollow portion (Fig. 2.25). In this case, the buckling of the compressed steel bars in the crushing zone was substantially less noticeable. The portion of the specimen where failure occurred was separated and also the interior of the walls was observed.

The axial load eccentricity (in this case 300 mm) put the hollow section both in tension and compression. The neutral axis was close to the internal side of the compressed wall: strain diagram was bitriangular. A wide crack opened in the tension wall and had a depth of about 270 mm on the side walls.



Figure 2.25 –Crushed wall and steel reinforcement buckling (U3)

In Figure 2.26 is reported the strain versus axial force P diagram. Strain diagrams are obtained from data of vertical LVDTs and good agreement was generally found with strain gage measurements on steel bars.

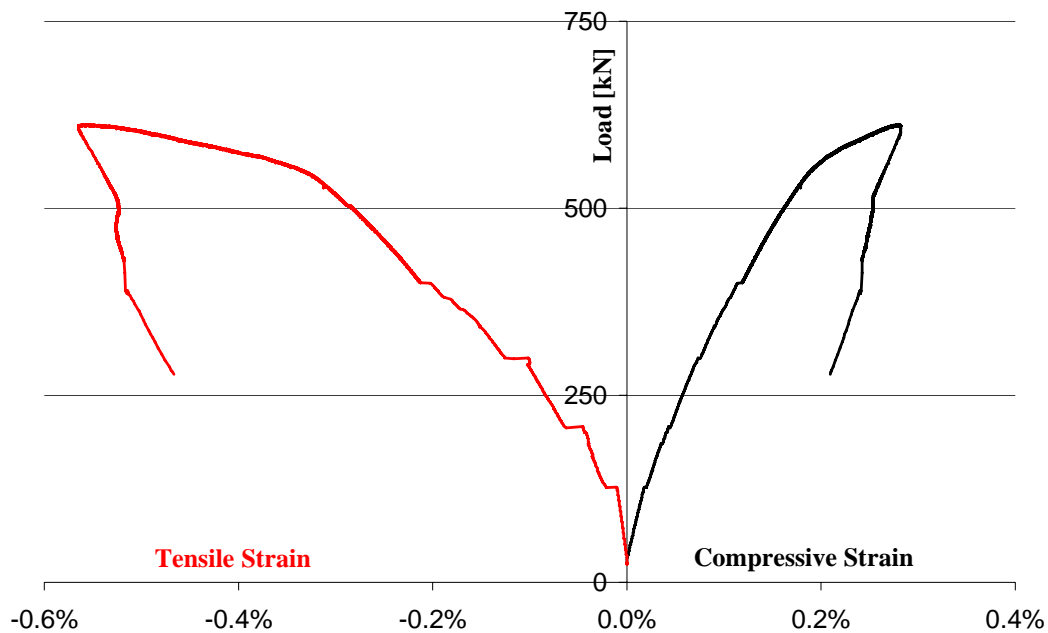


Figure 2.26 –Strains vs. Axial Load Diagram (U3)

It is clearly shown (Figure 2.26) the brittle failure, as a loss of load carrying capacity of the specimen after peak load when the concrete strains were as small as 3.0%. The ultimate axial capacity was 612 kN. Tension Reinforcement reached yielding strains.

In Figure 2.27 is the mid span deflection vs. axial load diagram: at peak load it was 18.57 mm, with respect to the imposed eccentricity it caused small P Δ effects of about 6%.

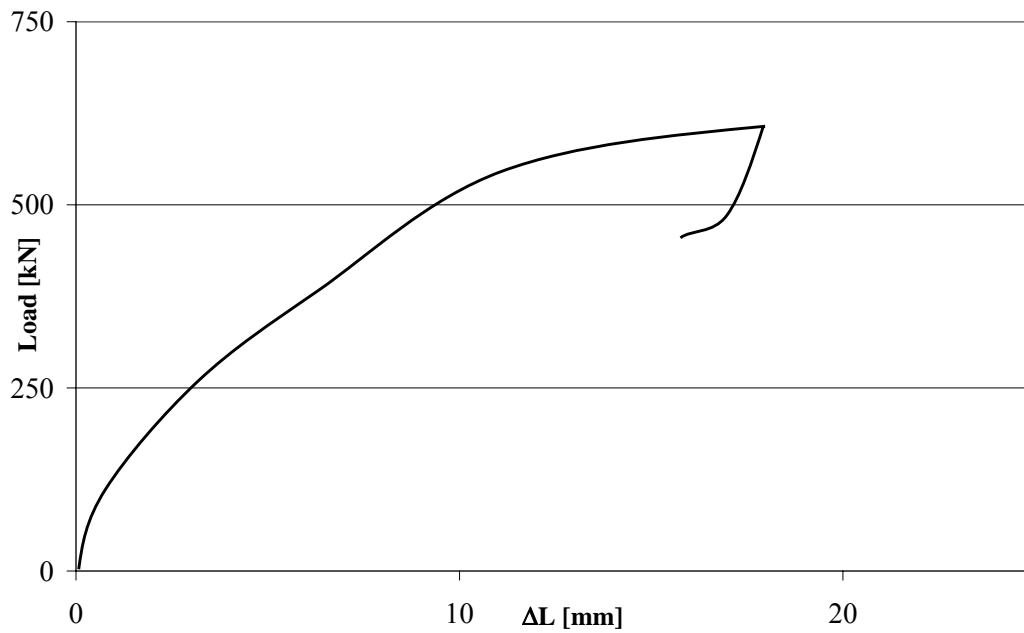


Figure 2.27 – Mid Span Deflection Diagram (U3)

In Figure 2.28a is plotted also the moment-curvature diagram: the brittle behavior of the U3 specimen is clear again. Due to the sudden bearing capacity drop there are no curvature increments after-peak. But a certain amount of ductility is given by the tensile steel yielding; the Yielding Moment M_y was about 168 kNm.

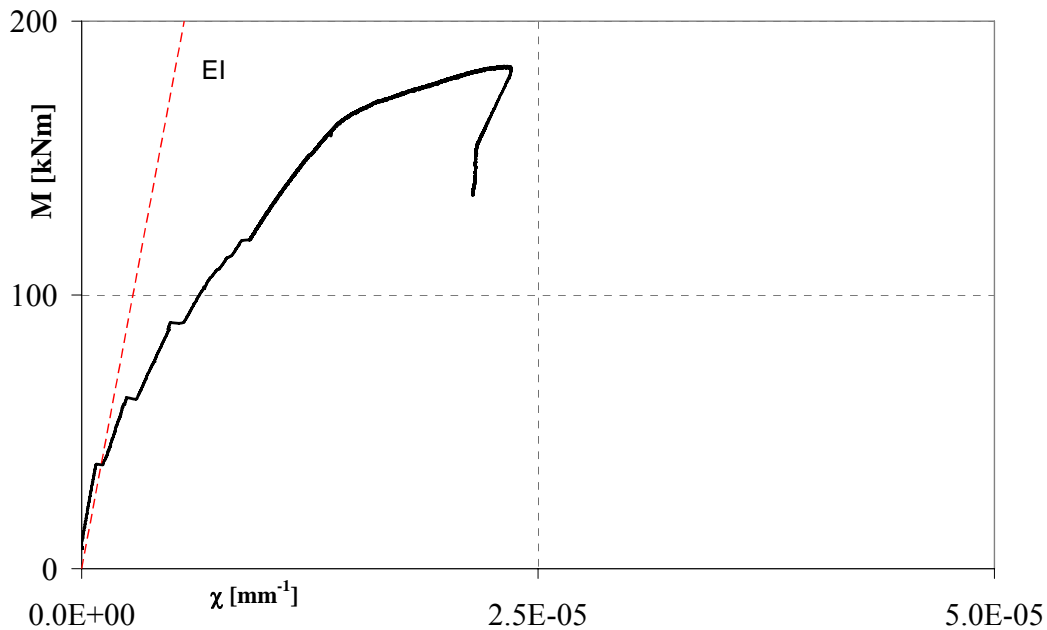


Figure 2.28a – Moment Curvature Diagram (U3)

Calculated hinge rotations can be compared with estimated rotations (Figure 2.28b). The two obtained curves are almost matching up before the peak load, the global rotation evaluated numerically is due to the uncracked section curvature (because failure occurred far from the instrumented portion of the column), and does not take into account well known tension stiffening effects that are important after peak: mid-span evaluated curvature underestimates average curvature.

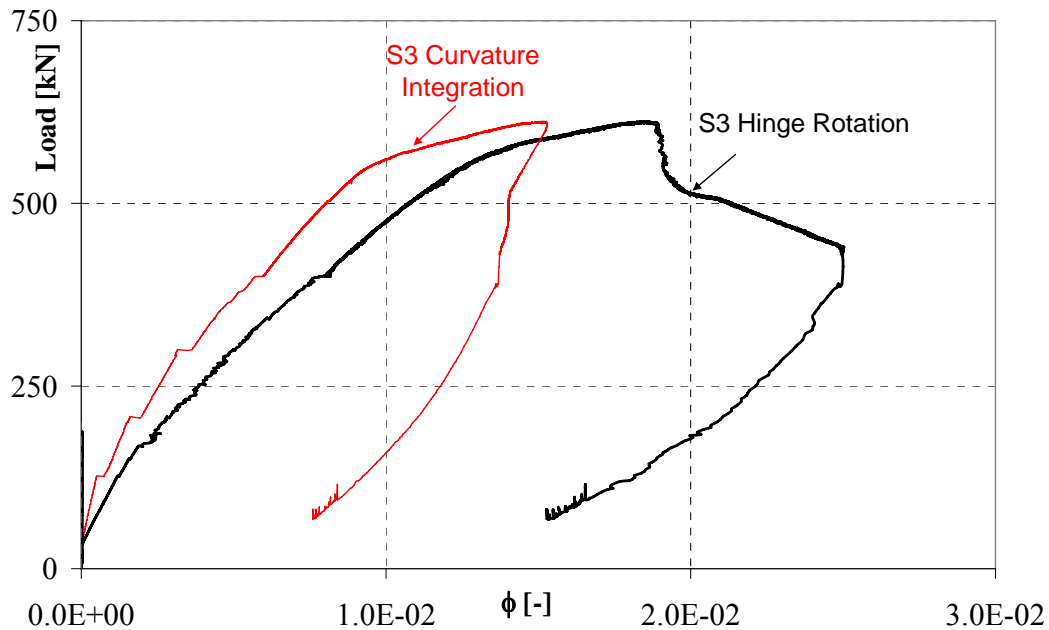


Figure 2.28b – Hinge rotations and estimated rotations Diagram (U3)

2.4.4 Specimen S1: test results

A construction issue did not allow testing of specimens S1 with the same eccentricity of U1 specimen; the actual eccentricity was 80 mm. The two specimens therefore are not directly comparable.

In the S series some strain gauges are placed on the FRP wraps on the front wall and gives also a measure of the strains over the corner (Figure 2.29).

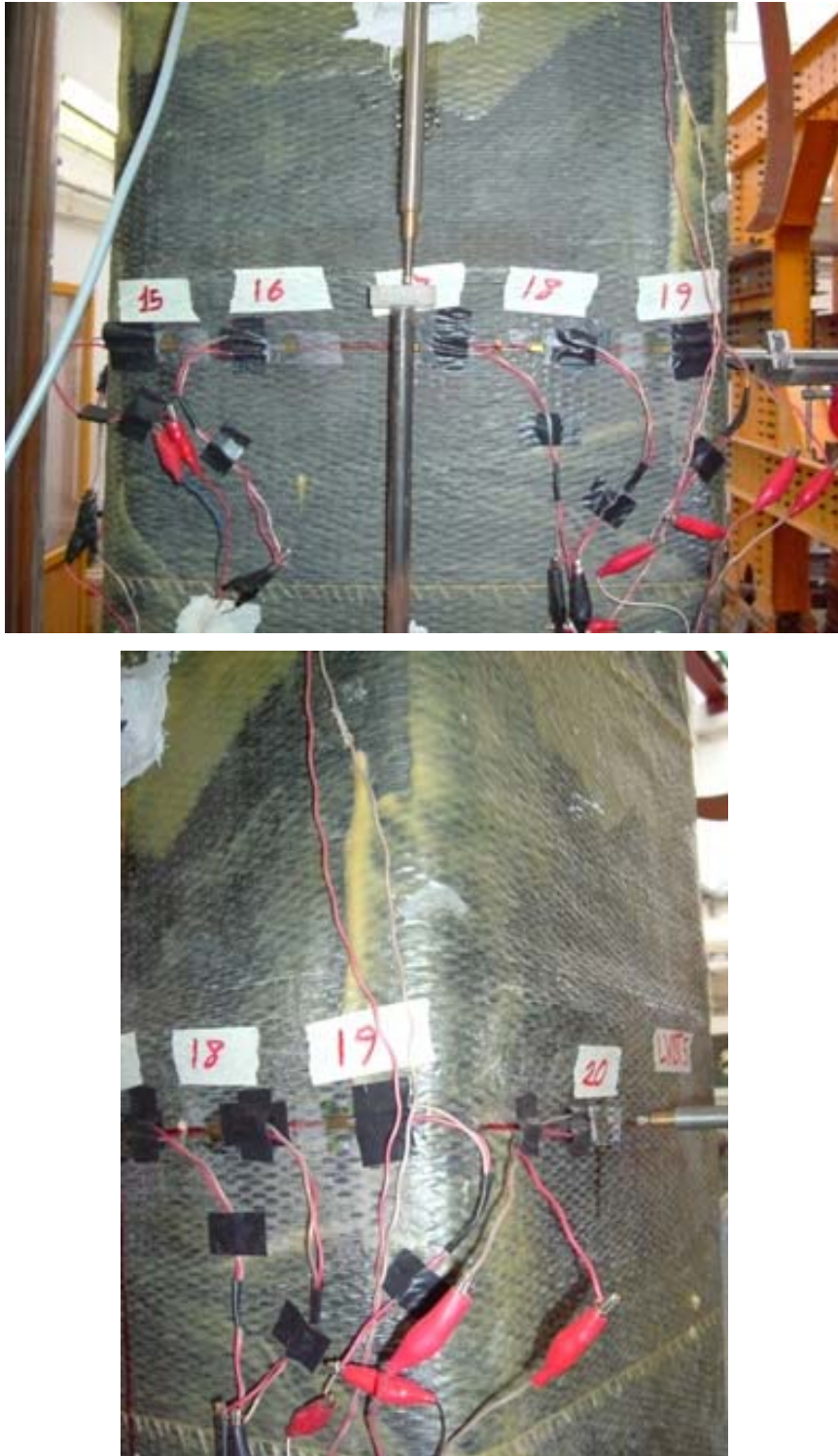


Figure 2.29 – Detail: Strain Gauges measuring FRP strains over the corner (S1)

The failure of this column has occurred at mid-span, where the $P-\Delta$ effects mostly impact flexural moment. The failure was ductile. Unlike U1 specimen, the axial load eccentricity was not enough small to allow the hollow section to be fully compressed. The neutral axis was inside the wall, in the middle of the rear wall: so strain diagram was almost triangular, with higher strains on the crushed wall and very low strains in the wall in tension. Wrapping has delayed the activation of the failure mechanism characterized by the combination of buckling of the compressive steel bars and concrete cover spalling; this has allowed for the full development of the load capacity of the concrete in the strengthened columns resulting in a strength increase of the member. The ultimate axial capacity was 2138 kN.

In Figure 2.30 is reported the strain versus axial force P diagram.

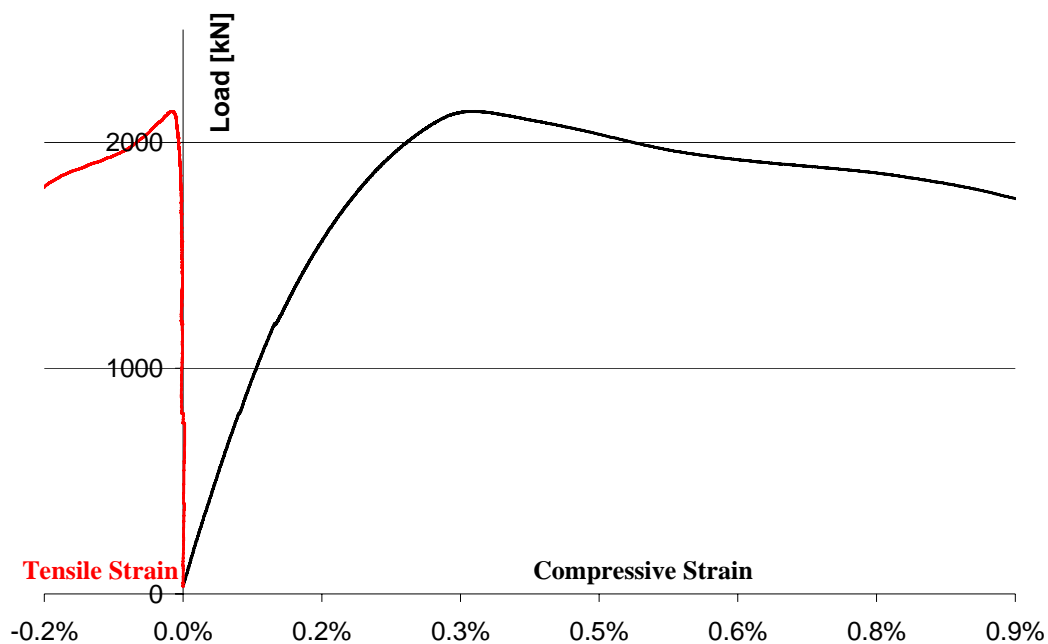


Figure 2.30 –Strains vs. Axial Load Diagram (S1)

Strain diagrams are obtained from data of vertical LVDTs and good agreement was generally found with strain gage measurements on steel bars up to peak.

It is clearly shown (Figure 2.31 where strain profiles are plotted over the section at different load levels) the beneficial effect of the FRP wrapping, the loss of load carrying capacity of the specimen occurred when the steel reached yielding in compression. Buckling of steel compressed bars occurred and strain data acquired after peak on the steel rebars were higher than strain gage threshold (about 3%), however concrete preserves good carrying capacity reaching strains higher than 1% in the post peak branch.

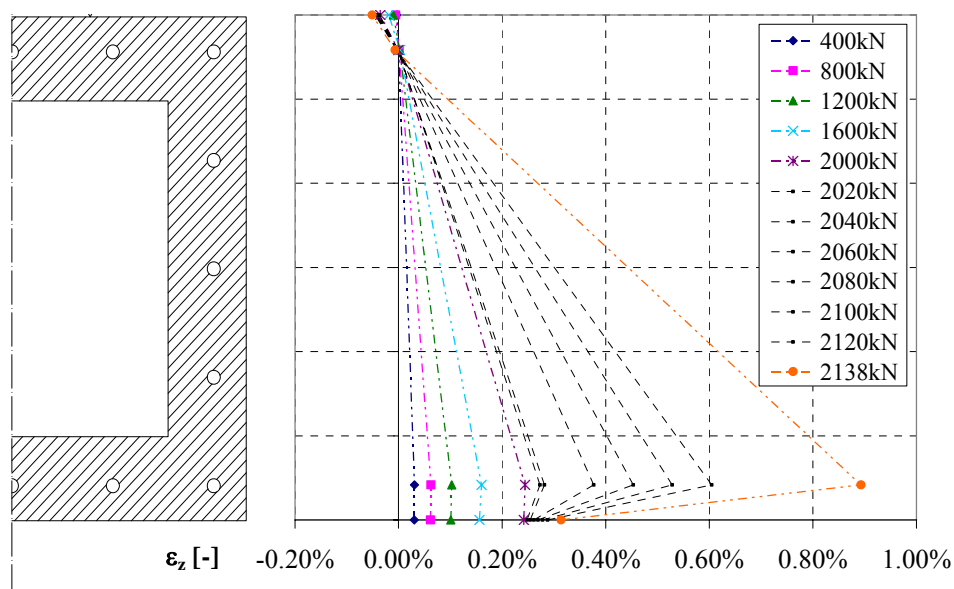


Figure 2.31 –Strains Profiles over the section (S1)

The only external appearance of failure was the formation of a bulge of the FRP due to the remarkable shortening of the column (figure 2.32). The failure of CFRP wraps was never observed and after some little crackling near peak load the bearing capacity of the strengthened column started decreasing.



Figure 2.32 –Bulge of FRP wraps at failure (S1)

Buckling of steel compressed bars occurred probably inward. The portion of the specimen where failure occurred was separated and also the interior of the walls was observed. Concrete cover spalling was observed in the inner side of the compressed wall (Figure 2.33)



Figure 2.33 –Inside view of the hollow portion after failure (S1)

In Figure 2.34 is the mid span deflection vs. axial load diagram: at peak load it was 7.41 mm, with respect to the imposed eccentricity it causes a small $P\Delta$ effect of about 9%.

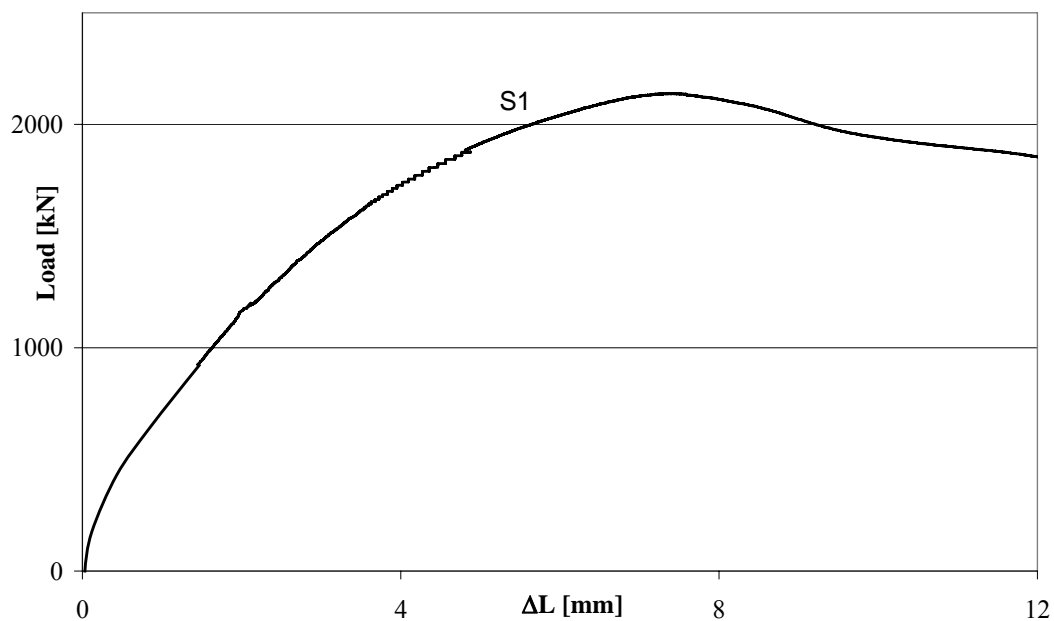


Figure 2.34 – Mid Span Deflection Diagram (S1)

In Figure 2.35 is plotted also the moment-curvature diagram: the ductile behavior of the S1 specimen is clear looking at this diagram. This specimen evidenced a remarkable improvement of the seismic behavior, after peak load it kept a good load carrying capability that is good energy dissipation with curvature increments after-peak. The tensile steel yielded and the yielding moment M_y was about 164 kNm.

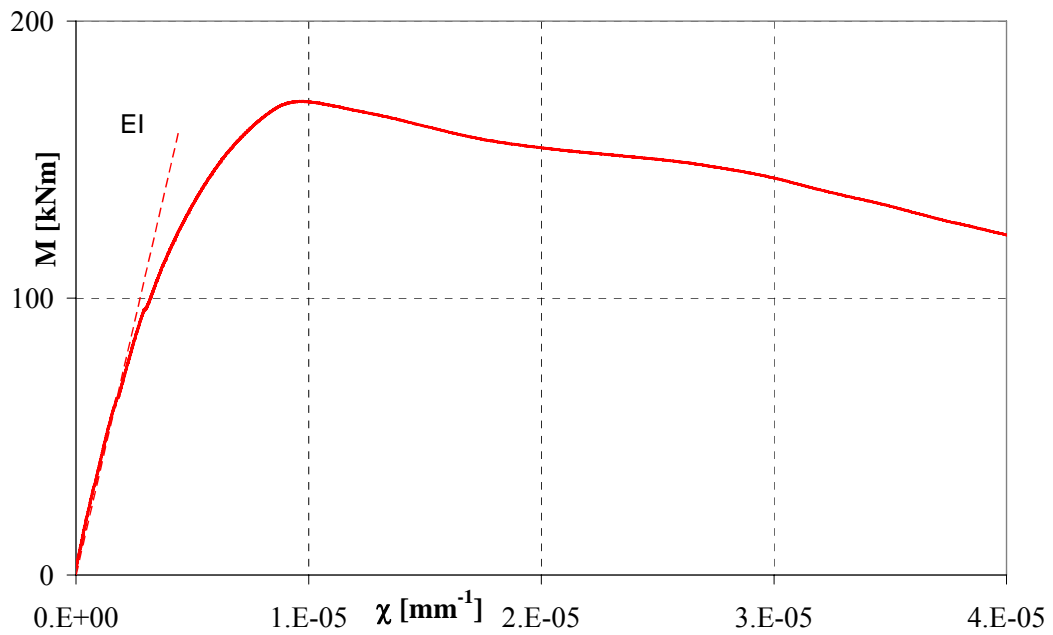


Figure 2.35 – Moment Curvature Diagram (S1)

Calculated hinge rotations can be compared with estimated rotations (Figure 2.36). The two obtained curves are almost matching up before the peak load.

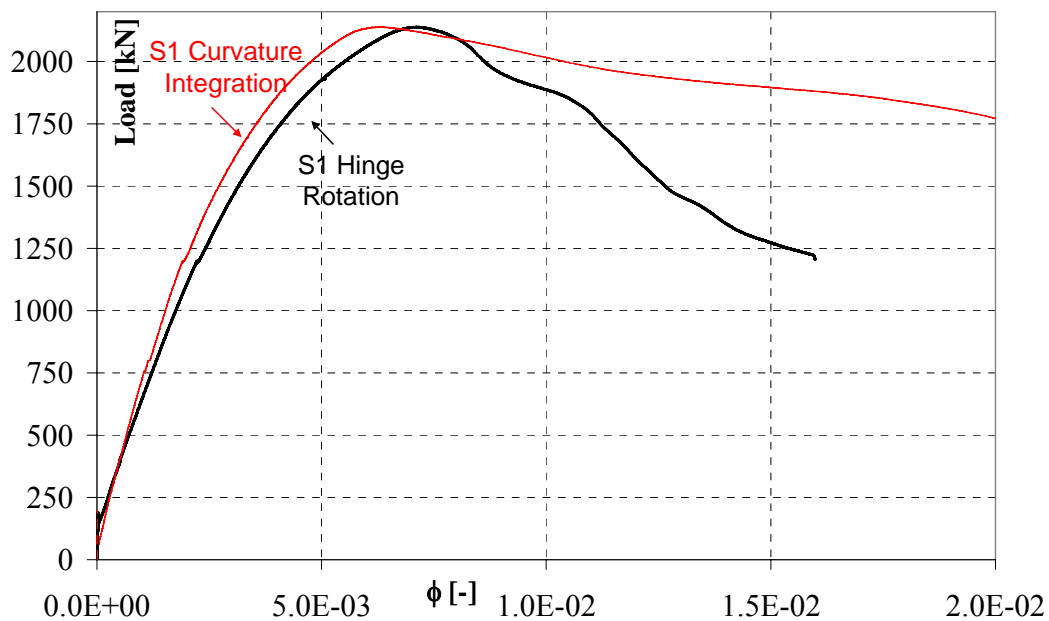


Figure 2.36 – Hinge rotations and estimated rotations Diagram (S1)

Longitudinal strain distributions into FRP confining wraps have been recorded and analyzed. In Figure 2.37 strain profiles are plotted over the length of the front wall and around corners at the mid span section, at different load levels maximum strains in FRP are reached at mid-span in the middle of the compressed wall where a bulge on the FRP wraps formed from the shortening of the column. At peak load, FRP lateral strains are smaller than 0.12%. After peak, a remarkable strain increment is noticed; the maximum value of 0.47% was recorded.

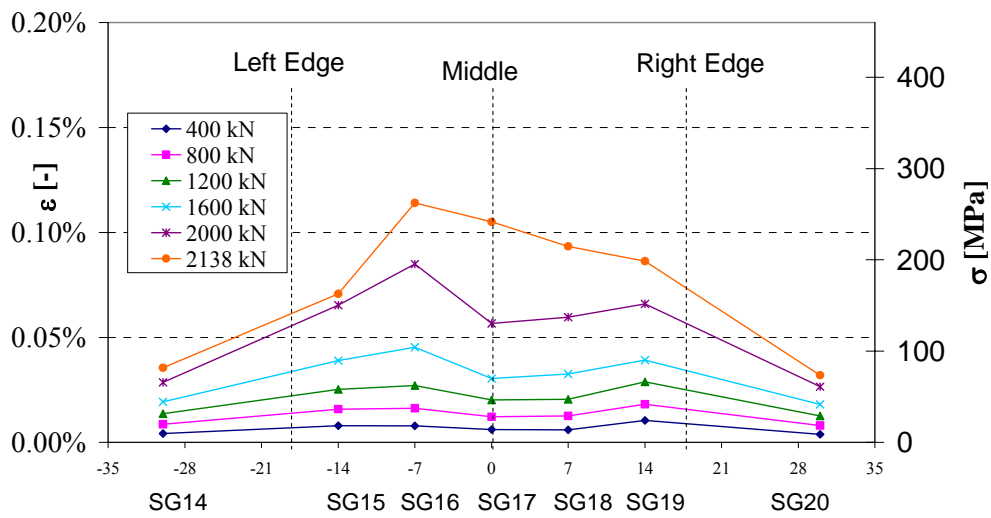


Figure 2.37 –FRP Strain Profiles at different load levels (S1)

2.4.5 Specimen S2: test results

The failure of this column has occurred at the top of the hollow column, in correspondence with discontinuity due to the change from the solid section of the ends to the hollow section. The failure was ductile. The axial load eccentricity (in this case 200 mm) put the hollow section both in tension and compression. The neutral axis was inside the section, in the middle of the hollow section: so strain diagram was bitriangular, with strains almost equal on the compressed and tension walls. Few wide cracks opened in the tension wall and had a depth of about 180 mm on the side walls (Figure 2.38).



Figure 2.38 –Bulge of FRP wraps and crack opening at failure (S2)

The only external appearance of failure was the formation of a bulge of the FRP due to the remarkable shortening of the column and few wide cracks opening. The failure of CFRP wraps was not observed and after some little crackling near peak load the bearing capacity of the strengthened column started decreasing.

Wrapping has delayed the activation of the brittle failure mechanism. The loss of load carrying capacity of the specimen occurred after the steel reached yielding in compression and concrete preserved good carrying capacity reaching strains close to 3‰ at peak load. The ultimate axial capacity was 1082 kN.

In Figure 2.39 is reported the strain versus axial force P diagram. Strain diagrams are obtained from data of vertical LVDTs and good agreement was generally found with strain gage measurements on steel bars.

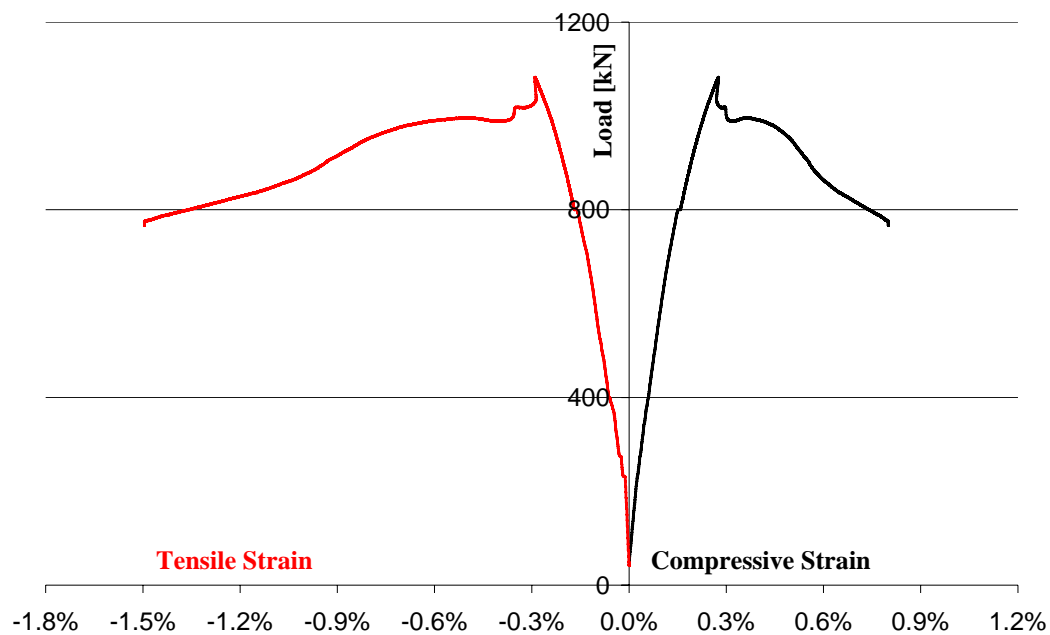


Figure 2.39 –Strains vs. Axial Load Diagram (S2)

A plastic hinge formed far from the instrumented portion of the specimen, so that it is clearly shown an unloading behavior in the instrumented portion.

Calculated hinge rotations were compared with estimated rotations evaluated on average curvature (of plastic hinge). The two obtained curves are almost matching up before the peak load, the section curvatures of plastic hinge has been derived by the global behavior of hinge rotations (Figure 2.40).

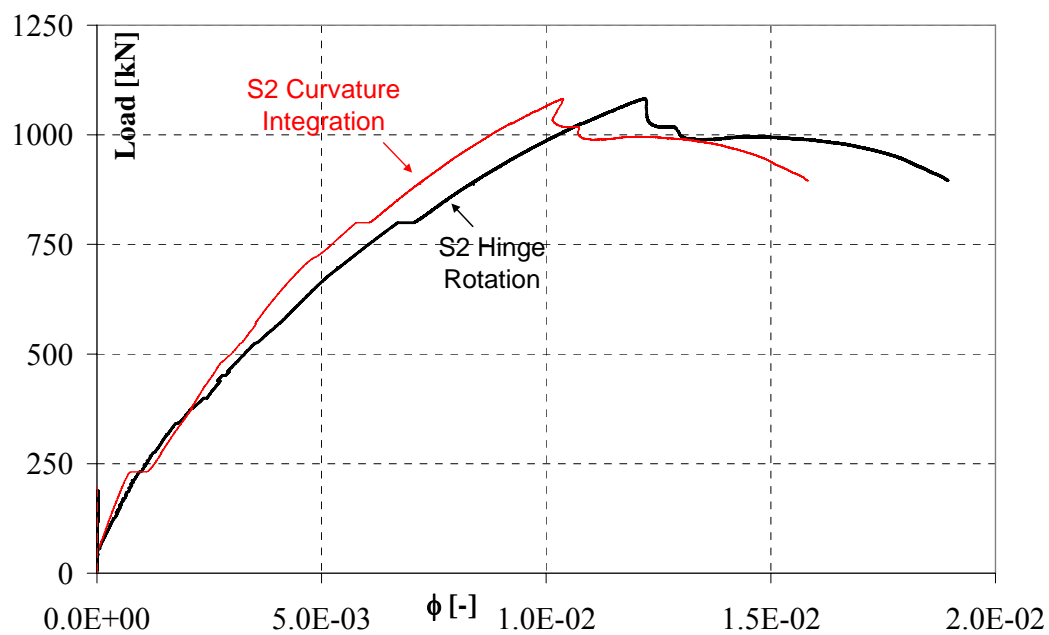


Figure 2.40 – Hinge rotations and estimated rotations Diagram (S2)

In Figure 2.41 is plotted the moment-curvature diagram: the ductile behavior of the S2 specimen is clear looking at the diagram derived by previous analysis. This specimen evidenced a remarkable improvement of the seismic behavior, keeping good load carrying capabilities after peak load. The yielding moment M_y was about 210 kNm.

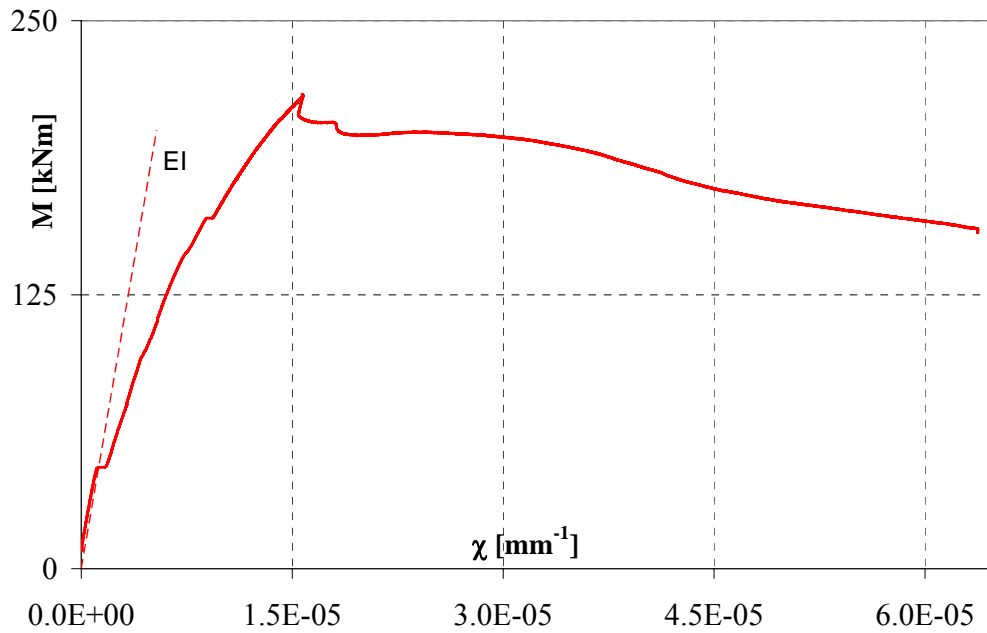


Figure 2.41 – Moment Curvature Diagram (S2)

In Figure 2.42 is the mid span deflection vs. axial load diagram: at peak load deflection was 13.35 mm, with respect to the imposed eccentricity it causes small $P\Delta$ effects of less than 7%.

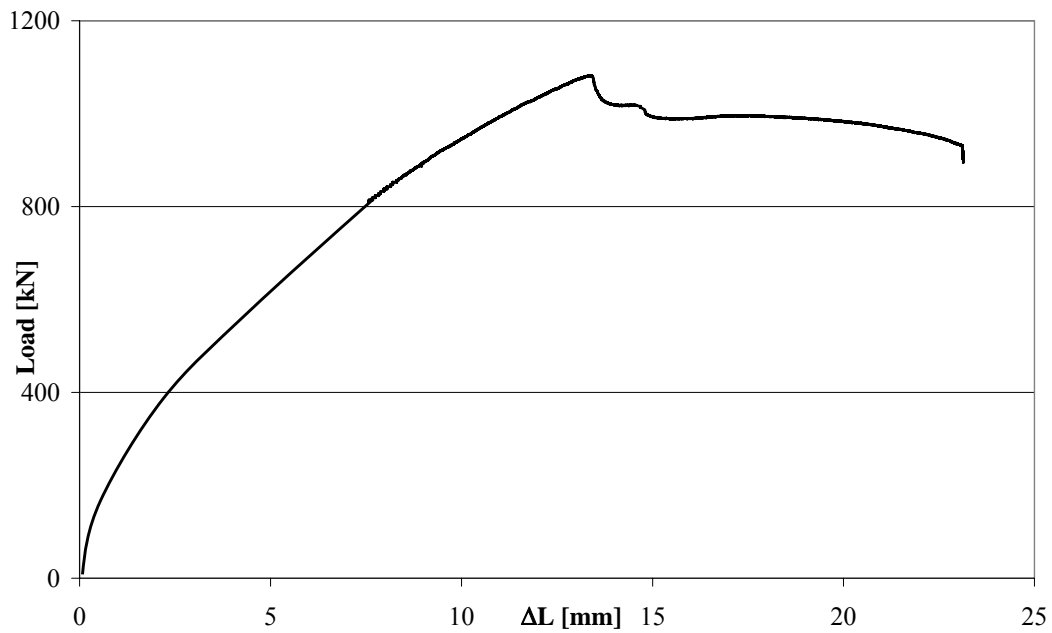


Figure 2.42 – Mid Span Deflection Diagram (S2)

Longitudinal strain distributions into FRP confining wraps have been recorded in a section far from the plastic hinge where maximum stretching of FRP jacket is expected. In Figure 2.43 strain profiles are plotted. Maximum strains in FRP are reached at mid-span in the middle of the compressed wall. At peak load, FRP lateral strains are smaller than 0.05% and are almost constant after peak load.

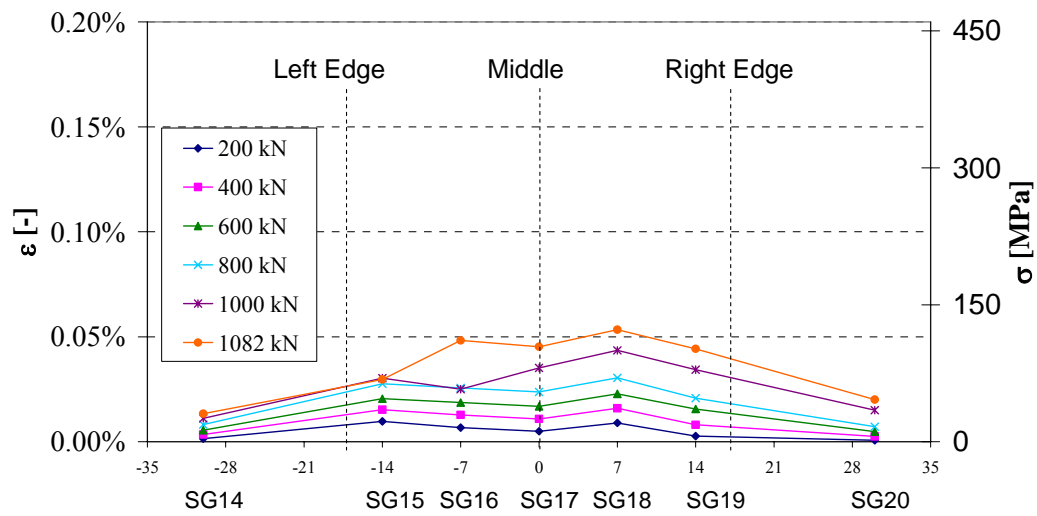


Figure 2.43 –FRP Strain Profiles at different load levels (S2)

2.4.6 Specimen S3: test results

The failure of this column has occurred at mid-span, where the P- Δ effects mostly impact flexural moment. The failure was ductile. The axial load eccentricity (in this case 300 mm) put the hollow section both in tension and compression. The neutral axis was close to the internal side of the compressed wall: strain diagram was bitriangular. Many wide cracks (about 5 mm) opened in the tension wall and had a depth of about 240 mm on the side walls (Figure 2.44).

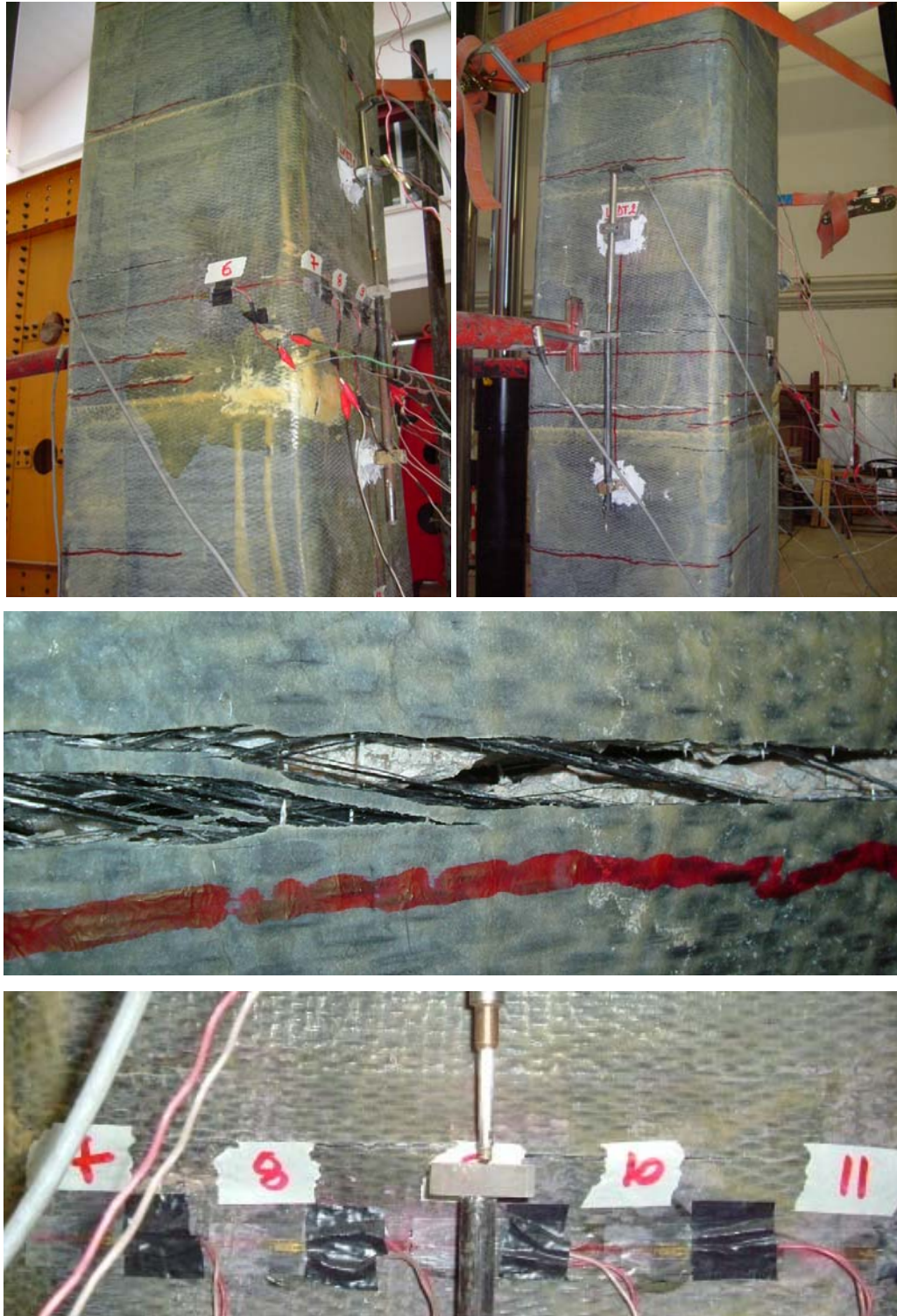


Figure 2.44 –Bulge of FRP wraps and crack opening at failure (S3)

The only external appearance of failure was the formation of a bulge of the FRP due to the shortening of the column and many wide cracks. The failure of CFRP wraps was never observed and after some little crackling near peak load the bearing capacity of the strengthened column started decreasing.

Wrapping has delayed the activation of the brittle failure mechanism. The loss of load carrying capacity of the specimen occurred gradually after the steel reached yielding in compression and concrete preserved good carrying capacity reaching strains higher than 2% after peak load. The ultimate axial capacity was 697 kN.

In Figure 2.45 is reported the strain versus axial force P diagram. Strain diagrams are obtained from data of vertical LVDTs and good agreement was generally found with strain gage measurements on steel bars. Strain data of tensile bars got lost after steel yielding before peak load was attained.

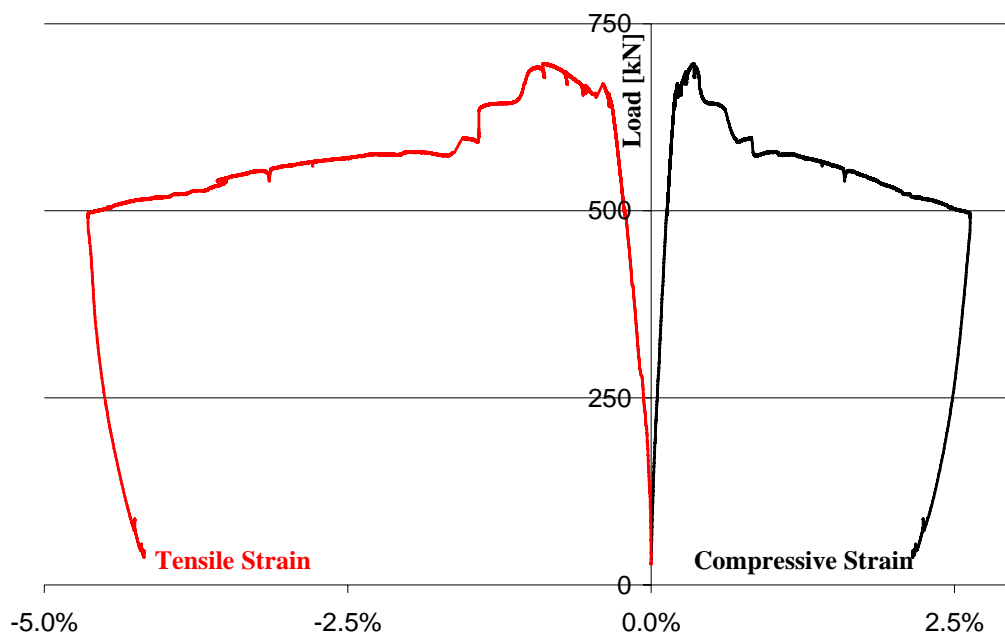


Figure 2.45 –Strains vs. Axial Load Diagram (S3)

In Figure 2.46 is plotted the moment-curvature diagram: the ductile behavior of the S3 specimen is clear looking at the diagram. This diagram is plotted based only on external concrete strains as the tensile reinforcement strain data were lost after steel yielding. Specimen evidenced a remarkable improvement compared to companion U3 specimen, keeping good load carrying capabilities after peak load. The yielding moment M_y was about 198 kNm.

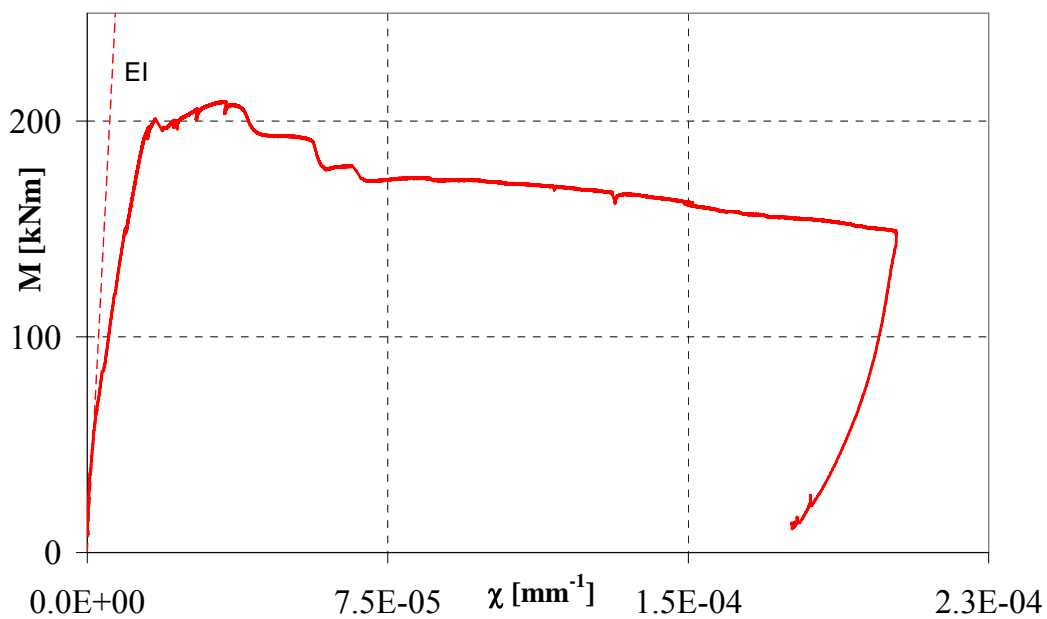


Figure 2.46 – Moment Curvature Diagram (S3)

In Figure 2.47 is the mid span deflection vs. axial load diagram: deflection was 26.51 mm at peak load, with respect to the imposed eccentricity it causes a $P\Delta$ effect of about 9%. Very high deflections (up to about 70 mm), clearly visible, have been recorded in the post peak branch.

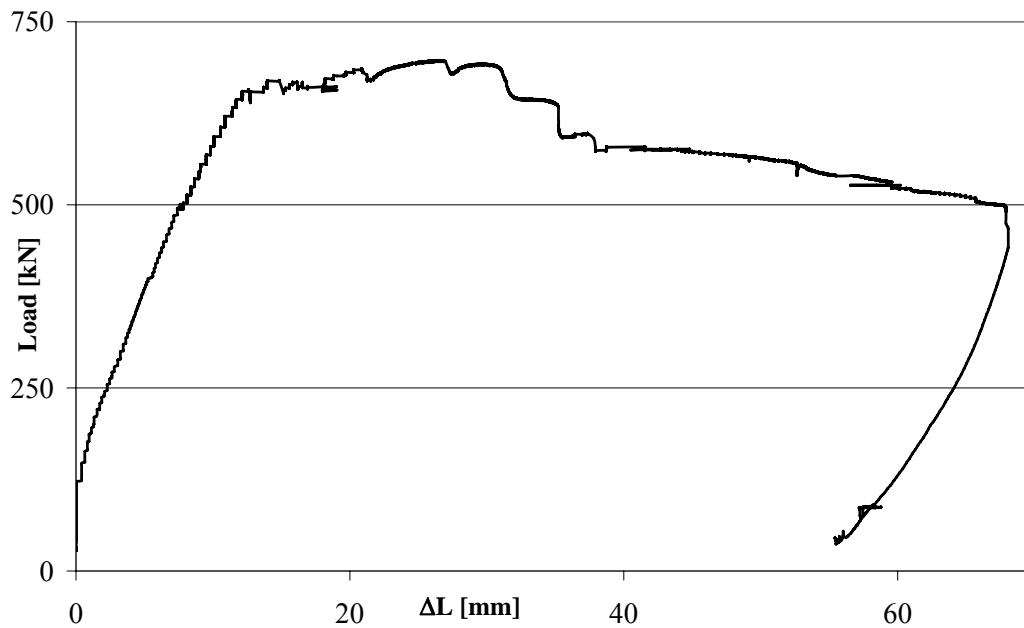


Figure 2.47 – Mid Span Deflection Diagram (S3)

Longitudinal strain distributions into FRP confining wraps have been recorded and in Figure 2.48 strain profiles are plotted. Maximum strains in FRP are reached at the corners of the compressed wall. At peak load, FRP lateral strains are smaller than 0.07% and are almost uniform after peak load. After peak, a remarkable strain increment is noticed; the maximum value of 0.44% was recorded.

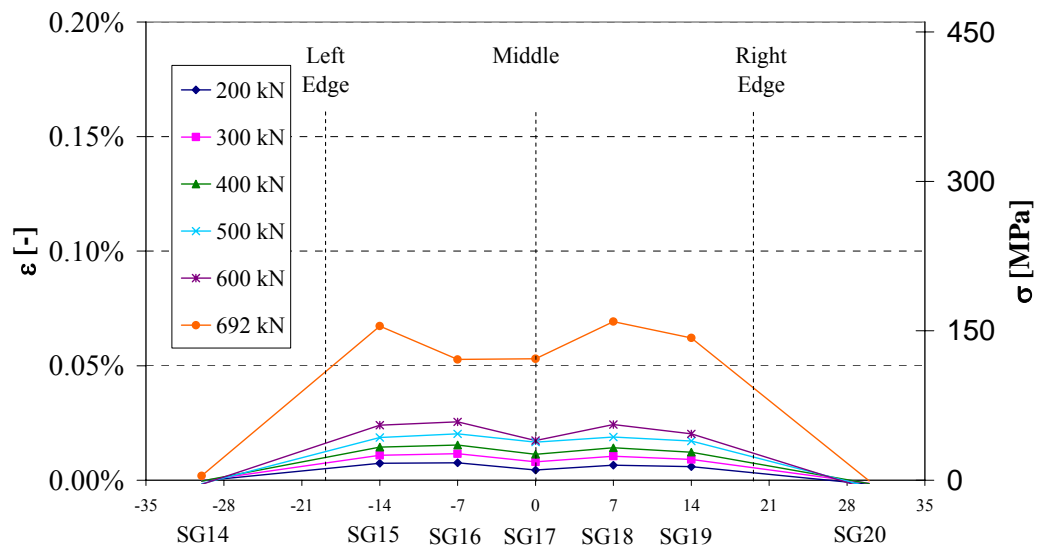


Figure 2.48 –FRP Strain Profiles at different load levels (S3)

2.5 Chapter References

Li J, Hadi MNS. (2003) Behavior of externally confined high-strength concrete columns under eccentric loading. *Journal of Composite Structures*; 62:145-153.

Chapter 3

Modeling Hollow Cross Sectional Behavior: Proposed refined nonlinear method

The existing models available for solid section assessment in terms of concrete modeling, including crack localization and accounting or not for steel and/or FRP confinement, and modeling of steel reinforcement stability and wall stability, are briefly described in the first section of this Chapter. A reliable stress-strain behavior of concrete, and of course of other structural involved materials, is necessary particularly when a member is subjected to combined bending and axial load.

The proposed refined nonlinear methodology is described as well in the second section. An automated algorithm has been developed and implemented in a computer program accounting for steel bars buckling and concrete cover spalling; the effect of concrete hollow core confinement by FRP wrapping has been also modeled. A further non-linear procedure has been also developed to theoretically evaluate ultimate flexural strength of the column taking into account second order effects due to column deflection, namely P- Δ effects.

3.1 Brief Review of Available Models

Reinforced concrete structures are made up of two materials, namely concrete and steel, with different characteristics. Another material, FRP has to be

included if concrete confinement by FRP wraps is considered. FRP and steel can be considered homogeneous materials and their material properties are generally well defined. Concrete is, on the other hand, a heterogeneous material made up of cement and aggregates. Its mechanical properties scatter more widely and cannot be defined easily. For the convenience of analysis and design, however, concrete is often considered as homogeneous material in the macroscopic sense.

A review of the axial stress-strain behavior of concrete, including dilation behavior, is presented in the following subsection. Unconfined behavior of concrete can be roughly considered a uniaxial behavior, while in presence of confining devices the state of stress in the materials becomes bi- and tri-axial.

3.1.1 Unconfined Concrete Behavior

The highly nonlinear response of a RC element can be roughly divided into three ranges of behavior: the uncracked elastic stage, the crack propagation and the plastic (yielding or crushing) stage.

The nonlinear response is caused by two major effects, namely, cracking of concrete in tension, and yielding of the longitudinal reinforcement or crushing of concrete in compression. Nonlinearities also arise from the interaction of the constituents of reinforced concrete, such as bond-slip between reinforcing steel and surrounding concrete, aggregate interlock at a crack and dowel action of the reinforcing steel crossing a crack. The time-dependent effects of creep, shrinkage and temperature variation also contribute to the nonlinear behavior.

Furthermore, the stress-strain relationship of concrete is not only nonlinear, but is different in tension and in compression and the mechanical properties are dependent on concrete age at loading and on environmental conditions, such as ambient temperature and humidity.

In general, the complete uniaxial stress-strain behavior of concrete, shown qualitatively in figure 3.1, may be further described as exhibiting the following five phases (Hsu et al., 1963):

(I) Applied axial load closes existing microcracks. The concrete stress-strain curve exhibits a small concavity. This phase is not always observed.

(II) Concrete behaves essentially as a linear elastic material up to the *discontinuity limit*. Microcracks begin to form at stress concentrations.

(III) Cracks propagate in a stable manner. Due to cracking, load is redistributed within the section causing a gradual softening of the behavior. If loading is stopped or kept constant, crack propagation terminates. Concrete volume reaches a minimum value at the *critical stress*.

(IV) Crack propagation becomes rapid and unstable. The dilation ratio of the concrete, defined as the ratio of transverse to longitudinal or axial strains, increases significantly as the gross concrete volume begins to exceed the initial volume.

(V) Concrete behavior in the final phase depends on the degree and nature of transverse axisymmetric confinement. The characteristics of Phase V behavior exhibited in concrete having different levels of confinement are described later.

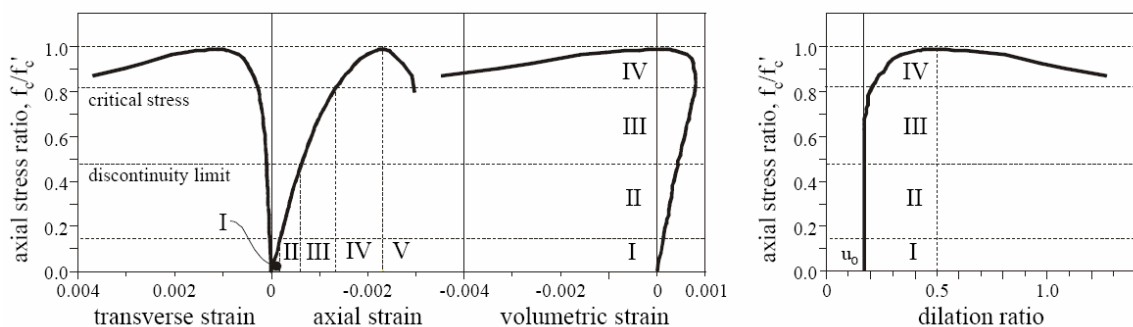


Figure 3.1a –Unconfined Concrete Behavior under axial load

Unconfined concrete post-peak (Phase V) behavior is characterized by rapid uncontrolled dilation as the concrete crushes (see Figure 3.1). It is primarily the dilation of the concrete section exhibited in Phases IV and V that engages significant confining pressure from either conventional transverse reinforcement or external jackets.

The dilation ratio, defined as the ratio of transverse to longitudinal, or axial strains, for axially loaded unconfined concrete is typically assumed to have a constant value, equal to Poisson's ratio for concrete, up to an axial stress level of about $0.7f_c'$, where f_c' is the compressive strength of concrete. Between $0.7f_c'$ and f_c' (phase IV in Figure 3.1a), the dilation ratio increases rapidly to a value of about 0.5 (Chen, 1982). The post-peak (phase V) behavior of unconfined concrete is characterized by rapid unstable dilation as the dilation ratio increases beyond 0.5.

As the axial strain ε_c falls between 0 and ε_{co} , the strain corresponding to f_c' , the stress-strain relation can be approximated by using the second-order polynomial equation:

$$f_c = A \cdot \varepsilon_c^2 + B \cdot \varepsilon_c + C \quad (1)$$

And, the corresponding three boundary conditions are shown as follows:

$$f_c = 0 \quad (\text{at } \varepsilon_c=0)$$

$$f_c = f_c' \quad (\text{at } \varepsilon_c=\varepsilon_{co})$$

$$\frac{df_c}{d\varepsilon_c} = 0 \quad (\text{at } \varepsilon_c=\varepsilon_{co})$$

Upon substituting the boundary conditions into Eq. (1), Eq. (1) can be rewritten as the following equation:

$$f_c = f_c' \cdot \left[2 \left(\frac{\varepsilon_c}{\varepsilon_{co}} \right) - \left(\frac{\varepsilon_c}{\varepsilon_{co}} \right)^2 \right] \quad \text{where } 0 < \varepsilon_c < \varepsilon_{co}$$

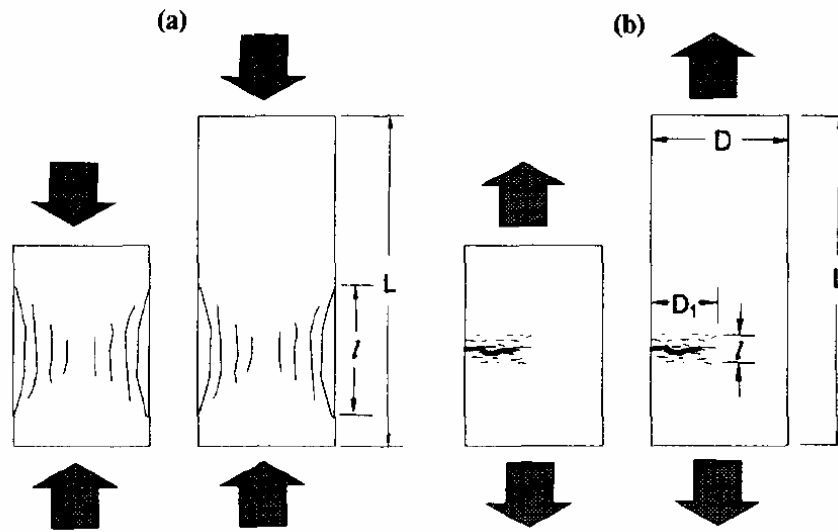


Figure 3.1b –Typical Patterns of cracking localization in post-peak response:

(a) Compression, (b) Tension

To completely evaluate the post-peak descending branch, it is necessary to evaluate also damage localization that causes softening.

Softening is a gradual decrease of mechanical resistance under a continuous increase of deformation applied on a specimen or structure. It is a salient feature of quasibrittle materials like concrete, clay brick, mortar, ceramics, or rock, which fail due to a process of progressive internal crack growth. Such mechanical behavior is commonly attributed to the heterogeneity of the material, due to the presence of different phases and material defects, like flaws and voids. Even prior to loading, concrete contains microcracks due to the shrinkage during curing and the presence of the aggregate. The initial stresses and cracks as well as variations of internal stiffness and strength cause progressive crack growth when the material is subjected to progressive deformation. Initially, the microcracks are stable which means that they grow only when the load is increased. Around peak load an acceleration of crack formation takes place and the formation of macrocracks starts. The macrocracks are unstable, which means that the load has

to decrease to avoid an uncontrolled growth. In a deformation controlled test the macrocrack growth results in softening and localization of cracking in a small zone while the rest of the specimen unloads.

For tensile failure this phenomenon has been well identified. For compressive failure, softening behavior is highly dependent upon the boundary conditions in the experiments and the size of the specimen.

It is general practice to identify the post-peak stress-strain relation from test data ignoring the fact that the deformation of the specimen within the gauge length often becomes non uniform, due to localization of cracking damage (Figure 3.2). The experimental data must be delocalized, but this needs not to be done with an high degree of accuracy and sophistication.

The strain, as commonly observed and evaluated, is the average strain ε_c on a gauge length L . In a coupling model: $L\varepsilon_c = \ell\varepsilon_{cz} + (L - \ell)\varepsilon_{un}$ where L is the gauge length on which the deformation is measured, ℓ is the length or crack bandwidth of the strain softening zone (measured in the same direction as L), ε_{cz} is the actual strain in the strain softening cracking zone and ε_{un} is the strain in the rest of the specimen which undergoes unloading from the peak stress point. The unloading strain is $\varepsilon_{un} = \varepsilon_{co} - (f'_c - f_c)/E$ where E is the Elastic Modulus.

Substituting in the coupling equation:

$$\varepsilon_c = \frac{\ell\varepsilon_{cz}}{L} + \frac{L - \ell}{L} \left(\varepsilon_{co} - \frac{f'_c - f_c}{E} \right) \quad \text{where } \varepsilon_c > \varepsilon_{co}$$

A constitutive model for damage predicts the strain ε_{cz} in the localization zone, while a constitutive model for element behavior prediction should consider the average strain ε_c . This size effect problem has been addressed by Hillerborg (1989), in his design equations. The ultimate strain of concrete is assumed to be inversely proportional to the depth of the compression zone, rather than fixed, and also depends on the type of concrete (smaller for high strength

concrete than for ordinary concrete). The average ultimate strain is given by the ratio of a formal localized deformation w_c when the stress reaches zero and the depth of the compression zone (neutral axis). The material parameter w_c is a length and can be determined from bending tests.

The size of localization zone is small, which reduces the accuracy of strain measurements; the location of the localization zone is uncertain and so it is not possible to know where to place the strain gauges. It is impossible to determine the value of the localization length ℓ from the reports on uniaxial, biaxial and triaxial tests on concrete found in literature. However a reasonable estimate can be made by experience: $\ell = d_0 \div 3d_0$, where d_0 is the maximum size of the aggregate in concrete (the smaller value is for higher strength concrete).

The model proposed by Popovics (1973) gives in one only equation the envelope of the concrete stress-strain curve until the concrete crushing strength is achieved and also for strains beyond that corresponding to the crushing strength.

The stress-strain relation is given by the equation:

$$f_c = \frac{f'_c \cdot x \cdot r}{r - 1 + x^r} \quad (2)$$

where $x = \varepsilon_c / \varepsilon_{co}$ is the relative strain and $r = \frac{E_c}{E_c - E_{sec}}$ accounts for the stiffness degradation. The initial tangent stiffness can be evaluated as $E_c = 15000\sqrt{f'_c}$ and secant stiffness is defined as $E_{sec} = \frac{f'_c}{\varepsilon_{co}}$.

Reliable stress-strain curves can be obtained if the initial tangent stiffness E_c and peak strain ε_{co} are as close as possible to the real experimental values.

Cracked Concrete Behavior in tension

The nonlinear response of concrete is often dominated by progressive

cracking which results in localized failure. A reinforced concrete member, in flexure, cracks at discrete locations where the concrete tensile strength f_{ct} is exceeded.

At the cracked section all tension is carried by the steel reinforcement. Tensile stresses are, however, present in the concrete between the cracks, since some tension is transferred from steel to concrete through bond. The magnitude and distribution of bond stresses between the cracks determines the distribution of tensile stresses in the concrete and in the reinforcing steel between the cracks.

Additional cracks can form between the initial cracks, if the tensile stress exceeds the concrete tensile strength between previously formed cracks. The final cracking state is reached when a tensile force of sufficient magnitude to form an additional crack between two existing cracks can no longer be transferred by bond from steel to concrete. Because concrete is carrying some tension between the cracks, the flexural stiffness is clearly greater between the cracks than at the cracks.

In order to improve the accuracy of finite element models in representing cracks and, in some cases, in order to improve the numerical stability of the solution, the tension stiffening effect was introduced in several models. The physical behavior in the vicinity of a crack can be described. As the concrete reaches its tensile strength, primary cracks form. The number and the extent of cracks are controlled by the size and placement of the reinforcing steel. At the primary cracks the concrete stress drops to zero and the steel carries the entire tensile force. The concrete between the cracks, however, still carries some tensile stress, which decreases with increasing load magnitude. This drop in concrete tensile stress with increasing load is associated with the breakdown of bond between reinforcing steel and concrete. At this stage a secondary system of internal cracks, called bond cracks, develops around the reinforcing steel, which begins to slip relative to the surrounding concrete.

Since cracking is the major source of material nonlinearity in the serviceability range of reinforced concrete structures, realistic cracking models need to be developed in order to accurately predict the load-deformation behavior of reinforced concrete members. The selection of a cracking model depends on the purpose of the analysis. If overall load-deflection behavior is of primary interest, without much concern for crack patterns and estimation of local stresses, the "smeared" crack model is probably the best choice. If detailed local behavior is of interest, the adoption of a "discrete" crack model might be necessary.

More details on these concrete crack models frequently adopted in Finite Elements analyses are given in Chapter 5. One way of including the tension stiffening effect in a smeared crack model is to increase the average stiffness of the concrete in tension which contains the crack. A descending branch is assigned to the tension portion of the concrete stress-strain curve. In this case the tension stiffening effect is represented as either a step-wise reduction of tensile stress or as a gradually unloading model (Figure 3.2).

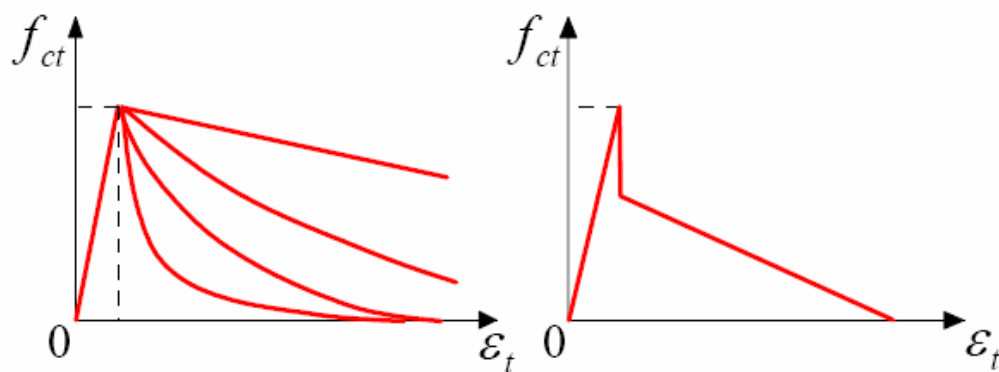


Figure 3.2 – Typical Tensile Stress Strain curve for quasi-brittle materials

These modifications are introduced in order to increase the computational efficiency of the model, and in view of the fact that the response of typical reinforced concrete structures is much more affected by the tensile than by the

compressive behavior of concrete. This stems from the fact that the concrete tensile strength is generally less than 10% of the compressive strength. In typical reinforced concrete beams and slabs which are subjected to bending, the maximum compressive stress at failure does not reach the compressive strength. This means that the compressive stresses in most of the member reach a small fraction of the compressive strength at failure. The behavior of these members is, therefore, dominated by crack formation and propagation, and the yielding of reinforcing steel.

Under biaxial tension concrete exhibits constant or perhaps slightly increased tensile strength compared with that under uniaxial loading. Under a combination of tension and compression the compressive strength decreases almost linearly with increasing principal tensile stress.

It can be assumed that the inelastic behavior both in tension and compression can be described by the integral of the σ - ϵ diagram. These quantities, denoted respectively as fracture energy G_f and compressive fracture energy G_c , are assumed to be material properties. With this energy-based approach tensile and compressive softening can be described within the same context which is reasonable, because the underlying failure mechanisms are similar, i.e. continuous crack growth at micro-level.

3.1.2 Confined Concrete Behavior

The axial stress-strain behaviors of unconfined and confined concrete differ significantly. Furthermore, the nature of the confinement provided affects significantly also the concrete behavior. In conventionally reinforced and externally jacketed concrete columns, confining pressure is typically *passive* in nature. That is, confining pressure is engaged by the transverse dilation of

concrete accompanying principal axial strain, the so called Poisson effect. There are cases where an initial *active* confining pressure is present, as is the case when an expansive grout is injected between the column and the external jacket. Active pressure is generally quite small in comparison to the passive pressure generated by concrete dilation. This study concerns only passive confinement.

Passive confinement may be *constant* or *variable* through an axial load history. Constant confining pressure is generated in cases where the confining material behaves in a plastic manner. This is typically assumed to be the case where confinement is provided by conventional transverse reinforcing steel which is yielding. FRP jackets and steel which is still elastic generate variable confining pressure. Variable passive confinement is dependent on the axial and transverse behavior of the concrete, which, in turn, is dependent on the level and stiffness of confinement provided.

Lightly and moderately confined concrete exhibits post-peak behavior characterized by the appearance of significant cracking. Although insufficient to stop the cracking, the presence of confining pressure controls the cracking, allowing interfacial friction forces to develop resulting in a residual concrete capacity. Such behavior is observed where confinement is provided by a material experiencing plastic behavior (such as reinforcing steel) or where elastic confining materials are insufficiently stiff to provide large amounts of confinement.

Heavily confined concrete exhibits an essentially bilinear stress-strain behavior (see Figure 3.3). Such behavior occurs where confinement is provided by an elastic material (such as an FRP jacket). In this case, the dilation ratio is observed to increase to some limiting value after which it remains essentially constant.

The peak axial stress and strain achieved is therefore related to the rupture strain of the confining material by the dilation ratio. Once the confining material fails, the now overloaded unconfined concrete experiences a very brittle failure.

Thus, no post-peak (Phase V) behavior is exhibited.

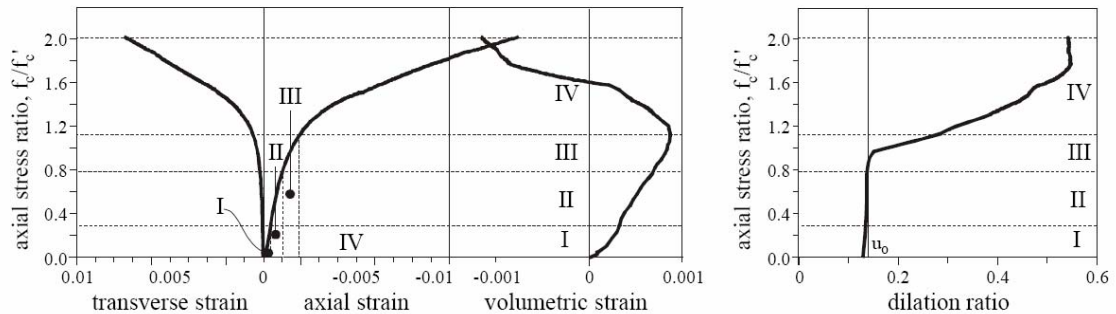


Figure 3.3 – Confined Concrete Behavior under axial load

In Phase I and Phase II the dilation ratio remains relatively constant, having a value approximately equal to Poisson's ratio for concrete. Where moderate or heavy confinement is provided, this constant dilation behavior will continue up to a concrete stress level equal to about the unconfined concrete strength, f_c' . In Phase III an increase in the dilation ratio becomes apparent. The rate of this increase is inversely proportional to the stiffness of the confining jacket. Then the dilation ratio continues to increase through Phase IV until an ultimate dilation ratio is reached.

First Confinement models based on Mohr's circle

A review of earlier literature indicates that the existing constitutive models for confined concrete are developed for steel reinforcement, and therefore might not be suitable for FRP composite material.

The analyzed method of seismic retrofitting the concrete bridge columns is to confine the bridge columns transversely, and this transverse confinement can improve the axial compressive strength, flexural strength, shear strength as well as ductility. Therefore, it is necessary to develop a theoretical stress–strain model for

confined concrete.

Confined concrete constitutive models have been researched extensively since early in the last century. Richart et al. (1928, 1929) were the first to study the nominal strength of concrete under lateral confinement provided by either hydrostatic pressure or spiral reinforcement.

The peak strength of the confined concrete is derived from the Mohr–Coulomb failure envelope theory which conforms to the fundamental theory of elasticity, but the strain at the peak strength is obtained from the regression analysis of the experimental results.

Therefore, the tri-axial stress relationship of the soil (or rock) can be used as the stress relationship of the confined concrete.

According to the Mohr–Coulomb failure envelop (figure 3.4) of the soil under lateral confined stress (σ_3), the axial stress (σ_1) can be expressed as follows:

$$\sigma_1 = 2c \cdot \tan\left(45^\circ + \frac{\phi}{2}\right) + \sigma_3 \cdot \tan^2\left(45^\circ + \frac{\phi}{2}\right) \quad (3)$$

In Eq. (3), σ_1 is the axial stress, c is the cohesion of the soil or rock, σ_3 is the lateral confined stress, and ϕ is the angle of internal friction. If the stress relationship of Eq. (3) is the tri-axial stress relationship of confined concrete, then the σ_3 is the effective confined stress and $\sigma_3 = f'_l$, while σ_1 is the maximum axial strength and $\sigma_1 = f'_{cc}$. When $\sigma_3 = 0$, i.e. in the unconfined situation, the unconfined concrete strength can be expressed as $f'_c = 2c \cdot \tan\left(45^\circ + \frac{\phi}{2}\right)$

By using the above mentioned physical-based constitutive model for confined concrete, Eq. (3) can be expressed as follows for the confined concrete:

$$f'_{cc} = f'_c + f'_l \cdot \tan^2\left(45^\circ + \frac{\phi}{2}\right) = f'_c + f'_l \cdot k_1$$

The angle of internal friction of concrete varies usually from 36° to 45° for most of the strengths of concrete. The angle of internal friction is not easily to be

obtained from the experimental observation; therefore, the angle of internal friction can be expressed as a function of concrete strength. For simplicity, ϕ can be expressed as the linear relationship of concrete strength: as

$$\phi = 36^\circ + 1^\circ \left(\frac{f'_c}{35} \right) \leq 45^\circ .$$

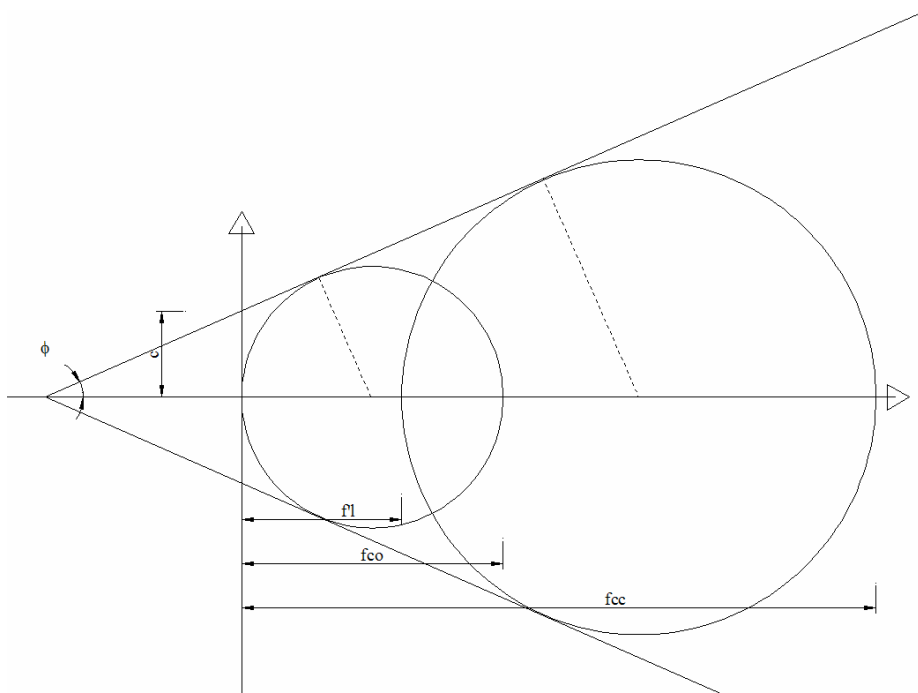


Figure 3.4 – Mohr–Coulomb failure envelop

The value proposed by Richart et al. (1928) was $k_1=4.1$ corresponding to $\phi=37^\circ$, which is an average value for the concrete subjected to low confinement pressure. Using triaxial tests, many authors proposed different expressions for k_1 . Recent studies revealed that the value of k_1 is a function of the confinement level and should take into account the influence of the concrete strength on the ultimate behavior.

Then ultimate compressive strength (f'_{cc}) can be calculated if the ultimate

effective confinement pressure (f'_1) is known. The confinement pressure can be obtained using the stress equilibrium in a cross section and the strain compatibility conditions between the concrete core and the jacket.

Confinement models based on the reinforcement yielding: Mander

Mander et al. (1988a, 1988b) then modified the confined peak strength and proposed a functional expression to represent the stress–strain curve (Figure 3.5).

The model is based on the Popovics (1973) formula

$$f_c = \frac{f'_{cc} \cdot x \cdot r}{r - 1 + x^r}$$

where the peak strength f'_{cc} is the confined concrete strength derived from the following equation used to define a failure surface for concrete under triaxial compressive stresses, which was based on the “five parameter” multiaxial failure surface given by William and Warnk (1975) and calibrated with data from triaxial tests:

$$f'_{cc} = f'_{co} \left(-1.254 + 2.254 \sqrt{1 + 7.94 \frac{f'_1}{f'_{co}}} - 2 \frac{f'_1}{f'_{co}} \right)$$

In previous equations, f'_{cc} is the peak compressive strength of the confined concrete, f'_{co} is the unconfined concrete compressive strength, and f'_1 is the effective lateral confining stress, $x = \varepsilon_c / \varepsilon_{cc}$ is the relative strain and

$r = \frac{E_c}{E_c - E_{sec}}$. The initial tangent stiffness can be evaluated as $E_c = 15000 \sqrt{f'_c}$

and secant stiffness is defined as $E_{sec} = \frac{f'_{cc}}{\varepsilon_{cc}}$.

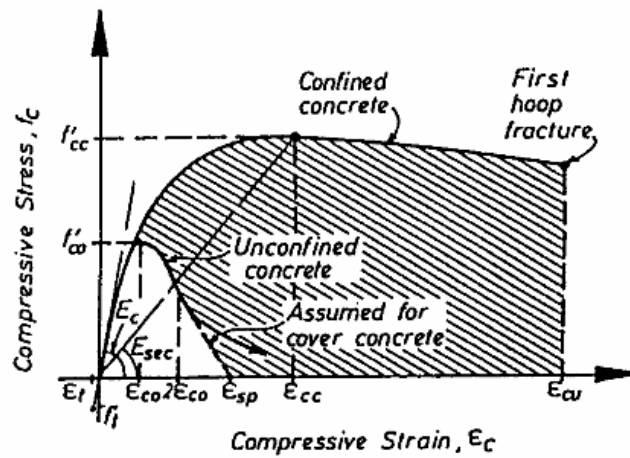


Figure 3.5 –Mander Model: Confined Concrete Behavior under axial load

The ultimate strain of the confined concrete is $\varepsilon_{cu} = 0.004 + 1.4 \frac{\rho_s f_{yh} \varepsilon_{hu}}{f'_{cc}}$, it is an experimentally derived formula accounting for first hoop fracture where f_{yh} is the yield strength of the transverse reinforcement, ε_{hu} is the ultimate strain of the transverse reinforcement and ρ_s is the transverse steel ratio.

The effective lateral confining stress f'_l is given by k_e , a confinement effectiveness coefficient multiplied by the (constant) pressure exerted by the yielded jacket (evaluated as the yield stress of the confining device).

The axial strain ε_{cc} at the peak compressive strength, f'_{cc} , can be expressed by the following experimental equation:

$$\varepsilon_{cc} = \varepsilon_{c0} \left[1 + 5 \left(\frac{f'_{cc}}{f'_{c0}} - 1 \right) \right]$$

In the above equation, ε_{c0} is the compressive strain at the unconfined peak concrete strength (f'_{c0}), usually setting $\varepsilon_{c0} = 0.002$.

Confinement models based on elastic reinforcement: Spoelstra-Monti

All of the above stress–strain models were derived for concrete confined by steel reinforcement instead of the FRP composite materials.

An FRP jacket, as opposed to a steel one that applies a constant confining pressure after yield, has an elastic behavior up to failure and therefore exerts a continuously increasing confining action. The amount of this action depends on the lateral dilation of concrete, which in turn is affected by the confining pressure.

All previous models are based on the assumption that the axial stress and axial strain of concrete confined by FRP at a given lateral strain are the same as those of the same concrete actively confined with a constant confining pressure equal to that supplied by the FRP jacket. This assumption is equivalent to assuming that the stress path of the confined concrete does not affect its stress–strain behavior. This assumption has not been rigorously validated, but appears to be widely accepted as any error caused by this assumption is believed to be small. Based on this assumption, a more reliable confinement model for concrete can be used to evaluate the axial stress and axial strain of FRP-confined concrete at a given confining pressure and the interaction between the concrete and the FRP jacket can be explicitly accounted for by equilibrium and radial displacement compatibility considerations.

As a result, the stress–strain curve of FRP-confined concrete crosses a family of stress–strain curves for the same concrete with different confining pressures, as demonstrated in Fig. 3.6 using Spoelstra and Monti's (1999) model.

Spoelstra and Monti (1999) developed an iterative procedure to calculate ultimate compressive strength of FRP confined concrete cylinders. This model explicitly accounts for continuous interaction with confining material due to lateral strain of concrete, through an incremental approach. This relation allows one to trace the state of strain in the jacket. By imposing concrete strain, ϵ_c , in

iterative procedure corresponding lateral dilation strain and confining pressure from confinement can be calculated. The whole procedure is repeated for each ε_c over the stress-strain curve and complete response of confined concrete can be obtained.

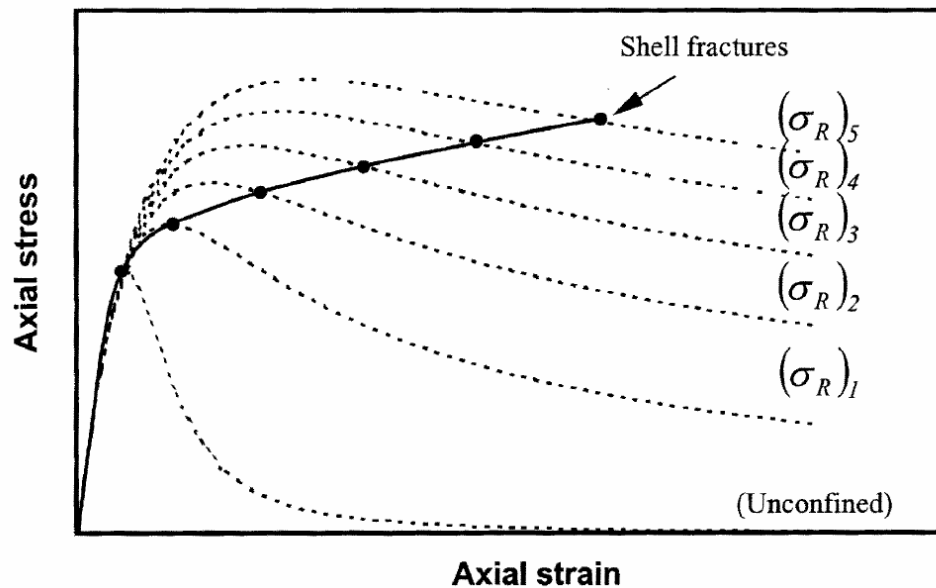


Figure 3.6 – Elastic confinement curve crosses constant confining pressure curves

The starting point is a well-known stress-strain model for confined concrete (Mander et al. 1988a,b), based on the Popovics formula (1973).

It is based on a constant value of the confining pressure throughout the loading history. In reality, passive confinement increases as concrete expands laterally, its amount depending on the stress-strain law of the confining device. Therefore, Mander's model correctly represents the behavior of steel-confined concrete, except for the initial phase when steel is still elastic.

Conversely, FRP behaves elastically up to failure, and the inward pressure increases continuously, so that this assumption is not appropriate.

The dependence of the current stress f_c and lateral strain ε_l on the current

strain ε_c and the confining pressure f_l is rendered explicit in the Pantazopoulou and Mills (1995) model.

For a given axial strain ε_c , a trial value ε_l is given, then the strain ε_j in the confining jacket can be found (e.g., for the case of axially loaded concrete cylinders ε_l in concrete is equal to ε_j in confining device for compatibility) along with its current stress $f_j = E_j \varepsilon_j$, where E_j is the modulus of the composite material of the jacket. The effective lateral confining stress f'_l is given by the confinement effectiveness coefficient multiplied by the pressure f_j exerted by the jacket.

This updated value of f'_l can be used for a new estimate of ε_l giving rise to an iterative procedure until f'_l converges to a stable value. The whole procedure is repeated for each ε_c , over the complete stress-strain curve.

This can be considered as a curve crossing a family of Mander's curves, each one pertaining to the level of confining pressure corresponding to the current lateral strain. All numerical tests have shown that convergence is very fast.

For FRP-confined concrete, the ultimate compressive axial strain of concrete is considered to be attained when the lateral strain of concrete reaches the ultimate strain of the FRP material.

Confinement models based on elastic theory: Fam and Rizkalla

The criteria used to formulate the interaction between the concrete and the confining surface utilizing the radial displacement compatibility at the interface between the core cylinder and the outer thin tube are based on the elastic theory.

In the analysis, the loading is considered by imposing an axial strain ε_{cc} .

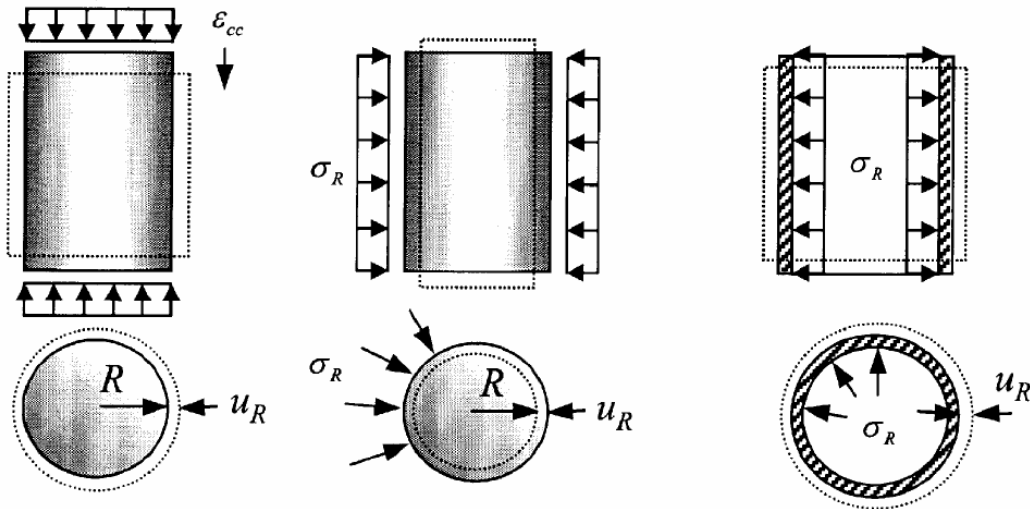


Figure 3.7 –Solid Cylinder and thin shell under different stresses

Considering the concrete cylinder placed inside the thin FRP tube, as shown in Fig. 3.7, the hybrid system can be analyzed in the elastic regime for the following two cases:

1. The solid concrete core is subjected to a uniform axial strain loading ϵ_{cc} . To estimate the interfacial pressure σ_R , both equilibrium and radial displacement compatibility are considered. The outward radial displacement of the core due to both the axial strain ϵ_{cc} and the radial pressure σ_R must be equal to the outward radial displacement of the tube due to the same radial pressure σ_R .

$$\sigma_R = \frac{v_{conc}}{\frac{R}{E_{frp}t} + \frac{1-v_{conc}}{E_{conc}}} \epsilon_{cc}$$

2. Both the core cylinder and the tube are axially loaded with strain ϵ_{cc} . As the concrete tends to expand outwards, the FRP tube expands as well with a different rate related to the Poisson's ratios. Therefore, the interface pressure developed is a direct function of the relative radial displacements.

$$\sigma_R = \frac{v_{conc} - v_{frp}}{\frac{R}{E_{frp}t} + \frac{1 - v_{conc}}{E_{conc}}} \varepsilon_{cc}$$

By examining previous equations it is obvious that increasing the stiffness of the tube in the hoop direction ($E_{frp}t/R$) and increasing Poisson's ratio v_{conc} will significantly increase the confining pressure. Latter equation also indicates that if Poisson's ratio of the tube is higher than that of concrete at a given load level, this will lead to a negative radial pressure σ_R , which indicates separation between the concrete core and the FRP tube as observed by other researchers stating that steel tubes are less effective in confinement when axially loaded with the concrete core, as Poisson's ratio of concrete at early stages (0.15 to 0.20) is less than that of steel (0.3), and tends to separate from the tube.

Previous equations are based on linear elasticity theory, which assumes linear elastic behavior for all the materials under consideration. Fam and Rizkalla (2001) developed a technique to account for the nonlinear characteristics of the concrete to determine E_c and v_c at each loading level ε_{cc} .

E_{ci} is the secant modulus at load level i . As the confined stress-strain curve is constructed, each point is obtained using the secant modulus of the previous point: $E_{c,i} = f_{c,i-1} / \varepsilon_{c,i-1}$.

Similar to the technique adopted for the secant modulus, the secant Poisson's ratio is used to obtain the lateral strain at a given axial strain in the incremental approach adopted in the model. Under the confinement conditions, the dilation of concrete is reduced because of the controlled microcracking; therefore, the Poisson's ratio at a given axial strain level is expected to be lower in the presence of confining pressure. In 1969, Gardner tested 29 MPa concrete cylinders under different confining hydrostatic pressures ranging from 0 to 25.86 MPa, and reported the average axial-lateral strain behavior for at least three

cylinders of each case. The behavior followed a second-order polynomial

$$\varepsilon_l = A\varepsilon_{cc}^2 + B\varepsilon_{cc}$$

where ε_l and ε_{cc} are the lateral and axial strains, respectively; and A and B are constants. The secant Poisson's ratio ν_{conc} , which is the ratio ($\varepsilon_l / \varepsilon_{cc}$), was estimated at different axial strain levels ε_{cc} . Based on the fact that the axial-lateral strain behavior followed a second-order polynomial, a simplified linear relationship is proposed for ν_{conc} under constant confining pressure in the following form derived from regression analysis:

$$\frac{\nu_{conc,i}}{\nu_{conc,o}} = 1 + \frac{\varepsilon_{c,i}}{\varepsilon_{cc,i}} \left(0.719 + 1.914 \frac{\sigma_{R,i}}{f'_c} \right)$$

In Figure 3.8 are the predictions of this model applied to a concrete cylinder with different jacket thickness to diameter ratios.

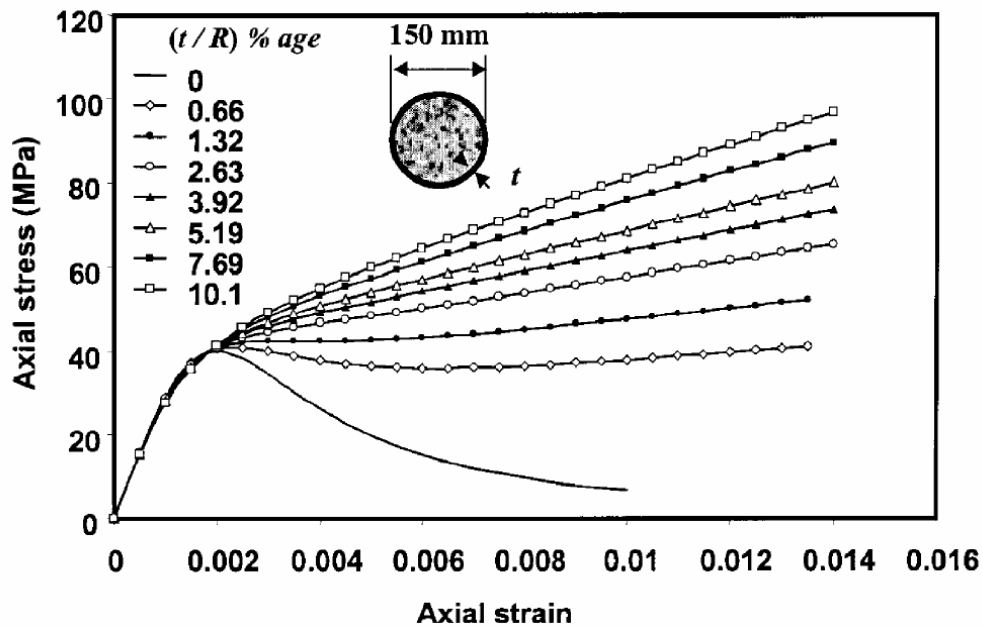


Figure 3.8 – Confinement curves for different reinforcement ratios

Failure of concrete confined by FRP members is mainly due to rupture of the FRP jacket. Once the hoop stress reaches the material tensile strength, rupture occurs, leading to overall failure of the member.

The presence of axial compression in this case reduces the strength of the jacket in the hoop direction, and a biaxial strength failure criterion must be adopted to account for the combined stresses (as shown in figure 3.9).

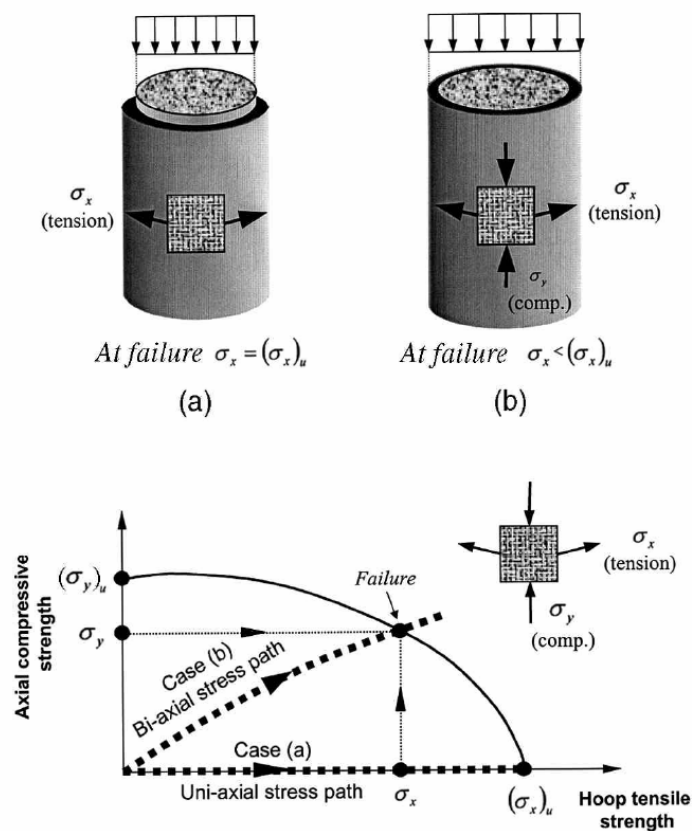


Figure 3.9 – Failure criteria for FRP jacket

Confinement models based on plain strain theory: Braga and Laterza

Braga and Laterza (1998) observed that the increment of stress in the concrete section is produced without any out-of-plane strain. In figure 3.10, given an axial strain, the total axial stress equals the sum of unconfined axial stress $\Delta\sigma_z = \nu(\sigma_x + \sigma_y)$ and of axial stress due to confinement $\Delta\sigma_z$, which appears without any further axial strain ($\varepsilon_z = \gamma_{zx} = \gamma_{zy} = 0$). It can be assumed that the increase $\Delta\sigma_z$ of concrete axial stress σ_z due to confinement respects plain strain conditions.

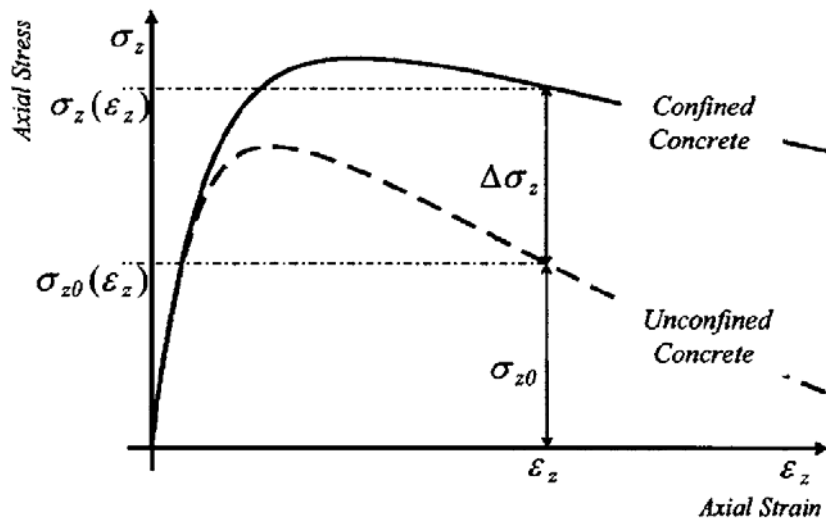


Figure 3.10 – Confinement respects plain strain conditions

The transversal stresses induced by a hoop, either of square or of circular shape, in the cross section of RC members (columns or beams) axially loaded, are evaluated through Airy's functions in plain strain states.

In plain strain states, when $\varepsilon_z = \gamma_{zx} = \gamma_{zy} = 0$, the strain and stress axial components (orthogonal to xy plane) on concrete are:

$$\Delta\varepsilon_z = \frac{1}{E_c} [\Delta\sigma_z - \nu(\sigma_x + \sigma_y)] = 0$$

$$\Delta\sigma_z = \nu(\sigma_x + \sigma_y)$$

If mass forces are constant or null, given an Airy's function $F(x,y)$ (introduced by G.B Airy in 1862), the stresses are expressed by:

$$\sigma_x = \frac{\partial^2 F}{\partial y^2}; \quad \sigma_y = \frac{\partial^2 F}{\partial x^2}; \quad \tau_{xy} = \frac{\partial^2 F}{\partial x \partial y}$$

The previous equations satisfy internal equilibrium, while compatibility is imposed through

$$\frac{\partial^4 F}{\partial x^4} + \frac{\partial^4 F}{\partial x^2 \partial y^2} + \frac{\partial^4 F}{\partial y^4} = 0$$

Equilibrium at the boundaries of a square shaped cross section, where the direction cosines of the boundary normal are α_x , α_y and the boundary stresses are p_x , p_y , is given trough

$$\sigma_x \alpha_x + \tau_{xy} \alpha_y = p_x; \quad \tau_{yx} \alpha_x + \sigma_y \alpha_y = p_y$$

Previous equations are based on linear elasticity theory, which assumes linear elastic behavior for all the materials under consideration. Braga and Laterza (1998) accounted for the nonlinear characteristics of the concrete considering ν_c at each loading level ε_z , but the relation they adopted is referred to unconfined tests:

$$\nu(\varepsilon_z) = \nu_o \left[1 + 0.2 \left(\frac{\varepsilon_z}{\varepsilon_{co}} \right) - \left(\frac{\varepsilon_z}{\varepsilon_{co}} \right)^2 + 1.55 \left(\frac{\varepsilon_z}{\varepsilon_{co}} \right)^3 \right]$$

The problem is therefore reduced determining the function $F(x,y)$ that satisfies the compatibility condition and the boundary conditions.

Applying this method, the distribution of confining pressures on two circumferences inside the square section is shown in Fig. 3.11 (Gigliotti 1998).

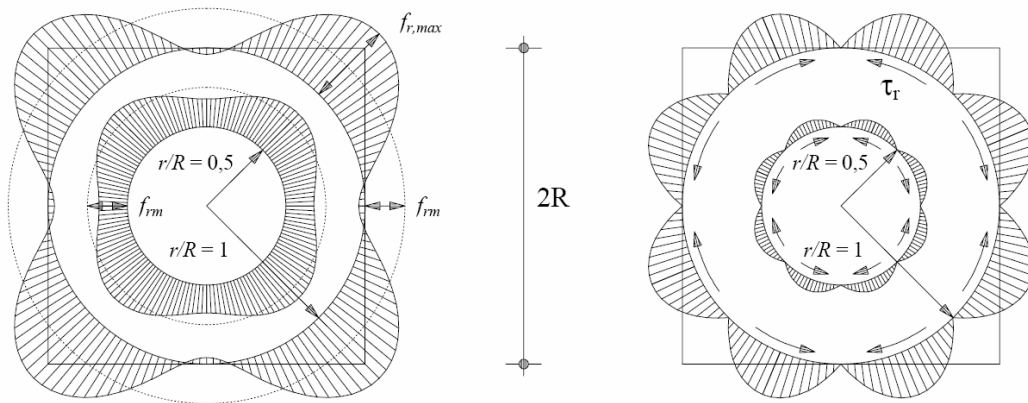


Figure 3.11 – Stress state along two circumferences within a confined square section

Shape factor for confinement effectiveness

In structural members, triaxial compression stress states are usually activated by prevention of lateral expansion. The amount of lateral expansion determines the confinement stress, which is called passive confinement. In Figure 3.12 the dilation of the concrete cylinders due to the axial load σ_{33} strains the confining material in the circumferential direction and activates radial stresses.

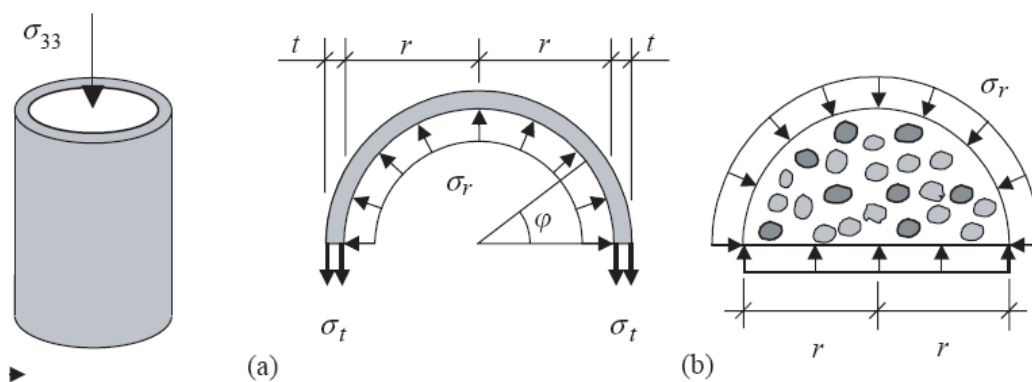


Figure 3.12 –Circular shape: effective confining pressure

The relation of the tangential stresses σ_t in the enclosing material to the radial stresses σ_r acting on the concrete specimen may be derived by stress equilibrium in the lateral direction as:

$$\int_0^\pi \sigma_r \sin \varphi \cdot r d\varphi = 2\sigma_t t$$

so that the lateral stress, σ_r , is:

$$\sigma_r = \frac{t}{r} \sigma_t .$$

The radial strain $\varepsilon_r = \frac{\Delta r}{r}$ is equal to the tangential strain $\varepsilon_t = \frac{\Delta U}{U} = \frac{2\pi\Delta r}{2\pi r} = \varepsilon_r$.

Rectangular sections do not experience uniform confining pressure from external confinement. Dilation of the concrete section results in a large confining pressure developed across the diagonals of a rectilinear section (Figure 3.13).

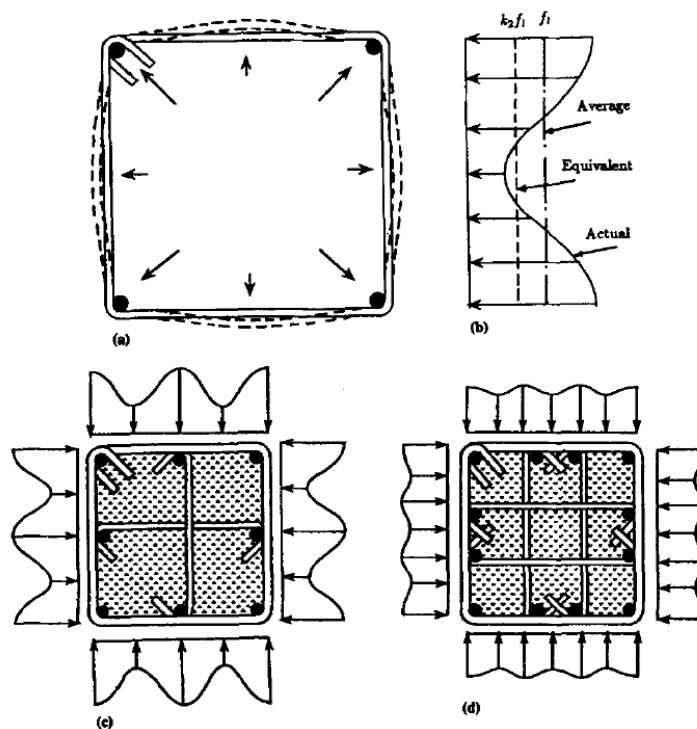


Figure 3.13 – Confinement pressure for different reinforcement arrangements

For circular sections, the confining pressure is uniform, and is a function of hoop strength of the jacket. On the other hand, for square sections, the confining pressure varies. The confining pressure at the corners is due to the membrane action in the transverse sides of the tube, whereas at other points it depends on the flexural rigidity of the FRP plate.

The jacket sides provide smaller levels of confinement since confining pressure there is engaged more by the flexural stiffness rather than the tensile stiffness of the jacket.

The corner radius R_c on a rectangular FRP jacket affects the confinement provided. As the size of the corner radius increases, stress concentrations are decreased and the effectively confined area becomes larger.

This however shows that even a circular jacket has a shape factor due to the radius of curvature.

For non-circular columns, section can be divided into two separate parts: sufficient and insufficient confined ones. Insufficiently confined parts are in the form of second order parabolas as shown in Figure 3.14. Initial slope of these parabolas is depth to width ratio of the section. For square section, this ratio meets the slope of 45° [Mander et al, 1988].

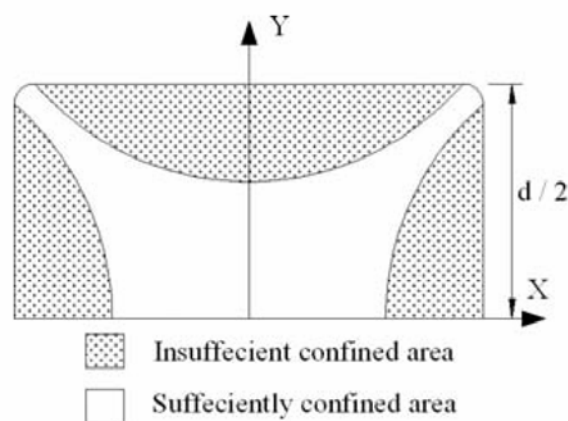


Figure 3.14 – Confined and Unconfined portion of the section

Separating parabola is given by:

$$Y = Ax^2 + Bx + C$$

with applying proper boundary conditions to the equation of parabola, constant coefficients can be found as follows.

$$\frac{dY}{dx} = 0 \quad (\text{at } x=0) \quad \text{resulting in } B = 0$$

$$\frac{dY}{dx} = 1 \quad (\text{at } x=d/2-R_c) \quad \text{resulting in } A = \frac{1}{d-2R_c}$$

$$Y = \frac{d}{2} \quad (\text{at } x=d/2-R_c) \quad \text{resulting in } C = \frac{d+2R_c}{4}$$

A shape factor, k_e , can be the ratio between the effectively confined concrete in a rectangular cross section, A_{con} , to the gross sectional area, $A_g=bd$. The effective confined area is defined using circular arc segments extending between the rounded corners of the section and ρ is the longitudinal steel reinforcement ratio:

$$k_e = \frac{A_{con}}{A_g} = \frac{1 - \left[\frac{(b-2r)^2 + (d-2r)^2}{3bd} \right] - \rho}{1 - \rho}$$

Masia and Shrive (2003) propose a simplified shape factor based on the geometry shown in Figure 3.15:

$$k_e = \frac{A_{con}}{A_g} = \frac{\left(\frac{b}{r}\right)^2 - \left(\frac{b}{r} - 2\right)^2 \tan \phi - 2}{\left(\frac{b}{r}\right)^2}$$

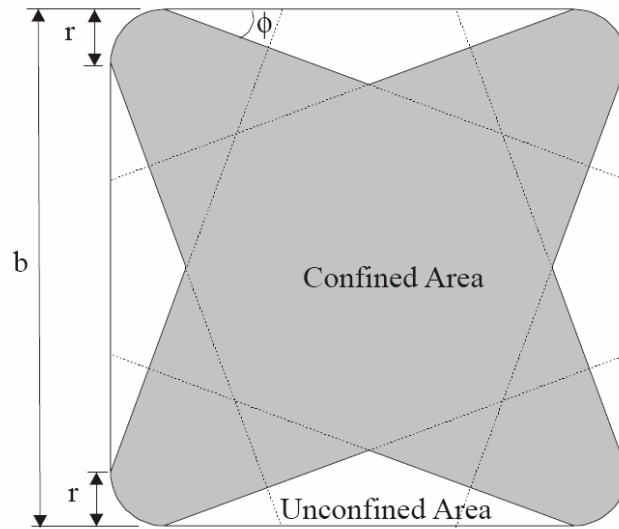


Figure 3.15 – Confined area as defined by Masia and Shrive (2003)

In the case of confinement model based on $f'_{cc} = f'_c + f'_l \cdot k_1$, the shape factor can be also adopted to evaluate an “effective” lateral confining pressure.

The average strength of confined concrete column can be evaluated as the axial capacity N_{cc} (given by the sum of strength contribution of the confined area A_{con} multiplied by f'_{cc} and the cover, unconfined, area A_{cov} multiplied by f'_c) divided by the gross area of the section A_g :

$$\begin{aligned} \overline{f'_{cc}} &= \frac{N_{cc}}{A_g} = \frac{(f'_c + f'_l \cdot k_1) \cdot A_{con} + f'_c \cdot A_{cov}}{A_g} = \frac{f'_c \cdot (A_{con} + A_{cov}) + f'_l \cdot k_1 \cdot A_{con}}{A_g} = \\ &= f'_c \cdot \frac{A_g}{A_g} + f'_l \cdot k_1 \cdot \frac{A_{con}}{A_g} = f'_c + f'_l \cdot k_1 \cdot k_e \end{aligned}$$

To investigate relationship between core and corner confining stresses and corner radius, free body diagram of the column section should be considered. Due to symmetry of the square section, only upper right quarter of the column will be shown in Figure 3.16. Hatched areas are effectively confined portions of the

column section.

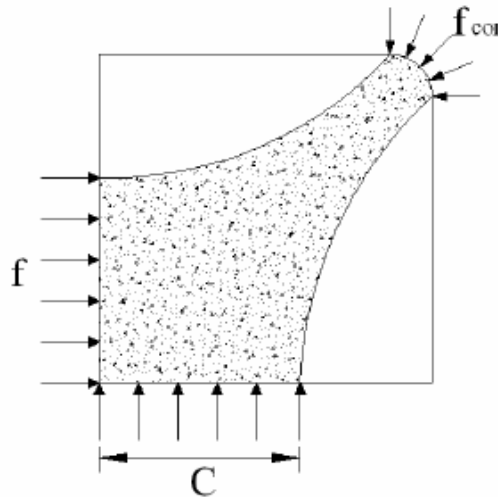


Figure 3.16 –Free Body diagram of the section portion

Force equilibrium of shown body in horizontal or vertical direction gives:

$$C \cdot f = R_c \cdot f_{cor}$$

where C is the length of efficiently confined core calculated in separating parabola equation, f is exerted effective confining stress on the core by FRP jacket, R_c is radius of corner rounding and f_{cor} is maximum confining stress on corner.

Rewriting previous equation gives:

$$f = \frac{R_c}{C} \cdot f_{cor} = k_e \cdot f_{cor}$$

where the ratio of effective confining stress on column core to corner confining stress is the shape factor $k_e = \frac{R_c}{C}$

If in a square section, column core area is under confining pressure resulting from both external confinement wraps and internal steel hoops, cover area (area between FRP wrap and core enclosed by transverse reinforcements) is affected

only by external confinement pressure. An equivalent confining pressure may be calculated as weighted mean confinement of both FRP and steel reinforcements over the whole cross section area:

$$f_{l, \text{equivalent}} = \frac{(f_l^{\text{FRP}} + f_l^{\text{steel}})A_{\text{con}} + (f_l^{\text{FRP}})A_{\text{cov}}}{A_g}$$

A_{con} and A_{cov} are column core area and cover area respectively.

A confinement effectiveness factor should be considered also in the case of discontinuous confinement in the longitudinal direction (i.e. stirrups or discrete wraps) where the confining pressure is not uniform along the element length.

Superimposed models to account for internal and external confinement

To account for both the steel reinforcement and FRP confining concrete in the retrofit design of columns using FRP composite materials, the lateral confinement should consider the confinements of the FRP and steel reinforcement together.

Therefore, the strength of the confined concrete with FRP and steel reinforcement will be the unconfined concrete strength plus strengths increased by the steel reinforcement and FRP.

The relations can be shown as follows:

$$f'_{cc} = f'_c + f'_{cs} + f'_{cf}$$

where f'_{cs} is the increased strength due to the steel reinforcement, and f'_{cf} is the increased strength due to FRP. In the above equation, f'_{cs} and f'_{cf} can be expressed according to the described models.

In this expression is implicitly considered that both confinements exert the maximum effect at the same concrete strain level.

FRP strain efficiency

In existing models for FRP confined concrete, it is commonly assumed that FRP ruptures, when hoop strain in the jacket reaches its ultimate tensile strain. However, FRP confined concrete experimental results show that in most cases, FRP experimental ultimate tensile strain is not reached at the rupture of FRP confining jacket. The difference is observed between *in situ* jacket rupture strains and FRP material rupture strains determined from standard coupon tests.

The discrepancies between *in situ* strain capacities and material strain capacities accounted for in this manner may include:

1. Misalignment or damage to jacket fibers during handling and lay-up;
2. The inclusion of residual strains during lay-up resulting from flaws in the substrate concrete, uneven tension during lay-up, or temperature, creep, and shrinkage incompatibility between the concrete and FRP jacket;
3. Cumulative probability of weaknesses in the FRP material since jackets are much larger than tensile coupons;
4. Multiaxial stress state due to transfer of axial load through bond with concrete; and,
5. Radius of curvature in FRP jackets on cylinders as opposed to flat tensile coupons.

Localized regions of high strain can occur in the jacket (i.e. bridging a splitting crack). The bond between the jacket and underlying concrete, however, allows jacket stresses to be transferred into the concrete away from the discontinuity and thus reduces the average strain in the jacket. Unless a measurement is made exactly at the strain concentration, measured jacket strains at rupture are lower than the material strain capacity.

For wrapped specimens, the average absolute error of all models shows a remarkable decrease when the confining device effective strain is inserted in the

equations.

3.1.3 Confined Concrete eccentrically loaded

The notion of the “ideal” column projected as a purely compression member is generally false, as eccentricities commonly exist in situ. Once a compressive force acts non-concentrically the element has additional bending forces applied to it. Hence, in a practical sense there is no column that is under perfect concentric loading. Due to many circumstances such as loads from adjoining members and columns being out of plumb, most columns are placed under some amount of eccentric loading.

There have been several studies on wrapping columns with FRP. All these studies are based on testing columns under concentric loads. Hence there is a gap in knowledge of the behavior of FRP wrapped concrete columns when tested under eccentric loads.

Yuan et al. (2001) presented a comparative study of concrete stress–strain models and applied these models for FRP-confined reinforced concrete columns under combined bending and compression. The authors showed that there are large differences between the different stress–strain models thus leading to large differences in the predicted ultimate strength and flexural ductility.

In a study performed by Parvin and Wang (2001), square concrete columns (height 305 mm, width 108 mm) were wrapped with varying layers of Carbon FRP and tested with the loading placed at different eccentricities. The eccentric loading was achieved by placing a knife edge at a given distance from the centre of the cross section of the column.

That study showed in each reinforcement category that the increase in eccentricity resulted in a decrease in strength capacity of the column. However it

was noted from that results that even under eccentric loading, the use of external reinforcement increases the load capacity of the column, with further increases in the load capacity achieved when the number of layers of external reinforcement is increased. The column specimens used by Parvin and Wang (2001) were short columns, and the conclusions are not easily extended to longer columns.

The strength gains obtained are marginal with an eccentric load, while ductility improvements are more distinctive than the gains in strength, particularly in the plain specimens. Confinement produced dependable gains in ductility that are shown by the improved behavior of load-lateral deflection. Such behavior can be interpreted as the rotational capacity of column structures being enhanced.

Although the effect of strain gradient has been the focus of some of these earlier researches, the significance of the strain gradient has continued to be a source of controversy. In spite of the apparent conflicting views, it is generally agreed (at least for unconfined concrete) that the stress-strain relationship of plain concrete under concentric loading is representative of the behavior of concrete under eccentric loading.

Transverse column reinforcement under eccentric loading is not stressed to the same level as under concentric loading. The tendency to expand in the lateral direction and the associated transverse strains in concrete near the extreme core compression fiber may be comparable to those attained under concentric compression, concrete near the neutral axis is subjected to relatively low compressive strains in the longitudinal direction and comparably low tensile strains in the transverse direction. This translates into a lower passive pressure produced by confinement devices.

A linear variation of equivalent pressure is more appropriate for the compression region of an eccentrically loaded column, undergoing a linear variation of longitudinal strains (Figure 3.17).

The effects of confinement on stress–strain characteristics of concrete

increases with increased compressive strains. In the low compressive range, typically near the neutral axis, the stress-strain relationship is not significantly affected by concrete confinement. Therefore inaccuracy in pressure computation near the neutral axis is not likely to result in appreciable differences in the overall section response

In Figure 3.17 the use of the same stress-strain strip 1 relationship for strips 2 and 3 toward the neutral axis causes an overestimation of concrete confinement, however in these regions the longitudinal strains are proportionally lower and the corresponding portions of the stress-strain relationships are not significantly different from those established for strip 1.

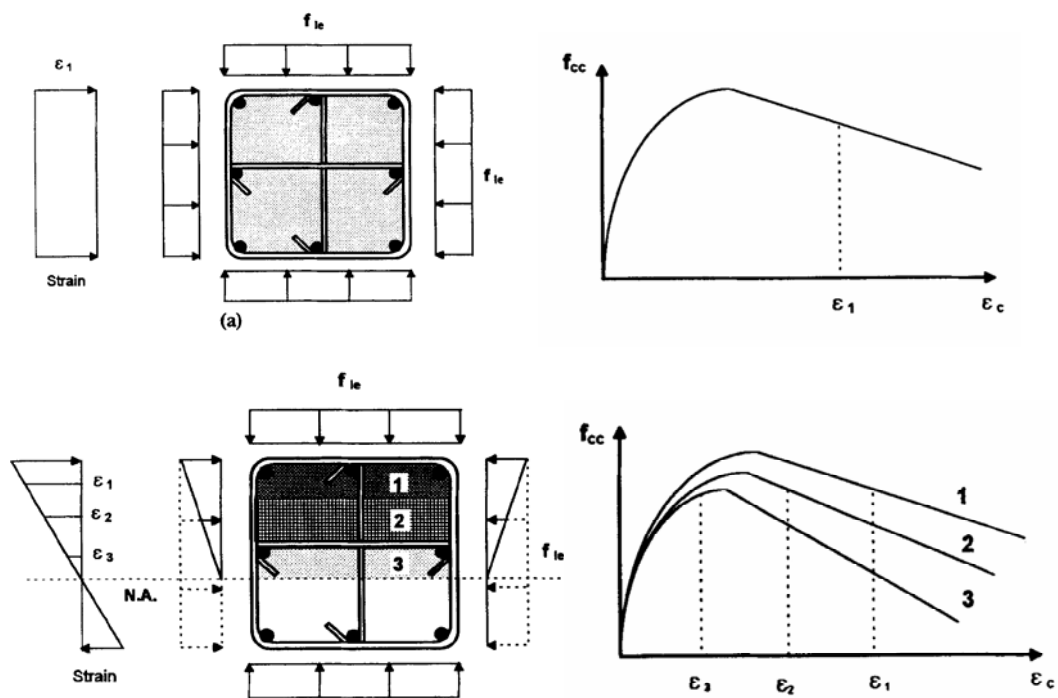


Figure 3.17 –Effect of strain gradient

The confinement pressure near the perimeter is higher than the uniform equivalent pressure used to evaluate confinement effects, so this underestimation

for strip 1 is likely to offset the overestimation for strips 2 and 3.

Three different mechanisms simulating the behavior of concrete in the compression/flexure zone can be categorized as follows:

Full confinement mechanism (Upper bound)

In this case, the stress-strain curve of the confined concrete can be determined using any of the confinement models available in the literature for the case of pure axial loading condition. The analysis in this case utilizes the same confined stress-strain curve, in the compression zone, for the full range of eccentricity, to establish the interaction diagram.

Unconfined concrete model (Lower bound)

In this case, an unconfined stress-strain concrete model is adopted in the compression zone for the full range of eccentricity to establish the interaction diagram. The curve could be terminated at unconfined concrete ultimate strain or could be extended to strain ϵ_{cc} .

Variable confinement mechanism

A variable confinement model assumes that the confinement level of concrete is gradually reduced as the eccentricity of the axial load increases. This mechanism is very representative to observed behavior. Test results indicated that increasing the eccentricity results in a strain gradient that subject large part of the cross-section to tensile strains, which would significantly reduce the level of confinement. The variable stress-strain curve of concrete ranges from the upper limit of the fully confined concrete (zero eccentricity) to the lower limit of the unconfined stress-strain curve with extended ductility for the case of infinite eccentricity (pure bending).

For a given general eccentricity e , the ultimate strength of concrete $f_{cc,e}$ can be calculated as a function of the fully confined strength f_{cc} and the unconfined stress f_{c0} at ultimate strain, from the following equation:

$$f_{cc,e} = f_{co} + (f_{cc} - f_{co}) \frac{D}{D+e}$$

where D is the outer diameter/dimension. This simple expression satisfies the upper and lower limits. For a case of pure axial load ($e = 0$), $f_{cc,e} = f_{cc}$, and for the case of pure bending ($e = \infty$), $f_{cc,e} = f_{co}$.

The strain $\varepsilon_{cc,e}$, which corresponds to the strength $f_{cc,e}$ and ranges from ε_{co} to ε_{cc} , is calculated from the following elliptical equation:

$$\varepsilon_{cc,e} = \varepsilon_{co} + (\varepsilon_{cc} - \varepsilon_{co}) \sqrt{1 - \left(\frac{f_{cc,e} - f_{co}}{f_{cc} - f_{co}} \right)^2}$$

It is worthy noted that for the case of pure bending the effect of confinement on concrete strength is insignificant, however, the ductility and strain of concrete are increased significantly beyond 0.003. It is also well established that failure of the system is normally governed by failure of the FRP or steel reinforcement before complete failure of the concrete. In all the cases where the concrete strains remain lower than the 0.002 (i.e. for low axial load compared to bending moment or in the case of large eccentricities), the effect of confinement is negligible, because that portion of the stress-strain relationships is almost equal in the case of concrete confined or not. If the concrete capacity is not attained at failure, then there are no differences in the PM interaction domain (in figure 3.18 is the interaction domains for the same section with different concrete strengths)

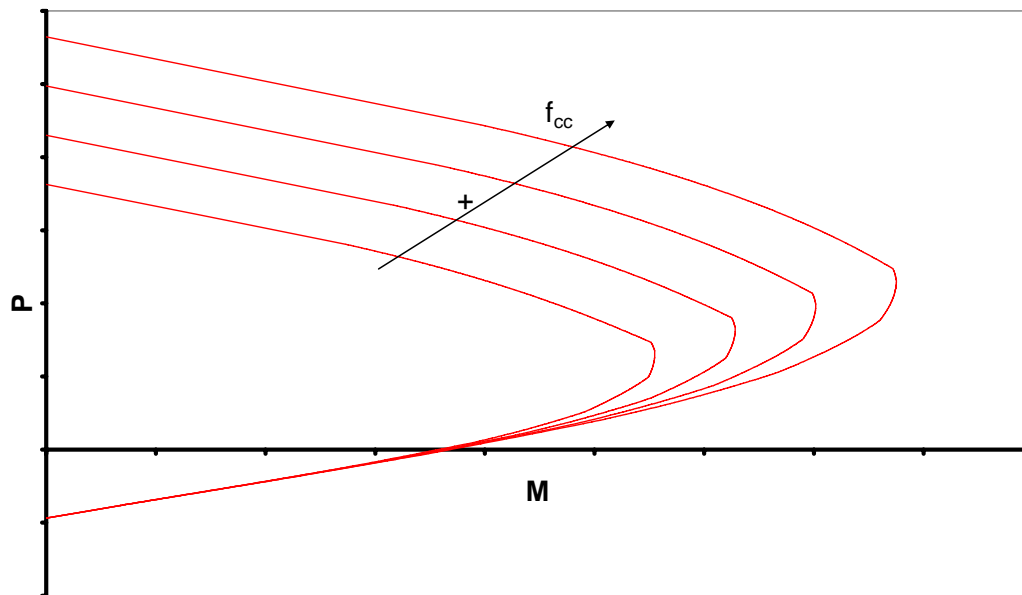


Figure 3.18 –PM interaction Diagram for different concrete strengths

3.1.4 Steel internal Reinforcement

The properties of reinforcing steel, unlike concrete, are generally not dependent on environmental conditions or time. Thus, the specification of a single stress-strain relation is sufficient to define the material properties needed in the analysis of reinforced concrete structures.

Typical stress-strain curves for reinforcing steel bars used in concrete construction are obtained from coupon tests of bars loaded monotonically in tension. For many practical purposes steel exhibits the same stress-strain curve in compression as in tension. The steel stress-strain relationship exhibits an initial linear elastic portion, a yield plateau, a strain hardening range in which stress again increases with strain and, finally, a range in which the stress drops off until fracture occurs. The extent of the yield plateau is a function of the tensile strength of steel. High-strength, high-carbon steels, generally, have a much shorter yield

plateau than relatively low-strength, low-carbon steels.

Since steel reinforcement is used in concrete construction in the form of reinforcing bars or wire, it is not necessary to introduce the complexities of three-dimensional constitutive relations for steel. For computational convenience it even often suffices to idealize the one dimensional stress-strain relation for steel.

A first idealization neglects the strength increase due to strain hardening and the reinforcing steel is modeled as a linear, perfectly plastic material. This assumption underlies the design equations of many design codes. If the strain at the onset of strain hardening is much larger than the yield strain, this approximation yields very satisfactory results. This is the case for low-carbon steels with low yield strength.

If the steel hardens soon after the onset of yielding, this approximation underestimates the steel stress at higher strains. In several instances it is necessary to evaluate the steel stress at strains higher than yield to more accurately assess the strength of members at large deformations. This is, particularly, true in seismic design, where assessing the available ductility of a member requires that the behavior is investigated under strains many times the yield strain. In this case more accurate idealizations which account for the strain hardening effect are required. The parameters of these models are the stress and strain at the onset of yielding, the strain at the onset of strain hardening and the stress and strain at ultimate. These parameters can be derived from experimentally obtained stress-strain relations.

Reinforcement Stability and Fracture of Concrete Cover

During earthquakes, reinforced concrete members may experience significant lateral deformation of the longitudinal reinforcing bars accompanied by the spalling of concrete cover due to large compressive strain. Analytical

models neglecting these inelastic material mechanisms cannot capture the post-peak softening behavior accurately, and will consequently overestimate the response ductility.

In reality, average behavior in compression is different from that in tension. This difference is mainly attributed to the geometrical nonlinearity associated with large lateral deformation of buckled reinforcing bars.

The average compressive response of bare bar is a function of the length-to-diameter ratio. Longitudinal reinforcing bars inside RC members, when subjected to large compressive strain, undergo lateral deformation. This behavior is referred to as buckling; similarly, the spalling is the detachment of a part of cover concrete from the core concrete, finally losing its load-carrying capacity. Because of their interdependency, these two mechanisms should be considered simultaneously and separating them may lead to an incorrect outcome.

The assumption that the buckling length of longitudinal reinforcing bars inside an RC member is equal to the spacing of lateral ties does not hold true except in some special cases, such as when lateral ties are very stiff, longitudinal reinforcing bars are very slender and tie spacing is very large.

Axial compression tests of reinforced concrete prisms (Kato et al. 1995) showed that the buckling length varies from one to several times tie spacing depending on the geometrical and mechanical properties of lateral ties and the longitudinal bar. If the size and spacing of lateral ties are properly designed to provide a rigid support to the longitudinal reinforcing bar at the tie locations, buckling confines between two adjacent stirrups. It is to be noted that if the buckling length changes from one to two times tie spacing, the length-to-diameter ratio will be doubled, and the average compressive stress-strain relationship of reinforcement over the buckling length domain is significantly changed.

The buckling tendency of longitudinal bars induces axial tension in the tie legs along the buckling direction. Hence, the resistance provided by the lateral ties

against buckling of the longitudinal bar is mainly contributed by the axial stiffness of these tie legs.

The tensile capacity of concrete cover in the transverse direction decreases with an increase in the splitting crack width. Two factors contribute to the formation of the splitting crack leading to cover concrete spalling. First, the compressive strain deteriorates the cover concrete creating some vertical cracks and the tensile capacity in the transverse direction is reduced. Next, the buckling tendency of the longitudinal bar widens these cracks, finally reducing the tensile capacity to zero and separating the cover concrete from the core concrete.

After a certain point in a test, the local longitudinal bar strains at a section measured by strain gauges started to differ from those obtained by drawing the strain profile based on the “plane sections remain plane” assumption of the beam bending theory. This phenomenon is presumed to indicate the initiation of buckling of the longitudinal bars. Results obtained from conventional sectional analyses up to the initiation of longitudinal bar buckling are quite valid, but beyond this point the response of a section can be predicted with reasonable accuracy only if the behavior of the longitudinal bars is determined by considering the phenomenon of buckling.

Cosenza and Prota (2006) investigated the compressive behavior of smooth bars for different values of the ratio L/D , L being the restraints distance and D the bar diameter. The stress-strain relationship is modeled ranging from an elastic-plastic behavior identical to that in tension ($L/D = 5$) to the elastic buckling behavior ($L/D > 20$). Their research was planned to cover a much broader range of L/D values than that dealt with by Monti and Nuti (1992) with respect to ribbed bars.

The experiments have highlighted that the stress-strain relationship of compressive bars depends on the ratio L/D , whereas it is not influenced by the bar diameter. The effect of the buckling in the plastic range becomes more significant

as L/D increases from 5 to 20 (Figure 3.19)

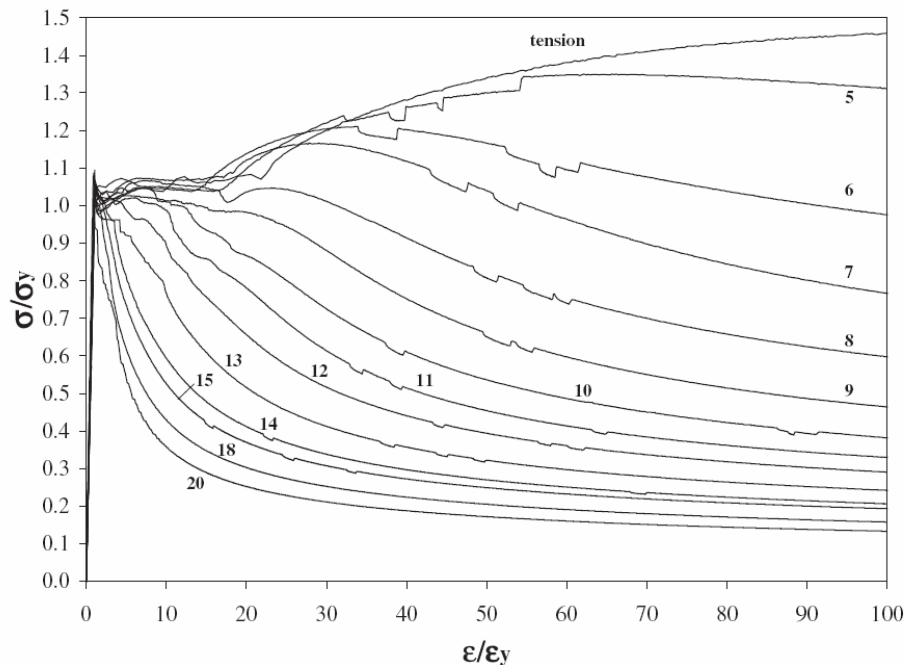


Figure 3.19 – Normalized compressive stress-strain curves for D12 bars

$L/D = 5$ is the value below which the ductility of the bar in compression is so large that its compressive behavior is very similar to that in tension.

$L/D = 8$ is the value below which the bar still exhibits a certain level of hardening before buckling;

$L/D = 20$ is the threshold beyond which the bar starts buckling close to the yielding and does not exhibit any hardening.

$$L/D = \frac{20}{\beta} \sqrt{\frac{320}{\sigma_{cr}}} = 40 \sqrt{\frac{320}{\sigma_y}}$$

occurs. Such threshold could be theoretically found recalling the Euler Elastic Buckling Theory assuming that $E = 205\text{GPa}$ and taking the critical stress, σ_{cr} , equal to the yielding stress, σ_y , the coefficient β is equal to 0.5 as for a beam fixed

at both ends.

The outcomes of the Cosenza and Prota (2006) model are depicted in Figure 3.20 that shows the “theoretical” curves for L/D ranging between 8 and 20.

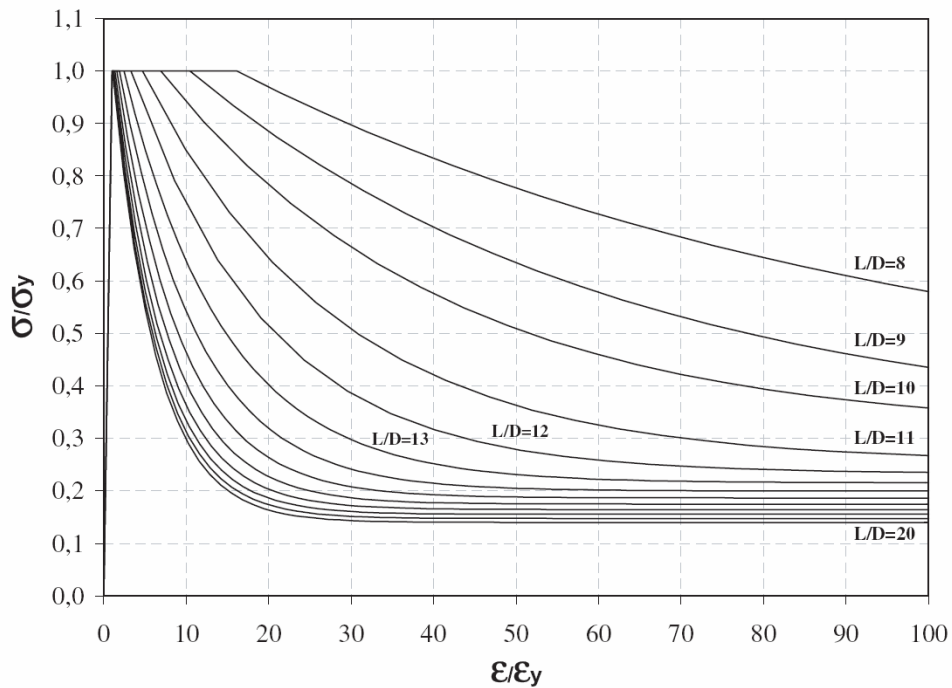


Figure 3.20 – Theoretical normalized compressive stress-strain curves (Cosenza and Prota 2006)

3.1.5 Wall Stability

With increasing use of higher strength concretes, and with improved construction methods, it is now possible to construct hollow concrete sections with relatively slender walls.

The "wall slenderness ratio" X_w/t is defined (Figure 3.21) as the longest unsupported wall width divided by the wall thickness.

Hollow rectangular sections with wall slenderness ratios in the range of 15 to 20 are now common. Such slender walls present the possibility of failure due to local buckling. While the local buckling behavior of thin walled metallic compression members has been studied extensively, little is known about the corresponding behavior of thin-walled concrete members.

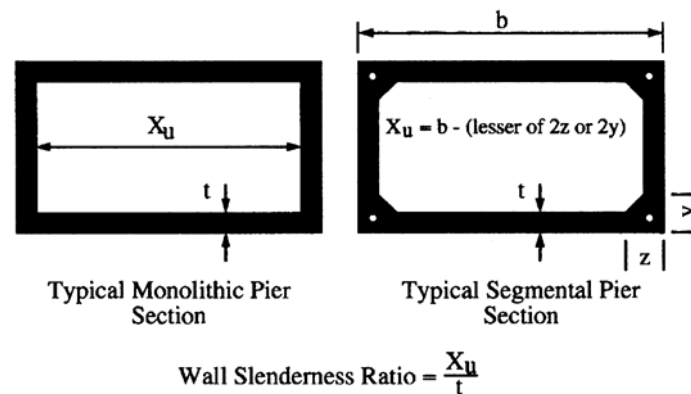


Figure 3.21 – Definition of wall slenderness ratio

The fundamental work on the elastic stability of short, thin-walled, axially loaded rectangular members was carried out in the early 1940s by Stowell et al. (1952). The two wider faces of the rectangular cross section were treated as flat plates whose longitudinal edges were elastically restrained against rotation by the two adjoining narrower faces.

Thin-walled concrete sections differ from metallic sections in several important respects. The stress-strain behavior for steel sections is usually modeled as linear elastoplastic, while the behavior of concrete is characterized by nonlinear ascending and descending branches of the stress-strain curve. Reinforced concrete is non-homogeneous: the presence of steel reinforcing bars affects the bending stiffness of concrete plates, and therefore the plate buckling stress. Finally, thin concrete plates do not demonstrate reliable post-buckling capacity.

The compression flange of the hollow cross section is treated as a thin, rectangular plate subject to uniformly distributed loads along two edges, as shown in Fig. 3.22.

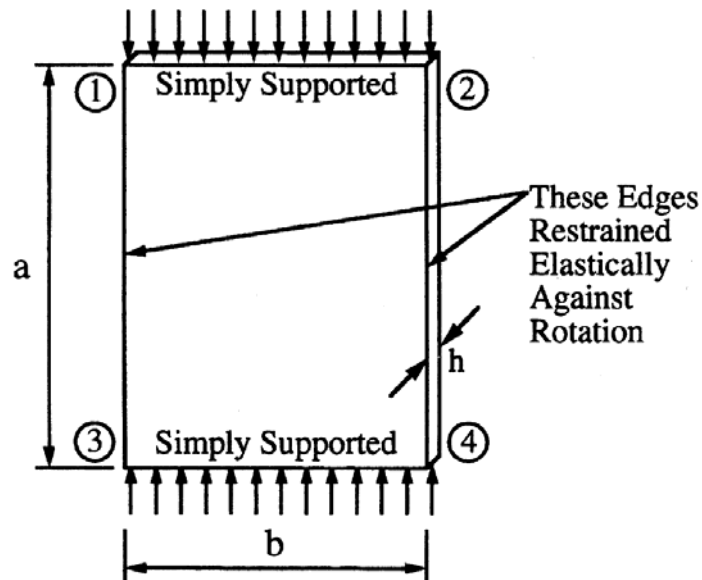


Figure 3.22 – Thin rectangular plate uniformly loaded along two edges

The boundary conditions along the two short edges (1-2 and 3-4) are assumed to be simply supported, even though there is some rotational restraint provided along the short edges of the compression flange in the hollow test specimens. The simply supported boundary condition can be chosen because the degree of rotational restraint along the short edges is uncertain, so a conservative assumption of simply supported edges is appropriate.

The boundary conditions along the two long edges of the flange (1-3 and 2-4) are shown in Fig. 3.22 as restrained elastically against rotation. The degree of rotational restraint depends on the relative plate bending stiffness of the four walls of the cross section.

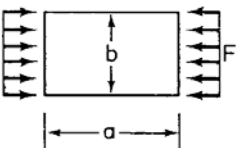
In classical elastic plate buckling theory, the length-to width ratio a/b and

boundary conditions of the plate are taken into account by a single plate buckling coefficient k (see table 3.1 for common values). The critical buckling stress f_{cr} of the plate according to this theory is

$$f_{cr} = \frac{k\pi^2 D}{hb^2} \text{ and } D = \frac{Eh^3}{12(1-\nu)}$$

where E is the modulus of elasticity, h is the thickness of the plate, b is the width of the plate, and ν is the Poisson's ratio.

Table 3.1– Plate buckling stress coefficient k for various cases

Loading condition	Unloaded Edge Condition	Buckling Stress Coeff. k
Both loaded Edges simply supported and uniaxial compression  $a/b > 4.0$	Both Simply Supported	4.00
	One fixed, one simply supported	5.42
	Both fixed	6.97
	One simply supported, one free	0.425
	One fixed, one free	1.28

Material nonlinearities of the concrete can be accounted for by using the tangent modulus of the concrete instead of the initial tangent modulus and the presence of reinforcing steel can be taken into account by expanding the flexural rigidity term D to include the contribution of reinforcing steel

$$D = \frac{E_t h^3}{12(1-\nu)} + E_s \rho_s h \cdot z^2$$

where E_t is the concrete tangent modulus, ρ_s is the total reinforcement ratio per unit width of plate, z is the distance from center of plate to centroid of steel layer and E_s is the elastic modulus of steel. If the reinforcing steel has yielded $E_s = 0$.

For flanges with wall slenderness ratios less than about 18, Poston et al. (1985) showed that the buckling stress of the flange is nearly equal to the peak stress of the stress-strain curve, $0.85f'_c$. For plates with wall slenderness ratios in the range 18 to 34, the buckling stress is 0.85 to 0.69 percent of f'_c .

Appropriate detailing of reinforcement is needed. First, cross ties must be provided between the two layers of reinforcing steel in each side of the cross section, especially along the top and bottom edges. Second, straight lap splices of lateral reinforcing bars should be avoided, and overlapping 90° bends at the corners of the cross section should be substituted.

3.2 Proposed nonlinear refined method

The study of axially loaded reinforced concrete members under bending (typically biaxial bending) is of particular interest in the case of structures subjected to earthquake motions; in such cases, in fact, the contemporary presence of bending moments, with respect to the centroidal principal axes, reduce the cross-section strength capacity. However, the three-dimensional character of the response of frame structures to seismic loads is overlooked by the present-day seismic codes that allow designing cross-sections under biaxial bending by analyzing such sections as subjected to two uniaxial bending and axial loads acting separately with a reduced moment capacity (i.e. Eurocode 8 suggests to reduce the moment capacity of a cross-section under biaxial bending by a factor of 30%).

The use of such simplified approaches, although unsafe in some cases, is justified by the difficulty to manually perform the computation of the cross-section capacity under axial load and bending (especially biaxial); such computation requires the integration of stresses associated with failure criteria that

can be numerically performed by discretizing the cross-section and iteratively locating the neutral axis depth. Thus, an integration procedure, implemented in a computer analysis program, that could allow providing a fast tool to perform an exact analysis of RC cross-sections under axial load and bending have been proposed. The proposed computation method is aimed at the analysis of arbitrary shape cross sections reinforced by mild steel and/or prestressing tendons as well as internal or external FRP bars or laminates. The developed algorithm allows, by using rectangular discrete elements (fibers in figure 3.23), providing the moment-curvature curve for cross sections subjected to axial load and biaxial bending; it allows to use different available linear and non-linear, also with softening branch, materials stress-strain relationships.

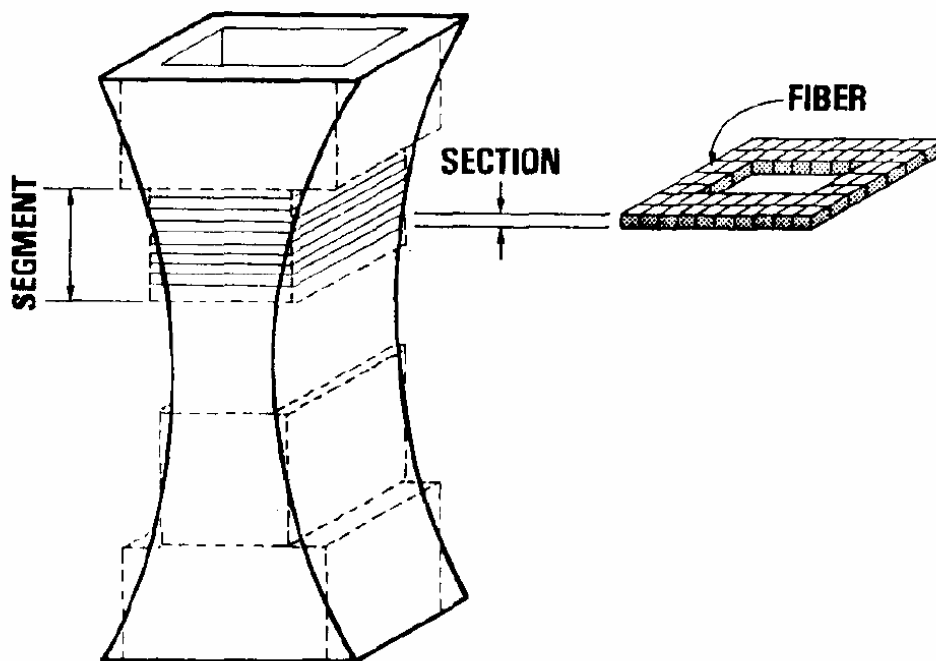


Figure 3.23 – Section discretization: rectangular discrete elements (fibers)

The theoretical load carrying capacity and general interaction relationships for hollow rectangular columns have been developed mainly for steel structures (Zhou and Chen 1985, Magdi and Ozkan 2004) and approximately for box concrete cross sections un-strengthened (Recupero et al. 2003).

3.2.1 Model assumptions

The analysis invokes the following assumptions: 1) plane sections remain plane (classical Bernoulli-Navier hypothesis); 2) Stress-strain relationships for the constituent materials are known; 3) The longitudinal stress at an element is dependent only on the longitudinal strain at that point so that the effects of creep and shrinkage are neglected; 4) Perfect bond is assumed at the interfaces between concrete and steel and/or FRP reinforcing bars or laminates; 5) Loading and deformation of the cross section are assumed to take place monotonically. Section behavior under cyclic loading conditions is not directly considered but could be addressed by implementing modified material stress-strain relationships.

The cross section is divided into elemental small areas, and each small area is assumed to have a constant strain and stress. Thus the integration of the stress field is performed adopting midpoint composite rule.

The strain within each bar is assumed to be uniform and equal to the strain generated at the centerline of the steel element (meshing procedure such as that used for the concrete cross section is unnecessary), and is assumed to be equal to the strain in the surrounding concrete (that is, perfect bond). The diameters of the bar reinforcements are assumed to be negligible when compared to the section dimensions. The same assumption is made for the FRP external reinforcement. External laminates are meshed as small lines on the contour of the section and only centerlines of them are considered; the width of the FRP is assumed to be

negligible when compared to the section dimensions and a uniform strain within each meshed element is considered (neglecting strain variations through both thickness and width).

Many stress-strain relationships have been implemented and many others can be added by simply developing a subroutine that for a given strain gives the corresponding stress (Constitutive Law). Stress-strain relationships for FRP composites are assumed to have different behavior in tension and in compression (i.e. very low, at least zero, elastic modulus in compression where they can suffer buckling). Debonding of the FRP composites is beyond the scope of the present work although it can be considered adopting an ultimate stress of the material equal to the debonding stress.

3.2.2 Cross Section Discretization

The concrete cross section should be defined by a closed polygonal boundary having straight sides; linear segments represent the exterior and interior boundaries of the section and curved boundaries can be approximated using a set of straight segments. After that the section is automatically meshed into small rectangles and to each discrete element is “attached” a material.

The smallest rectangle area enveloping the full section is identified considering maximum and minimum coordinates of vertices: x_{\min} , x_{\max} and y_{\min} , y_{\max} . To divide the section in $n_d \times m_d$ fibers (elements) a grid with horizontal spacing of $x_{el} = \frac{x_{\max} - x_{\min}}{n_d}$ and vertical spacing of $y_{el} = \frac{y_{\max} - y_{\min}}{m_d}$ is defined (see Fig. 3.24).

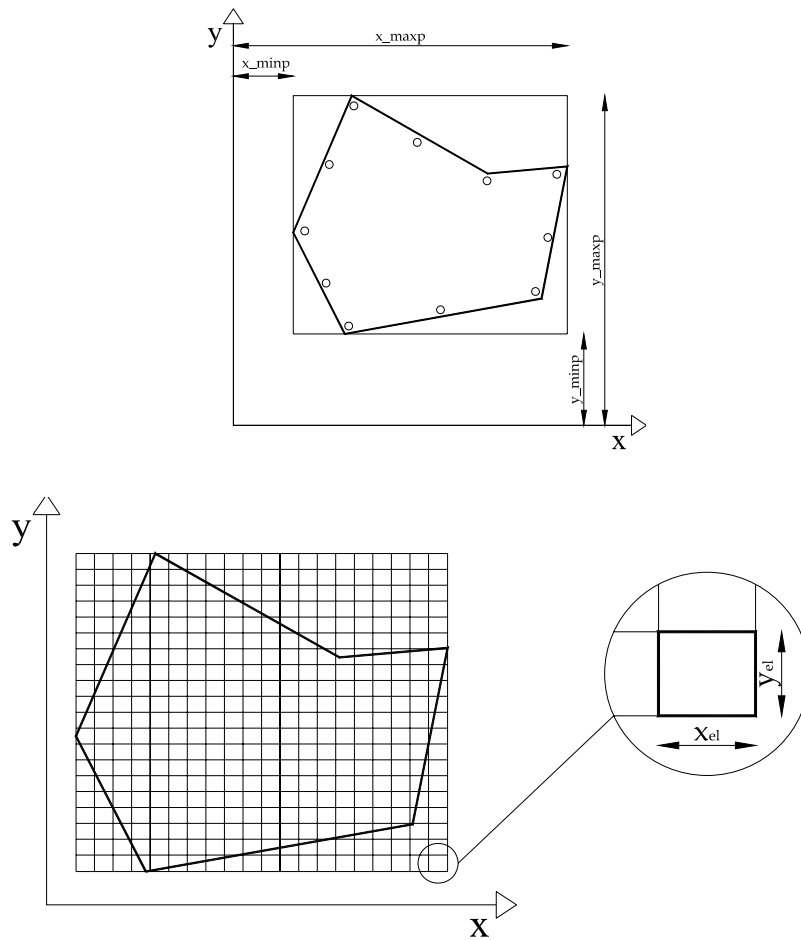


Figure 3.24 – Grid Spacing and Cross Section Discretization

This method is also well suited for spread-sheet calculation. All data can be stored into a three-dimensional matrix. Each element of the bi-dimensional $n_d \times m_d$ matrix (layer) represents data concerning a single concrete fiber, while each layer (third coordinate of the matrix) contains an information about the fiber (i.e. abscissa of the centroid of the element, ordinate, material multiplier, perpendicular distance from neutral axis, etc - see Fig. 3.25).

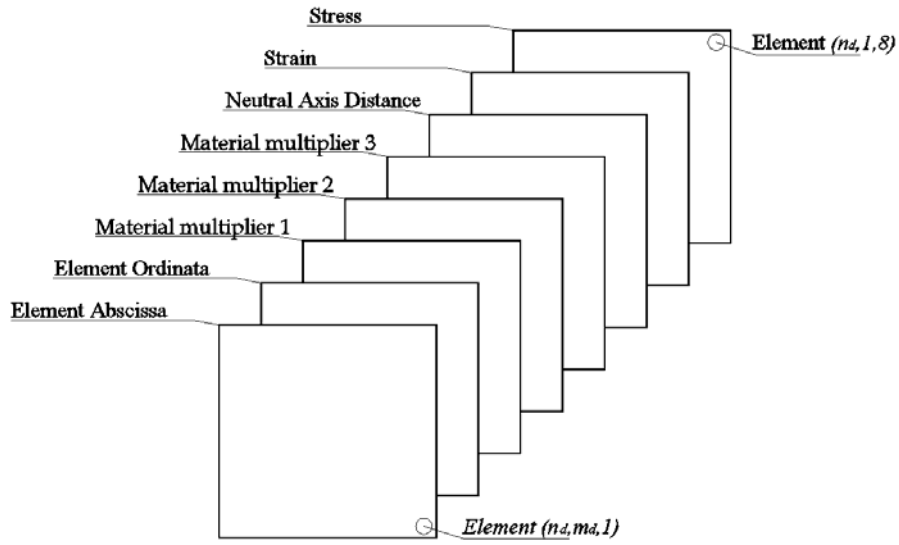


Figure 3.25 – Geometry and mechanical properties Matrix

If the centroid of an element lies inside the boundary of the section and is made by material k then the element material k multiplier (figure 3.26), θ_k , is set to 1 (that means it belongs to the section and is active in the calculation) otherwise θ_k is set to 0 (inactive).

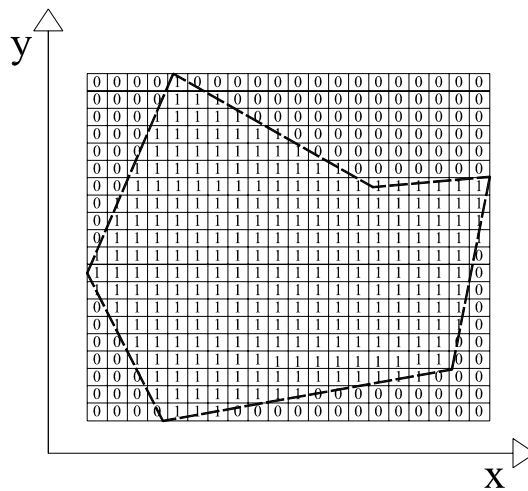


Figure 3.26 – Material coefficient θ activation of elements in the meshed section

A point is inside a polygonal closed envelope (also with some inside voids) if the sum of all angles defined by the point and two consecutive vertices of the envelope is 360° . In this procedure is crucial the order of the vertices: the vertices of the exterior boundary are numbered counter clockwise, while the ones of the interior boundaries, if any, are consecutively numbered clockwise. (see Fig. 3.27).

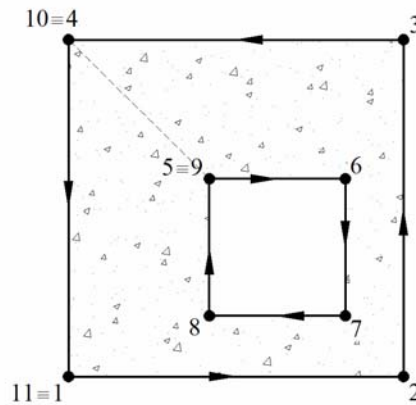


Figure 3.27 – Vertices numeration: exterior boundary counter clockwise, interior boundaries clockwise

A measure of the quality of the mesh can be given by the ratio of meshed area measure over the real area A measure.

The total meshed area value is the sum of all the (equal) areas $A_i = x_{el} \cdot y_{el}$ of the rectangular elements and the real area is given by the integral over the regular

$$\text{plane domain } \Omega: A = \int_{\Omega} d\Omega = \frac{1}{2} \int_{\partial\Omega} \mathbf{r} \cdot \mathbf{n} ds = \frac{1}{2} \sum_{i=1}^n \mathbf{r}_i \cdot \mathbf{r}_{i+1}^{\perp}.$$

According to divergence theorem of Gauss, the integral over the plane surface domain is transformed into an integral around its boundary and in a closed polygonal boundary domain (having n straight sides) the curvilinear integral becomes a sum involving only the vertices vectors and the vectors orthogonal to them: \mathbf{r} and \mathbf{r}^{\perp} ; \mathbf{r}_i denotes the position vector of the vertex i and \mathbf{r}_i^{\perp} is the vector

obtained by rotating \mathbf{r}_i of 90° clockwise: if $\mathbf{r}=(x,y)$ then $\mathbf{r}^\perp=(y,-x)$.

The boundary $d\Omega$ is defined by n vertices numbered consecutively and counter clockwise, while any void is defined clockwise and the position vector \mathbf{r}_n of the last vertex is assumed to coincide with \mathbf{r}_1 . (see Fig. 3.27).

For the consistency of the procedure, the centroid of the cross section is evaluated according to the meshed section rather than the actual section defined by the vertices.

After discretizing the concrete gross section, separate tables are defined for each type of reinforcement. Mild steel and FRP bars and prestressing tendons have negligible dimensions and are not meshed; each of them is defined only by the coordinate of the centerline.

Instead surface bonded FRP is discretized in piecewise segments with given thickness which are described by their centroid and have lumped area. Each meshed segment of surface bonded FRP has a constant strain and stress. In this case a table is representative of each type of reinforcement, each row contains information about a reinforcement element (i.e. first column contains abscissa of the element; second column contains the ordinate, then perpendicular distance from neutral axis, etc).

3.2.3 Computation Algorithm

Once the coordinate of each concrete fiber or reinforcement element are known, it is possible to evaluate the perpendicular distance of each of them from the neutral axis.

The neutral axis is characterized by two parameters, i.e. a passing through point on the plane of the section and an orientation angle. From a programming point of view, the passing through point can be evaluate by one parameter,

ordinate y and point's coordinates are $(0,y)$ when the orientation angle is in the range $(-45^\circ,+45^\circ)$, abscissa x and point's coordinates are $(x,0)$ when the orientation angle is outside the previous range.

It is important to define a direction on the neutral axis because the perpendicular oriented distance of the elements is used to evaluate the strain in the elements. The neutral axis is the zero strain line, so the points at the same perpendicular distance d from it have a constant strain (isoline) equal to the curvature in the direction normal to that neutral axis multiplied by the perpendicular distance of the point itself. In the sign convention the fibers on the same semi-plane of the externally applied axial load resultant should have the same strain sign of the external load (i.e. if designer assumes that compressions are positive, then compression axial load will be positive and compressive strains will be positive too). The curvature is opportunely evaluated according to the scope of the analysis (see next sections "*Moment curvature analysis*" and "*Interaction diagrams plot*"). Particular care must be taken in prestressing elements. The value of strain to account for is the sum of the effective prestrain in the tendon (prior to curvature and after losses have been accounted for) and the increment of strain caused by section curvature.

Once the strain field is known it is possible to evaluate the stresses into each fiber using the appropriate constitutive law of the involved materials.

As previously stated the integration of the stress field is performed adopting midpoint composite rule after meshing the cross section into rectangular elements.

The integral P_{int} , axial force resultant, of the internal stress field over the section is

$$P_{int} = \int_{grid} \theta \cdot \sigma dA + \sum_{j=1}^{n_{rein}} \sigma_j \cdot A_j = \sum_{i=1}^{n_d \cdot m_d} \theta_i \cdot \sigma_i \cdot A_i + \sum_{j=1}^{n_{rein}} \sigma_j \cdot A_j = \sum_{i=1}^{n_d \cdot m_d} N_i + \sum_{j=1}^{n_{rein}} \sigma_j \cdot A_j$$

A constant stress σ_i is considered inside an active ($\theta_i \neq 0$) element, either concrete or reinforcement, equal to the value corresponding to the centroid (x_i, y_i)

strain of the element; N_i is the axial force resultant in a meshed element, $N_i = \theta_i A_i \sigma_i$. The integral is approximated by a sum over all the active concrete element and all the n_{rein} reinforcement elements, accounting in this way for the contributions from concrete, steel and FRP.

Similarly the bending moment is then evaluated, first around origin system axes x and y,

$$\begin{aligned}
 M_x &= \int_{grid} \theta \cdot \sigma \cdot y dA + \sum_{j=1}^{n_{rein}} \sigma_j \cdot A_j \cdot y_j = \\
 &= \sum_{i=1}^{n_d \cdot m_d} \theta_i \cdot \sigma_i \cdot A_i \cdot y_i + \sum_{j=1}^{n_{rein}} \sigma_j \cdot A_j \cdot y_j = \sum_{i=1}^{n_d \cdot m_d} N_i \cdot y_i + \sum_{j=1}^{n_{rein}} \sigma_j \cdot A_j \cdot y_j \\
 M_y &= \int_{grid} \theta \cdot \sigma \cdot x dA + \sum_{j=1}^{n_{rein}} \sigma_j \cdot A_j \cdot x_j = \\
 &= \sum_{i=1}^{n_d \cdot m_d} \theta_i \cdot \sigma_i \cdot A_i \cdot x_i + \sum_{j=1}^{n_{rein}} \sigma_j \cdot A_j \cdot x_j = \sum_{i=1}^{n_d \cdot m_d} N_i \cdot x_i + \sum_{j=1}^{n_{rein}} \sigma_j \cdot A_j \cdot x_j
 \end{aligned}$$

and then transported to the centroid of the section (or any other user defined reference point) $M_{x,g}$ and $M_{y,g}$.

Then the internal emerging orientation angle is given by $tg \beta_{int} = -\frac{M_{y,g}}{M_{x,g}}$.

Convergence Criteria

In the case of compression and bending along the principal axes of the section, only a nonlinear equation has to be solved to account for equilibrium. The internal emerging stress field, integrated over the section domain, S_{int} , associated to a given neutral axis depth and curvature, must be equal to (that is in equilibrium with) external soliciting forces, S_{ext} . This problem is generally non-linear in the post-elastic range and can be solved by changing iteratively the neutral axis depth

until equilibrium is found. Usually the convergence criteria concerns axial load P : $|P_{\text{int}} - P_{\text{ext}}| \leq \textit{tolerance}$. The end result is found if the gap between external axial force and internal emerging axial load is less than a given user-defined tolerance value (i.e. a percentage of the external axial load P_{ext}). Therefore it is crucial to keep in mind that computers use a fixed number of binary digits to represent floating point numbers, so it is possible that computed value of a function on a root is never zero.

In the case of compression and biaxial bending such procedure is not sufficient; a system of two nonlinear equations has to be solved simultaneously to account for equilibrium and prescribed load orientation angle. The convergence criterion for the second non-linear equation concerns the load orientation angle: $|\beta_{\text{int}} - \beta_{\text{ext}}| \leq \textit{tolerance}$. This problem is now non-linear with respect to both neutral axis depth and orientation angle, and involves the simultaneous convergence with two criteria. It can be solved in a double iterative process: by changing the orientation of neutral axis until the internal emerging stress field (in equilibrium in the axial direction with the external axial load according to the previously described iterative procedure) and corresponding internal emerging bending moment, evaluated with respect to the concrete gross section centroid, has the same (with a prescribed tolerance) orientation angle as the external applied bending moment.

The applied axial load P_{ext} remains constant during the load process and the direction of the horizontal load, or the application point, is supposed to remain onto the line passing through the centroid of the gross concrete section with a given orientation angle β_{ext} . The internal emerging stress field, integrated over the section domain, must be in equilibrium with the external applied axial force for each value of the neutral axis orientation angle. So for each value of the orientation angle of the neutral axis (main variable) an iterative procedure is performed to grant axial equilibrium (the main variable of this iterative procedure

is the neutral axis depth), and an emerging orientation angle of the bending moment is associated. The second iteration involves the orientation angle of the neutral axis that is changed until the emerging orientation angle of bending moment reaches the orientation angle of external bending moment.

The double iterative procedure flow chart is depicted in fig. 3.28.

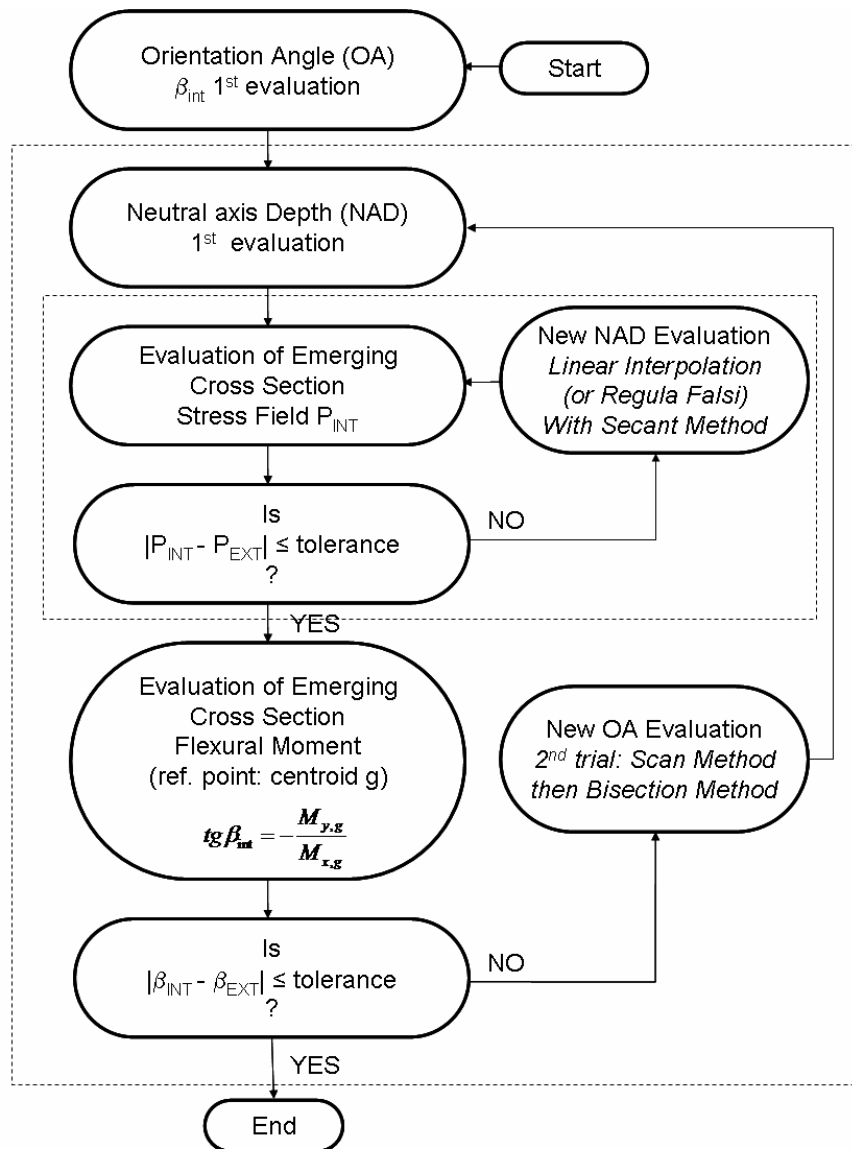


Figure 3.28 – Flow Chart of the double iterative procedure

Due to the high non-linearity of the problem optimal strategy of iteration procedures and convergence criteria have to be chosen to have a fast convergence and to quickly solve the nonlinear problem.

First the problem must be brought into the standard form $f(x)=0$, i.e. $P_{ext}-P_{int}(x)=0$ where $x=neutral\ axis\ depth$, and thus can be attacked by nonlinear equation methods. A method for solving $f(x)=0$ has at least two parts: iteration and convergence test. The iteration generates estimates of the solution and the test says when to stop iterating. The convergence tests have been previously described, while the iteration procedures are shown at the moment.

To solve the axial equilibrium an iterative procedure consisting of a modified linear interpolation (or regula falsi) with secant method can be adopted.

This method simply relies on the fact that, between any pair of points (a,b) that give opposite signs to a continuous function $f(x)$ smooth near the root, there must be a zero of $f(x)$. Closer estimate of the zero is taken by linear interpolating the values of the function in the two bounds of the interval [a,b], adopting a straight line, or chord, connecting $f(a)$ and $f(b)$ with a slope $\phi = \frac{f(b)-f(a)}{b-a}$ and crossing the x axis in the new estimate value of the root $x_{new} = a - \frac{f(a)}{\phi}$. The function is assumed to be approximately linear in the local region close to the root.

This method is sometimes ineffective if the slope of the function is very high: one end of the line is “stuck” and the convergence is low. To avoid this, a secant method is adopted along with the regula falsi method (see Fig. 3.29). This is a variation of the Newton’s method that avoids computing the derivative of $f(x)$ at each step and does not breaks down if $f'(x)\approx 0$ in a trial. It uses a linear model based on the previously evaluated constant slope ϕ of the straight line connecting the first two boundary values $f(a)$ and $f(b)$. If the convergence is still slow it is

possible to reduce that slope.

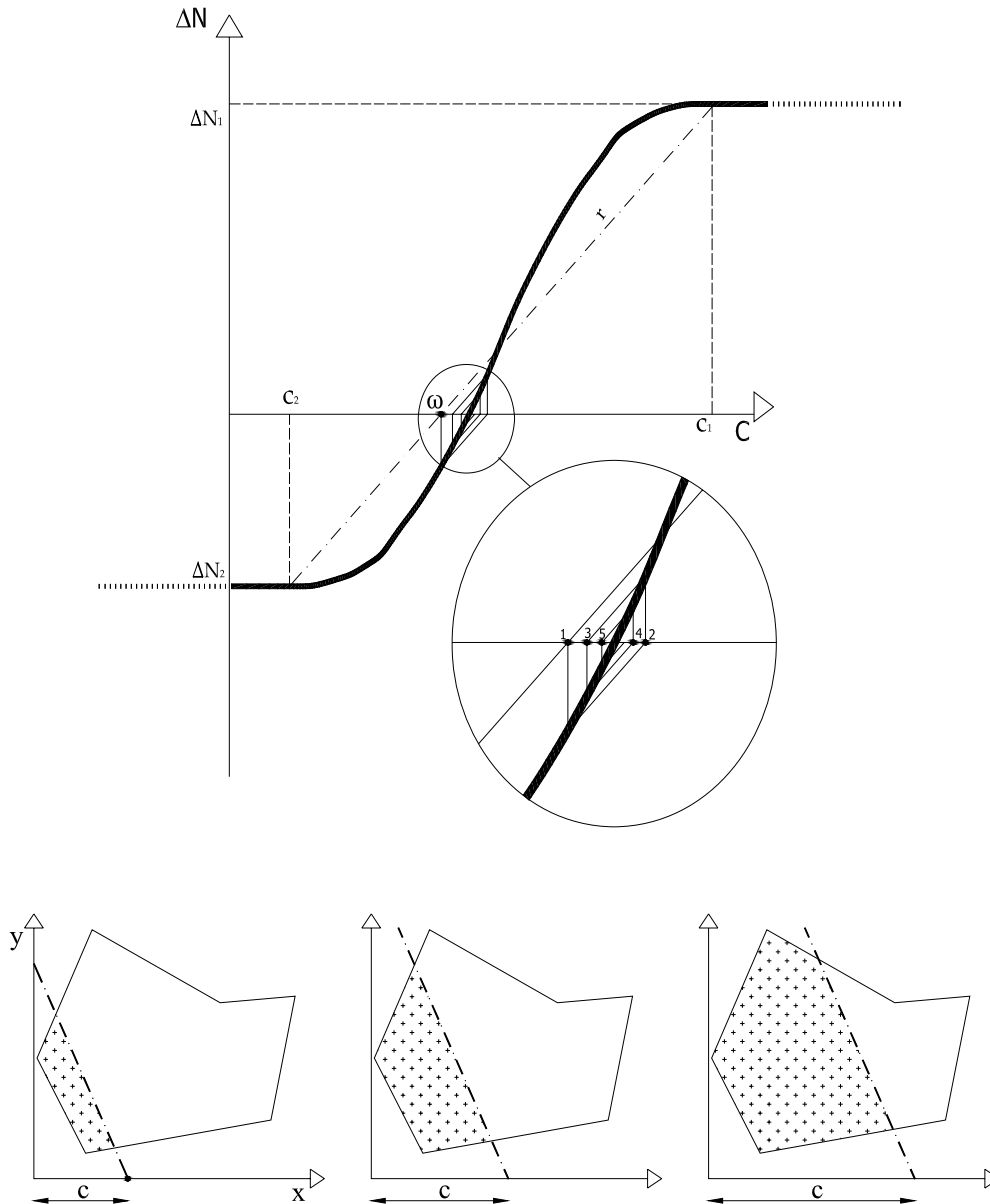


Figure 3.29 – Regula Falsi method coupled to Secant method for axial equilibrium

The first two boundary values can be estimated according to two notable

positions of the neutral axis corresponding to two limit isoline tangent to the section: so that first time all the section is not compressed (a) and second time all the section is compressed (b). The regula falsi is a bracketing method, so the neutral axis position is supposed to be in between these two limit position. This is a limit of the regula falsi method that cannot be always adopted. This problem can be overtaken adopting the secant method along with the slope ϕ evaluated at the first step of the regula falsi method, so that the root must not necessarily be bracketed.

To solve the orientation angle problem it is instead always possible to adopt bracketing methods, because the solution domain is smaller than 180° , in the sense that the neutral axis assumes the same positioning (with opposite direction) when it is rotated by an angle of 180° ; so the solution can be found in a limited domain. Once we know that the interval contains a root, several procedures exist that are guaranteed to converge, but plod along most slowly. In this section a strategy to speed up convergence is shown.

If the first trial value of neutral axis orientation angle is the orthogonal to orientation angle β_{ext} , then the solution is supposed to be close to this value and a method for locating closer estimates of the root is to scan the entire domain by small increments and to observe the steps in which a change of sign in the function occurs. This signals that the function crosses the solution within the particular step. This “scan method” may be a rather time-consuming procedure if the solution lies in a large region of search and first guess is far from the solution. An initial trial value closer to the real solution can be the direction of the neutral axis evaluated in the elastic range.

A variation of this search is the method of bisection which divides the interval of search by two and always retains that half of the search interval in which the change of sign has occurred, using midpoint to replace whichever interval limit has the same sign. After each iteration the bounds containing a root

decrease by a factor of two, thus we know in advance the maximum number of iterations $n = \log_2 \frac{\varepsilon_0}{\varepsilon}$ required to achieve a given tolerance ε in the solution where ε_0 is the size of initially bracketing interval (i.e. not greater than 180°). When the range of search has been narrowed down sufficiently, a more accurate search technique (i.e. one of the above mentioned) would then be applied within that step in order to refine the value of the root.

3.2.4 Numerical Strategies

Once the coordinate of each concrete fiber or reinforcement element are known, it is possible to evaluate the perpendicular distance of each of them from the neutral axis.

Moment Curvature Diagram

In this case a fast converging procedure is necessary because to plot the moment curvature diagram it is required the fast repetitive solution of two simultaneous nonlinear equations for both neutral axis depth and orientation angle, at each curvature level.

To evaluate moment curvature curve it is possible to increase the strain in the most compressed element of concrete mesh from zero to an ultimate value. This procedure can lead to a severe error if the applied axial load is high, so that under pure compression, without section curvature, the strain is higher than the starting imposed strain. To overtake this pitfall, a key innovative feature of this work is that a first evaluation of the section without section curvature is performed, in this deformation case the maximum strain attained in the concrete is

known and is assumed as the first imposed strain value, then a fixed-length increment of strain is adopted until ultimate strain in concrete is attained.

This procedure can account for the debonding of FRP reinforcement or the rupture of prestressed tendons or bars, automatically. The constitutive laws can be considered as step function and stress goes to zero when ultimate strain is attained; this leads to an automatic exclusion of the contribution of failed material (actual strain greater than ultimate strain) in the cross section stress integration. It is a key aspect as the curvature cannot represent fully the section behavior, when the cross section has the same curvature, but different maximum strain, leading to dramatically different axial stress resultant). If a high axial load is applied, then only small curvature can be gained at ultimate, as small is the ultimate flexural moment as clearly seen in an RC section PM interaction diagram.

Interaction Diagram Plot

The interaction diagram is easier to evaluate because there is no need to converge to a given orientation angle, because ultimate flexural moment is required for different load orientation angles. In fact only axial equilibrium is needed and maximum flexural moment is evaluated in correspondence of considered ultimate curvature. Once the axial load is defined, the axial equilibrium procedure is repeated for different values of neutral axis orientation angles instead of flexural moment resultant orientation angle, so that the second convergence iterative procedure is skipped. This procedure allows designing a slice of the three-dimensional interaction domain for a given axial load, than the same procedure has to be repeated for different values of external axial load values. To have a faster algorithm it is also possible to evaluate only the emerging stress field (and then emerging axial load and moment) for a given neutral axis depth that can be a-priori defined and changed in a given range, avoiding to find

equilibrium with a given external axial load. In this case the evaluated points lie somewhere in the three-dimensional space P - M_x - M_y because the evaluated axial load is in equilibrium with a random external axial load and it is not possible to state clearly a resolution in the spacing of the diagram.

Last issue to address is the evaluation of section ultimate curvature. Given a neutral axis depth and orientation angle, for each material is checked the element furthest from the neutral axis and ultimate value of strain is considered. The ultimate curvature for each material is evaluated dividing ultimate strain by perpendicular distance of corresponding material from neutral axis. Afterwards the ultimate curvature value is taken equal to the smaller curvature just evaluated, so that one material (or more at the same time) fails.

In the case of softening constitutive laws, the problem is highly nonlinear and it is not possible to know a-priori the value of curvature corresponding to maximum flexural capacity, because it is smaller than ultimate curvature. This means that maximum flexural moment is not achieved when ultimate strain is attained in one of the materials involved. To overtake this pitfall it is possible to search the maximum moment after evaluating moment curvature diagram, but this leads to an almost time-consuming procedure.

3.2.5 Taking into account second order effects

A non-linear procedure has been also developed to theoretically evaluate ultimate flexural strength $M^{\text{II}} = P^{\text{II}} (e+\delta)$ of the column taking into account theoretical column deflection δ .

The pinned end rotation ϕ and the mid-span deflection δ of the member are obtained by simple and double integration of the curvature, respectively. The curvature is supposed constant due to first order flexural moment, and the solid

part of the column is supposed rigid (gives only a deflection contribution).

The rotation φ of the brackets (hinges) of the column is supposed to be due to the *constant* curvature of the hollow portion of the column (hollow portion length is ℓ). The solid part is supposed rigid compared to the hollow one.

$$\varphi(z=0) = \int_0^{\frac{\ell}{2}} \frac{M}{EI} dz = \int_0^{\frac{\ell}{2}} \chi dz = \chi \cdot \frac{\ell}{2} \quad (4)$$

The mid-span deflection is calculated double integrating theoretical curvature distribution (supposed constant due to constant moment first order distribution) in the hollow portion of the column.

$$\begin{aligned} \bar{\delta}(z) &= -\int \varphi(z) dz = -\iint \frac{M}{EI} dz = -\iint \chi dz = \int \chi \left(z - \frac{\ell}{2} \right) dz = \chi \left(\frac{z^2}{2} - \frac{\ell z}{2} \right) \quad (5) \\ \bar{\delta} \left(z = \frac{\ell}{2} \right) &= \chi \frac{\ell^2}{8} \end{aligned}$$

then the solid part (i.e. with a length of 850 mm as in the examined case), supposed rigid, gives only a deflection contribution due to the rigid rotation of the hinge

$$\delta = \bar{\delta} \left(z = \frac{\ell}{2} \right) + \varphi(z=0) \cdot 850 \text{mm} = \chi \left(\frac{\ell^2}{8} + \frac{\ell}{2} \cdot 850 \text{mm} \right)$$

The procedure is iterative: the curvature χ is evaluated according to flexural moment M^{II} that is update according to new value of total eccentricity ($e+\delta$) where, in turn, δ is the integral of curvature χ . All numerical tests showed fast convergence of the non linear algorithm.

Lateral deflection of a slender column causes an increase in the column moments, as in figure 3.30; in turn these increased moments cause an increase in the deflection. If the axial load is below the critical load, the process converge to a stable situation, otherwise this second order process leads to stability failure.

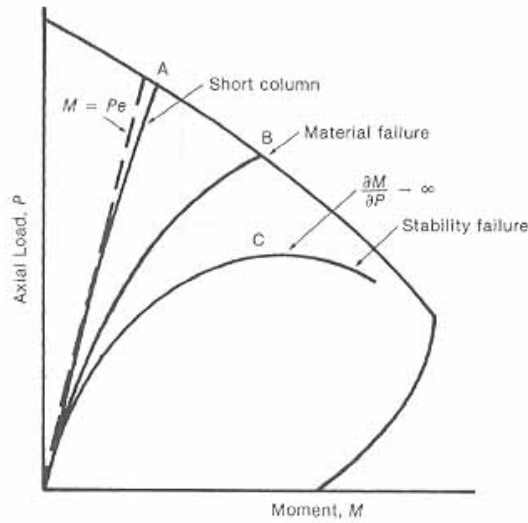


Figure 3.30 – Material and Stability Failure

Slender column interaction curves are convenient to use, i.e. the column with slenderness $l/h=30$ fails when the load-moment curve intersects the interaction curve diagram at point B1. At the time of failure the load and moment are given by point A1 if not accounting explicitly for the slenderness effect. A family of slender column interaction diagram can be plotted for different slenderness ratios (Fig. 3.31).

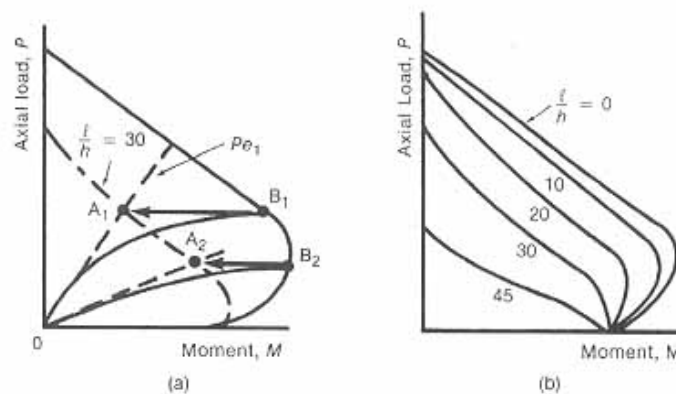


Figure 3.31 – Slender Column Interaction Curves

All this is particularly true if a single bent column is considered, because the deflections at mid span are able to increase the maximum static moment evaluated at mid span (Fig. 3.32). If the column has a double bent, then the increase in column deflections is not able to increase the maximum moments at the two ends of the column, thus resulting in negligible second order effect.

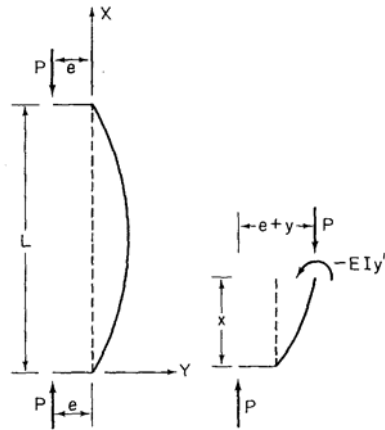


Figure 3.32 – Eccentrically loaded column

In the elastic range, equating the internal resisting moment $-EI y''$, at any section, to the corresponding applied moment $P(e+y)$ gives:

$$EIy'' + Py = -Pe$$

The solution of this differential equation at mid span ($L/2$) gives the mid span deflection δ :

$$\delta = e \left[\sec \left(\frac{\pi}{2} \sqrt{\frac{P}{P_E}} \right) - 1 \right] \text{ where } P_E = \pi^2 \frac{EI}{L^2}. \text{ Bending begins as soon as the}$$

load is applied; the deflection increases slowly at first and then more and more rapidly as P approaches P_E . At $P=P_E$ the deflection increases without bound.

3.3 Proposed Hollow Section Confinement model

The described numerical method uses nonlinear stress-strain relationships for concrete and steel. A reliable stress-strain behavior of concrete is necessary particularly when a member is subjected to combined bending and axial load and confinement effects should be accounted for.

To simulate the effect of the FRP confinement two approaches were used to assess the behavior of the FRP confined hollow members. In the first part an approach that considers the interaction of the four walls forming the hollow member is taken. In the second part, instead, an approach that consider the confinement of the hollow section lone forming the hollow member is taken

Following previous discussions, the stress-strain relationship of plain concrete under concentric loading is believed to be representative of the behavior of concrete under eccentric loading.

3.3.1 First Part: walls interaction and confinement

This approach considers the interaction of the four walls forming the hollow member. According to a preliminary FEM analysis and to the behavior observed in the wall-like columns tested by Prota et al. (2006) similar (see Chapter 4.1.2) to the behavior of the walls forming the hollow member, the confinement of the walls have been analyzed.

The transverse dilation of the compressive concrete walls stretches the confining device, which along with the other restrained walls applies an inward confining pressure. The effective pressure f_1' is reduced by a reduction factor k_{eff} due to the so-called arching effect. The reduction factor is given by the ratio of the effective confinement area, the core of the walls, to the total area of concrete

enclosed by the FRP jacket; in the present case is $k_{\text{eff}}=0.69$. For FRP-confined concrete, the ultimate compressive axial strain of concrete is considered to be attained when lateral strain is equal to FRP ultimate strain however experimental evidence shows that FRP failure did not occur. The confining pressure is provided by an FRP jacket of the same thickness to an equivalent circular column of a diameter D equal to the average (longer) side length (in the present case, $D \approx 300\text{mm}$).

One of the previous, or more widely, a general model for rectangular solid section can be adapted to assess the behavior of the confined wall forming the hollow section. The behavior of the hollow member, both in terms of load deflection and of moment curvature, can be assessed considering for confined concrete a stress-strain relationship derived by solid rectangular cross section confinement models.

A major improvement of FRP wrapping on member behavior is highlighted considering that in unconfined columns, when steel reinforcement reaches in compression the buckling stress, as it pushes outward surrounding concrete, the concrete cover spalls out. The spalling of concrete cover and the buckling of the reinforcement can be taken into account by considering for the concrete cover fibers a brittle (step-like) concrete behavior after peak load with zero stress corresponding to reinforcement buckling strain. The improved stress-strain relationship with stress reductions due to the buckling phenomenon has been adopted for steel in compression. In the case of members wrapped with FRP the steel bars push internal concrete cover in the inward direction (in the hollow part) when they start buckling and in the numerical model concrete cover spalling can be simulated adopting the linear descending branch according to Hillerborg (1989) at peak strain, as already done in the case of concrete in unconfined members.

A preliminary F.E.M. analysis has been conducted in the elastic range to evaluate the stress field generated by external wrapping on hollow concrete core.

A square solid section column has been wrapped with an elastic reinforcement only in the transversal direction (no reinforcement has been applied in the longitudinal direction) and a distributed load has been applied on the top in displacement control. The boundary constraints were only vertical supports and two pairs of supports in the plane of the load to restraints only rigid movement so that the specimen was free to expand laterally.

To evaluate the effect of concrete confinement, no longitudinal bars have been inserted in the model. A cross section at mid height of the specimen has been extracted and the principal confining stress vector field is plotted in figure 3.33.

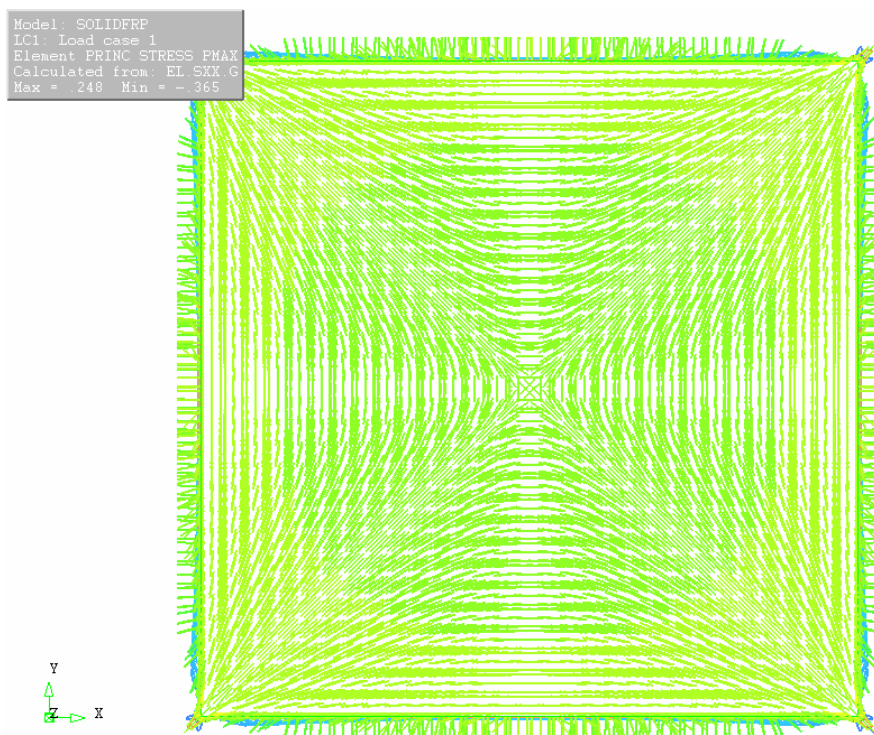


Figure 3.33 – FEM confining stress vector field: solid section

Depicted vector field shows clearly the well known arching effect. From the corners starts two struts that connect opposite corners and in each quarter of the section are clearly visible the arch-shaped paths of the confining stresses.

Hence this elastic FEM analysis confirms the previously discussed shape effect theories.

Subsequently the inner core of concrete has been removed and the same analysis has been conducted on a hollow cross section column, with the same load and boundaries conditions.

The principal confining stress vector field on the mid height section is plotted in figure 3.34.

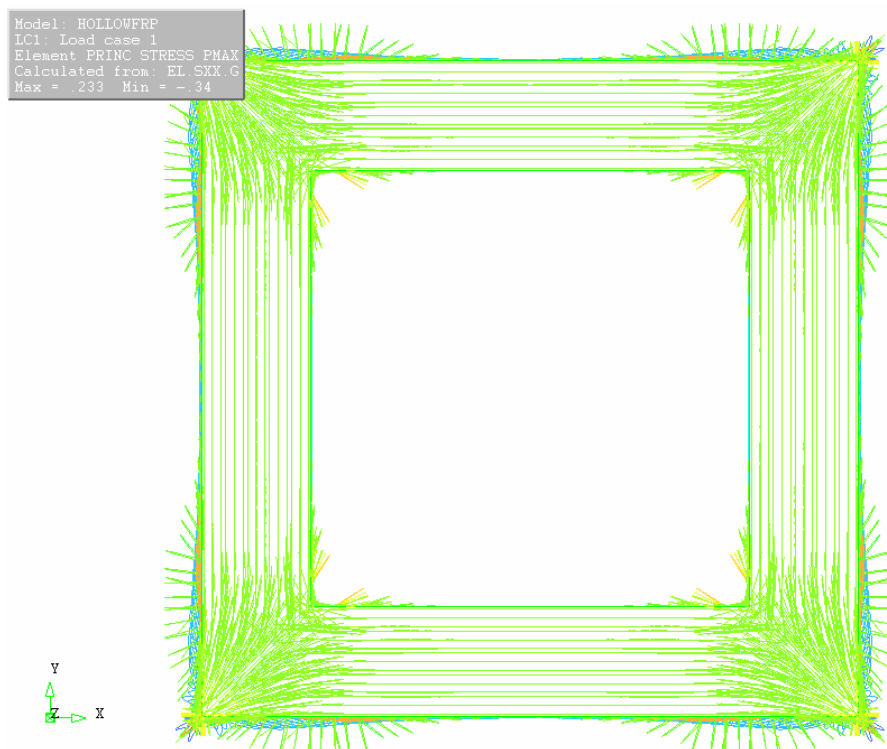


Figure 3.34 – FEM confining stress vector field: hollow cross section

In the vector field plot it is still clearly noticeable an arching effect, but in the case of hollow section, it seems that the strut between two opposite corners spreads along the walls leading to a confining stress field compatible with a wall-like column confinement. This fact allows considering the effect of confinement on the four walls interacting together. The arch-shaped paths of the confining stresses moving off the corner rapidly changes in a straight distributed confinement stress field. A synthetic representative scheme of this confinement configuration is depicted in figure 3.35.

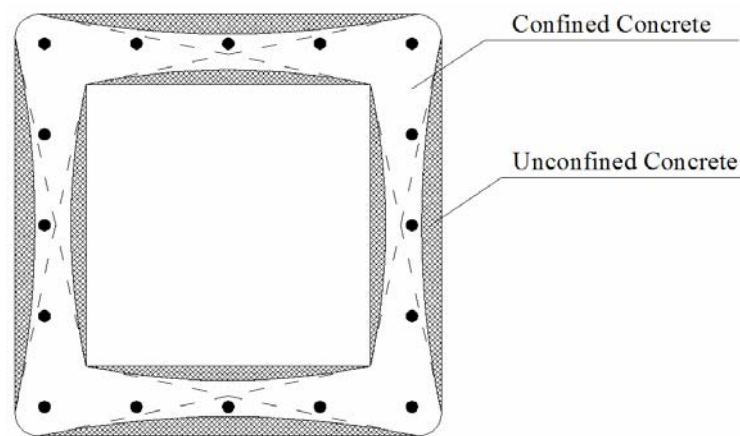


Figure 3.35 – Scheme of confinement in a hollow cross section

3.3.2 Second Part: square hollow section confinement

This approach considers the confinement of the whole hollow section forming the hollow member. Following previous discussions, again, the stress-strain relationship of plain concrete under concentric loading is believed to be representative of the behavior of concrete under eccentric loading.

Recently Fam and Rizkalla (2001) proposed an analytical model to predict the response of circular concrete members confined with FRP. The model is based

on equilibrium and radial displacement compatibility and through the equations proposed by Mander et al. (1988) adopts a step-by-step strain increment technique to trace the lateral dilation of concrete. The failure of the confined concrete member is due to the rupture of the FRP confinement which is controlled by the multiaxial Tsai-Wu failure criteria.

The passive confinement on axially loaded concrete members is due to the transverse dilation of concrete and the presence of a confining device which opposes to this expansion and puts the concrete in a triaxial state of stress. Gardener (1969) tested concrete cylinders under different confining levels (uniform in the transverse direction) thus providing dilation ratios of concrete under different transverse confinement pressures.

Braga and Laterza (1998) proposed a model based on the assumption that the increment of stress in the concrete is achieved without any out-of-plane strain. In their model proposed to adopt plain strain conditions to simulate the confinement effect.

3.3.3 Plane Strain Conditions

In plane strain conditions the following stress-strain relations can be written:

$$\{\boldsymbol{\sigma}\} = \begin{Bmatrix} \sigma_x \\ \sigma_y \\ \sigma_z \\ \tau_{xy} \end{Bmatrix} = \frac{E}{(1+\nu)(1-2\nu)} \begin{bmatrix} (1-\nu) & \nu & \nu & 0 \\ \nu & (1-\nu) & \nu & 0 \\ \nu & \nu & (1-\nu) & 0 \\ 0 & 0 & 0 & \frac{(1-2\nu)}{2} \end{bmatrix} \begin{Bmatrix} \varepsilon_x \\ \varepsilon_y \\ \varepsilon_z = 0 \\ \gamma_{xy} \end{Bmatrix} = [\mathbf{d}]\{\boldsymbol{\varepsilon}\} \quad (1a)$$

$$\{\boldsymbol{\varepsilon}\} = \begin{Bmatrix} \varepsilon_x \\ \varepsilon_y \\ \varepsilon_z = 0 \\ \gamma_{xy} \end{Bmatrix} = \frac{1}{E} \begin{bmatrix} 1 & -\nu & -\nu & 0 \\ -\nu & 1 & -\nu & 0 \\ -\nu & -\nu & 1 & 0 \\ 0 & 0 & 0 & 2(1+\nu) \end{bmatrix} \begin{Bmatrix} \sigma_x \\ \sigma_y \\ \sigma_z \\ \tau_{xy} \end{Bmatrix} = [\mathbf{a}]\{\boldsymbol{\sigma}\} \quad (1b)$$

where $\mathbf{a}=\mathbf{d}^{-1}$ and ε_z strains are zero. The other two equations, considering xz and yz components, have been omitted because are identically zero.

Analyzing the third row of eq.(1a), it is clearly shown that the σ_z stress component is independent and can be evaluated after the problem has been resolved in the other stress components:

$$\sigma_z = \nu(\sigma_x + \sigma_y) \quad (2)$$

In polar coordinates the stress and strain vectors become:

$$\{\boldsymbol{\sigma}\} = \begin{Bmatrix} \sigma_r \\ \sigma_\theta \\ \sigma_z \\ \tau_{r\theta} \end{Bmatrix}, \quad \{\boldsymbol{\varepsilon}\} = \begin{Bmatrix} \varepsilon_r \\ \varepsilon_\theta \\ \varepsilon_z = 0 \\ \gamma_{r\theta} \end{Bmatrix} \quad (3a,b)$$

where r is the radial component and θ is the circumferential component.

In the hypothesis of axial symmetry and zero body forces, the indefinite equilibrium and compatibility equations are:

$$\frac{d\sigma_r}{dr} - \frac{\sigma_\theta - \sigma_r}{r} = 0, \quad \frac{d\varepsilon_\theta}{dr} + \frac{\varepsilon_\theta - \varepsilon_r}{r} = 0 \quad (4a,b)$$

The radial displacement s_r is the only displacement component and system (1b) can be rewritten as:

$$\varepsilon_r = \frac{ds_r}{dr} = \frac{1+\nu}{E} [(1-\nu)\sigma_r - \nu\sigma_\theta] \quad (5a)$$

$$\varepsilon_\theta = \frac{s_r}{r} = \frac{1+\nu}{E} [(1-\nu)\sigma_\theta - \nu\sigma_r] \quad (5b)$$

Eq.(4b) can be manipulated (substituting eqs.(5a) and (5b) and deriving eq.(5b) with respect to r) and can be rewritten as:

$$\frac{d}{dx}(\sigma_r + \sigma_\theta) = 0 \quad \Rightarrow \quad \sigma_r + \sigma_\theta = 2C_1 \quad (4c,d)$$

Eq.(4a) can be rewritten as:

$$r \frac{d\sigma_r}{dr} + 2\sigma_r = 2C_1 \quad \Rightarrow \quad \sigma_r = C_1 + \frac{C_2}{r^2} \quad (6a,b)$$

and the two constants C_1 and C_2 can be evaluated according to boundary conditions (i.e. applied external (at $r = R_e$) inward pressure q and internal (at $r = R_i$) outward p pressure).

$$\begin{cases} \sigma_r(R_i) = C_1 + \frac{C_2}{R_i^2} = q_i \\ \sigma_r(R_e) = C_1 + \frac{C_2}{R_e^2} = q_e \end{cases} \Rightarrow \begin{cases} C_1 = \frac{q_e R_e^2 - q_i R_i^2}{R_e^2 - R_i^2} \\ C_2 = -R_i^2 (C_1 - q_i) \end{cases} \quad (7)$$

Stress equations become:

$$\sigma_r = \frac{q_e R_e^2 - q_i R_i^2}{R_e^2 - R_i^2} - \frac{1}{r^2} \frac{(q_e - q_i) R_e^2 R_i^2}{R_e^2 - R_i^2} \quad (8a)$$

$$\sigma_\theta = \frac{q_e R_e^2 - q_i R_i^2}{R_e^2 - R_i^2} + \frac{1}{r^2} \frac{(q_e - q_i) R_e^2 R_i^2}{R_e^2 - R_i^2} \quad (8b)$$

And also eq.(5b) can be rewritten as:

$$\varepsilon_\theta = \frac{s_r}{r} = \frac{1+\nu}{E} \left[(1-2\nu) \frac{q_e R_e^2 - q_i R_i^2}{R_e^2 - R_i^2} + \frac{1}{r^2} \frac{(q_e - q_i) R_e^2 R_i^2}{R_e^2 - R_i^2} \right] \quad (5b)$$

In the case of external pressure only ($q_i=0$) the stress equations (8) and displacement equation become:

$$\sigma_r = \frac{q_e R_e^2}{R_e^2 - R_i^2} \left(1 - \frac{R_i^2}{r^2} \right) \quad (9a)$$

$$\sigma_{\theta} = \frac{q_e R_e^2}{R_e^2 - R_i^2} \left(1 + \frac{R_i^2}{r^2} \right) \quad (9b)$$

$$s_r(r) = \frac{1+\nu}{E} \frac{q_e R_e^2}{R_e^2 - R_i^2} \left[(1-2\nu)r + \frac{R_i^2}{r} \right] \quad (9c)$$

In the case of internal pressure only ($q_e=0$) the stress equations (8) and displacement equation become:

$$\sigma_r = \frac{q_i R_i^2}{R_e^2 - R_i^2} \left(\frac{R_e^2}{r^2} - 1 \right) \quad (10a)$$

$$\sigma_{\theta} = -\frac{q_i R_i^2}{R_e^2 - R_i^2} \left(\frac{R_e^2}{r^2} + 1 \right) \quad (10b)$$

$$s_r(r) = -\frac{1+\nu}{E} \frac{q_i R_i^2}{R_e^2 - R_i^2} \left[(1-2\nu)r + \frac{R_e^2}{r} \right] \quad (10c)$$

In this case, if the thickness $t=R_e-R_i$ of the cylinder is very small compared to the average radius $R=(R_e+R_i)/2$ (i.e. an FRP jacket where $t \ll R$), then:

$R_e^2 - R_i^2 = 2Rt$, $R_i^2/R \approx 1$, $R_e^2 - R \approx Rt$, $R_e^2 + R \approx 2Rt$. Eqs.(10) can be rewritten:

$$\sigma_r \approx \frac{q_i}{2}, \quad \sigma_{\theta} \approx -\frac{q_i R}{t}, \quad s_r(r) \approx -\frac{q_i R^2}{Et} (1-\nu) \quad (11a,b,c)$$

3.3.4 Concrete model with variable confined pressure

In the following page is briefly reported the basis of the present model, the stress-strain model of confined concrete proposed by Mander et al. (1988), in turn based on the Popovics (1973) formulas, are briefly recalled:

$$f_c = \frac{f'_{cc} \cdot x \cdot r}{r - 1 + x^r} \quad (12)$$

where the peak strength f'_{cc} is the confined concrete strength derived from

the following equation used to define a failure surface for concrete under triaxial compressive stresses, which was based on the “five parameter” multiaxial failure surface given by William and Warnk (1975) and calibrated with data from triaxial tests:

$$f'_{cc} = f'_{co} \left(-1.254 + 2.254 \sqrt{1 + 7.94 \frac{f'_l}{f'_{co}}} - 2 \frac{f'_l}{f'_{co}} \right) \quad (13)$$

In previous equations, f'_{cc} is the peak compressive strength of the confined concrete, f'_{co} is the unconfined concrete compressive strength, and f'_l is the effective lateral confining stress, $x = \varepsilon_c / \varepsilon_{cc}$ is the relative strain and

$r = \frac{E_{co}}{E_{co} - E_{sec}}$. The initial tangent stiffness can be evaluated as $E_{co} = 5000 \sqrt{f'_c}$

and secant stiffness is defined as $E_{sec} = \frac{f'_{cc}}{\varepsilon_{cc}}$. In these equations:

$$\varepsilon_{cc} = \varepsilon_{co} \left[1 - 5 \left(\frac{f'_{cc}}{f'_{co}} - 1 \right) \right] \quad (14)$$

In the above equation, ε_{co} is the compressive strain at the unconfined peak concrete strength (f'_{co}), usually setting $\varepsilon_{co} = 0.002$.

This model is suitable to predict the behavior of confined concrete with a constant confining pressure equal to f'_l . Spoelstra and Monti (1999) showed that modeling the FRP confinement that behaves elastically up to failure and therefore provides a continuously increasing confining pressure, it is needed to account for different Mander's curves, each one pertaining to the confining pressure level corresponding to the current lateral strain. The complete stress-strain curve crosses a family of Mander's curves.

3.3.5 Radial Displacement Compatibility

Fam and Rizkalla (2001) explicitly considered the dependence of the lateral strain with the axial strain through radial displacement compatibility and equilibrium equations.

A key aspects of the proposed model is that plain strain conditions are considered to evaluate the radial displacement of the elements confined by FRP and in the case of hollow core sections, the different contributions of radial and circumferential stresses are explicitly considered through an equivalent average confining pressure (actually the confining stress field is not equal in the two transverse directions and the effect of confinement should be evaluated in each point of the section with the effective confining pressures different in the two orthogonal direction with massive computational efforts).

A concrete cylinder free to expand laterally loaded with a uniform axial strain ε_c has a radial displacement:

$$s_{cc} = -R_e \nu_c \varepsilon_c \quad (15a)$$

and independently if it is hollow or solid, the radial displacement is due to the Poisson ratio (ν_c) and the external radius of concrete cylinder (R_e).

In reality the confined cylinder is not free to expand laterally, so a confining pressure q is exerted by the confining device. This pressure is externally applied to the concrete cylinder.

In plane strain conditions the pressure exerted by the confining device induces an inward radial displacement s_{cq} that reduces the previously evaluated radial displacement.

$$s_{cq} = \frac{1 + \nu_c}{E_c} \frac{q R_e^3}{R_e^2 - R_i^2} \left[(1 - 2\nu_c) + \left(\frac{R_i}{R_e} \right)^2 \right] \quad (15b)$$

and the radial displacement is due to the Poisson ratio (ν_c) and the elastic

modulus (E_c) of the concrete. The higher is the internal radius (that is the thinner is the concrete tube), the higher is the displacement. For a given pressure q , the tube has higher deformability.

At the same time, the pressure q acts inside the FRP thin cylinder causing an outward radial displacement s_{fq} that is, in thin tube hypothesis about:

$$s_{fq} = -\frac{q R_e^2}{E_f t} (1 - \nu_f) \quad (15c)$$

and this radial displacement is due to the Poisson ratio (ν_f) and the elastic modulus (E_f) of the confining device (i.e. FRP).

The radial displacement compatibility (the sum of the radial displacements of concrete $s_{cc} + s_{cq}$ is equal to the confining device displacement s_{fq} if there is no detachment) gives the following equation:

$$s_{cc} + s_{cq} = s_{fq} \quad (16a)$$

that can be explicated in the form $q = q(\varepsilon_c)$, so that at each axial strain ε_c is associated the pressure q exerted by the confinement:

$$q = \frac{\nu_c}{\frac{q R_e}{E_f t} (1 - \nu_f) + \frac{1 + \nu_c}{E_c} \frac{q R_e^2}{R_e^2 - R_i^2} \left[(1 - 2\nu_c) + \left(\frac{R_i}{R_e} \right)^2 \right]} \varepsilon_c \quad (16b)$$

A more accurate analysis can consider also the effect of axial compression of the confining device. This device can be directly loaded with the confined member, so that a uniform axial strain ε_c produces a radial displacement:

$$s_{fc} = -R_e \nu_f \varepsilon_c \quad (15d)$$

In this case, the confining device radial displacement is the sum $s_{fc} + s_{fq}$ and the equation (16b) changes in the form:

$$q = \frac{\nu_c - \nu_f}{\frac{q R_e}{E_f t} (1 - \nu_f) + \frac{1 + \nu_c}{E_c} \frac{q R_e^2}{R_e^2 - R_i^2} \left[(1 - 2\nu_c) + \left(\frac{R_i}{R_e} \right)^2 \right]} \varepsilon_c \quad (16c)$$

Radial stresses and circumferential stresses in the concrete are due to the inward pressure q and are given by eqs.(9a,9b). For the sake of simplicity, an equivalent average confining pressure can be evaluated as:

$$f_l = \frac{\sigma_r + \sigma_\theta}{2} = \frac{q R_e^2}{R_e^2 - R_i^2} \quad (17)$$

f_l is a constant confining pressure inside the concrete cylinder.

3.3.6 Non Linear Characteristics

Previous equations are based on linear elasticity theory for all the involved materials. This hypothesis is almost good for the elastic confining device (i.e. FRP), but it is too coarse in the case of concrete.

Before peak strength the concrete dilation in the transverse direction is very low (due to a constant, elastic Poisson ratio). As the deformation increases after peak, confined concrete exhibits post-peak behavior characterized by the appearance of significant cracking. Although insufficient to stop the cracking, the presence of low to moderate confining pressure controls the cracking. Heavily confined concrete exhibits an essentially bilinear stress-strain behavior that occurs when confinement is provided by an elastic material (such as an FRP jacket). In this case, the dilation ratio is observed to increase. The ultimate axial stress and strain achieved is therefore related to the rupture strain of the confining material by the dilation ratio. Once the confining material fails, the now overloaded unconfined concrete experiences a very brittle failure.

To account for the nonlinear behavior of concrete, a secant approach can be considered. The elastic modulus and the Poisson ratio are function of the axial strain and confinement.

The secant elastic modulus of concrete is the slope of the line connecting the origin and the present stress-strain point on the stress-strain curve. To simplify and to avoid an iterative procedure to determine the actual $E_c(\varepsilon_c)$, it is assumed the Secant modulus of the iteration (i) as the secant modulus of the previously evaluated stress-strain point ($i-1$) of the confined concrete curve. The first value is the initial tangent elastic modulus E_{co} .

The secant Poisson's ratio is used to obtain the lateral strain at a given axial strain in the incremental approach. The dilation of confined concrete is reduced by the confinement; therefore, the Poisson's ratio at a given axial strain level is lower in the presence of confining pressure. In 1969, Gardner tested many concrete cylinders under different confining hydrostatic pressures. Fam and Ritzkalla (2001), fitting the results curve with a second-order polynomial provided a simplified linear relationship for ν_c under constant confining pressure, and from regression analysis:

$$\frac{\nu_c}{\nu_{co}} = 1 + \frac{\varepsilon_c}{\varepsilon_{cc}} \left(0.719 + 1.914 \frac{f'_l}{f'_{co}} \right) \quad (18)$$

Where ν_c is the actual Poisson ratio at a given axial strain ε_c and actual confining pressure f'_l . The actual peak compressive strain (evaluated for the actual confining pressure f'_l) is ε_{cc} . The initial values are the unconfined peak concrete strength (f'_{co}), and the Poisson ratio (ν_{co}) usually ranging between 0.1 and 0.3.

At any given axial strain ε_c , the Poisson ratio is reduced with the increase of f'_l , because the ratio $\varepsilon_c/\varepsilon_{cc}$ decreases at growing of ε_c . This expression (obtained by linear regression on a definite range of confining pressures) is not suitable for

concrete subjected to very high confinement pressure at low axial strain and for concrete subjected to very low confinement pressure at high axial strain.

Usually the Poisson ratio of a confining device made by uniaxial FRP fibers applied by wet lay-up technique, can be considered about zero. In the case of confining device made by laminates with multiaxial fibers or steel tubes, the Poisson ratio can be usually greater than the initial concrete Poisson ratio. This means that at early stages of load, the pressure acting on the concrete is negative, that is a detachment of the confining device. In the calculations, in these cases, the pressure q is considered zero until the concrete's Poisson ratio overcomes ν_f . From that load levels up only the confining device is effective, because concrete engages the confining device (Fam and Rizkalla 2001).

3.3.7 Iterative Procedure

An iterative procedure is then performed to evaluate, at any given axial strain ϵ_c , the corresponding stress f_c , pertaining to a Mander curve at a certain confining pressure f'_1 (effective lateral pressure if a shape factor k_e – see Section 3.1.2 - is adopted).

A first trial value of the Poisson ratio is determined (i.e. the initial value at the beginning of the procedure or the previously evaluated value at iteration i) and along with the secant elastic modulus E_c , a confining pressure f'_1 is evaluated by eqs.(16c,17) (in the case of circular sections, $f'_1=f_l$). Now the peak compressive strain ϵ_{cc} can be evaluated and in turn an emerging Poisson ratio is determined. This is the new value of the Poisson ratio to repeat the procedure that converges when the emerging value of Poisson ratio is close enough to the Poisson ratio in input. Once the correct Poisson ratio is known at actual axial strain, a Mander curve at given confining pressure f'_1 can be drawn and the stress point f_c can be

determined corresponding to the actual strain ε_c . At each level of load/deformation (namely ε_c), the complete stress and strain regime in both the concrete cylinder and confining device is known (i.e. the circumferential stress in the confining device is $\sigma_\theta \approx -\frac{qR}{t}$).

The procedure is repeated up to a value of axial strain that induces failure of the confining device. In figure 3.36 is depicted the flow chart of the iterative procedure.

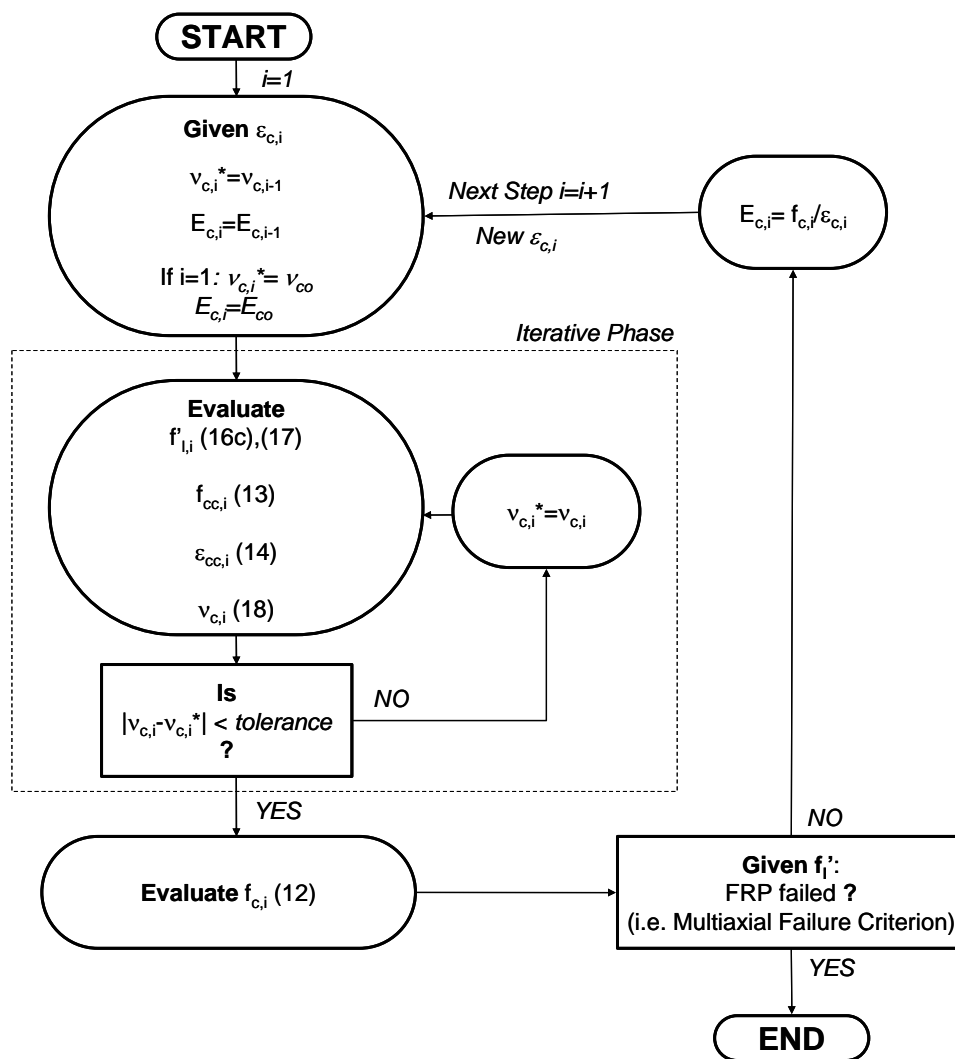


Figure 3.36 – Flow Chart of the proposed iterative procedure to evaluate $f_c = f_c(\varepsilon_c)$

3.3.8 Ultimate Strain and Failure of the Confining Device

The ultimate axial stress and strain is achieved when the failure of the confining material occurs. Once the confining material fails, the now overloaded unconfined concrete experiences a very brittle failure.

A multiaxial failure criterion can be adopted (i.e. Tsai-Wu criterion for FRP) considering axial, circumferential and radial stresses. Usually the axial and circumferential stresses are higher than the radial, in fact the radial stresses are about $\sigma_r \approx -\frac{t}{2R}\sigma_\theta$ (usually circumferential stresses are in tension, while axial stresses are in compression), much smaller than circumferential stresses for usual values of confinement thickness (t) and Diameter (2R) of the section.

The interaction of multiaxial stresses in the confining device can justify the experimental evidence of FRP failure for stresses lower than straight coupon tests. In straight coupon tests, only axial stress is present (i.e. analogous to circumferential stress in the wraps), while in real applied wraps two stresses in orthogonal directions are coupled to axial thus reducing the confining device axial performances.

This phenomenon (related to radial stresses) is secondary for bigger sections with bigger diameters, thus resulting in higher circumferential performances.

In the case of FRP wraps made by unidirectional fibers, the failure criterion can be uniaxial accounting only for longitudinal stresses (σ_θ). In fact the axial stresses are almost zero and the radial stresses are usually negligible.

3.3.9 Parametric Study

To evaluate the effect of parameters on the global stress strain response of

the confined concrete, some parametric evaluations have been performed. First has been plotted the distribution of stresses (i.e. radial compared to circumferential) in the concrete cylinders for different R_i/R_e ratios producing the confining pressure. Then has been considered the confinement effectiveness f'_{cc}/f'_{co} for a circular section varying the confinement stiffness $E_f t/R$ and the R_i/R_e ratios.

The latter study concerns the complete evaluation of the axial stress vs. strain curve, the axial vs. lateral strain curve, the axial stress vs. dilation ratio. This study has been conducted on a solid section with different jacket thickness and on a hollow section with different R_i/R_e ratios, but the same confinement stiffness $E_f t/R$.

Radial and Circumferential Stresses

Figure 3.37 shows the relative ratio between radial and circumferential stresses. In the horizontal axis is reported the radial position ρ normalized to the external radius R_e . The reported lines represent the relative percentage of the circumferential stress compared to the sum of radial and circumferential stresses (that is constant in a given section). Each curve pertains to a given $\beta=R_i/R_e$ section, where obviously $\beta=0$ refers to a solid section. In this case ($\beta=0$) the radial and circumferential stresses are equal thus contributing at 50% to the confining pressure. In the case of hollow sections, the radial stress is zero at the internal surface and is equal to q at the external surface. Note that in the case of hollow sections, the circumferential stress can be higher than q at the external surface, $\rho=1$.

$$\text{In a closed form: } \frac{\sigma_{\theta}}{\sigma_r + \sigma_{\theta}} = \frac{1}{2} \left[1 + \left(\frac{\beta}{\rho} \right)^2 \right] \quad \text{where } \beta \leq \rho \leq 1$$

The state of stress in the tube wall changes drastically from a uniform load in a fully filled, solid, section where radial and circumferential stresses are equal to the pressure exerted by the confining device, to a prevalent state of circumferential stresses that increases when the thickness of the tube is small compared to the diameter (i.e. β close to 1) and can be several times higher than the pressure q exerted by the confining device.

In figure 3.37 is evidenced the case of $\beta=0.4$ (the internal radius is 40% of the external radius). When $\rho=\beta$, that is on the internal surface, the stress is only in the circumferential direction because due to boundary conditions, the radial stress is zero. Going closer to the outer surface, (i.e. $\rho=1$), a different distribution is found, the radial stress is equal to q (due to the boundary condition where confining device is bonded) and represent only 42% of the sum of the stresses (the complement to 100% of the circumferential stress that is 58%). This means that the circumferential stress is bigger than q by a factor of about 1.4 ($\approx 0.58/0.42$) and this factor rises to about 10 in the case of $\beta=0.9$.

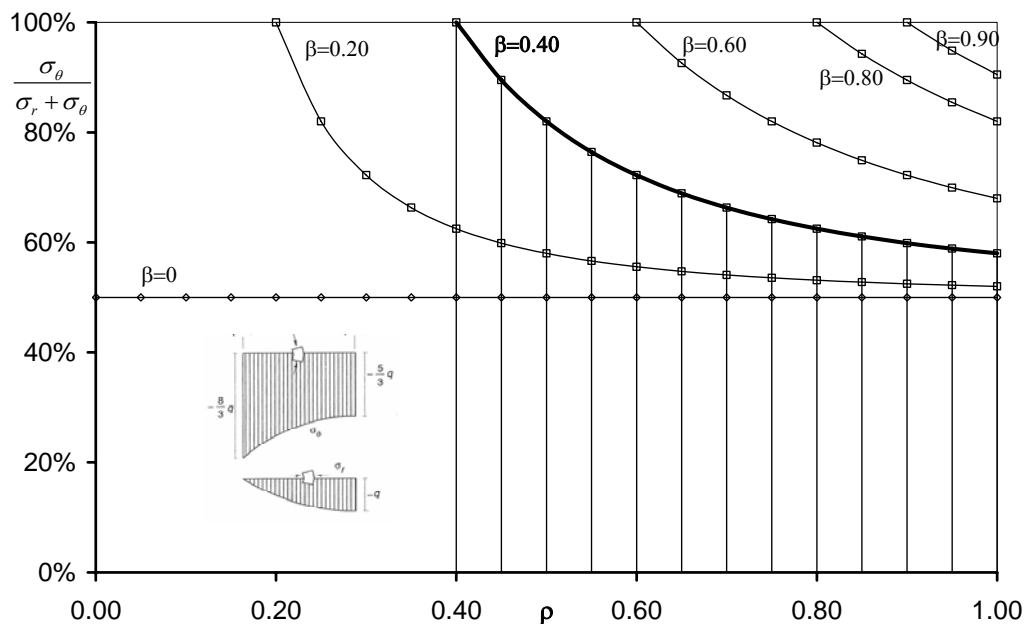


Figure 3.37 – Relative ratio between radial and circumferential stresses

In the case of hollow sections with very small wall thickness compared to the sectional diameter, the circumferential stresses become predominant.

Effect of Confining Device Relative Stiffness

In previous paragraph it has been clearly demonstrated that in the case of hollow sections with very high β ratios, the circumferential stresses are many times bigger than the pressure exerted by the confining devices, thus resulting in higher confinement pressures (see eq.(17) where the confining pressure f_i is related to β ratio). In this section a realistic hollow column confinement effectiveness is defined. Due to the higher deformability of a hollow column with large β ratio, the pressure exerted by the confining device in this case is much lower than in solid cases, due to compatibility considerations.

In the case of hollow core section is very important to introduce the relative confinement stiffness $E_f t / (R_e - R_i)$. If the stiffness is evaluated in the traditional manner, $E_f t / R$, an increase in the mechanical confinement ratio is overlooked. For the same external radius, if the confining device thickness t is constant, hole size increments result in increases of the mechanical confinement ratio, thus resulting in increases of the global confinement performances.

Effect of Hole Size

The latter study concerns the complete evaluation of the axial and lateral stress vs. strain curve, the axial stress vs. dilation ratio. This study has been conducted on a solid section with different jacket thickness and on a hollow section with different $\beta = R_i / R_e$ ratios, but the same relative confinement stiffness $E_f t / (R_e - R_i)$.

A concrete specimen with an external radius $R_e = 200\text{mm}$, unconfined

concrete strength $f'_{co}=30$ MPa with an unconfined peak strain $\epsilon_{co}=0.02$ and an initial Poisson ratio $\nu_{co}=0.15$ is considered. The specimen is confined with an FRP wrap made by uniaxial fibers with a nominal thickness of 0.333 mm. The FRP is applied by manual wet lay-up so that the Poisson ratio ν_f can be neglected and the Elastic modulus and ultimate uniaxial strength are 230 GPa and about 2000 MPa respectively. The relative confinement stiffness (related to a solid section) is about 1150 MPa (this means that increasing the hole size, the thickness t is reduced).

In figure 3.38 is a comparison of unconfined concrete stress strain curve with the confined concrete curves for different $\beta=R_i/R_e$ ratios, but the same relative confinement stiffness $E_f t/(R_e-R_i)$. Compared to the solid section ($\beta=0$), the effect of confinement is smaller as the hole size increases. The behavior changes from a hardening post peak to an almost perfectly plastic behavior in the case of very thin walls ($\beta=0.75$). Also the strength enhancement is smaller as the β ratio increases.

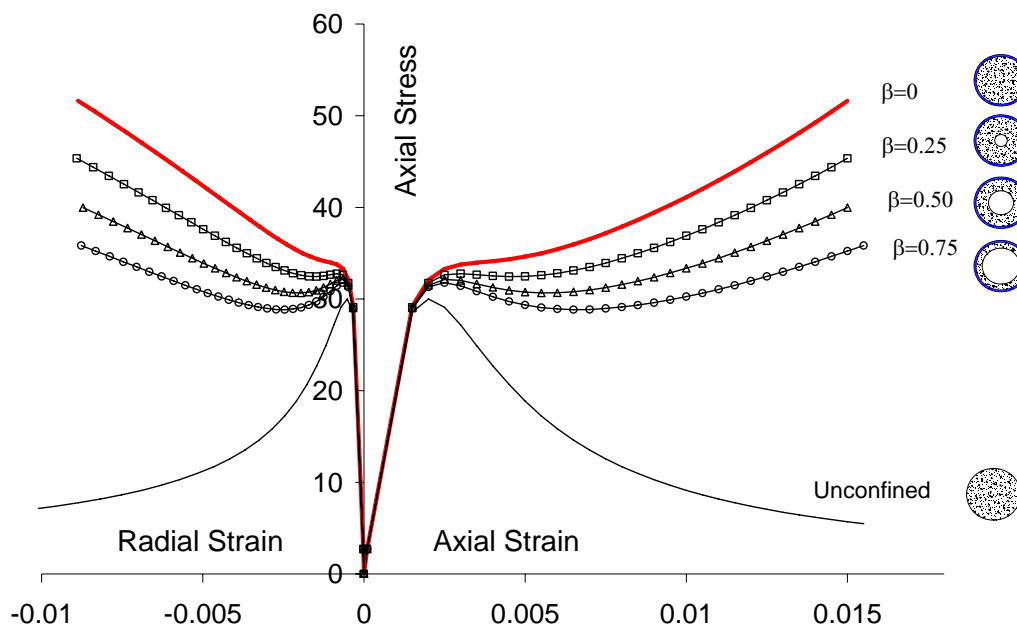


Figure 3.38 – Confined concrete: axial stress versus axial and radial strain

In figure 3.39 are the dilation ratio versus axial stress curves for different $\beta=R_i/R_e$ values but the same relative confinement stiffness $E_{ft}/(R_e-R_i)$. The mechanical and geometrical properties are the same as in the cylinders considered in figure 3.38.

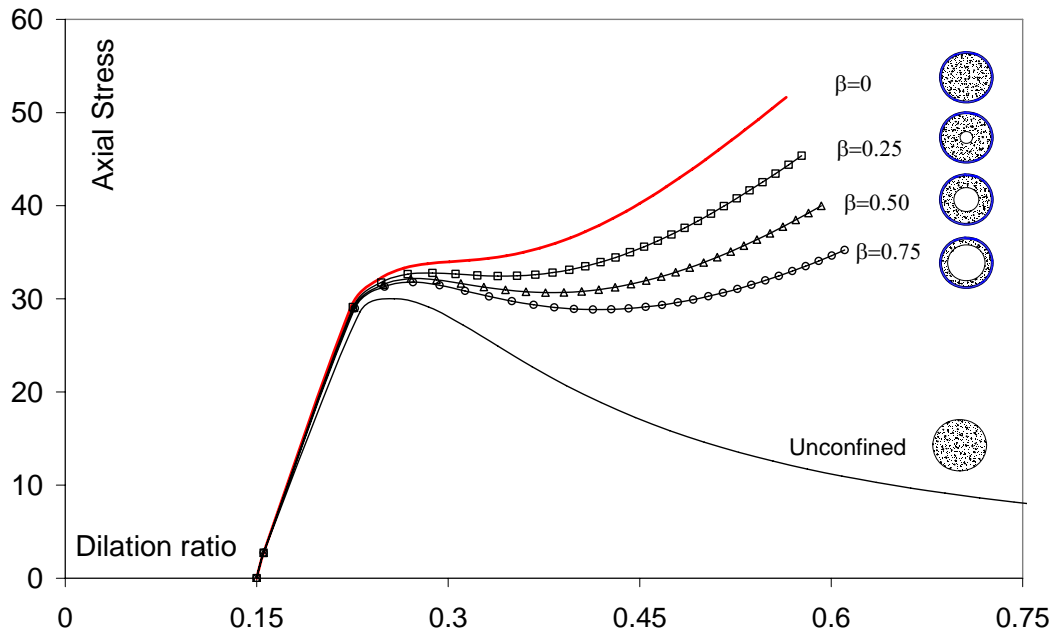


Figure 3.39 – Confined concrete: axial stress versus dilation ratio

The dilation ratio is almost constant, or slightly rising, up to peak unconfined concrete stress and equal to the initial Poisson ratio. After that peak point the dilation ratio grows, but the effect is different in the case of solid and hollow sections. The bigger is the hole, the higher is the deformability of the element thus resulting, for similar level of dilation, in different stress paths: in the case of solid section the dilation of concrete is restrained by the FRP wraps and this interaction causes a strength enhancement, while in the case of thin walls, the excessive deformability does not allow to gain any strength improvement, even though a significant ductility enhancement is achieved.

3.4 Chapter References

Braga, F., and Laterza, M. (1998). "A new approach to the confinement of RC columns." *Proc., 11th European Conf. on Earthquake Engineering*, A. A. Balkema, Rotterdam, The Netherlands.

Chen, W.F. (1982). *Plasticity in Reinforced Concrete*. McGraw Hill, New York.

Cosenza E and Prota A (2006) "Experimental Behavior and Numerical Modeling of Smooth Steel Bars under Compression", *Journal of Earthquake Engineering*. 10(3):313-329.

Fam, Amir Z. and Rizkalla, Sami H., (2001) "Confinement Model for Axially Loaded Concrete Confined by FRP Tubes," *ACI Structural Journal*, Vol.98, No.4, July-August 2001(b), pp.251-461.

Gardner, N. J., (1969), "Triaxial Behavior of Concrete," *ACI JOURNAL, Proceedings*, V. 66, No. 2, Feb., pp. 136-146.

Gigliotti, R. (1998). "Concrete confinement and ductility of the RC members." Thesis, Structural Engineering, *Univ. della Basilicata*, Potenza, Italy (in Italian).

Hillerborg A. (1989) "The compression stress-strain curve for design of reinforced concrete beams". *Fracture Mechanics: Application to Concrete*, ACI SP-118:281-294.

Hsu, T.T.C., Slate, F.O., Sturman, G.M. and Winter, G. (1963). Micro-cracking of Plain Concrete and the Shape of the Stress-Strain Curve. *ACI Journal Proceedings*, 60(2), 209-224.

Kato, D., Kanaya, J., and Wakatsuki, K. (1995). "Buckling strains of main bars in reinforced concrete members." *Proc., 5th East Asia and Pacific Conf. in*

Structural Engineering and Construction EASEC-5, Gold Coast, Australia, 699–704.

Magdi Mohareb M. and Istemi F. Ozkan. (2004) Plastic Interaction Relationships for square hollow structural sections: Lower Bound Solution. *ASCE Journal of Structural Engineering*, 130(9):.

Mander, J.B., Priestley, M.J.N., Park, R., (1988a). Theoretical stress–strain model for confined concrete. *Journal of the Structural Division ASCE* 114, 1804–1826.

Mander, J.B., Priestley, M.J.N., Park, R., (1988b). Observed stress–strain behavior of confined concrete. *Journal of the Structural Division ASCE* 97, 1969–1990.

Masia, M.J. and Shrive, N.G., (2003). Carbon Fiber Reinforced Polymer Wrapping for the Rehabilitation of Masonry Columns. *Canadian Journal of Civil Engineering*. 30(4), 734-744.

Monti, G. and Nuti, C. (1992) “Nonlinear cyclic behavior of reinforcing bars including buckling,” *ASCE Journal of Structural Engineering* 118(12), 3268–3285.

Pantazopoulou, S.J. and Mills, R.H. (1995). Microstructural Aspects of the mechanical response of plain concrete, *ACI Materials Journal*, Vol. 92, November-December, 605-616.

Popovics, S. (1973). " A numerical approach to the complete stress strain curve for concrete." *Cement and concrete research*, 3(5), 583-599.

Poston, R. W.; Gilliam, T. E.; Yamamoto, Y.; and Breen, J. E., (1985) "Hollow Concrete Bridge Pier Behavior," *ACI JOURNAL Proceedings* V. 82, No. 6, pp. 779-787.

Recupero A, D’Aveni A, Ghersi A. (2003) N-M-V Interaction Domains for box and I-shaped reinforced concrete members. *ACI Structural Journal*;100(1):113-119.

Richart, F.E., Brandtzaeg, A., Brown, R.L., (1928). A study of the failure of concrete under combined compressive stresses. Engineering Experimental Station, *University of Illinois, Bulletin* no. 185.

Richart, F.E., Brandtzaeg, A., Brown, R.L., (1929). The failure of plain and spirally reinforced concrete in compression. Engineering Experimental Station, *University of Illinois, Bulletin* no. 190.

Spoelstra MR, Monti G. (1999) FRP-confined concrete model. *ASCE Journal of Composites for Construction*, 1999, 3(3):143-150.

Stowell, E.; Heimerl, G. J.; Libove, C. and Lundquist, E. E., (1952) "Buckling Stresses for Flat Plates and Sections," *Transactions, ASCE*, Paper 2506, V. 115, pp. 545-578

William, K. J., and Warnke, E. P. (1975). "Constitutive model for the triaxial behaviour of concrete." *Proc., Int. Assoc. Bridge Structural Eng.*, 19, 1–30.

Yuan XF, Lam L, Teng JG, Smith ST (2001). FRP-confined RC columns under combined bending and compression: a comparative study of concrete stress–strain models. In: Teng JG, editor. *Proceedings of the International Conference on FRP Composites in Civil Engineering*, 12–15 December, Hong Kong, China. *FRP Composites in Civil Engineering 2001*;I:749–58.

Zhou SP and Chen WF. (1985) Design criteria for box columns under biaxial loading. *ASCE Journal of Structural Engineering*, 111(12):.

Chapter 4

Experimental-Theoretical Comparison

4.1 Experimental Outcomes: Comparative Discussion

The aim of this section is to deeply analyze the behavior of square hollow piers subjected to combined high level of axial load and flexure and the effect of strengthening with FRP jacketing.

Laboratory outcomes highlighted that composite wrapping can enhance the structural performance of concrete piers under eccentric loading: In the following sections will be presented the comparisons between unstrengthened and strengthened specimens performances in terms of strength and failure modes, in terms of ductility (curvature, local deformability and specific energy assessment), in terms of longitudinal strains evaluation and FRP strains development, in terms of theoretical model restraints validation.

Experimental results and the related database has been used for validation of the proposed FRP strengthening design method addressing hollow cross section. Results of experiments and theoretical analyses show that a good agreement was achieved between the experimental performances and the analytical results calculated using the developed refined method.

The effect of the neutral axis position with respect to the ultimate failure mode experienced by the cross section is analyzed and the effect of external wrapping by using FRP composite materials is studied and whether the retrofit solution adopted may change the ultimate failure mode by improving the overall

section behavior is analyzed.

When the neutral axis moves into the cross section the failure mode is modified as the state of stress changes from pure compression into combined compression and flexure, and the flexural stresses become predominant.

Un-strengthened columns failed due to the combination of two brittle mechanisms: steel reinforcement compressive bars buckling and concrete cover spalling (both occurred at similar strain levels). Since the failure of un-strengthened members is strongly affected by the occurrence of premature mechanisms (compressed bars buckling and concrete cover spalling), great attention was given to the assessment of these phenomena and to check how the FRP confinement allows delaying these mechanisms, thus resulting in both strength and ductility increases of members even under large eccentricities.

The strength improvement was more relevant in the case of specimens loaded with smaller eccentricity, while the ductility improvement was more relevant in the case of bigger eccentricity. Such result is encouraging as the confinement on members subjected to pure axial force is essentially considered as a solution to improve the strength, while in the case of combined axial force and bending moment is essentially considered to develop ductility rather than strength enhancements.

4.1.1 Strength

Figure 4.1 shows two experimental interaction diagrams. An unstrengthened hollow cross section experimental interaction diagram is plotted connecting U series results, while connecting the S series results is plotted the strengthened experimental domain.

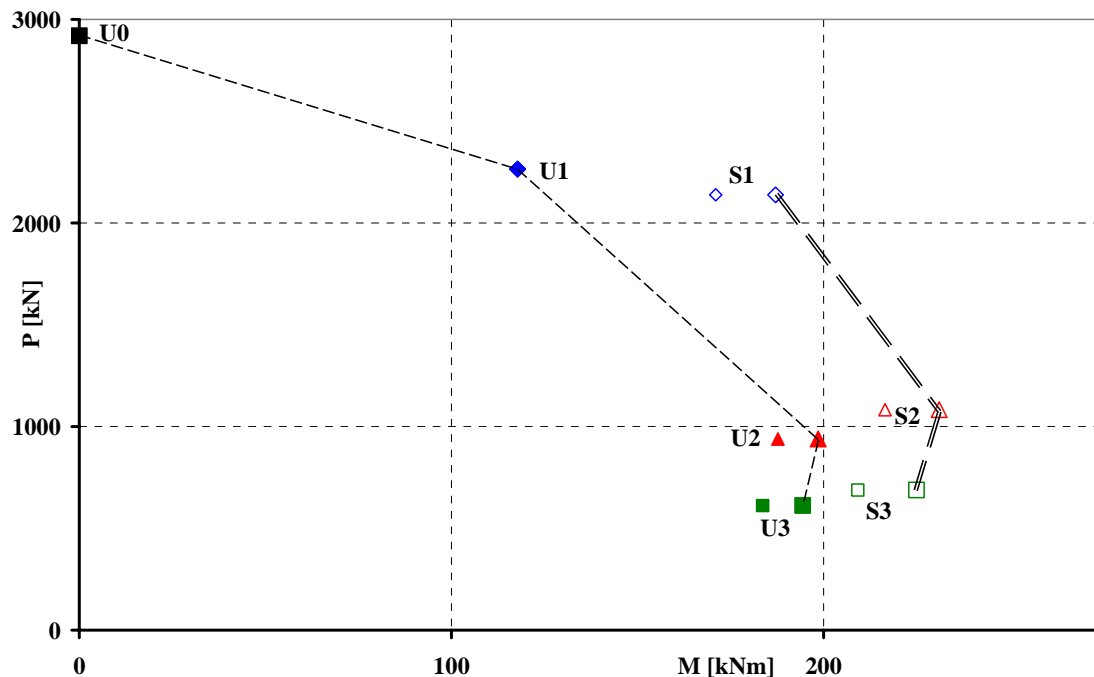


Figure 4.1 – Experimental Interaction Domains

Big blank (S Series) and solid (U Series) marks are experimental values accounting for column mid-span deflections (i.e., M_{II}). Small marks are experimental values not accounting for P- Δ effects (i.e., M_I). P_{\max} is defined as the experimental ultimate axial load, and δ is defined as the measured mid-span deflection at peak load. For experimental moments, the moments based on equations $M_{II} = P_{\max} (e + \delta)$ (taking into account P- Δ effects) and $M_I = P_{\max} \cdot e$ are reported in Table 4.1. The deflection measured data of Specimen U1 were missed and only ultimate moment M_I is reported.

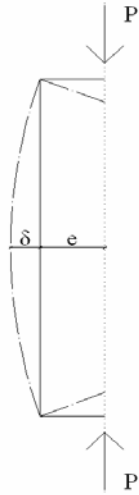
It is pointed out that the strength increment found experimentally in the strengthened columns is rather smaller for the columns loaded with greater eccentricities; such result is explained theoretically because the beneficial effect of confinement increases as the compressed part of the cross section increases.

The executed tests evidenced a strength increment of FRP confined columns

with respect to the un-strengthened columns in the order of 15 percent. The strength increase was about 14% in the case of larger eccentricity (i.e., S3 versus U3 in table 4.1) and higher in the case of smaller eccentricity, while a gradually more ductile behavior when increasing the eccentricity has been observed.

The exhibited ductile increment enhances also the flexural strength of the specimens and the evaluated benefits of the FRP wrappings. Considering M_{II} , the S columns wrapped with FRP show a bigger deflection δ compared to the U series, so that, i.e., the strength increase was about 17% in the case of larger eccentricity if the P- Δ effects are considered. Wrapping has delayed the activation of the failure mechanism characterized by the combination of compressive steel bar buckling and concrete cover spalling; this delay has allowed for full development of the concrete's load capacity in the strengthened columns resulting in a strength increase of the member.

Table 4.1 – Test Results

Specimen Code	P_{max} (kN)	e (mm)	δ (mm)	M_I (kNm)	M_{II} (kNm)	
U0	2929	0	N.A.	0	N.A.	
U1	2264	52	N.A.	117.73	N.A.	
U2	939	200	11.51	187.73	198.53	
U3	612	300	18.57	183.64	195.00	
S1	2138	80	7.41	171.03	186.88	
S2	1082	200	13.35	216.48	230.93	
S3	697	300	26.51	209.20	227.68	

4.1.2 Failure Modes

The brittle failure of the tested members occurred at the base of the hollow portion for specimens U1, U3, and S2, in correspondence with the discontinuity due to the change from the solid section at the ends to the hollow section. For specimens U2, S1, and S3, the failure occurred at mid-span, where the P- Δ effects mostly impact flexural moment.

The walls failed due to concrete crushing or combined bars buckling and concrete cover spalling, while the local buckling of compressed thin wall never occurred.

Un-strengthened columns failed because of the combination of two brittle mechanisms: steel reinforcement compressive bars buckling and concrete cover spalling: both occurred at similar strain levels (Figure 4.2).



Figure 4.2 – Compressed Bars Buckling and Concrete Cover Spalling (U1)

The concrete cover spalled out in the compression side, and bars buckled on the external side. The observation of failed elements showed that bar buckling occurred on a span length of two ties spacing in the middle of the wall.

The steel reinforcement bars situated on the outermost corners of the front compressed wall, were restrained by the bend of the stirrup and buckling occurred on a span length of one tie spacing (figure 4.3).



Figure 4.3 –Buckling of the outermost bar (U2)

In the case of U2 specimen, some compressed bars buckled on a length of two or more ties spacing in the inward direction. After the tests' executions all the crushed concrete was removed and the steel reinforcement cage exposed (Figure 4.4).



Figure 4.4 –Crashed concrete removed and steel cage exposed (U2)

If the neutral axis pass trough the void at some distance from the inside face of the tube, the column can be expected to fail in a brittle manner as a result of rapid disintegration of the concrete in the compression zone and deterioration of the flexural strength. There is a little margin for the strain to grow with increasing curvature before failure commences because the resulting high longitudinal compressive strain on the inside face causes early vertical splitting and crushing of the concrete. This can lead to an inward buckling of steel compressed bars.

A gradually more ductile behavior was observed when the eccentricity was increased; in fact, for small eccentricity the section was fully compressed, the axial load was bigger and also buckling was more noticeable. The brittle behavior of the compressed concrete affected the total behavior of the element. When increasing the eccentricity, the neutral axis actually moved towards the inside of the section, and some ductility was attained from the tensile property of the steel. Neutral axis close to the inside face of the tube wall results also in small longitudinal strains in the compression wall, especially in the unconfined region of the concrete compression zone.

The CFRP wrapping in S columns delayed the longitudinal steel bars buckling and prevented external concrete cover spalling, preserving the most compressed concrete fibers responsible in particular of the flexural strength.

The failure of CFRP wraps was never observed, but after some crackling near peak load, the bearing capacity of the strengthened column started decreasing. The descending branch slope grew as the eccentricity increased. The S3 test was deliberately stopped at about 70 percent of ultimate load, and wide cracks were observed in the tensile side (see Figure 4.5). The only external appearance of failure was the formation of a bulge in the FRP (see Figure 4.6) due to the remarkable shortening of the column.



Figure 4.5 –Wide cracks opening in tension side (S3)

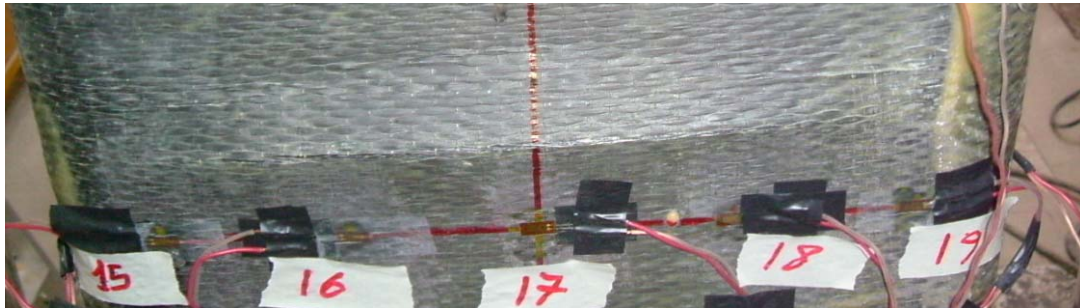


Figure 4.6 –Bulge of FRP jacket in tension side (S3)

After the test's executions, a segment of the hollow portion of columns was extracted (by means of two cuts) to analyze the inner surface of the walls close to the failure zone of the element; a view of the interior of specimen S1 is shown in Figure 4.7.



Figure 4.7 –Failed portion of the specimen after test (S1)

Bars buckling was also found on the interior side. The observation of failed elements showed that bar buckling occurred on a span length of two ties spacing that was probably a consequence of the buckling of the bars on the interior side. Tests (see Chapter 2.1.1) were done on compressed bars with Length/Diameter ratios of 8 and 16 (corresponding to a ties spacing of 80 mm and 160 mm, respectively, for a longitudinal bar with a 10 mm diameter). In the case of $L/D=16$, the buckling occurred in the elastic range (*Cosenza and Prota 2006*). This finding confirms that when concrete reached strains of about 2%, the bar started buckling and lost its load carrying capacity. The two brittle mechanisms acting together are consistent with the very brittle behavior observed in the tests of un-strengthened columns.

This failure mode is similar to the one observed on slender walls with high aspect ratio subjected to axial load (*Prota et al. 2006*). In the case of wall-like columns (ratio between sides higher than about 3), the effectiveness of the FRP jacket is reduced and the failure of the member occurred at FRP strains far lower than the ultimate coupon test strains. In tested specimens with ratio between sides

higher than about 7:2, the failure occurred when the average axial strain approached the ultimate strength of the unconfined concrete (ranging between 2.5‰ and 3‰). The concrete cover started crushing on one of the two long sides of the cross section. The longitudinal steel bars bulged within the spacing between two consecutive stirrups and determined the spalling of the concrete cover, at that stage the column became unable to carry further loads. The failure of strengthened columns was similar to that of those unstrengthened, it did not occur as a result of the FRP fibers failure, but due to the bulging of the composite system. Concrete average axial strain approached 6.2‰ when the column was wrapped with FRP.



Wall-like column failure unstrengthened and strengthened (Prota et al. 2006)

4.1.3 Ductility

In the case of flexural elements, the ductility can be evaluated by considering the moment-curvature diagrams. Figures 4.8-4.9 show comparison of experimental moment-curvature diagrams for the U-series and S-Series (no comparison have been made between U1 and S1 specimens since they have a different load eccentricity). In the first linear elastic phase it is possible to refer to the well known elastic relationship: $\chi = M/EI$, then, after concrete cracking, the effective moment of inertia has to be considered and tension stiffening effects take place. The moment-curvature relationships were calculated using the axial load value and imposed constant eccentricity without accounting for deflections.

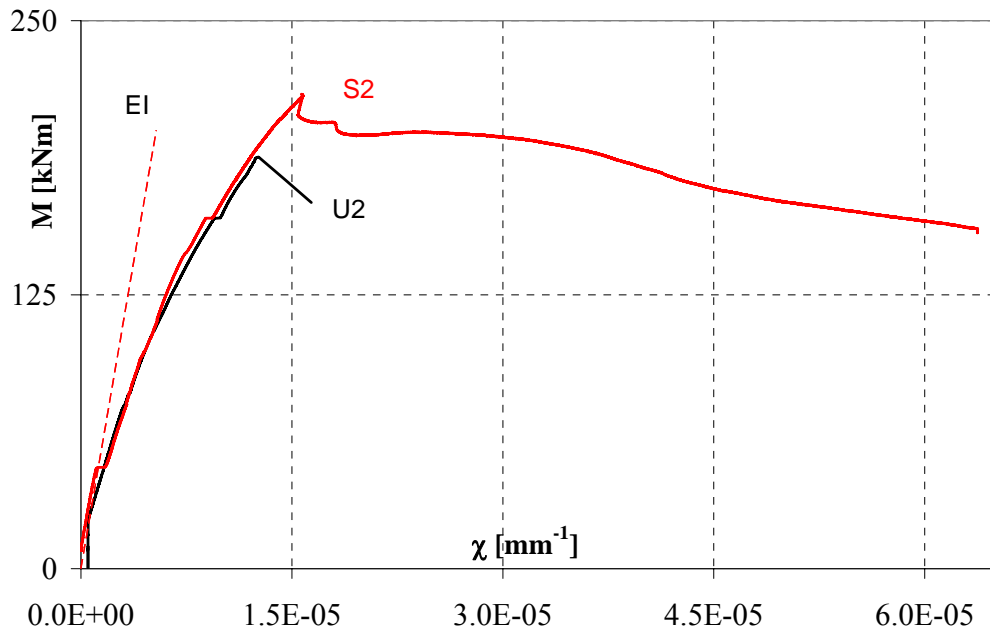


Figure 4.8 –Moment-Curvature Diagram: U2 and S2 experimental comparison

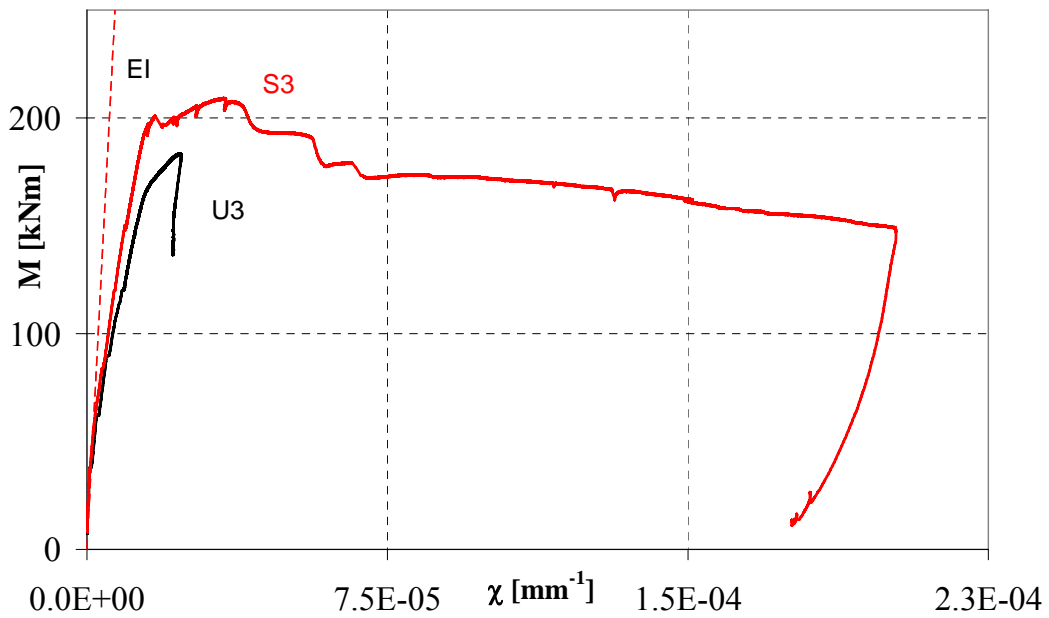


Figure 4.9 –Moment-Curvature Diagram: U3 and S3 experimental comparison

Rotations in potential plastic hinges are the most common and desirable source of inelastic structural deformations. For elements failing in flexure the curvature ductility μ_χ gives a measure of the ductility of the cross section that gives information about the shape of the descending branch in moment-curvature relationships. The curvature ductility can be defined as the ratio of the curvature on the softening branch at 80% of ultimate load, $\chi_{80\%max}$, and the yielding curvature, χ_y (corresponding to the yielding flexural moment M_y). M_y is the flexural moment evaluated when steel yielding was measured by strain gauges; if yielding did not occur, as for U1 and U2 specimens, M_y is assumed equal to the moment corresponding to the peak load. M_y is evaluated not accounting for P- Δ effects (i.e., like M_I).

Ductility is reduced by the increment of axial load. When increasing the eccentricity (that is axial load reduction) it is observed that the neutral axis moves towards the inside of the section and some ductility was attained due to tensile properties of steel. Table 4.2 reports curvature ductility values.

Table 4.2 – Experimental Curvature Ductility

Specimen Code	e (mm)	M_y (kNm)	χ_y (10^6mm^{-1})	$\chi_{80\%max}$ (10^6mm^{-1})	μ_χ (-)
U1	52	117.73	5.183	5.183	1
U2	200	187.73	12.644	12.644	1
U3	300	167.42	15.126	23.294	1.54
S1	80	163.68	7.811	33.080	4.24
S2	200	210.41	14.943	45.180	3.02
S3	300	197.65	15.584	128.819	8.27

It is pointed out that the curvature ductility is one for the unstrengthened columns U1 and U2: this is due to the sudden bearing capacity drop that does not

allow any curvature increment after-peak (i.e., yielding of steel bars was not attained).

In the Strengthened series, it is clearly pointed out the benefit of confinement. Confinement allows the development of larger curvatures after peak load and curvature ductility is larger than three for the strengthened columns.

Test S2 experienced curvature ductility smaller than S1, even though its eccentricity was larger. This could be explained by considering that its failure occurred far from the portion across mid-span where strain data were gauged. For specimens U3 and S3 it can be observed that the increase of μ_χ from 1.54 to 8.27 corresponds also to a significant gain in terms of area under the curve that is proportional to the specific energy.

Actually the increment of ductility supplied by confinement can be also appreciated comparing the values of the specific energies obtained (Table 4.3) and remarkable increases of dissipating capabilities for strengthened columns are found. Energy values are computed as the area under the M/χ diagram at any given χ (refer to illustrative Fig. 4.10).

The maximum ductility, μ_χ , is recorded for the column S3. For instance, (Table 4.2) when μ_χ is 8.27, for the same eccentricity the dissipated specific energy, $E_{80\%max}$, of S3 specimen computed on the softening branch at 80% of ultimate load is more than 7 times the dissipated specific energy at peak, E_{max} , of the brittle U3 specimen (Table 4.3). Specific energy increment $E_{80\%max}/E_{max}$, i.e. in S3 column, is more than 3.71 emphasizing the meaningful increase of ductility of the confined structural elements.

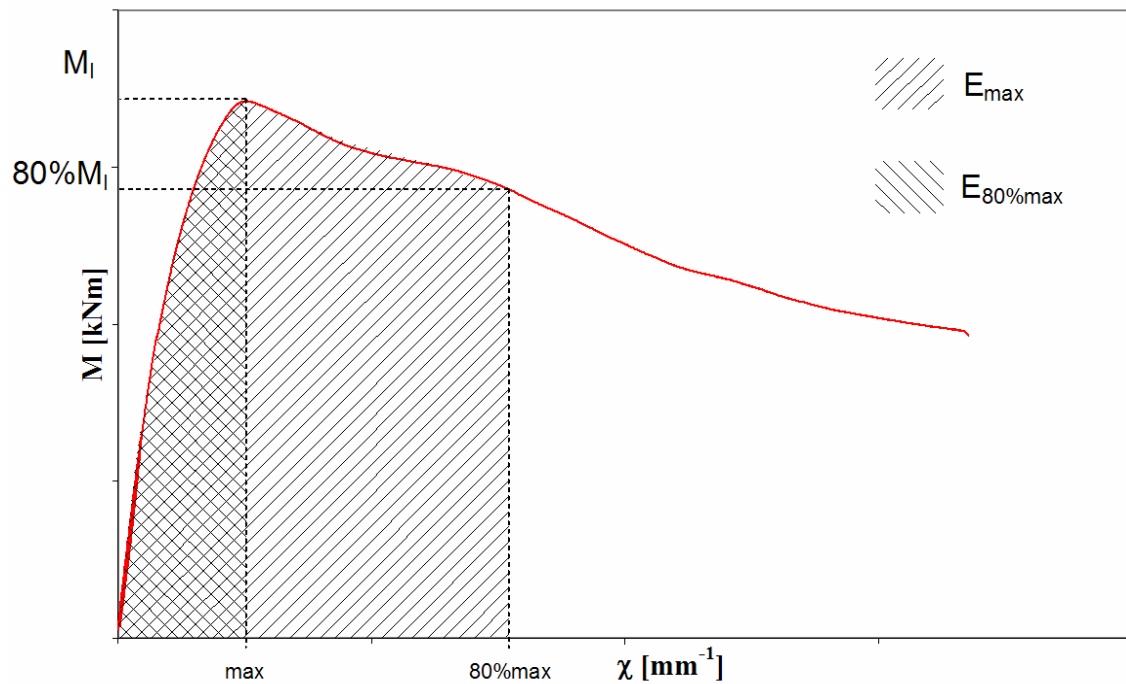


Figure 4.10 – Illustrative Curvature Ductility and Specific Energy evaluation

Table 4.3 – Experimental Specific Energy

Specimen Code	e (mm)	M _I (kNm)	E _{max} (10 ⁶ kNm·mm ⁻¹)	E _{80%max} (10 ⁶ kNm·mm ⁻¹)	E _{80%max} /E _{max} (-)
U1	52	117.73	398	398	1
U2	200	187.73	1462	1462	1
U3	300	183.64	3375	3375	1
S1	80	171.03	1183	4797	4.05
S2	200	216.48	2134	7907	3.71
S3	300	209.20	5615	23113	4.12

4.1.4 Longitudinal Strains

Strain diagrams are obtained from data of vertical LVDTs placed on the exterior wall; a good agreement was generally found with strain gauge measurements on steel bars. The experimental curvature was computed connecting three data points, one on most compressed concrete fiber and two on internal steel reinforcement bars (compressive strains are positive).

Mid-span strain diagrams refer to peak load. The local effect of bar buckling in the U1 specimen affected the global behavior of the column that was brittle with sudden crushing and cover spalling of the concrete in the compressive part at concrete strain level as small as 2‰. Also in column U2 and U3 the concrete reached strains lower than 2,5‰ and 3‰ at peak load, respectively.

The premature failure is clearly a consequence of compressed steel bars buckling that is highlighted by strains plainly bigger than those of the compressed concrete cover.

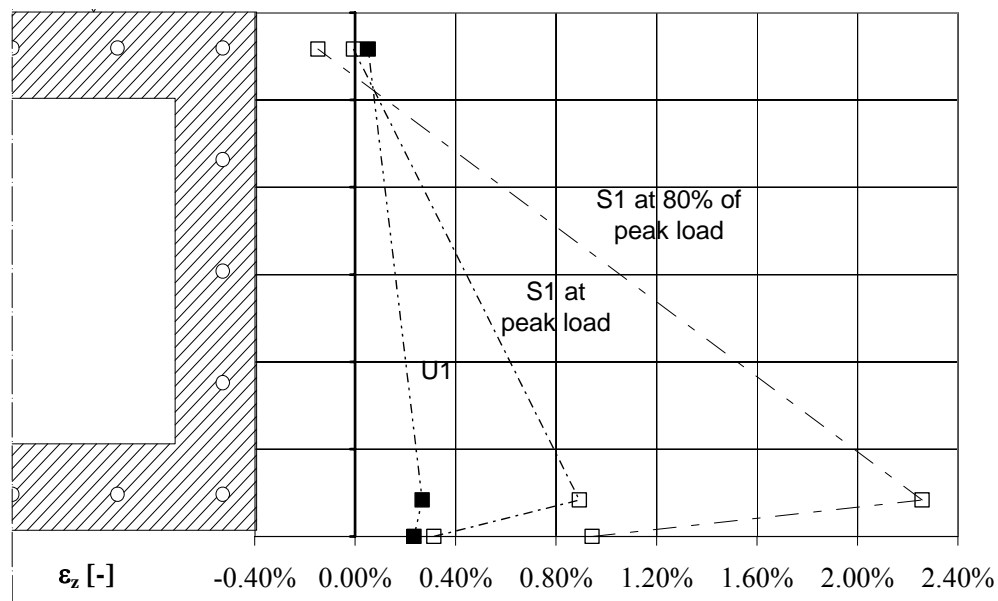


Figure 4.11 – Comparison: Experimental U1 and S1 strains

In the S1 column close to peak load, a remarkable increment of the compressed steel bars strain is attained due to buckling that in fact took place just at mid-span where strain gauges have been applied. The local effect of bar buckling (clearly noticeable in Fig. 4.11 where experimental strain distributions that took place in the S1 column are shown at peak and at 80% of peak load) did not affect the post peak carrying capacity of the strengthened specimen.

In Table 4.4, concrete strains ϵ_{\max} at peak load and on the softening branch at 80 percent of ultimate load, $\epsilon_{80\% \max}$, are shown. Notice that the reported strains for the U specimen are related to peak load due to sudden bearing capacity drop as a result of the brittle failure. The effect of buckling on concrete cover damage is clearly noticeable because the strains attained by concrete at peak load are greater when the eccentricity is higher. In fact, as the eccentricity increases, the axial load reduces, and buckling is also less noticeable. The effect of FRP wrapping is highlighted by the values of concrete strains that for eccentricities of 200 mm and 300 mm increased by a factor of about 2 and 5, respectively (see Table 4.4).

Table 4.4 – Concrete axial Strains

Specimen Code	P_{max} (kN)	e (mm)	ε_{max} (με)	ε_{80%max} (με)
U0	2929	0	1590	1590
U1	2264	52	2219	2219
U2	939	200	2613	2613
U3	612	300	2820	2820
S1	2138	80	3145	9450
S2	1082	200	2755	5941
S3	697	300	3508	15406

A plastic hinge formed far from the instrumented portion of the specimen S2, so that it is clearly shown an unloading behavior in the concrete strains of that specimen.

The comparison between experimental results is encouraging for confinement effects. Confinement appears to be unable to change actual failure mode (steel reinforcement compressive bars buckling), but it is able to delay bars buckling and to let compressive concrete strains attain higher values.

The fact that columns tested within the presented experimental work were characterized by an ultimate load behavior controlled by concrete crushing is also consistent with recommendations provided by AASHTO 2002. In fact, this guideline states that if the slenderness ratio of the compression flange reaches a value of 15 or greater, then the flange could fail by buckling; for lower values (in the present work equal to 4), the flange could fail from the crushing of concrete.

4.1.5 FRP Strains

Strain rate development and longitudinal stress distributions into FRP confining wraps have been recorded and analyzed by means of seven strain gauges (SG14÷SG20, Figure 4.6). Strain gauges have been applied at mid-span of the column and in some cases they were able to record strain development nearby the failure zone. The CFRP wraps confinement effectiveness can be checked by strain rate and strain distribution. In table 4.5 strain data for each strain gauge at peak load, ϵ_f , and on the softening branch at 80% of ultimate load, $\epsilon_{f,80\%}$, are summarized.

Table 4.5– Strain Gauges on FRP

Strain Gauge	S1		S2		S3	
	ϵ_f [%]	$\epsilon_{f,80\%}$ [%]	ϵ_f [%]	$\epsilon_{f,80\%}$ [%]	ϵ_f [%]	$\epsilon_{f,80\%}$ [%]
SG 14	0.036	0.194	0.013	0.013	0.002	0.065
SG 15	0.071	0.524	0.030	0.024	0.067	0.351
SG 16	0.114	0.450	0.048	0.053	0.053	0.326
SG 17	0.105	0.379	0.045	0.042	0.053	0.296
SG 18	0.093	0.359	0.053	0.050	0.069	0.370
SG 19	0.086	0.465	0.044	0.038	0.062	0.437
SG 20	0.032	0.157	0.020	0.016	0.001	0.166

Maximum tensile stresses in FRP are reached in the middle of the front compressed wall at mid-span and this fact disagrees with theoretical predictions. Maximum predicted stress concentrations in solid cross sections are at the cross section corners, but a bulge on the FRP wraps formed near mid-span due to the shortening of the column, and that bulge probably affected some strain data.

In figure 4.12 are shown maximum strains/stresses attained at peak load in each test (on strengthened columns S1 to S3). At peak load FRP lateral strains are smaller than 1.14% as shown in Table 4.5.

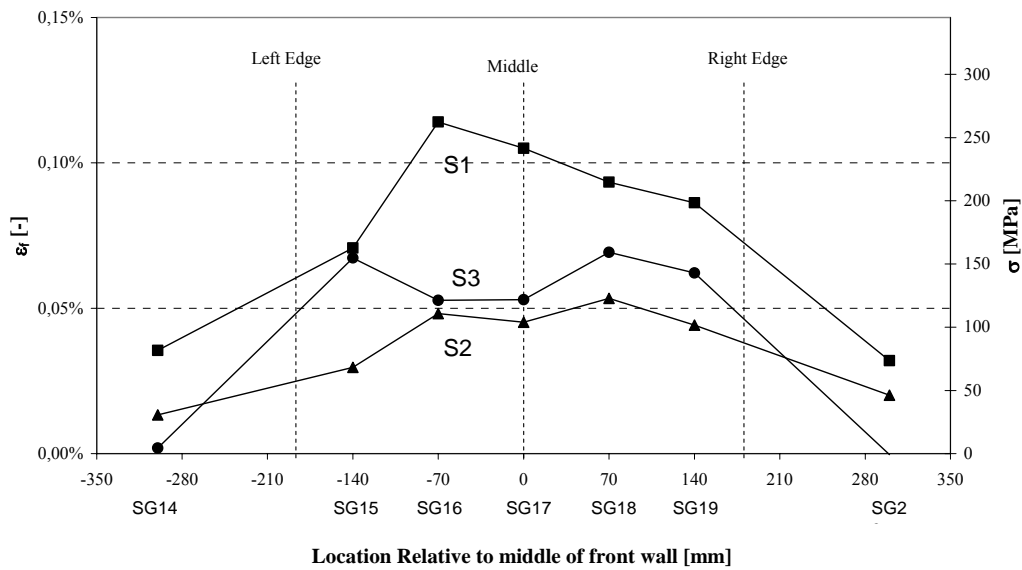


Figure 4.12 –FRP maximum strains/stresses at peak load

Actual theoretical models adopt a maximum feasible strain in the FRP wraps that results from experimental test data and thus a post-peak analysis has also been performed. From a theoretical point of view, FRP confinement strains are expected to grow. Maximum recorded strains in the post-peak phase are expected to be smaller in the columns loaded with bigger eccentricity, that is a lower effectiveness of the confinement as a result of bigger load eccentricity.

In Figure 4.13, post-peak behavior is shown with strain distribution diagrams at 80% of peak load in the S-series specimen. After peak a remarkable strain increment is noticed. An average strain around 4‰ with a maximum value of 5.24‰ in column S1 is recorded. Smaller strains in column S3 were found, but FRP strains in S2 were quite smaller than S3, even though the latter has a bigger load eccentricity. This can be explained looking at the failure zone of column S2. This column failed at the transition from the solid section to the hollow section in the upper part, far from the instrumented FRP confined portion of the column.

Acquired strains after peak are stationary or decrease slightly leading to an unloading behavior (or perhaps it is due to a connection failure) that influenced acquired data, in particular strain data were smaller than those likely attained in the failure zone.

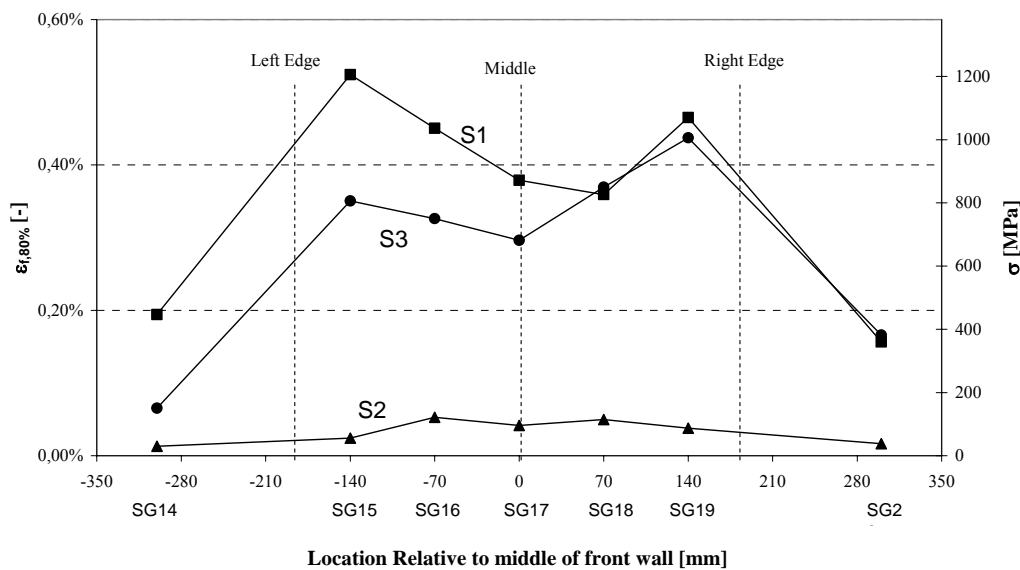


Figure 4.13 –FRP maximum strains/stresses at 80% of peak load

However good validation of maximum feasible FRP lateral strain of 4‰ in many international codes is pointed out.

At low load levels, strains are almost low and constant along the compressed side, symmetrically on the wall with a minimum value in the middle of the wall. This is totally in accordance with theoretical previsions, where strain peaks are expected at the cross section corners where stress concentrations are predictable

In the post-peak branch of S3 test, strains after peak load suddenly increased to very high values and lost their symmetric distribution. These readings are clearly influenced by a pronounced bulge in the FRP wrapping just below strain

gauges due to column remarkable shortening (see figure 4.6).

Inconsistent behavior of S2 test is once again pointed out in the post-peak phase. In this phase FRP strains are reduced rather than grown. Such thing is due to the failure of the column in the upper part, far from the instrumented FRP confined portion of the column. A plastic hinge formed and focused strains and rotations in the upper portion of the column. Accordingly the lower and mid-span portion, where strain gauges and other instruments were applied, eventually unloaded.

4.1.6 Theoretical Model Restraints Validation

Model assumptions on restraints can be carefully proved comparing measured hinge rotation and mid-span deflections with numerical predictions based on available data. As explained in the theoretical analysis section: hinge rotation is assumed to be due to the *constant* curvature of the hollow portion of the column (constant moment hypothesis and curvature evaluated from the experimental strain data on longitudinal steel bars and concrete walls). The mid-span deflection is calculated by double integration of curvatures.

Hinge rotations have been recorded by two LVDTs placed on the steel plate at the lower end of the column. Calculated hinge rotations have been compared with estimated rotations. Figure 4.14 shows the validation for S3 column; in this test the largest rotations were expected. Symmetry considerations allow evaluating rotations by multiplying constant mid-span curvature by the length of half column (only the hollow portion, because in order to evaluate rotations, solid portions are supposed rigid).

The two obtained curves (Figure 4.14) are almost matching up before the peak load, validating the hypothesis on different stiffness of hollow and solid

portions. The different slope in the post-peak phase can be easily explained instead. The global rotations evaluated numerically by integration are due to the cracked section curvature, and do not take into account the well known tension stiffening effects. Besides the curvature is not really constant along the column (i.e P- Δ effects) and mid-span evaluated curvature overestimates average curvature. Bars buckling can also affect experimental local data.

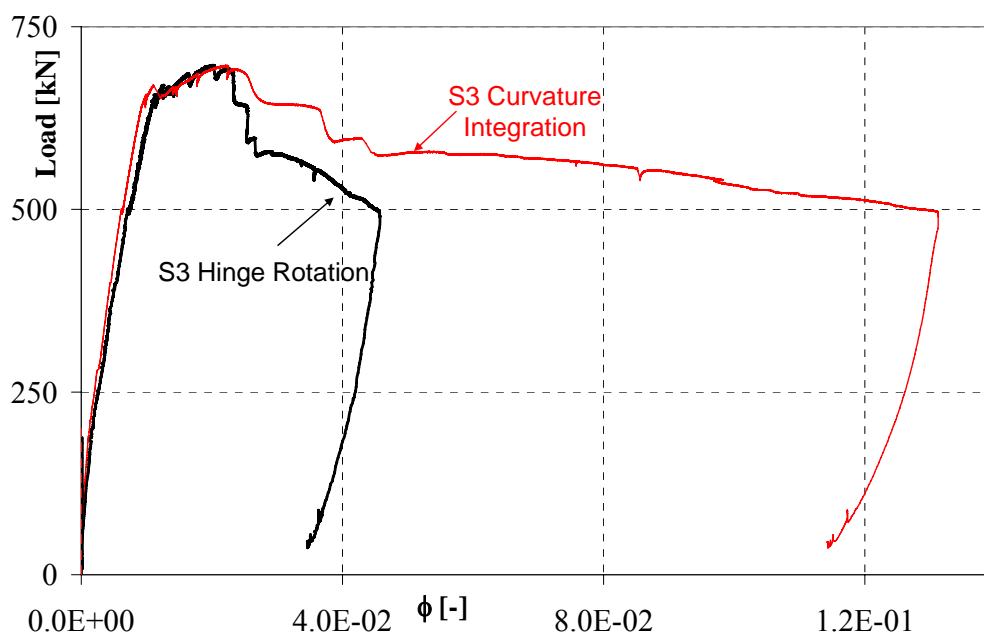


Figure 4.14 – Restraints Validation: brackets rotation and average curvature integration

Curvature increases as eccentricity grows and consequently column deflection increases. The good agreement achieved between the experimental measured hinge rotation and the calculated rotation based on curvature shows that the hinges properly worked (constraint assumption).

Mid-span deflections diagrams δ (Figure 4.15) show the same trend as the hinge rotations. Good agreement between acquired data and experimental estimations is found before peak load, the cracking effect and second order effect

take place decisively in the post peak behavior.

The solid part, supposed rigid, gives only a deflection contribution due to the rigid rotation of the hinge. Nevertheless higher sensitivity was found on displacement predictions due to the double integration, solid portion stiffness hypothesis and constant moment assumption.

Figure 4.15 shows the comparisons with theoretical load deflection curve.

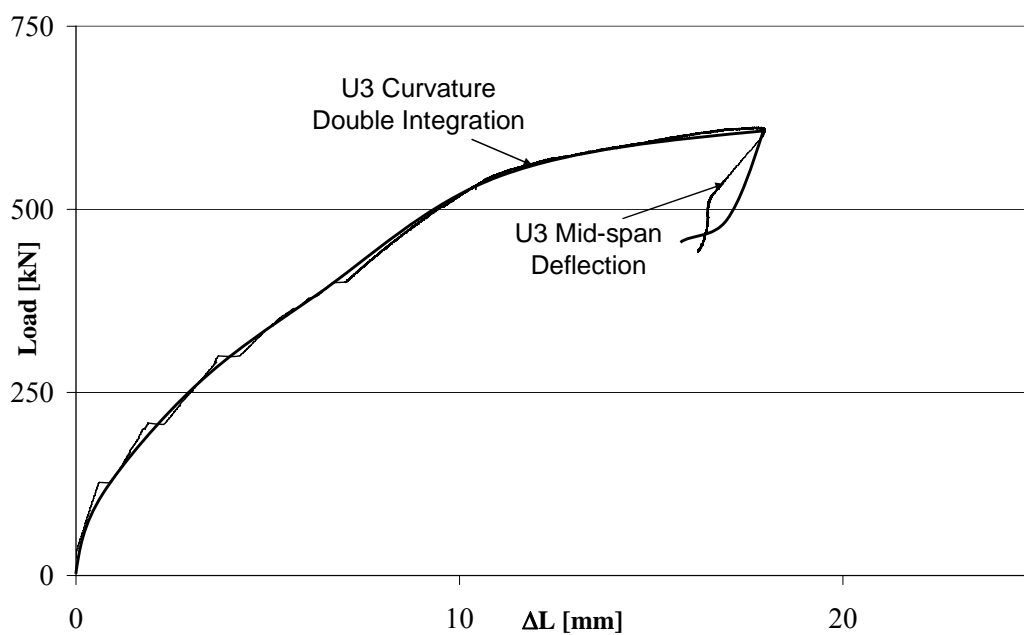


Figure 4.15 –Mid-span deflection and average curvature double integration

The calculated displacements from the curvature overestimate column deflections. More accurate deflections can be predicted if a non-linear distribution of curvature is considered instead of a constant one, as effective axial load eccentricity vary along the hollow and solid portions of the column. Bars' buckling is especially noticeable in small eccentrically loaded column, while tension stiffening in bigger eccentricity loads.

4.2 Experimental-Theoretical Comparison

The proposed refined nonlinear methodology described in previous Chapter 3 has been adopted to analyze experimental outcomes.

This algorithm permitted to draw the theoretical P-M interaction diagram as well as moment curvature diagram and diagrams for local deformability, specific energy and longitudinal strains assessment, and theoretical model restraints validation. Flexural moments computed by the algorithm, including those used to plot moment-curvature diagrams, are computed with respect to concrete gross section centroid.

Confined concrete has been modeled according to the two approaches proposed in previous Chapter 3.3 and the stress-strain relationship of plain concrete under concentric loading is assumed to be representative of the behavior of concrete under eccentric loading (Chapter 3.1.3).

The fact that columns tested within the presented experimental work were characterized by an ultimate load behavior controlled by concrete crushing is also consistent with wall stability considerations in previous Chapter 3.1.5. In fact, if the slenderness ratio of the compression flange reaches a value of about 18 or greater, then the flange could fail by buckling; for lower values (in the present work equal to 4), the flange could fail from the crushing of concrete. Therefore local buckling of the thin compression flange is not accounted for, so that the ultimate strength is attained when material failure and/or steel reinforcement bar buckling occur.

Tension stiffening effect, compressed bars buckling and concrete cover spalling are included in the model. When steel reinforcement reaches in compression the buckling stress, as it pushes outward surrounding concrete, the concrete cover spalls out. The spalling of concrete cover and the buckling of the reinforcement are taken into account by considering a more brittle behavior (step-

like) of concrete cover compared to concrete core and adopting the stress-strain curve with stress reductions due to buckling for reinforcement steel in compression. The concrete cover spalling is rather brittle in specimens loaded with small eccentricity and becomes more gradual when increasing the eccentricity. In the proposed method the concrete cover spalling has been modeled adopting a descending branch in the stress-strain relationship for external concrete cover fibers with zero stress corresponding to buckling strain of steel reinforcement.

In the case of member wrapped with CFRP the steel bars push internal concrete cover in the inward direction (in the hollow part) when they start buckling and in the numerical model concrete cover spalling has been simulated adopting for internal concrete cover fibers a descending branch in the stress-strain relationship according to Hillerborg (1989) theory with peak stress corresponding to steel buckling (unconfined concrete). Reinforcement stability has been evaluated according to Cosenza and Prota (2006) (Chapter 3.1.4).

The refined methodology developed so far with the selected material models and the assumptions made seems to predict well both the global behavior and the local deformability of the hollow columns.

4.2.1 Constitutive Laws of materials

A reliable stress-strain behavior of concrete is necessary particularly when a member is subjected to combined axial load and bending. The theoretical analyses have been carried out considering five constitutive models for concrete. For the unstrengthened members the Mander model (Mander et al. 1988) and the Model Code 1990 concrete model were adopted combined with the size effect theory after Hillerborg (1989) where the compressive concrete ultimate strain is assumed

to be inversely proportional to the depth of the compression zone. According to this theory, as soon as the stress-strain curve comes into the descending branch, stress localization is expected to occur on a certain band length, so that the shape of this curve is not a material property and may be different for the same material in different positions in a structure. This length can be assumed to be proportional to the depth of the compression zone x , so that it is possible to define an ultimate concrete strain $\varepsilon_u = w_c / 0.8 \cdot x$, where w_c is defined as a formal localized deformation when the stress reaches zero. The confinement of the compression zone is less important in hollow cross sections compared to solid ones. This means that the ductility is reduced and also the ultimate strain should be chosen smaller.

The two concrete models curve were adopted for the ascending branch of the stress-strain curve, while regarding the descending branch, a straight line descending from peak compressive stress to zero at ε_u was adopted (Figure 4.16).

The parameters which are of influence are hence the concrete peak strength (cylindrical compressive strength of 32 MPa estimated according to a pure axial load test on column U0) and corresponding strain (that was assumed equal to 2.2‰ according to Model Code 1990 or 2.0‰), localized deformation band length w_c (that was varied in the analyses between 1 to 1.5 mm) and ultimate concrete strain ε_u that is evaluated iteratively from the neutral axis depth, according to Hillerborg theory.

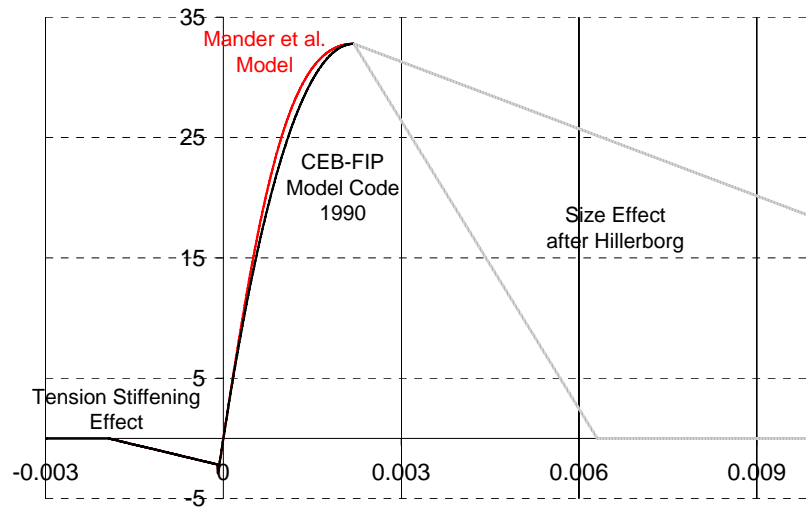


Figure 4.16 – Theoretical concrete constitutive laws ($\alpha=20$; $w_c=1,5\text{mm}$, $\varepsilon_o=2,2\text{‰}$)

Concrete is assumed to crack when it reaches its flexural tensile strength calculated according to Model Code 1990 (that is assumed as 3.86 MPa). The behavior of tensile concrete is linear up to tensile strength and, after concrete cracks, tension stiffening occurs in concrete reinforced with steel bars. Tension stiffening accounts for load transfer mechanism between steel reinforcement and surrounding tensile concrete and is generally represented by a gradual degradation of the concrete tensile stress after cracking. The tensile stress due to tension stiffening effect is assumed to decrease linearly from 70% of the cracking stress, at cracking stress, to zero, at α times the concrete cracking strain.

The enhanced stress-strain relationship accounting for buckling was used for the reinforcing steel (Figure 4.17).

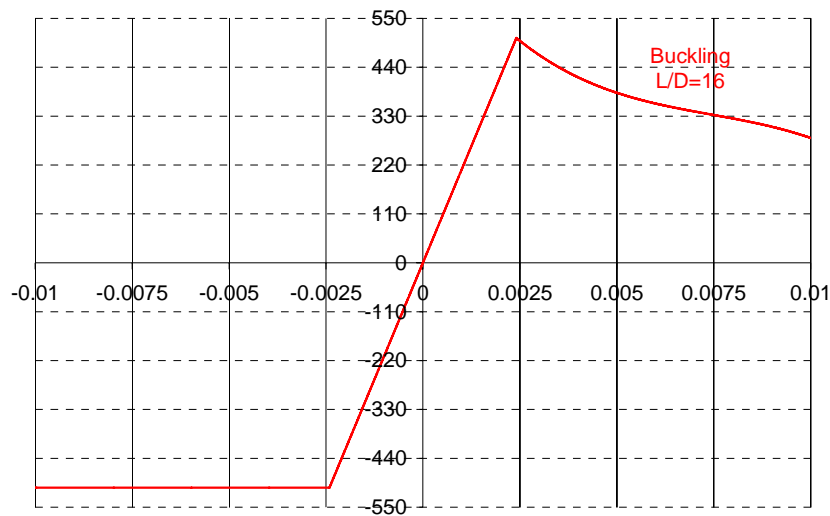


Figure 4.17 – Theoretical reinforcement steel constitutive law

Tests were done on compressed bars with Length/Diameter ratios of 8 and 16 (corresponding to a ties spacing of 80 and 160 mm for a longitudinal bar with diameter of 10 mm). In the case of $L/D=16$, the buckling occurred in the elastic range (Cosenza and Prota 2006), when steel reached strains in the order of 2.5‰, the bar started buckling and gradually lost its load carrying capacity. The main parameters are the tensile strength of 600 MPa, the yield stress of 506MPa (that in compression roughly correspond to buckling stress in the case of $L/D=16$), the modulus of elasticity, and the hardening branch after the yielding plateau.

First Part: walls interaction and confinement

For the strengthened members the steel properties are the same as above whereas the constitutive relationship for compressive concrete is changed. To simulate the effect of the FRP confinement, the interaction of the four walls forming the hollow member has been considered, hence the FRP confinement of the walls have been considered.

Spoelstra-Monti (1999) model and the model recommended by the CNR DT200 Italian Instructions (2004) have been adapted. Spoelstra-Monti model is an evolution of the Mander model, its related stress-strain curve of confined concrete can be regarded as a curve crossing a family of Mander's curves, each one pertaining to the level of confining pressure corresponding to the current lateral strain.

The transverse dilation of the compressive concrete walls stretches the confining device, which along with the other restrained walls applies an inward confining pressure. The effective pressure f_l' is reduced by a reduction factor k_{eff} that is related to the ratio of the effective confinement area to the total area of concrete enclosed by the FRP jacket (Chapter 3.1.2); in the present case is $k_{\text{eff}}=0.69$. For FRP-confined concrete, the ultimate compressive axial strain of concrete is considered to be attained when lateral strain is equal to FRP ultimate strain (in this case is 9‰ equal to 60% of design ultimate strain, according to FRP strain efficiency, Chapter 3.1.2) however, experimental evidence shows that FRP failure did not occur. The confining pressure is provided by an FRP jacket of the same thickness to an equivalent circular column of a diameter D equal to the average (longer) side length ($D \approx 300\text{mm}$ and $f_l' = 6.2\text{MPa}$). In the present case the confined concrete stress becomes about 36 MPa corresponding to a strain of 2.2‰ while the confined concrete peak strength becomes 60 MPa corresponding to an ultimate strain of 9.9‰ according to CNR model.

It is noted that the Spoelstra-Monti model is rather more conservative than CNR. In fig. 4.18 are the constitutive laws of confined concrete according to the adopted models compared to the one of unconfined concrete according to Model Code 1990.

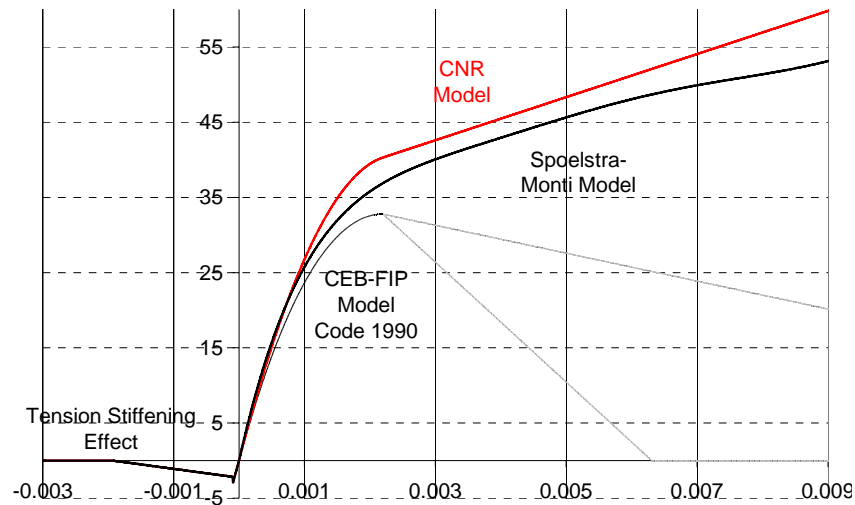


Figure 4.18 – Theoretical confined concrete constitutive laws

Second Part: square hollow section confinement

For the strengthened members the steel properties again are the same as above whereas the constitutive relationship for compressive concrete is derived by the proposed confinement model for hollow circular sections (Chapter 3.3.2). This model is not directly applicable to square hollow RC section in which the concrete is not uniformly confined by the FRP jacket. The commonly accepted approach to deal with confined concrete in noncircular sections is to find an equivalent model in terms of the average axial stress, reflecting the evidence that FRP confinement has a different level of efficiency in a square section than in a circular section in which all the concrete is confined to the same degree. In order to determine the effective confining pressure an equivalent circular column confined by an FRP jacket of the same thickness is considered. In this analysis a circumscribed circle is considered with the same relative wall thickness (in this case $\beta=R_{in}/R_{out}=0.666$).

The shape factor (according to Free Body diagram analysis of a section portion – figure 3.16) is equal to 0.7.

Concrete cover is considered as a softening material and, according to Hillerborg (1989) size effect theory, has a softening behavior after peak concrete strength.

Compared to the two previous adapted models for solid section confinement (as the four lone walls were considered solid), the proposed model has intermediate stress increment at peak unconfined strain and a gradual plastic behavior with stress almost constant, or gradually increasing, after peak.

The mechanical parameters adopted to delineate the confined concrete relationship (figure 4.19) are similar to those used before and adopted in the subsequent F.E.M. analyses (Chapter 5). The initial Elastic modulus is 37 GPa and the initial Poisson Ratio is 0.12.

The behavior of concrete in tension is assumed not to be affected by the confinement.

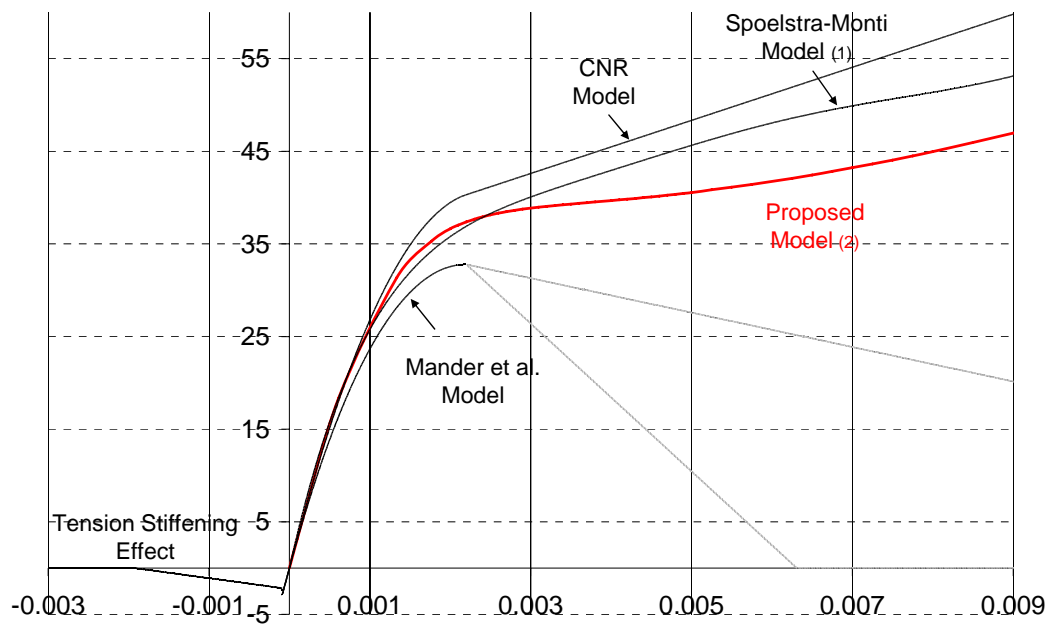


Figure 4.19 – Theoretical confined concrete constitutive law (hollow section)

4.2.2 Strength

Only the Mander model in the following will be considered, because for the modeling of strengthened walls will be adapted the Spoelstra-Monti model, that is an evolution of the Mander model for confined concrete. The Model Code 1990 has been adopted for a code comparison. It is outlined that the model that better fits experimental data is the Mander model, while the Model Code 1990 is slightly more conservative (i.e. P-M interaction diagram Fig.4.20 where for a given P_{max} , small signs correspond to M_I , while bigger ones to M_{II}).

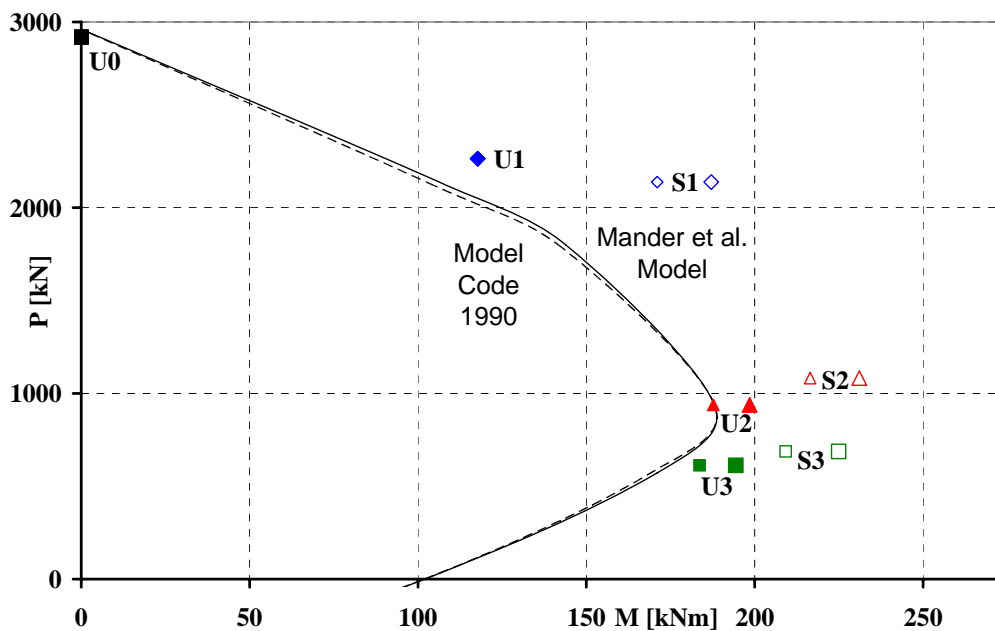


Figure 4.20 – Test results and numerical comparison (unstrengthened) on P-M diagram

The theoretical predictions according to wall interaction and adapted confinement approach will be denoted by (1) mark while predictions according to original hollow section confinement proposed model with (2) .

The proposed algorithm allowed drawing the theoretical P-M interaction

diagram. The comparison of theoretical P-M interaction diagram according to the concrete models and the experimental outcomes is depicted in figure 4.21.

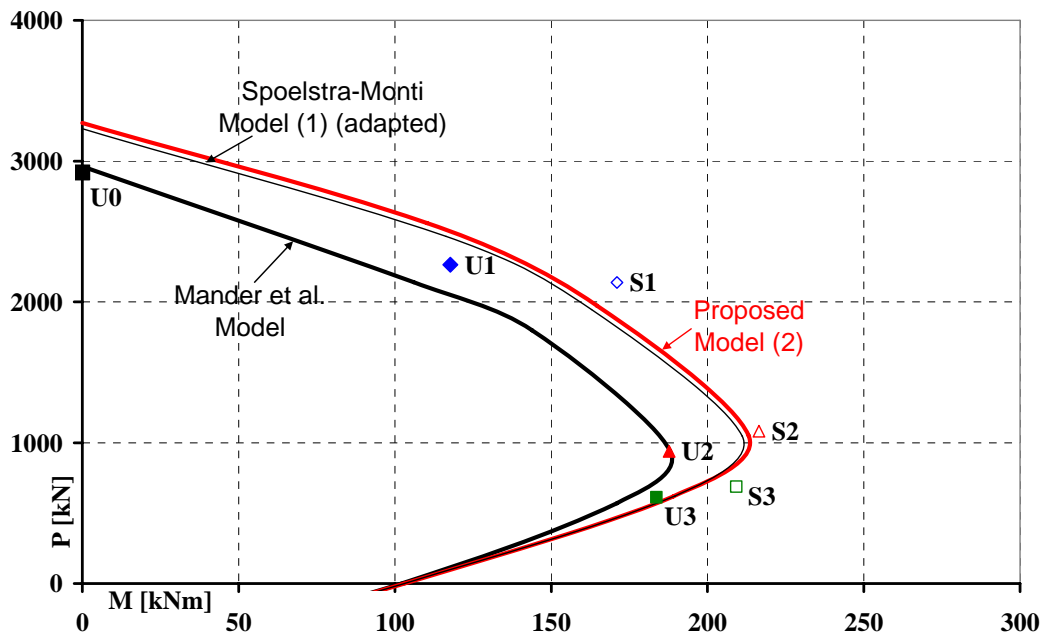


Figure 4.21 – Test results and numerical comparison on P-M diagram

In figure 4.21 experimental outcomes and numerical predictions are compared and P- Δ effects are not taken into account. All the experimental results of specimens were noted to be in good agreement with the theoretical predictions. Compared to the experimental values, the theoretical P-M predictions are on the conservative side (with the only exception of U2).

A non-linear procedure has been also developed to theoretically evaluate ultimate flexural strength $M_{II}^{th} = P_{II}^{th} (e + \delta_{II}^{th})$ of the column taking into account second order effects due to theoretical column deflection δ_{II}^{th} . The mid span deflection depends on curvature (due to the flexural moment M_{II}^{th}). The equilibrium and compatibility conditions are granted for a section subjected to an axial load with an increased eccentricity $e + \delta_{II}^{th}$.

Table 4.6 and 4.7 report theoretical ultimate axial load P^{th} and ultimate flexural capacity of un-strengthened and strengthened, respectively, columns corresponding to the eccentricity e related to each specimen: M^{th} (without accounting for column deflection) and P_{II}^{th} and M_{II}^{th} predictions taking into account P- Δ effects.

Table 4.6– Theoretical ultimate capacities of un-strengthened columns

e (mm)	First Order Analysis			Second Order Analysis		
	$P_{th,U}$ (kN)	$M_{th,U}$ (kNm)	$\delta_{th,U}$ (mm)	$P_{II}^{th,U}$ (kN)	$M_{II}^{th,U}$ (kNm)	$\delta_{II}^{th,U}$ (mm)
0	2919	0	0	2919	0	0
52	2038	106.00	4.24	1988	112.02	4.35
200	942	188.39	10.47	899	189.49	10.88
300	571	171.36	17.31	521	164.88	16.42

Table 4.7– Theoretical ultimate capacities of strengthened columns

e (mm)	First Order Analysis			Second Order Analysis		
	$P_{th,U}$ (kN)	$M_{th,U}$ (kNm)	$\delta_{th,U}$ (mm)	$P_{II}^{th,U}$ (kN)	$M_{II}^{th,U}$ (kNm)	$\delta_{II}^{th,U}$ (mm)
80	1946 ₍₁₎	155.72 ₍₁₎	6.31 ₍₁₎	1883 ₍₁₎	162.83 ₍₁₎	6.48 ₍₁₎
	1973 ₍₂₎	157.81 ₍₂₎	6.82 ₍₂₎	1908 ₍₂₎	165.02 ₍₂₎	6.47 ₍₂₎
200	1045 ₍₁₎	208.91 ₍₁₎	13.29 ₍₁₎	964 ₍₁₎	206.79 ₍₁₎	14.62 ₍₁₎
	1054 ₍₂₎	210.82 ₍₂₎	14.41 ₍₂₎	971 ₍₂₎	208.59 ₍₂₎	14.81 ₍₂₎
300	622 ₍₁₎	186.52 ₍₁₎	33.96 ₍₁₎	496 ₍₁₎	174.08 ₍₁₎	38.03 ₍₁₎
	616 ₍₂₎	184.82 ₍₂₎	27.62 ₍₂₎	537 ₍₂₎	173.07 ₍₂₎	22.35 ₍₂₎

Table 4.8 and 4.9 report experimental comparison of ultimate axial load P^{th} and ultimate flexural capacity of un-strengthened and strengthened, respectively,

columns (without accounting for column deflection) and P_{II}^{th} and M_{II}^{th} predictions taking into account P- Δ effects.

Table 4.8– Experimental Comparison of un-strengthened columns

e (mm)	P_{max} vs. $P_{th,U}$ (%)	P_{max} vs. $P_{th,U}^{II}$ (%)	M_{II} vs. $M_{th,U}^{II}$ (%)	δ vs. $\delta_{th,U}^{II}$ (%)
0	+0.34	+0.34	N.A.	N.A.
52	+11.09	+13.88	N.A.	N.A.
200	-0.32	+4.45	+4.77	+5.79
300	+7.18	+17.47	+18.27	+13.09

Table 4.9– Experimental Comparison of strengthened columns

e (mm)	P_{max} vs. $P_{th,U}$ (%)	P_{max} vs. $P_{th,U}^{II}$ (%)	M_{II} vs. $M_{th,U}^{II}$ (%)	δ vs. $\delta_{th,U}^{II}$ (%)
80	+9.87 ₍₁₎	+13.54 ₍₁₎	+14.77 ₍₁₎	+14.35 ₍₁₎
	+8.36 ₍₂₎	+12.05 ₍₂₎	+13.25 ₍₂₎	+14.53 ₍₂₎
200	+3.54 ₍₁₎	+12.24 ₍₁₎	+11.67 ₍₁₎	-8.69 ₍₁₎
	+2.66 ₍₂₎	+11.43 ₍₂₎	+10.71 ₍₂₎	-9.86 ₍₂₎
300	+12.06 ₍₁₎	+40.52 ₍₁₎	+30.79 ₍₁₎	-30.29 ₍₁₎
	+13.15 ₍₂₎	+29.80 ₍₂₎	+31.55 ₍₂₎	+18.61 ₍₂₎

All the experimental results of unstrengthened specimens were noted to be in good agreement with the theoretical predictions (figure 4.20). Compared to the experimental values, the theoretical P-M predictions are on the conservative side and the scatter is about 10% (with the only exception of U2 test where capacity is overestimated of less than 0.5% by first order analysis). Taking into account column deflection, which increases as curvature increases with growing of eccentricity e , further reduction in predicted capacity is achieved and the theoretical predictions are still on the conservative side with a scatter about 13%,

with the exception of S3 tests.

The strength increment found experimentally in the strengthened columns is rather smaller for the columns loaded with greater eccentricities; such result is confirmed by the theoretical analyses where the strength increment of FRP confined sections with respect to the unstrengthened ones is about 7% in the case of larger eccentricity and 15% in the case of smaller eccentricity (see also P-M diagram in figure 4.21). Compared to the two confined concrete models shown, the CNR model gives strength predictions closer to the experimental outcomes but is only some times on the conservative side and is not able to predict the post peak behavior due to the unrealistic hardening branch after peak.

4.2.3 Ductility

Figures 4.22 to 4.25 show moment-curvature diagrams where comparison of experimental results with theoretical previsions for the U-series and S-Series are reported (no comparison have been made between U1 and S1 specimens because they have a different load eccentricity).

Relevant ($M-\chi$) values corresponding to significant material strains are shown on theoretical curves. In the first linear elastic phase before concrete cracking it is possible to refer to the well known elastic relationship: $\chi = M/EI$, then, after cracking, the effective moment of inertia has to be considered and tension stiffening effects take place. The theoretical moment-curvature relationships proposed were calculated using the axial load value and imposed constant eccentricity without accounting for second order effects.

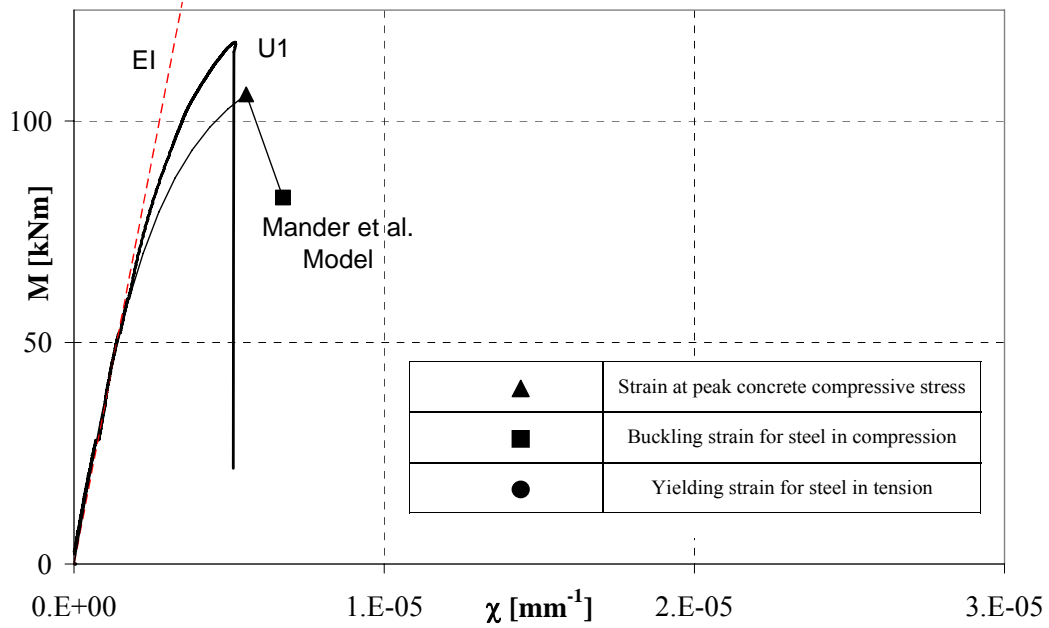


Figure 4.22 – Moment-Curvature Diagram: U1 Theoretical-experimental comparison

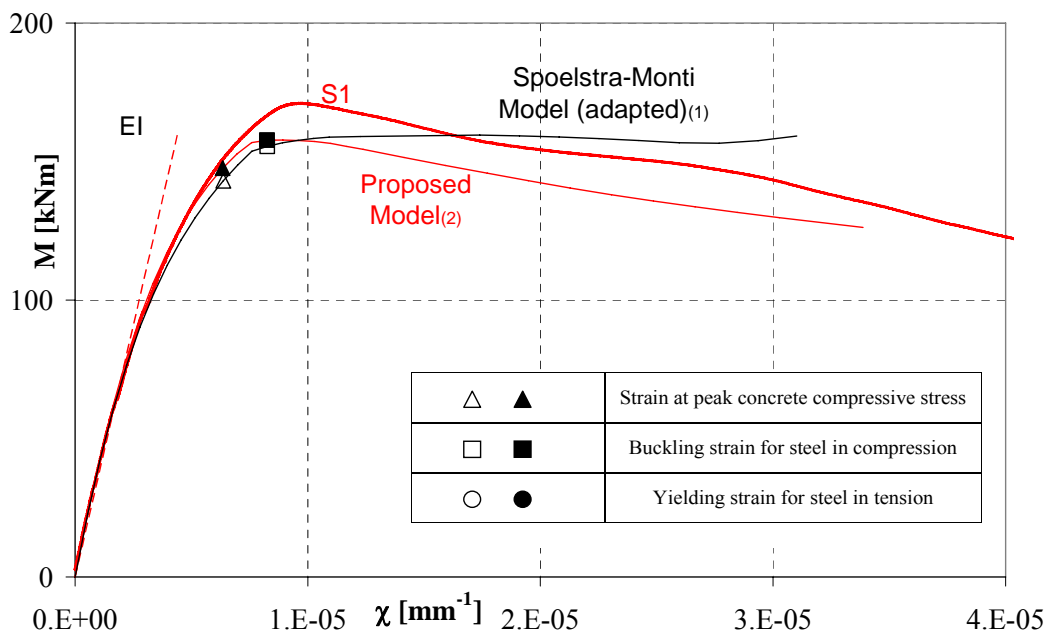


Figure 4.23 – Moment-Curvature Diagram: S1 Theoretical-experimental comparison

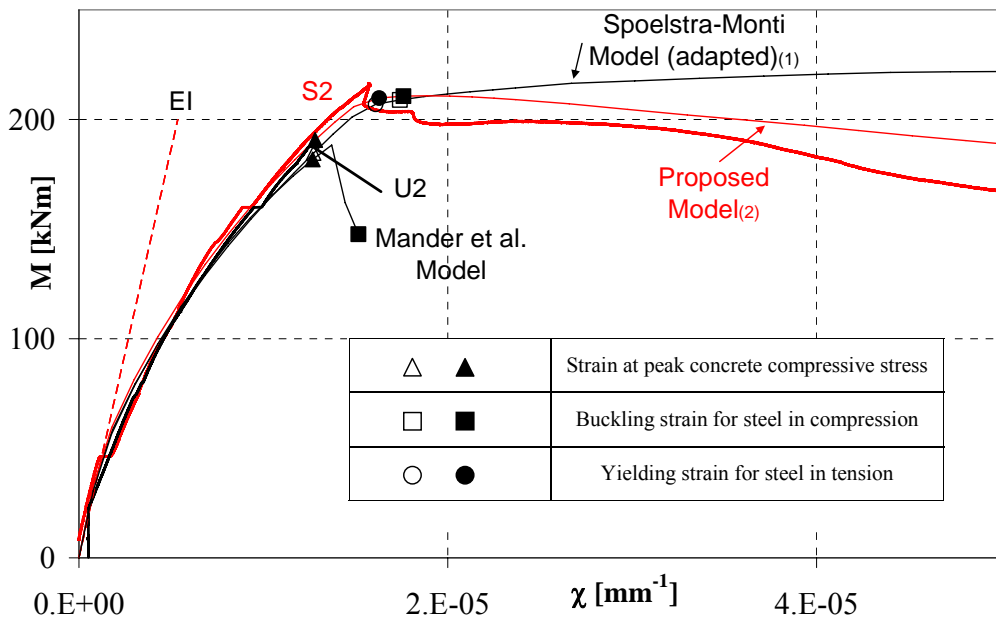


Figure 4.24 – Moment-Curvature Diagram:U2-S2 Theoretical-experimental comparison

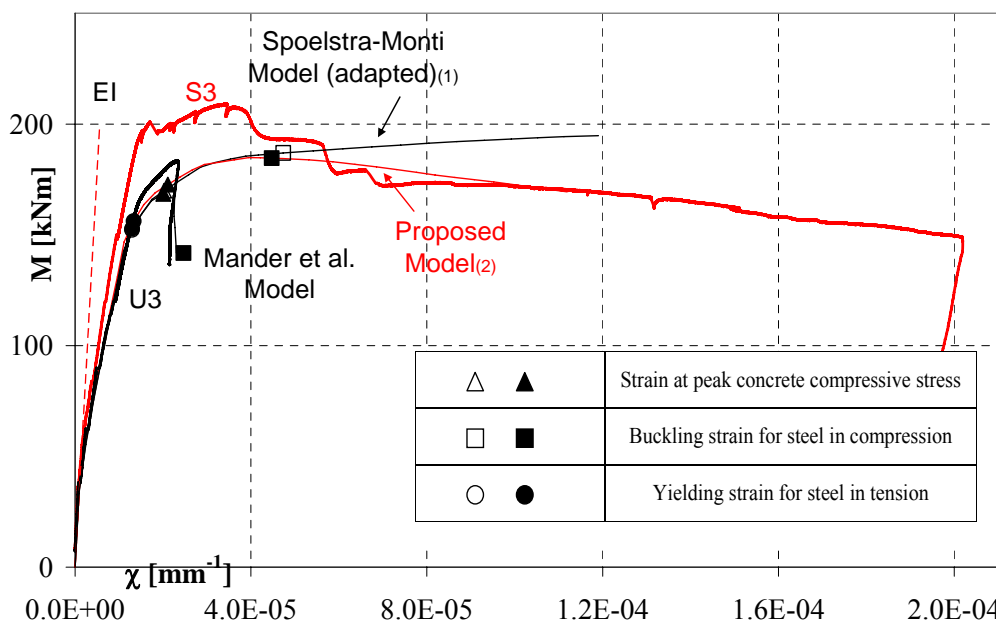


Figure 4.25 – Moment-Curvature Diagram:U3-S3 Theoretical-experimental comparison

It is clearly noticeable a drop in the load-carrying capacity of the section when steel in compression get close to the buckling strain and concrete cover starts spalling.

A curvature ductility measure (curvature ductility μ_χ), that gives information about the shape of the descending branch in moment-curvature relationships, is related (Chapter 4.1.3) to the curvature on the softening branch at 80% of ultimate load, $\chi_{80\%max}$.

Tables 4.10 and 4.11 shows the comparative study of the theoretical curvature, χ_{th} , and specific energy, E_{th} , for un-strengthened and strengthened specimens, respectively.

Table 4.10a – Experimental Theoretical Comparison: Curvature Ductility (un-strengthened.)

e (mm)	M_{th,y} (kNm)	$\chi_{th,y}$ (10^6mm^{-1})	$\chi_{th,80\%max}$ (10^6mm^{-1})	$\mu_{th,\chi}$ (-)	μ_χ exp. vs. th.(%)
52	N.A.	5.55	5.55	1	0.00
200	N.A.	13.71	13.71	1	0.00
300	148.52	11.61	22.67	1.95	-21.13

Table 4.10b – Experimental Theoretical Comparison: Curvature Ductility (strengthened)

e (mm)	M_{th,y} (kNm)	$\chi_{th,y}$ (10^6mm^{-1})	$\chi_{th,80\%max}$ (10^6mm^{-1})	$\mu_{th,\chi}$ (-)	μ_χ exp. vs. th.(%)
80	153.72 ₍₁₎	7.60 ₍₁₎	N.A. ₍₁₎	N.A. ₍₁₎	N.A. ₍₁₎
	156.83 ₍₂₎	7.59 ₍₂₎	33.87 ₍₂₎	4.46 ₍₂₎	-4.98 ₍₂₎
200	203.89 ₍₁₎	15.17 ₍₁₎	N.A. ₍₁₎	N.A. ₍₁₎	N.A. ₍₁₎
	206.50 ₍₂₎	15.03 ₍₂₎	75.78 ₍₂₎	5.04 ₍₂₎	-40.08 ₍₂₎
300	148.01 ₍₁₎	11.63 ₍₁₎	N.A. ₍₁₎	N.A. ₍₁₎	N.A. ₍₁₎
	150.25 ₍₂₎	11.52 ₍₂₎	103.10 ₍₂₎	8.95 ₍₂₎	-7.59 ₍₂₎

The curvature ductility index is not available in the case of analyses carried out considering adapted Spoelstra and Monti confined concrete model because the post peak behavior is characterized by an inaccurate hardening branch and it was not possible to evaluate the curvature and corresponding specific energy at 80% of peak load on the softening branch.

The increment of ductility supplied by confinement can be also appreciated comparing the values of the specific energies obtained (Table 4.11) and remarkable increases of dissipating capabilities for strengthened columns are found.

Table 4.11a – Experimental Theoretical Comparison: Specific Energy (un-strengthened)

e (mm)	$M_{th,I}$ (kNm)	$E_{th,max}$ ($10^6 kNm \cdot mm^{-1}$)	$E_{th,80\%max}$ ($10^6 kNm \cdot mm^{-1}$)	$E_{th,80\%max}/E_{th,max}$ (-)	E_{max} vs. $E_{th,max}$ (%)
52	107.76	393	393	1	+1.27
200	188.39	1657	1657	1	-11.77
300	171.36	2824	2824	1	+19.51

Table 4.11b – Experimental Theoretical Comparison: Specific Energy (strengthened)

e (mm)	M_I (kNm)	E_{max} ($10^6 kNm \cdot mm^{-1}$)	$E_{80\%max}$ ($10^6 kNm \cdot mm^{-1}$)	$E_{80\%max}/E_{max}$ (-)	$E_{80\%max}/E_{max}$ exp. vs. th.(%)
80	155.72 ₍₁₎	854 ₍₁₎	N.A. ₍₁₎	N.A. ₍₁₎	N.A. ₍₁₎
	157.81 ₍₂₎	988 ₍₂₎	4512 ₍₂₎	4.57 ₍₂₎	-11.38 ₍₂₎
200	208.91 ₍₁₎	2416 ₍₁₎	N.A. ₍₁₎	N.A. ₍₁₎	N.A. ₍₁₎
	210.82 ₍₂₎	2788 ₍₂₎	13042 ₍₂₎	4.68 ₍₂₎	-20.73 ₍₂₎
300	186.52 ₍₁₎	4473 ₍₁₎	N.A. ₍₁₎	N.A. ₍₁₎	N.A. ₍₁₎
	184.82 ₍₂₎	3733 ₍₂₎	18176 ₍₂₎	4.87 ₍₂₎	-15.40 ₍₂₎

The increment of ductility supplied by confinement, remarked in the experimental discussion, has been also appreciated in the theoretical predictions (i.e. comparing the values of the curvature ductility index and specific energies obtained).

The experimental results of un-strengthened specimens were noted to be close to the theoretical predictions with a higher scatter in the case of S2 specimen and this can be due to the formation of the plastic hinge outside the instrumented portion of the tested element (lower ductility was found experimentally compared to S1). Ductility is increased by the reduction of the axial load. When increasing the eccentricity (that is axial load reduction) it is observed that the neutral axis moves towards the inside of the section and some ductility was attained due to tensile property of the steel. The strains in the internal concrete cover grow with a smaller gradient and the brittle effects of concrete cover spalling regress.

The maximum ductility, μ_{χ} , and specific energy ratio is recorded for the column S3. For instance, (Table 4.10b) when $\mu_{th,\chi}$ is 8.95, for the same eccentricity the dissipated specific energy, $E_{th,80\%max}$, of S3 specimen computed on the softening branch at 80% of ultimate load is more than 7 times the dissipated specific energy at peak, $E_{th,max}$, of the brittle U3 specimen (Table 4.11). Specific energy increment $E_{th,80\%max}/E_{th,max}$, in S series' columns, is bigger than 4.5 emphasizing the meaningful increase of ductility of the confined structural elements.

4.2.4 Longitudinal Strains

Figures 4.26 to 4.31 show a comparison between theoretical (based only on proposed confinement model₍₂₎) and experimental strain development. The numerical model can predict reasonably well the strain evolution. The ascending

branch is very well predicted, and curve drop was generally attained (in the numerical analysis the global response deteriorate when concrete cover starts spalling and compressed steel reinforcement bars get close to the buckling strain). The branch after peak is better predicted adopting stress-strain curves for confined concrete with descending branch after peak (i.e. proposed model prediction).

In general, the CFRP wrapping in S columns has delayed the longitudinal steel bars buckling that caused the brittle behavior in the reference U columns and reduced the strains compared to those expected theoretically. For example, in S3 column the concrete reached strains up to 25‰.

In accordance with existing design practice, usually the FRP confinement effect is evaluated according to an effective predetermined FRP strain, set in order to evaluate confined concrete strength increment: some codes refer to a specified percentage of the FRP design strength; others refer to a particular fixed value to avoid excessive damage to the confined concrete (i.e. compromising shear strength, etc). Theoretical proposed confinement model₍₂₎ is able to trace the strain evolution and, according to the multiaxial failure criterion considering axial, circumferential and radial stresses described in Chapter 3.3.2, it is possible to simulate the experimental evidence of FRP failure for stresses lower than straight coupon test strength, the usual specified strength (FRP strain efficiency - see Chapter 3.1.2).

The adapted Spoelstra and Monti model predicts an ultimate concrete compressive strain of less than 10‰ and adopted FRP ultimate strain is 9‰.

In the proposed confinement model, instead, maximum predicted concrete strain is 0.15% in S3 specimen corresponding to an FRP strain of about 6.79‰ while a maximum value of 5.24‰ is recorded in the S1 specimen at 80% of peak load.

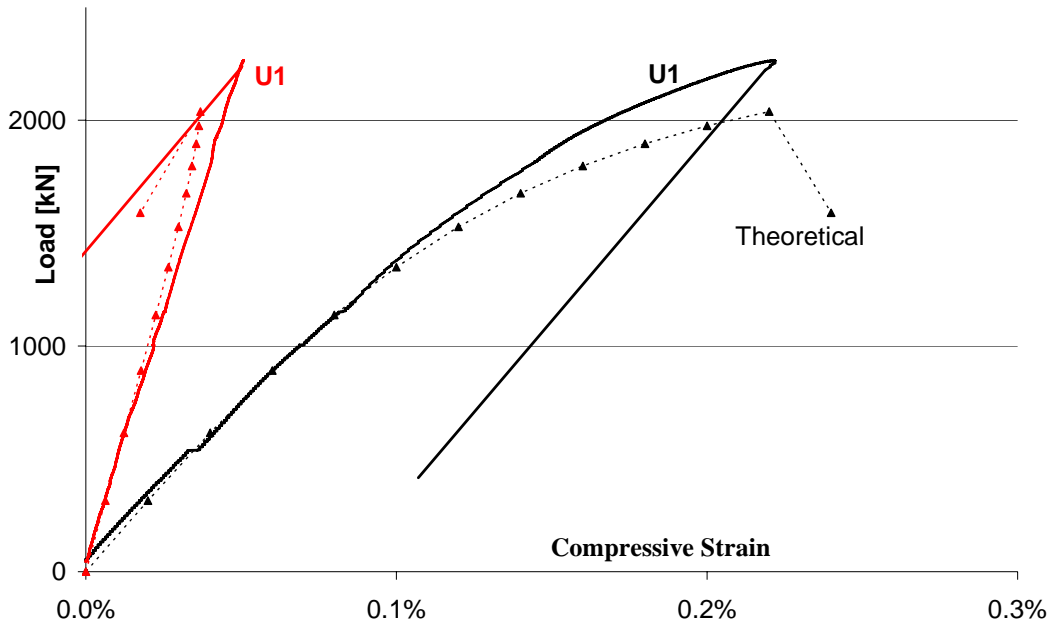


Figure 4.26 – Comparison: Experimental U1 strains vs. Load and theoretical $e=52mm$

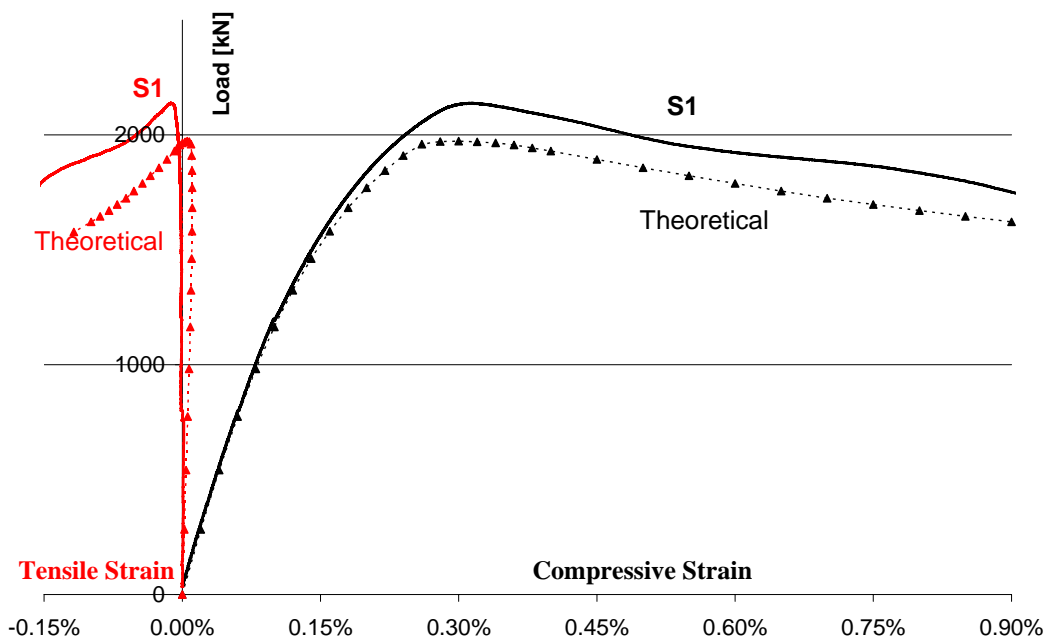


Figure 4.27 – Comparison: Experimental S1 strains vs. Load and theoretical $(2) e=80mm$

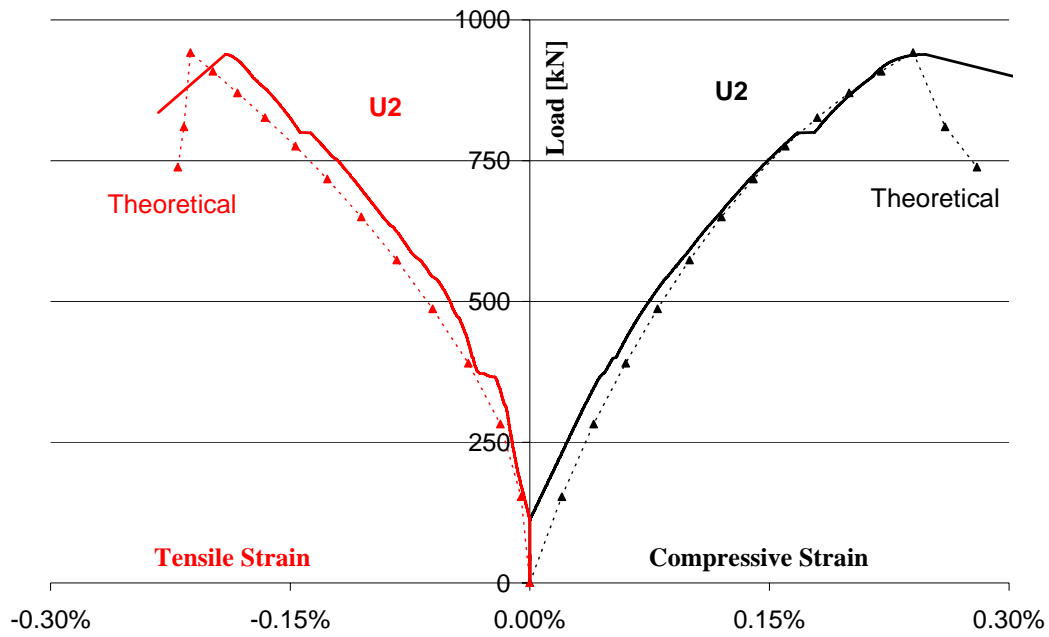


Figure 4.28 – Comparison: Experimental U2 strains vs. Load and theoretical $e=200\text{mm}$

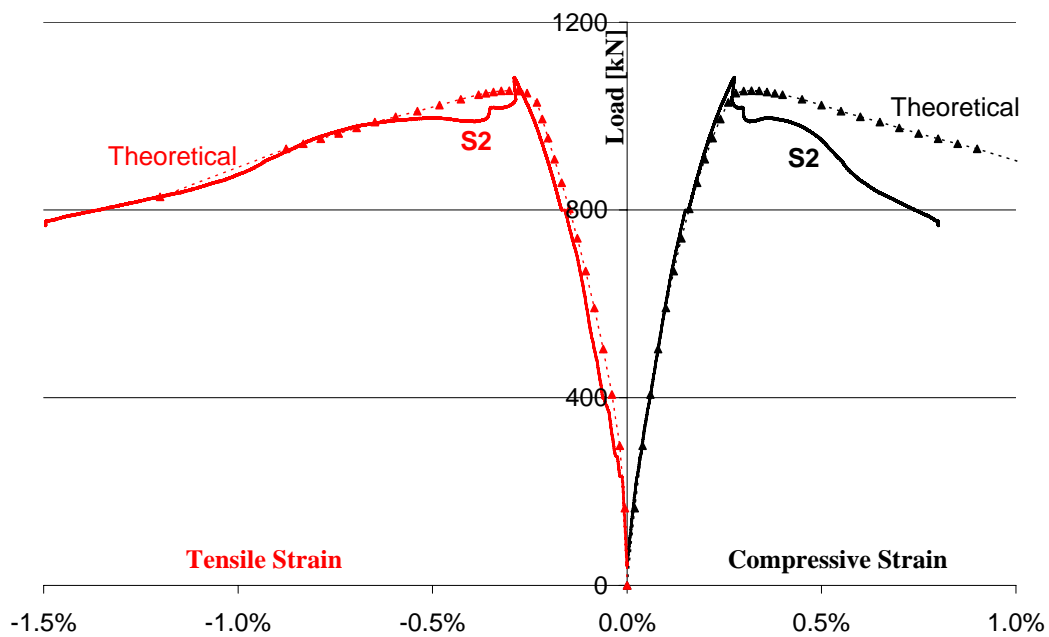


Figure 4.29 – Comparison: Experimental S2 strains vs. Load and theoretical $(2) e=200\text{mm}$

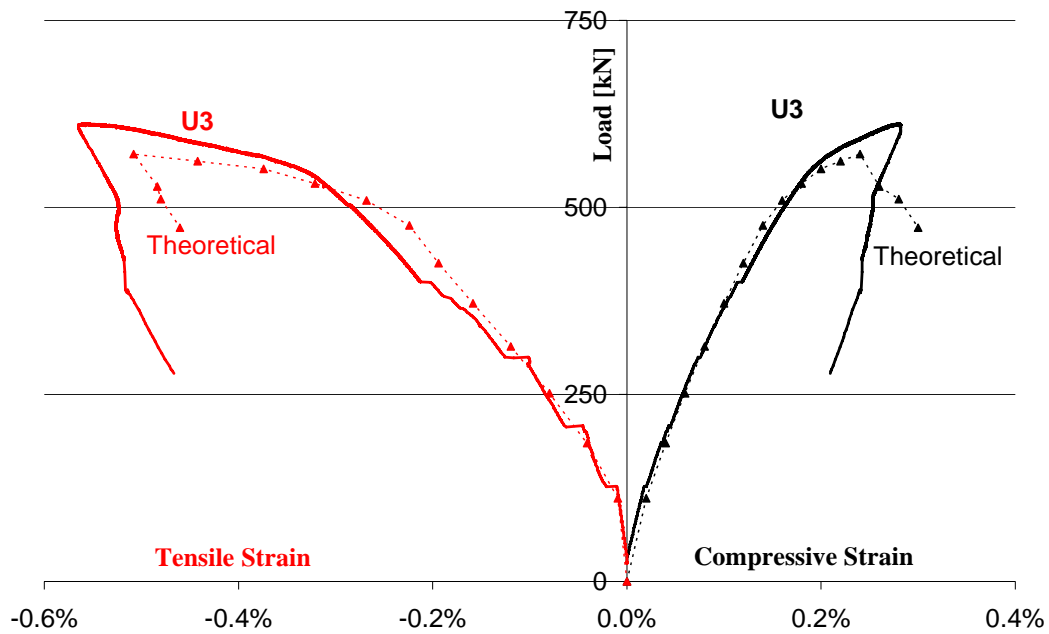


Figure 4.30 – Comparison: Experimental U3 strains vs. Load and theoretical $e=300\text{mm}$

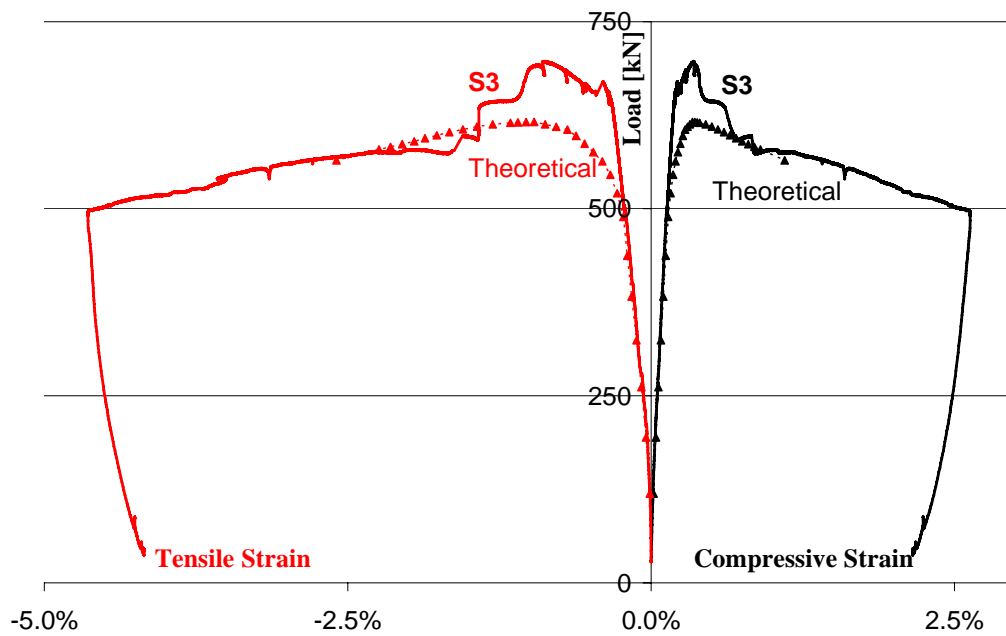


Figure 4.31 – Comparison: Experimental S3 strains vs. Load and theoretical $(2) e=300\text{mm}$

In table 4.12 is the experimental theoretical comparison of concrete strains at peak and at 80% of peak load on the softening branch. The model is able to predict quite well this deformability aspect and a clear trend is found: concrete strains both at peak and on softening branch at 80% of peak load increases when eccentricity increases (it is not confirmed by S2 experimental test for the cited effect of plastic hinge formed far from the instrumented portion of the column). This fact is due to the brittle failure mechanisms prevailing when higher level of axial load is applied.

Table 4.12 – Experimental Theoretical Comparison: Concrete axial Strains

Specimen Code	e (mm)	ϵ_{\max} (‰)	$\epsilon_{80\% \max}$ (‰)	$\epsilon_{th, \max}$ (‰)	$\epsilon_{th, 80\% \max}$ (‰)
U1	52	2.2	2.2	2.2	2.4
U2	200	2.6	2.6	2.4	2.8
U3	300	2.8	2.8	2.4	3.0
S1	80	3.1	9.5	3.0	10.0
S2	200	2.8	5.9	3.2	13.0
S3	300	3.5	15.4	3.4	15.0

Confinement did not change actual failure mode (steel reinforcement compressive bars buckling and concrete cover spalling), but it was able to delay bars buckling and to let compressive concrete strains attain higher values, thus resulting in higher load carrying capacity of the column and ductility. The increase in confined concrete strength turns into load carrying capacity increase mainly in the columns loaded with small eccentricity (see figure 3.18 where it is clear that close to pure bending load the effect of concrete strength enhancement - i.e. due to confinement - is insignificant because failure swaps to tension side).

However in small loading eccentricity cases, concrete ductility and strains are increased significantly thus resulting in ductility improvements. At lower levels of axial load also the brittle effect of reinforcement buckling is less noticeable.

4.2.5 FRP Strains

The proposed model is able to trace the evolution of longitudinal (parallel to fibers) stress and strain into FRP confining wraps. Theoretical values have been compared with experimental strain gauges measurements at mid-span of the compressed wall. The CFRP effectiveness can be checked by strain rate and strain thresholds. In table 4.13 strain data for mid span strain gauges at peak load, ε_f , and on the softening branch at 80% of ultimate load, $\varepsilon_{f,80\%}$, both mean experimental data and theoretical predictions are compared.

Table 4.13– Experimental Theoretical Comparison: FRP Strain

Strain Gauge	S1		S2		S3	
	ε_f [‰]	$\varepsilon_{f,80\%}$ [‰]	ε_f [‰]	$\varepsilon_{f,80\%}$ [‰]	ε_f [‰]	$\varepsilon_{f,80\%}$ [‰]
Exp. Mean	0.938	4.354	0.440	0.414	0.608	3.560
Theor. ₍₂₎	0.688	3.709	0.749	5.485	0.810	6.790

The failure of the FRP wraps was never attained (maximum predicted strain is less than 7‰) as confirmed by the experimental evidence.

FRP strains are relatively low, but the benefits in the overall performances are evident also at peak load where the wraps are able to delay the brittle mechanism even if the FRP strains are much smaller than 1‰.

In the case of FRP strains, although the maximum effect of confinement in terms of strength takes place in the columns loaded with smaller eccentricity, the

higher strains are predicted by the proposed model in the columns loaded with higher eccentricity, even though the strength increment is smaller. The high ductility enhancement in those columns is due to the higher values of compressive strains that concrete attains prior to fail, engaging and loading the FRP wraps.

A definite trend in the experimental theoretical comparison is not delineated because the already described inconsistent behavior of S2 test and the formation of a pronounced bulge in the FRP wrapping just below strain gauges due to S3 column remarkable shortening blur the experimental deductions.

In Figure 4.32, experimental FRP strain data in the middle of the compressed wall are compared with theoretical predictions throughout the entire load history for specimen S1. Good agreement is found both on the load path and the ultimate value.

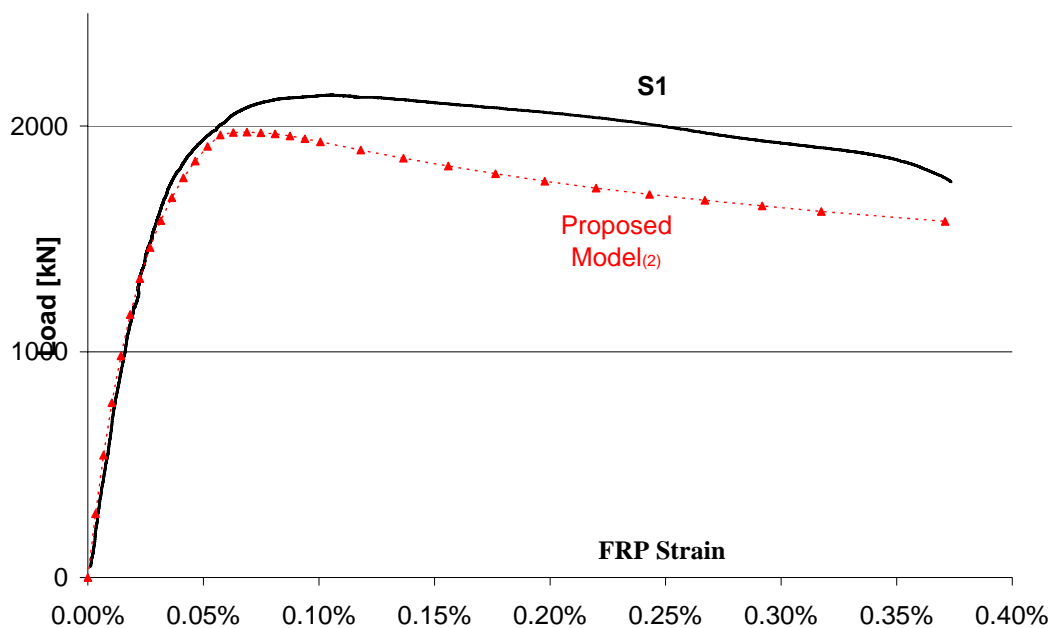


Figure 4.32 – Comparison: Experimental S1 FRP strains vs. Load and theoretical₍₂₎

4.2.6 Theoretical Displacement Assessment

Figures 4.33 and 4.34 show the experimental comparisons with theoretical load deflection curves; dashed lines refer to first order analysis and second order analysis (including the $P-\Delta$ effect). The analytical model underestimates column deflections. More accurate theoretical deflections can be predicted if a non-linear distribution of curvature is considered instead of a constant one, as effective axial load eccentricity vary along the hollow and solid portions of the column. Bars' buckling is especially noticeable in small eccentrically loaded column, while tension stiffening in bigger eccentricity loads.

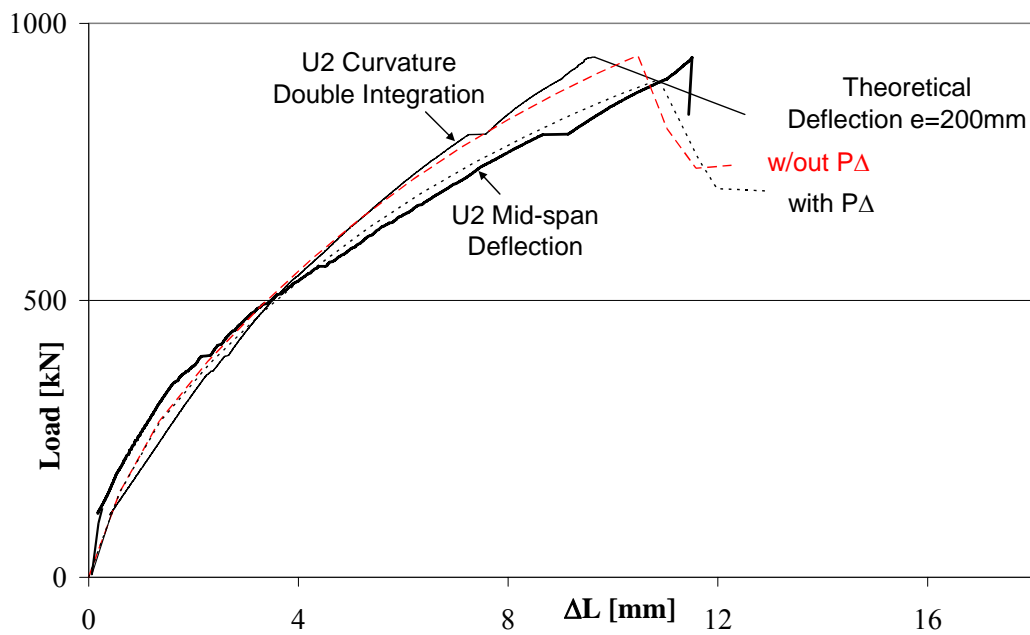


Figure 4.33 – U2 Restraints Validation: mid-span deflection, average curvature double integration and theoretical comparison₍₂₎

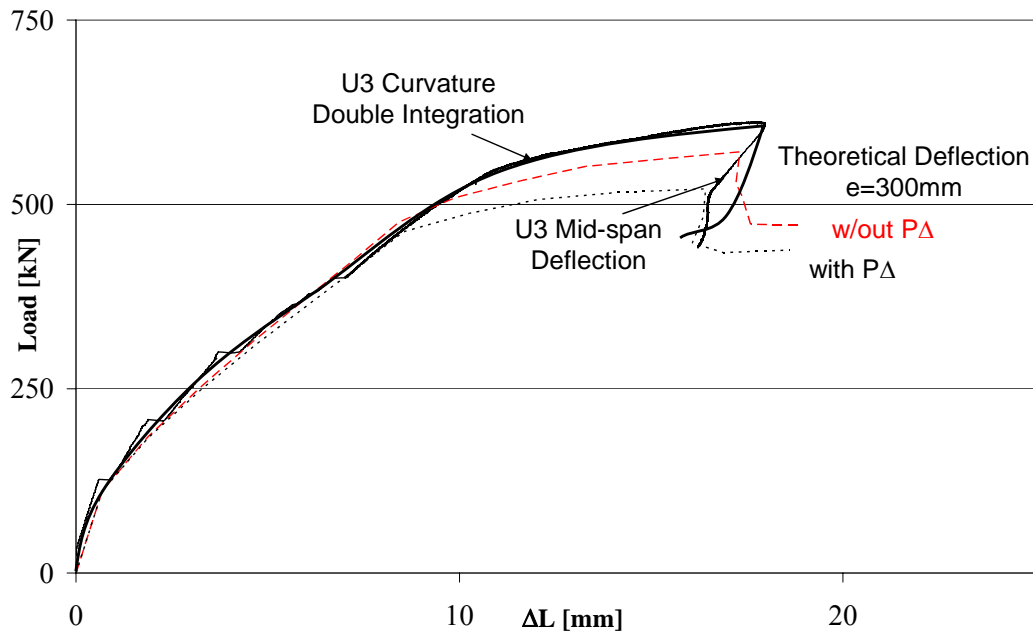


Figure 4.34 – U3 Restraints Validation: mid-span deflection, average curvature double integration and theoretical comparison₍₂₎

4.2.7 Effect of Constitutive Models

The models adopted can predict curvature, neutral axis depth and strain development in the case of hollow cross sectional members. The concrete main parameters are compressive peak strain, localized deformation w_c length and parameter α related to ultimate strain for tension stiffening effect corresponding to zero stress.

The analyses have underlined that the first two parameters affecting compressive behavior of concrete are relevant for the smaller eccentricities, where the concrete behavior is dominant. These parameters affect only the yielding point in the case of $e=300\text{mm}$ and, for bigger values of peak strain and w_c , the ultimate predicted moment increases. On the contrary the tension stiffening effect is more

relevant in the case of bending and high eccentricities. Increasing the parameter α , the shape of the ascending branch changes and the transition from un-cracked state to cracked one is softer. The best fitting value for this parameter is $\alpha = 20$ according to experimental data.

Softening in material constitutive law leads to softening behavior in the section and in the structural element. In a section without rebar buckling, only concrete has a softening behavior: thus moment-curvature relationship softens in presence of high axial compression force only. If steel has a softening behavior due to buckling, the response of the section becomes softening for any value of axial force too.

The Mander et al. model compared with the adapted Spoelstra and Monti₍₁₎ and the model proposed₍₂₎ by the author accounting for the confinement of a hollow monolithic section have been considered in the previous comparisons. In the confined concrete models great influence has the evaluation of FRP reinforcement ratio and the reduction factor k_{eff} . Both models₍₁₎ are calibrated for solid circular cross sections and have been extended and adapted to the case of those square hollow considering walls interaction and confinement. It is outlined that the model that better fits experimental data are the Mander and CNR models, while the Model Code 1990 and Spoelstra-Monti models are slightly more conservative.

The Spoelstra and Monti model has been adapted to account for the confinement of a hollow section divided into four connecting walls. The effect of confinement is overestimated in the post-peak branch where in reality the presence of the internal void reduces the efficiency of the confinement exerted by the FRP wraps. This model has been adapted and can be successfully used to predict essentially the strength of the column since it presents an unrealistic hardening behavior after peak. The model proposed by CNR DT200 includes again an unrealistic hardening behavior, but gives strength predictions closer to

the experimental values. Both these models are not able to simulate reasonably the post peak behavior of hollow core sections.

Compared to these two confinement model₍₁₎, adapted to simulate the behavior of hollow square columns by considering the effect of confinement of a single wall, the proposed confinement model, denoted with subscript ₍₂₎, gives a confined concrete strength, corresponding to the peak unconfined strain, in-between the previous ones. The main difference is in the subsequent branch, where an almost constant plastic behavior is predicted instead of a hardening branch, common in highly confined solid concrete sections.

The proposed confinement model predicts quite well the behavior of hollow section confinement, in particular the strength increment and the remarkable ductility enhancement. The proposed model predictions usually underestimate the experimental outcomes with a scatter in the order of less than ten percent. The effect of confinement, on the contrary, is reliably evaluated when theoretical predictions for unstrengthened and corresponding strengthened elements are considered (the same strength increments and curvature ductility increments as experimentally found in performed tests are predicted).

The proposed confinement model, coupled with the proposed computation algorithm is able to predict the fundamentals of the behavior of hollow members confined with FRP both in terms of strength and ductility giving a clear picture of the mechanisms affecting the response of this kind of element. The model is able to trace the occurrence of the brittle mechanisms, namely concrete cover spalling and reinforcement buckling, the evolution of stress and strains in the confinement wraps allowing to evaluate at each load step the multiaxial state of stress and the failure of the external reinforcement also accounting for the potential initial disengagement of the wraps (as seen when the confining device has a Poisson ratio higher than the concrete's initial Poisson ratio). The main output of the proposed model is also the assessment of the member deformability in terms of

both curvature and displacement ductility.

4.3 Chapter References

AASHTO, (2002): “Standard Specifications for Highway Bridges”, 17th Edition, Published by the *American Association of State Highway and Transportation Officials*, Washington D.C.

CEB-FIP Model Code 1990, Design Code. *Comité Euro-International du Béton*, Lausanne, Switzerland, Thomas Telford.

CNR-DT 200, 2004, “Guide for the Design and Construction of Externally Bonded FRP Systems for Strengthening Existing Structures, Published by *National Research Council*, Roma, Italy.

Cosenza E., Prota A. (2006). Experimental behavior and numerical modeling of smooth steel bars under compression. *Journal of Earthquake Engineering*, Vol. 10, n. 3, pp. 313-329.

Hillerborg A. (1989). The compression stress-strain curve for design of reinforced concrete beams. *Fracture Mechanics: Application to Concrete*, ACI SP-118:281-294.

Mander JB, Priestley MJN and Park R. (1988). Theoretical stress-strain model for confined concrete. *ASCE Journal of Structural Engineering*, 114(8):1804-1826.

Prota A., Manfredi G., Cosenza E. (2006). Ultimate behavior of axially loaded RC wall-like columns confined with GFRP. *Composites: pt. B, ELSEVIER*, vol. 37, pp. 670-678.

Spoelstra MR, Monti G. (1999). FRP-confined concrete model. *ASCE Journal of Composites for Construction*, 3(3):143-150.

Chapter 5

Finite Elements Non Linear Modeling of Hollow cross section RC Piers and FRP confinement effects

In this Chapter is presented a Finite Elements Method (F.E.M.) modeling of the tested specimens both strengthened and unstrengthened. The methodology proposed in previous Chapters has been also validated with the F.E.M. in terms of both global and local deformability. The nonlinear behavior of concrete in tension (cracking) and in compression and the effect of FRP wrapping have been modeled by means of the commercial code TNO DIANA v. 9.1.

The F.E.M. was originated from the needs for solving complex elasticity, structural analysis problems in civil engineering and aeronautical engineering. It is a numerical method for calculating approximate stresses and deformations in complex geometrical structures.

In its application, the structure is divided into so called "finite elements" representing a geometrically similar model consisting of multiple, linked, simplified representations of discrete regions connected through nodes. Equations of equilibrium, in conjunction with applicable physical considerations such as compatibility and constitutive relations, are applied to each element, and a system of simultaneous equations is constructed. The method is used for finding approximate solutions of differential equations governing the structural problem.

A detailed model of the tested specimens has been built and available models for concrete, steel and elastic reinforcement have been adopted. The effect

of concrete cover spalling and bars buckling, crucial aspects of the previously proposed refined methodology, are not considered at date in the F.E.M. analysis. This fact leads to an overestimation of the post peak capacity of the hollow sections (in terms of both strength and ductility) and can be seen as a measure of the performance loss due to reinforcement buckling and concrete cover spalling if compared to numerical predictions according to the refined methodology proposed. A good agreement of the numerical predictions on the ascending (pre peak) branch was found between F.E.M. model and refined proposed method, until brittle concrete cover spalling and steel reinforcement buckling take place. The F.E.M. analysis allowed also tracing the crack pattern evolution in the tested specimens and the FRP jacket strain development.

A F.E.M. analysis of the tested specimens have been performed simulating in great detail concrete nonlinearities in tension (cracking) and compression, steel reinforcement yielding, elastic FRP wrapping, load applying devices, etc. In spite of that, numerical outcomes clearly show that to predict hollow column behavior is crucial to consider these two brittle mechanisms acting together: concrete cover spalling and steel reinforcement buckling. However good agreement on the ascending (pre peak) branch between F.E.M., proposed method predictions and experimental evidences and also in the post peak between proposed method predictions and experimental outcomes, validate the refined proposed methodology.

5.1 Finite Element Non Linear Modeling of RC members

The non linear modeling of the tested specimens has been performed with commercial code TNO DIANA v 9.1. A very brief description of the peculiarities of these analyses involving F.E.M. theory is discussed (de Witte and Kikstra,

2005). DIANA (DISplacement ANALyzer) is a multi-purpose finite element program (three-dimensional and nonlinear) with extensive material, element and procedure libraries based on advanced techniques. Based on the displacement method, it has been under development at TNO since 1972.

DIANA offers a variety of elements such as solids and special elements to model embedded reinforcement in concrete structures. To model these reinforcements DIANA has a built-in preprocessor in which reinforcement can be defined globally. For physical nonlinear analyses various material models are available including plasticity and cracking,

5.1.1 Solid Elements

Solid elements are general purpose elements and have been adopted to model the concrete member. The dimension of an element in three axial directions X, Y and Z are of the same order of magnitude.

The basic variables in the nodes of solid elements are the translations u_x , u_y , and u_z in the local element directions

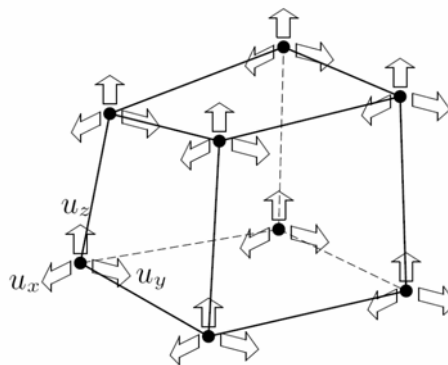


Figure 5.1 – Displacements in Solid Elements

The displacements in the nodes yield the deformations du_x , du_y and du_z of an infinitesimal part dx dy dz of the element. From these deformations, DIANA derives the strains (Figure 5.2).

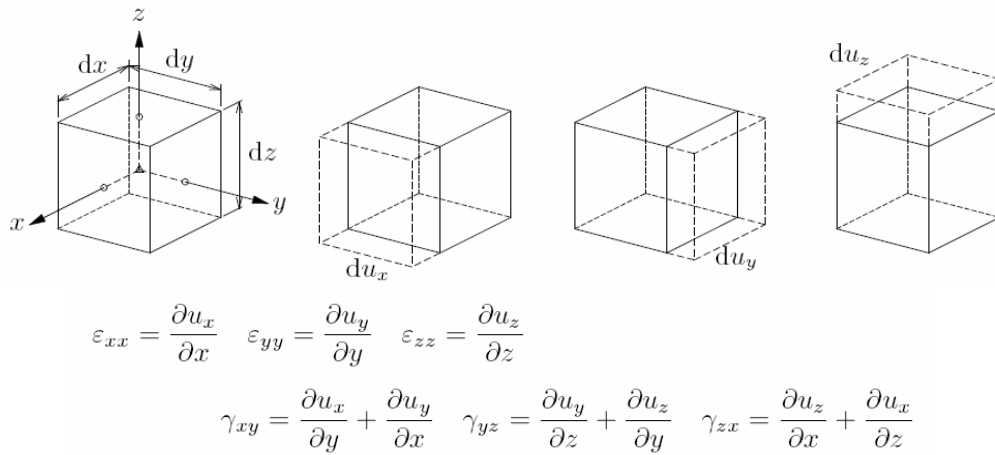


Figure 5.2 – Deformations in Solid Elements

These strains are derived for all integration points and are extrapolated to the nodes. The sign convention for strains is that an elongation yields a positive strain. From the strains DIANA derives the stresses in the integration points. Figure 5.3 shows these stresses on a unit cube in their positive direction. Note that tension stresses are positive.

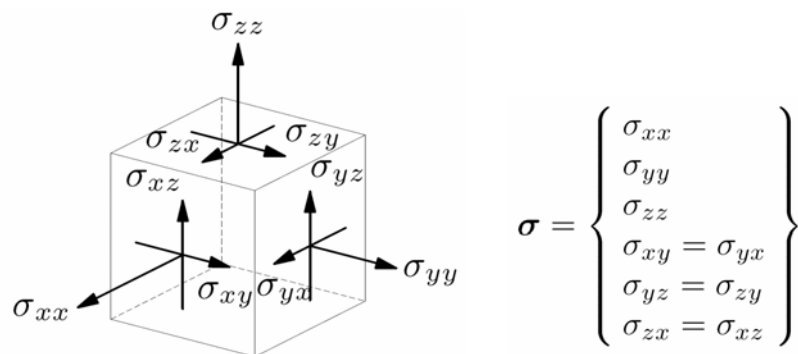


Figure 5.3 – Stresses in Solid Elements

DIANA calculates the generalized stresses for solid bricks in requested points from the stresses in the integration points.

The CHX60 element (Figure 5.4) is a twenty-node isoparametric solid brick element. It is based on quadratic interpolation and Gauss integration. The polynomials for the translations u_x , u_y , u_z can be expressed as

$$\begin{aligned} u_i(\xi, \eta, \zeta) = & a_0 + a_1\xi + a_2\eta + a_3\zeta + a_4\xi\eta + a_5\eta\zeta \\ & + a_6\xi\zeta + a_7\xi^2 + a_8\eta^2 + a_9\zeta^2 + a_{10}\xi\eta\zeta + a_{11}\xi^2\eta \\ & + a_{12}\xi^2\zeta + a_{13}\xi\eta^2 + a_{14}\xi\zeta^2 + a_{15}\eta^2\zeta + a_{16}\eta\zeta^2 \\ & + a_{17}\xi^2\eta\zeta + a_{18}\xi\eta^2\zeta + a_{19}\xi\eta\zeta^2 \end{aligned}$$

Typically, a rectangular brick element approximates the following strain and stress distribution over the element volume. The strain ε_{xx} and stress σ_{xx} vary linearly in x direction and quadratically in y and z direction. The strain ε_{yy} and stress σ_{yy} vary linearly in y direction and quadratically in x and z direction. The strain ε_{zz} and stress σ_{zz} vary linearly in z direction and quadratically in x and y direction.

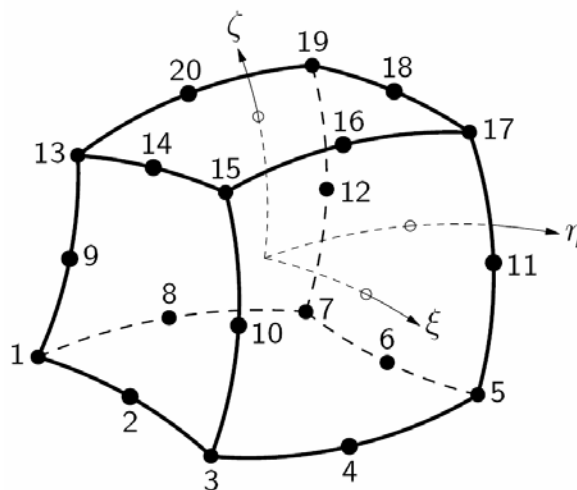


Figure 5.4 – Solid Brick Element CHX60: 20 nodes

5.1.2 Concrete Model

The Maekawa concrete model in DIANA combines a multi-axial damage plasticity model for the effect of crushing in the compressive regime with a crack model based on total strain for the tensile regime.

The damage plasticity model has been developed by the research group of professor Maekawa at the Tokyo University. The crack model is directly related to the Total Strain crack models in Diana. The model also describes hysteresis in tensile and compressive unloading–reloading loops according to the experiences of the research group. Total Strain models describe the tensile and compressive behavior of a material with one stress–strain relationship. These models are very well suited for Serviceability Limit State (SLS) and Ultimate Limit State (ULS) analyses which are predominantly governed by cracking or crushing of the material.

The attractive points of the Maekawa concrete model are that it is defined by engineering parameters such as the tensile and compressive strength and the fracture energy, and that it covers all loading situations. Other models, focused on a specific loading situation, might provide better results in that specific situation. However, these models generally perform not so well under conditions for which they are not intended.

The Maekawa Concrete model is derived from two-dimensional and three-dimensional cyclic loading data. The derivation uses four material parameters (K, F, H, and D) for concrete with normal aggregate and strength ranging from 15 MPa to 50 MPa.

For the compression regime the Maekawa Concrete model assumes that the damage-elasticity is governed by the elastic part of the total strain alone. Before determining the contribution of the damaged-elasticity part, the elastic and the plastic components of the strain vector must first be determined.

Comparing elastic and plastic material behavior, a fundamental observation is that in elastic behavior no permanent deformations occur in the structure, whereas in plastic behavior permanent, or irreversible, deformations can be observed.

In the context of small strains, the basic assumption of additive strain decomposition into an elastic part and an irreversible, or plastic, part can be made. According to the usual approach of the flow theory of plasticity to describe the elastoplastic material behavior, the total stress at time t is modeled as a function of the total strain at time t , but also as a function of the stress and strain history. The stress and strain history of the material is usually taken into account implicitly by introducing an internal parameter, governed by a specific evolution law.

Once the elastic strain vector has been determined, then the so-called fracture parameter K is calculated as a function of the invariants of the elastic strain tensor and other elastic parameters. Due to damage it is assumed that the shear modulus will be reduced by a factor K , i.e. the initial shear modulus G is multiplied with K . Factor K runs from 1 to 0, where 0 stands for complete deterioration and 1 for no damage. The parameter F is the indicator (equivalent elastic strain) to express the macroscopic intensity of internal stress which develops the damage under an arbitrary level of confinement. The function H indicates the plastic hardening of the internal plastic element in the damaged concrete. The derivative D indicates the plastic dilatancy induced by the shear plastic dislocation along the internal defects.

$$K = K(F) = e^{-\frac{F}{3.25}} e^{0.8F}$$

$$F = F(I_{1e}, I_{2e}, I_{3e}) = \frac{1}{5} \left[6 + \frac{3\sqrt{3}}{2} \left(\frac{I_{3e}}{I_{2e}} \right)^3 \right] \frac{I_{2e} \sqrt{2}}{0.23 \varepsilon_o - I_{3e} \sqrt{3}}$$

$$H = H(I_{2e}) = \frac{9}{10} \varepsilon_o \left(\frac{I_{2e}}{\varepsilon_o} \right)^3$$

$$D = D(I_{1e}, K) = \frac{2\nu - 1}{\sqrt{3}(1 + \nu)} 4K^2 + \frac{0.38\varepsilon_o + I_{2e}\sqrt{2}}{0.28\varepsilon_o} (1 - 4K^2)$$

where Scalars I_{1e} , I_{2e} , I_{3e} , are respectively the first, second, and third elastic strain invariants. Previous equations include the material constant ε_o which was adopted as a function of the compressive strength f_c , Young's modulus E , and Poisson's ratio ν :

$$\varepsilon_o = 1.6(1 + \nu) \frac{f_c}{E}$$

so that these material functions would be applicable to concrete of normal aggregate and strength.

The model also describes hysteresis in tensile and compressive unloading–reloading loops according to the experiences of Prof. Maekawa research group.

The Maekawa concrete model checks in the total strain directions whether the total strain is unloading/reloading or loading toward new extreme tensile or compressive values. In case of unloading/reloading conditions the hysteresis behavior is depicted in figure 5.5.

A constitutive model based on total strain describes the stress as a function of the strain. One commonly used approach is the coaxial stress-strain concept, in which the stress-strain relationships are evaluated in the principal directions of the strain vector. This approach, also known as the *Rotating crack model*, has been applied to the constitutive modeling of reinforced concrete during a long period and has shown that the modeling approach is well suited for reinforced concrete structures. During loading the concrete is subjected to both tensile and compressive stresses which can result in cracking and crushing of the material. The crack directions are continuously rotating with the principal directions of the

strain vector. The basic concept of the Total Strain crack models is that the stress is evaluated in the directions which are given by the crack directions.

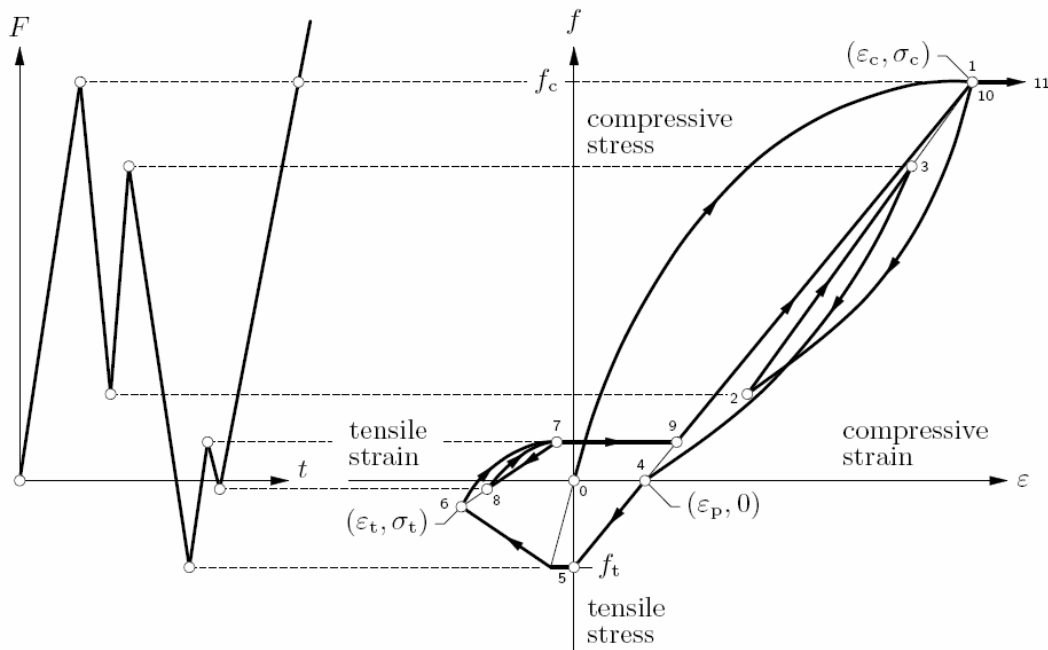


Figure 5.5 – Hysteresis for Maekawa model

Crack Modeling

The most powerful tool for numerical analysis of fractures is based on the F.E.M., where two approaches have been traditionally used: the Discrete crack approach and the Smeared Crack Approach.

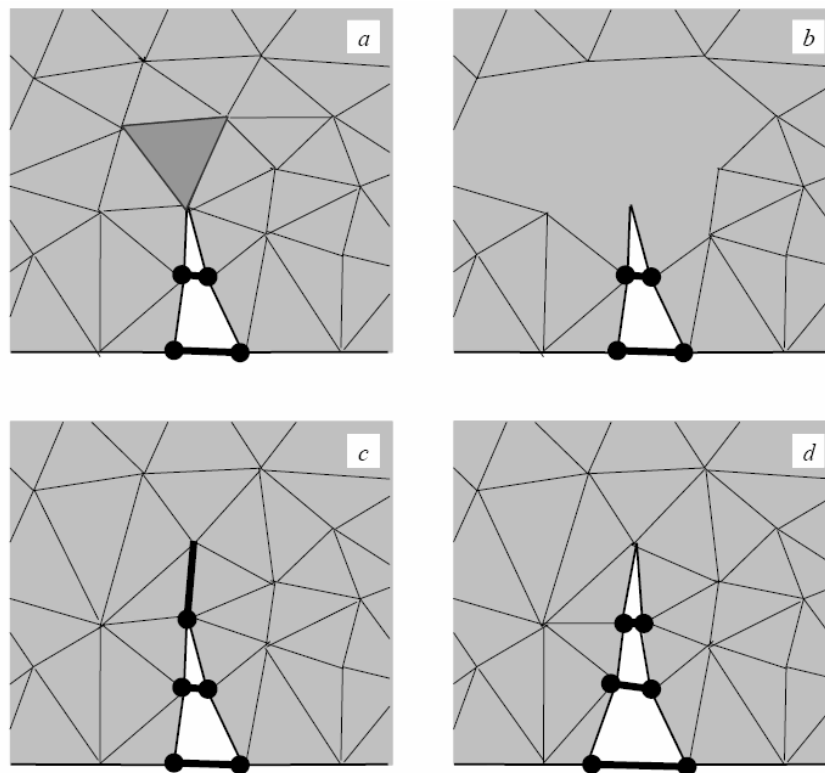
The *Discrete Crack Models* explicitly represent each individual discontinuity. The discrete crack approach is attractive from a physical point of view as it reflects the localized nature of the cracking; so, the entire fracture process zone is lumped into the crack line. This may be integrated into the FE mesh in a very convenient way by means of joint or interface elements with the appropriate constitutive laws.

Among this type of elements, we may emphasize on the zero-thickness interface elements, that were originally developed by Goodman et al. (1968) and offer a great simplicity, as well as being able to capture the basic structural behavior of rock (in origin) discontinuities and other types of interfaces. We may differentiate those schemes based on the Linear Elastic Fracture Mechanics (LEFM), where a remeshing is needed in order to model the fracture progress, and those based on the Non-Linear Fracture Mechanics (NLFM), which may be also formulated either with remeshing or by using a fixed FE mesh in which an interface element is introduced within each line of the mesh, or in those which are expected to be fractured (Rots, 1988). Generally speaking, the remeshing introduces in the method a great complexity and robustness lack, resulting in more costly computations or even the researcher/user participation to follow the fracture propagation. Furthermore, more than one or two fissures cannot be followed at the same time. The insertion of the joints within the mesh lines also demands on topologic changes that, although being of less magnitude, are also complex. On the other hand, the inclusion from the beginning of the analysis of joint elements along the most significant mesh lines significantly increases the number of nodes but it simplifies the numerical implementation.

The explicit modeling of discontinuities using the F.E.M. and the so-called joint elements goes back to the 1960-70's with the works developed by Goodman et al. (1968), Zienkiewicz et al. (1970). They proposed a joint element with zero-thickness to model the discontinuities in which the contact stresses and the relative displacements followed a linear relationship, with constant normal and tangential stiffness. This interface element has been traditionally introduced in some FE codes for application to a great number of practical problems in civil engineering. A basic concept in the modeling of any joint element is the constitutive law to be used, i.e. the relationship between the stresses in the mid-plane of the joint, and the corresponding relative displacements. This law must

adequately model the considered behavior, differentiating between the models for pre-existing joints and those based in Fracture Mechanics concepts for developing cracks.

The criterion to insert the discrete crack is based on the fracture energy G_f . The discrete crack is inserted or propagated in the finite element model when the dissipated energy during the post-peak behavior of the material at the integration points reaches G_f . Once the discrete crack is inserted with the stresses totally released through its surfaces, the geometry of the model is modified and the region around the crack is remeshed (Figure 5.6).



Procedure for discrete crack insertion sing nodal interface elements: *a)* Identification of the element where the stress at the Gauss point reaches the ultimate stress. *b)* The identified element and all the surrounding elements are eliminated. *c)* Discrete crack propagation and remeshing of the region around the crack. *d)* Sequence of the analysis.

Figure 5.6 – Discrete Crack Insertion

The singularity introduced in the structural model after discrete crack insertion causes jumps in the load-deflection diagram and also causes elastic unloading. The magnitude of the remained unbalanced forces in the split region turns to be a factor of instability in the numerical process. This is a consequence of the fact that the discrete crack is inserted in the finite element model before the total dissipation of the fracture energy. The numerical instability, due to the abrupt transition from a continuum representation to a totally opened crack, the representation of cracked material induces locked-in stresses in the elements close to the localization zone. For this reason, it was not possible to dissipate all the fracture energy in the corresponding Gauss point, and unbalanced forces remain at the cracked nodes as the analysis restart. Difficulties in obtaining the numerical equilibrium after the remeshing process can be attributed to these remained unbalanced forces. Second, as a consequence of the remeshing of the region around the discrete crack, the history-dependent variables need to be mapped from the old mesh to the new mesh configuration.

As an alternative to the zero-thickness interface elements, Desai et al (1984) formulated and developed the thin-layer elements. The main idea of the method is that the behavior near the interface involves a very thin zone that behaves according to a constitutive model specially developed for contact and frictional sliding. In general, the thin-layer elements may give some numerical problems since they are just continuous elements with extreme length-width ratio. Therefore, it seems that the existing tendency is to use the zero-thickness interface elements.

Inelastic behavior of concrete structures is intimately related to crack formation. In a first stage microcrack nucleation and growing can be observed in the so-called fracture process zone. After that, in a second stage micro cracks coalesce and macrocracks, which propagate throughout the body, are visible.

In the first stage, the number of microcracks is large and densely distributed,

which makes suitable the continuum model hypothesis for the analysis. Strain softening and elastic stiffness degradation are fundamental characteristics of these models.

The *Smearred Crack models* (Rashid, 1968) are based on a continuous type modeling of the problem where the possible existence or development of discontinuities is incorporated into the stress/strain constitutive laws of the material, so that a generalized constitutive model is used for the fractured material that will be non-linear and with softening. Equilibrium, compatibility, and constitutive response are considered in terms of average stresses and average strains.

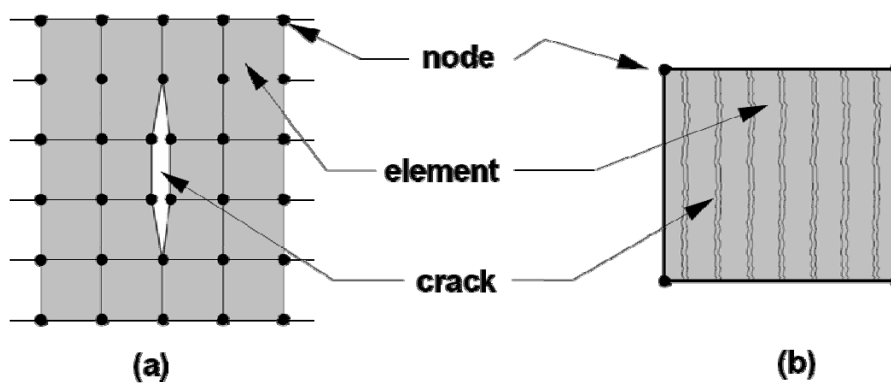


Figure 5.7 – Cracking Models: (a) Discrete Crack, (b) Smearred Crack

The smeared approach offers a number of advantages over the discrete approach. With this continuum approach the local displacement discontinuities at cracks are distributed over some tributary area within the finite element. In contrast to the discrete crack concept, the smeared crack concept fits the nature of the finite element displacement method, since the continuity of the displacement field remains intact. Remeshing techniques and continuous topological redefinition are not necessary in the smeared process. Nevertheless, a major drawback of the smeared analysis is its inability to model the surfaces of the

crack. Also, the representation of cracked materials as a continuum induces locked-in stresses in the elements close to the localization zone and a too stiff response of the structure is frequently found in the analysis.

Although this method may be used with a fixed FE mesh during the whole analysis, it usually brings associated a large number of material parameters. However, this is not the only drawback of this method, since for instance it lacks from objectivity when refining the mesh if there exists softening. There they exist also problems in the deformation modes of the elements that, in general, are not able to accommodate localized strains of arbitrary orientation, with the consequent bands that occupy a different number of elements (different thickness) depending on their orientation.

Although this approach is simple to implement and is, therefore, widely used, it has nevertheless a major drawback, which is the dependency of the results on the size of the finite element mesh used in the analysis: it yields very satisfactory results when the size of the finite element mesh is relatively small.

This happens because if a uniform distribution of microcracks is assumed over a significant portion of a relatively large finite element, the actual microcracks are diffused over a cracked region of the element much larger than it is in reality. When large finite elements are used, each element has a large effect on the structural stiffness.

When a single element cracks, the stiffness of the entire structure is greatly reduced. Higher order elements in which the material behavior is established at a number of integration points can slightly change this situation, because, in most cases, when a crack takes place at one integration point, the element stiffness is reduced enough so that a crack will occur at all other integration points of the element in the next iteration. Thus, a crack at an integration point does not relieve the rest of the material in the element, since the imposed strain continuity increases the strains at all other integration points. The overall effect is that the

formation of a crack in a large element results in the softening of a large portion of the structure.

The modeling of the concrete is based on an energy approach. The development of the fracture (or process) zone is introduced by a “fictitious” crack and is shown in Figure 5.8a, where the stress-deformation behavior is investigated in a deformation controlled uniaxial tension test.

As the deformation is increased in the tensile test, the stress is increasing almost linearly with moderate strain hardening prior to the attainment of their ultimate tensile capacity. That point corresponds to the tensile strength f_t of the concrete (see Figure 5.8b). At this stage microcracks are developing which is a reason for the nonlinear $(\sigma - \varepsilon)$ diagram. If unloading is performed, the unloading branch is almost linear as shown in the Figure 5.8b.

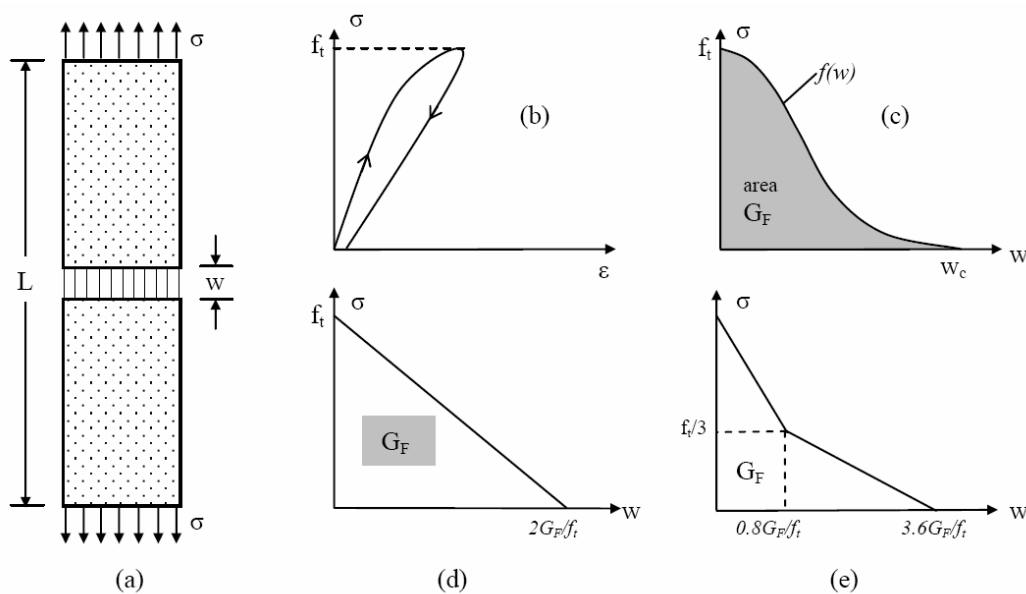


Figure 5.8 – Idealized uniaxial tensile test on a concrete specimen

Further loading will result in a descending branch, called “softening in tension”, to distinguish it from strain softening in compression. As the stress decreases, the parts outside the fracture zone are unloaded and that part of the

body volume remains elastic (figure 5.8b). Thus, the fracture zone does not spread, but is concentrated in the local zone where it started. The remaining part of the specimen simultaneously contracts elastically due to the decreasing stress. The nonlinearity is included within the narrow zone with considerable strain localization. The size of the “strain localization” zone for concrete is estimated to be of the order of maximum aggregate size.

In order to define the strain softening branch of the tensile stress-strain relation of concrete by fracture mechanics concepts three important parameters need to be defined: (1) the tensile strength of concrete at which a fracture zone initiates; (2) the area under the stress-strain curve; and (3) the shape of the descending branch (Figure 5.8c-d-e). Among these parameters, the first two can be considered as material constants, while the shape of the descending branch varies in the models that have been proposed.

A relation between the area under the tensile stress-crack strain diagram in Figure 5.9a and the fracture energy G_f is shown. This relation can be readily derived by the following procedure.

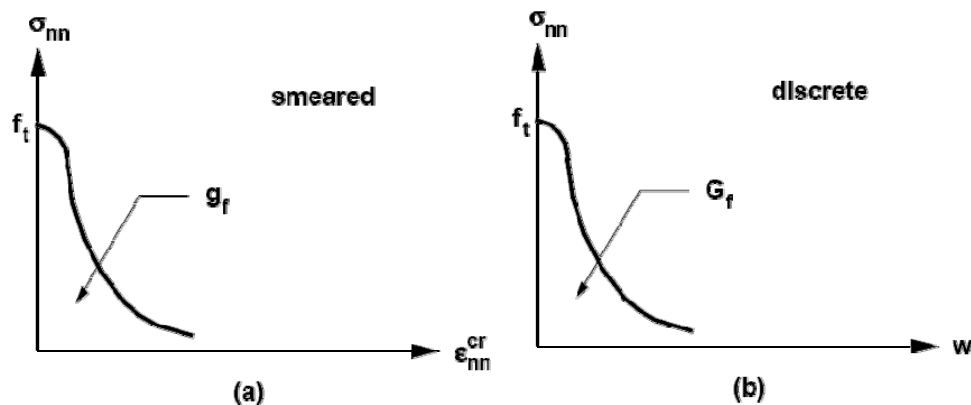


Figure 5.9 –Strain Softening Behavior Of Concrete: Tensile Stress vs. (a) Crack Strain, (b) Crack Opening Displacement

The area g_f under the curve in Figure 5.9a can be expressed as:

$$g_f = \int \sigma_m d\varepsilon_m^{cr}$$

The fracture energy G_f is defined as the amount of energy required to crack one unit of area of a continuous crack and is considered a material property. This definition results in the following expression for the fracture energy (Figure 5.9b)

$$G_f = \int_0^{w_c} \sigma_m dw$$

where w represents the sum of the opening displacements of all microcracks within the fracture zone.

In the smeared crack model w is represented by a crack strain which acts over a certain width within the finite element called the crack band width h . Since w is the accumulated crack strain, or crack opening displacement, this is represented by the following relation

$$w = \int d\varepsilon_m^{cr} dn$$

Assuming that the microcracks are uniformly distributed across the crack band width, $w = h \cdot \varepsilon_m^{cr}$ and yields the relation between G_f and g_f : $G_f = h \cdot g_f$.

The simplicity of this equation is misleading, because the actual size of the crack band width h depends on the selected element size, the element type, the element shape, the integration scheme and the problem type to be solved.

A general description of the stress-deformation properties of the concrete can be given by two curves, one stress-strain (σ - ε) curve up to the peak value and one stress-displacement (σ - w) curve for the descending branch, see Figure 5.8c. As w increases, the stress gradually falls, until the ultimate crack width w_c is reached upon zero normal stress. At this point, a real crack will develop, so the stress transfer between the two parts terminates. G_f is the fracture energy absorbed within the fracture process zone.

The deviation of the concrete from materials presumed ideally brittle, such as ceramic or glass, is mainly related to the development of a large inelastic zone

ahead of the crack tip. Different fracture behavior can be seen between linear elastic (ideal brittle), ductile and quasibrittle materials (Bazant and Planas 1998).

In general, the fracture process zone is a nonlinear zone characterized by progressive softening, for which the stress decreases at increasing deformations. This zone is surrounded by a no softening nonlinear zone characterized by hardening or perfect plasticity, for which the stress increases or remains constant at increasing deformations. These two zones form the nonlinear zone. Depending on the *relative size* of these two zones and the structure, three types of fracture behavior can be distinguished, as shown in Figure 5.10. In the first type of behavior the whole nonlinear zone is relatively small, compared to the structural size, thus the fracture is concentrated at almost one point, namely the tip of the crack. This type of behavior is typical for ideally brittle materials (glass, ceramics). The second type of behavior is very typical for ductile metals where the second zone is much bigger than the softening zone, so in this case the methods of elasto-plastic fracture mechanics should be applied.

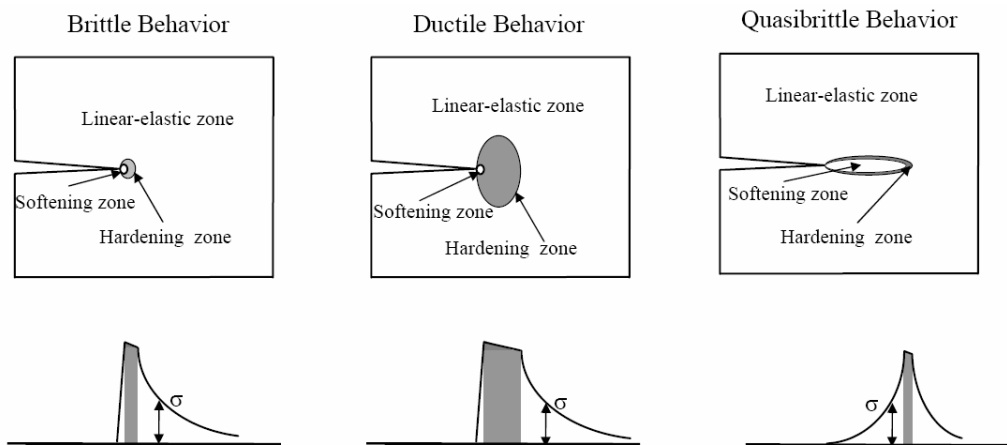


Figure 5.10 – Types of fracture process zone and stress distribution around the crack

In the third type of behavior the major part of the nonlinear zone undergoes

progressive damage with material softening, due to microcracking, void formation and other similar phenomena. The zone of plastic hardening is often negligible and this happens for concrete, rocks, cemented sands, etc. These materials are called quasibrittle, because the size of the fracture process zone is large enough and it should be taken into consideration in calculations, in contrast with the pure brittle behavior.

Various so-called smeared cracking models are available in DIANA to simulate cracking of brittle materials like concrete. Basically these models are a combination of tension cut-off, tension softening and shear retention criteria.

In addition to the smeared cracking models, two constitutive models based on total strain are available: the fixed and the strain rotating concept. These models describe the cracking and crushing behavior of the material with a non-linear elasticity relationship.

DIANA implements the decomposed crack model where the total strain is decomposed into an elastic strain and a crack strain. This decomposition of the strain allows also for combining the decomposed crack model with for instance a plastic behavior of the concrete in a transparent manner. The sub-decomposition of the crack strain gives the possibility of modeling a number of cracks that simultaneously occur.

A basic assumption is that the crack stresses are given as a function of the crack strains. Modeling of coupling effects between the different cracks is possible within this general formulation but taking coupling into account would lead to an increasing and unnecessary level of sophistication. The initiation of cracks is governed by a tension cut-off criterion. For the concrete plasticity model and for the Total Strain models Diana assumes a default for the crack bandwidth h . For solid elements the default is $h = \sqrt{V}$ where V is the volume of the element.

For the Total Strain crack model, four softening functions based on fracture energy are implemented: in the present analyses a nonlinear softening curve

according to Hordijk (1991) has been adopted.

Hordijk proposed an expression for the softening behavior of concrete which results in a crack stress equal to zero at an ultimate crack strain. The relation of the crack stress is given by (Figure 5.11)

$$\sigma_{nn}^{cr}(\varepsilon_{nn}^{cr}) = \begin{cases} f_t \left[\left(1 + c_1 \frac{\varepsilon_{nn}^{cr}}{\varepsilon_{nn,ult}^{cr}} \right)^3 \cdot e^{-c_2 \frac{\varepsilon_{nn}^{cr}}{\varepsilon_{nn,ult}^{cr}}} - \left(1 + c_1^3 \right) \frac{\varepsilon_{nn}^{cr}}{\varepsilon_{nn,ult}^{cr}} \cdot e^{-c_2} \right] & \text{if } 0 < \varepsilon_{nn}^{cr} \leq \varepsilon_{nn,ult}^{cr} \\ 0 & \text{if } \varepsilon_{nn}^{cr} > \varepsilon_{nn,ult}^{cr} \end{cases}$$

with the parameters $c_1 = 3$ and $c_2 = 6.93$ and where the ultimate crack strain

$$\text{is } \varepsilon_{nn,ult}^{cr} = 5.136 \frac{G_f}{h \cdot f_t}$$

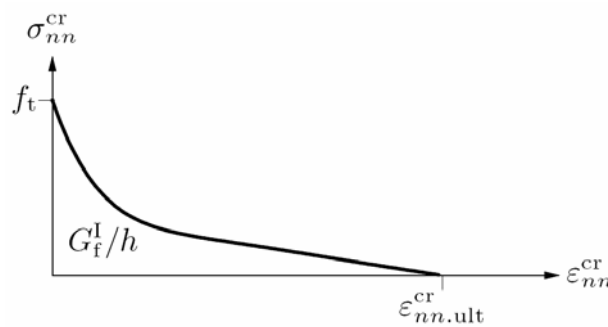


Figure 5.11 – Hordijk nonlinear Tension Softening

5.1.3 Reinforcement Elements

DIANA considers both bar type and grid type reinforcements. The former type is very well suited to simulate the presence of longitudinal steel reinforcement, while the latter permits to easily simulate the effect of the FRP confinement induced by the externally applied wraps.

DIANA implements the technique of embedding reinforcements. This

technique allows the lines of the reinforcement to deviate from the lines of the mesh. This permits the user to generate the finite element mesh without having to anticipate on the location of reinforcements. To embed bar reinforcement in solid elements, DIANA needs for each solid element the location points of the particle that is embedded in that element. These location points can be generated by preprocessing the input of sections.

Embedded reinforcements add stiffness to the finite element model. They are embedded in structural elements, the so-called mother elements and do not have degrees of freedom of their own.

By default, reinforcement strains are computed from the displacement field of the mother elements. This implies perfect bond between the reinforcement and the surrounding material.

The total length of the bar is considered to be divided in several particles that must be completely inside a structural element. The so-called location points define the position of the particles in the finite element model. Some location points are the intersections of the bar with the element boundaries. Other location points are in-between these intersections, and eventually define the curvature of the bar. Usually, the location points are determined automatically by DIANA from input of larger sections in the preprocessing of reinforcement location.

The two-node reinforcement element which may be used in one-, two-, and three-dimensional models has the interpolation polynomial for the displacement u_x expressed as $u_x = a_0 + a_1\xi$. This polynomial yields a strain ε_{xx} which is constant along the bar axis.

Plane shaped reinforcement grids can be embedded on surfaces of solid elements. The total area of the grid is considered to be divided in several particles contributing to the stiffness of the element that embeds it. The three-node triangular reinforcement plane stress element has the geometry interpolated by a linear function and the displacements by linear and hierarchical quadratic

functions. The polynomial for the translations u_x and u_y can be expressed as

$u_i(\xi; \eta) = a_0 + a_1\xi + a_2\eta + a_3\xi\eta + a_4\xi^2 + a_5\eta^2$. Typically, this polynomial yields a strain which varies linearly over the element area.

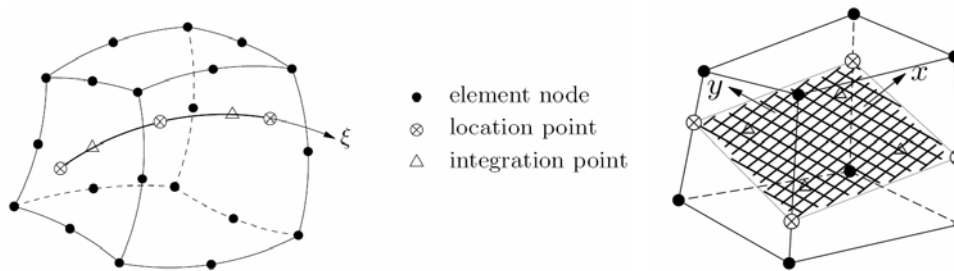


Figure 5.12 –BAR and GRID particle in solid element

For embedded reinforcements Diana offers a linear elastic material model and a plasticity model to evaluate yielding of the reinforcement, Von Mises plasticity is available.

5.2 DIANA models of tested specimens

One of the aims of this study was to develop finite-element models (F.E.M.) that could simulate the behavior of tested specimens, evaluate and confirm the FRP confinement effect, represent the crack pattern evolution.

The columns were modeled by 1952 twenty-node, three-dimensional solid brick elements type CHX60, and the steel embedded reinforcement by 800 three-node truss elements. In figures 5.13a-b are outlined the edges of the concrete and the internal longitudinal steel reinforcement. In figure 5.13c is the mesh of the unstrengthened (U-series) specimens and it is noted that the outer layers of elements at the two ends of the columns are modeled as steel elastic plates to distribute the line load applied at given eccentricity, avoiding stress

concentrations and localized failures (see remarkable distortion at load line in figure 5.14a where the deformed S1 model is depicted).

The FRP confinement was modeled by 1632 three-node plane bonded elements. In figures 5.13d is the mesh of the strengthened (S-series) specimens and the external FRP reinforcement jacket applied on the square part of the column.

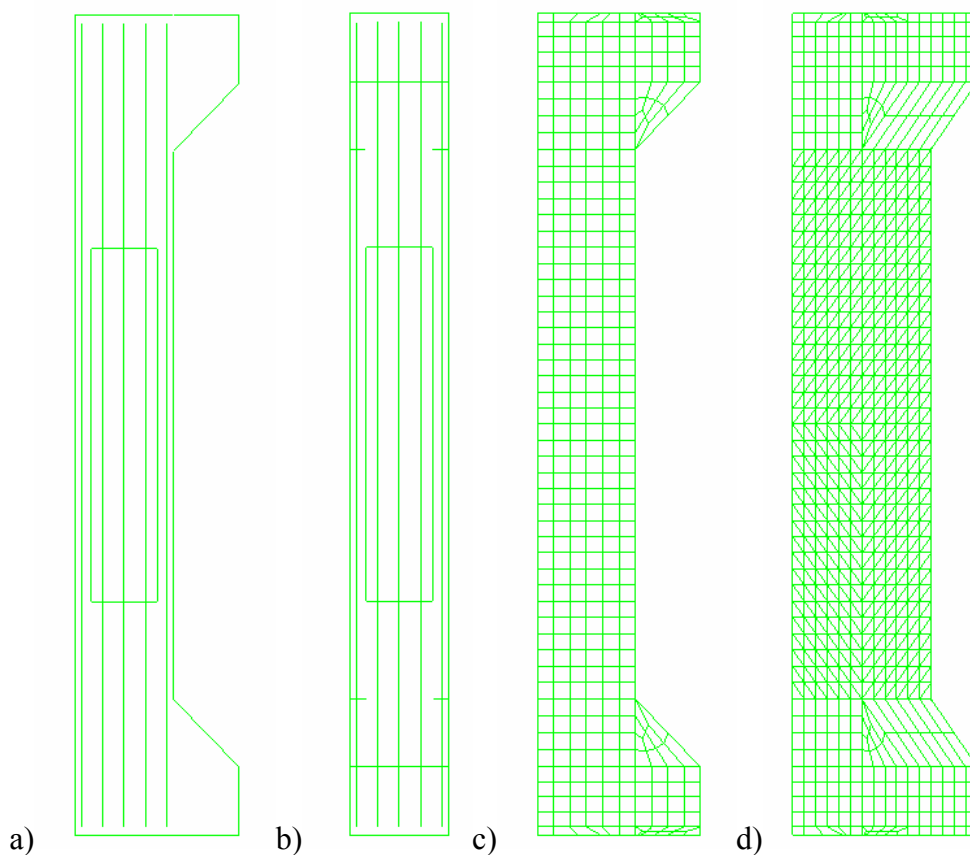


Figure 5.13 –Geometry and Mesh of Specimens model

The hollow portion has been modeled with an internal void, neglecting the presence of the foam-polystyrene (half column is depicted in Figure 5.14b)

In the F.E.M. the concrete is modeled according to Modified Maekawa Concrete Model (see previous Paragraph) and Total Strain Rotating crack with

Concrete Model (see previous Paragraph) and Total Strain Rotating crack with nonlinear softening in tension (Table 5.1).

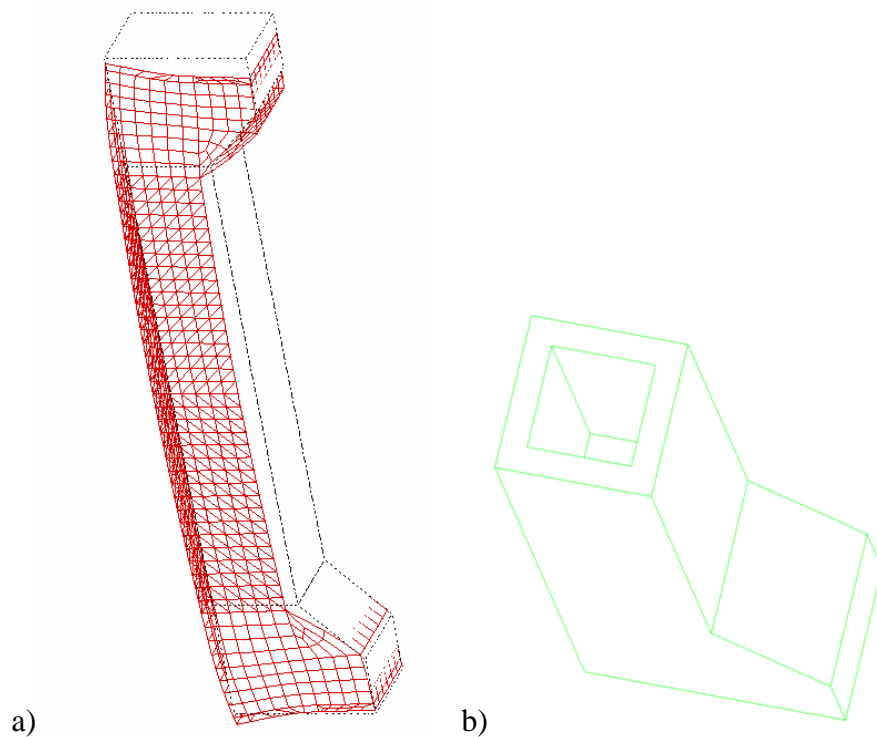


Figure 5.14 –a) Deformed Shape and b) Half portion of the hollow column

Steel reinforcement is ideally elasto-plastic (Table 5.2), while FRP is modeled as an elastic material (Table 5.3 where the equivalent thicknesses in the longitudinal and transverse direction of the jacketed column are reported).

It is remarked that at date the F.E.M. analysis does not take into account reinforcement buckling and concrete cover spalling, but only concrete cracking, plasticity and steel yielding.

Table 5.1– Material Properties of Concrete (Modified Maekawa model)

Property	Value
Elastic Modulus E	37 GPa
Poisson Coefficient ν	0.12
Compressive Strength	32.0 MPa
Tensile Strength	3.21 MPa
Fracture Energy G_f	0.05 N/mm
Total Strain	Rotating Crack
Tension Softening	Nonlinear Hordijk

The effect of confinement is simulated, the modified Maekawa concrete model is able to account for the confinement through the previously described four internal parameters.

Table 5.2– Geometrical and Material Properties of Steel Reinforcement

Property	Value
Elastic Modulus E	210 GPa
Poisson Coefficient ν	0.30
Yielding Stress	506 MPa
Cross Section	78.54 mm ² each bar

Table 5.3– Geometrical and Material Properties of FRP jacket

Property	Value
Elastic Modulus E	230 GPa
Equiv. Thickness, long.	0 mm
Equiv. Thickness, transv.	0.666 mm

The load was applied as a line displacement load on the steel outer plates on the two opposite ends of the column at a rate of 0.5 mm/step. Compared to

experimental displacement rate, an equivalent sampling rate of 1/250 Hz is adopted.

A comparison of F.E.M. results and experimental outcomes for each tested specimen is illustrated in next sections: in terms of local and global behavior of the specimens with and without FRP reinforcement: results and graphs for each specimen are reported to underline the differences in behavior. A good agreement of the numerical predictions on the ascending (pre peak) branch was found between F.E.M. model and refined proposed method (according two proposed confinement model₍₂₎), until brittle concrete cover spalling and steel reinforcement buckling take place (after the occurrence of these brittle mechanisms the F.E.M. diagrams are reported in dashed lines). The F.E.M. analysis allowed also tracing the smeared crack pattern evolution in the tested specimens and the FRP jacket strain development.

In unstrengthened columns, the area between the ascending portion of the curve after steel buckling (extending the numerical predicted curve beyond compressed steel buckling) and the actual curve covered after buckling can be seen as a measure of the load carrying capacity loss due to buckling and concrete cover spalling. Concrete confinement allows gaining a big portion of that loss and gives higher strength and ductility to the specimen.

Strain diagrams are obtained from data of vertical relative displacements on the same gauge length as the LVDT applied on tested specimens and strain measurements on steel bars; a good agreement was generally found with experimental data of LVDTs placed on the exterior walls and strain gauge measurements on steel bars. The numerical curvature was computed connecting three data points, one on most compressed concrete fibers and two on internal steel reinforcement bars (reported compressive strains are positive).

Due to symmetry conditions, in some cases, to have a better insight view of the pictures, only half column is shown.

5.2.1 Specimen U1: F.E.M. numerical predictions

The experimental failure of this column was particularly brittle and occurred at the basis of the hollow column, in correspondence with discontinuity due to the change from the solid section of the ends to the hollow section. In figure 5.15 is the F.E.M. smeared crack pattern (external and internal view of the specimen) at an axial load of about 2129 kN, corresponding to steel compressive bars buckling (figure 5.16) and experimental failure. Some cracks are visible in correspondence with discontinuity due to the change from the solid section at the ends to the hollow section. On the whole compressed wall steel reinforcement got close to the buckling stress so that the experimental failure is confirmed by the F.E.M. analysis (steel buckling in the concrete crushed zone).

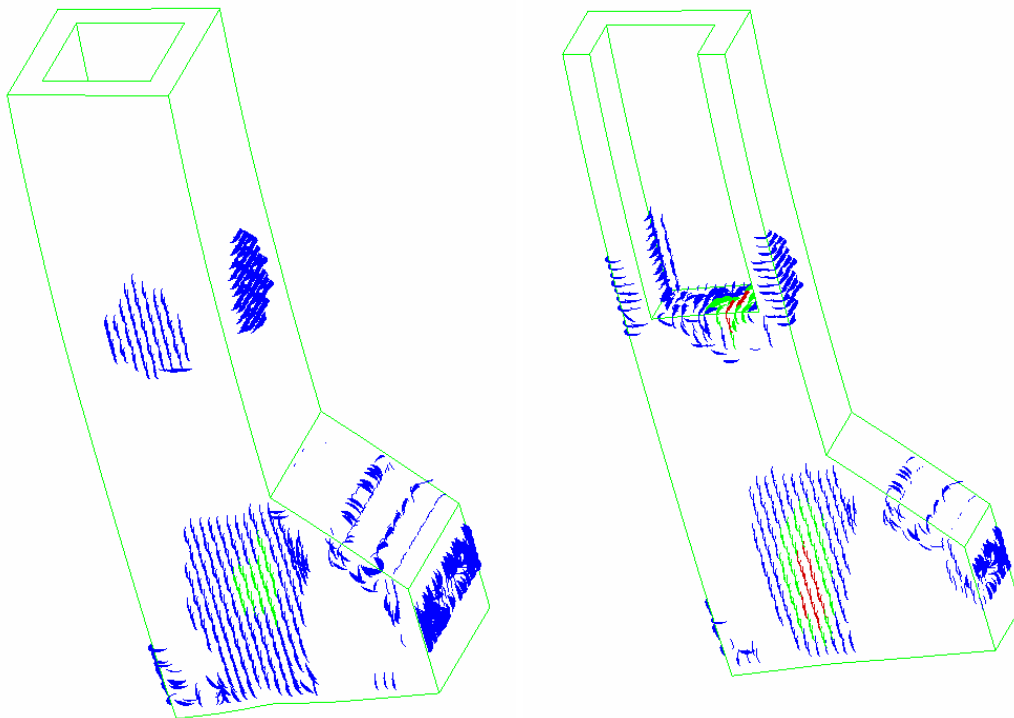


Figure 5.15 –Crack pattern at peak load (U1-F.E.M.)

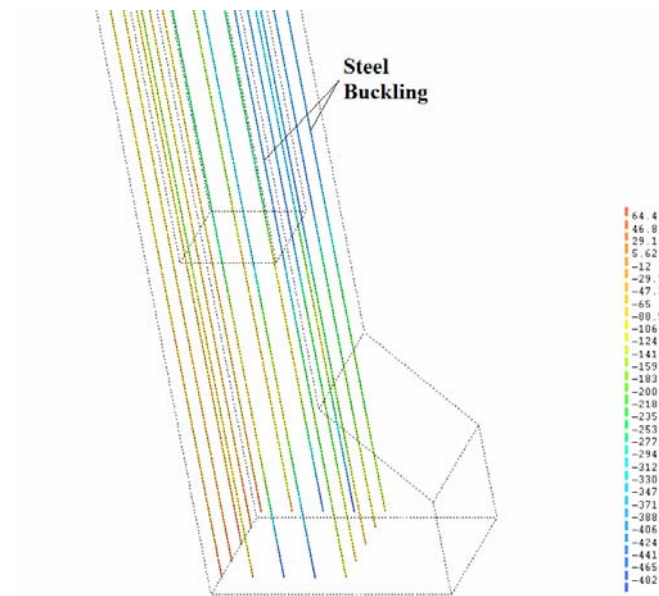


Figure 5.16 – Steel reinforcement stresses at peak load (U1-F.E.M.)

In Figure 5.17 is reported the strain versus axial force P diagram. The recover of load carrying capacity after concrete cracking can be considered a virtual measure of the loss due to the brittle mechanisms occurred during U1 test.

It is clearly shown the brittle failure due to steel reinforcement buckling and concrete cover spalling, the loss of load carrying capacity of the specimen when the concrete strains were about 2%. Also the F.E.M. model shows a sudden drop in the load carrying capacity, then a recover of capacity is evidenced because the model does not take into account buckling of steel reinforcement and concrete cover spalling that caused experimental brittle behavior.

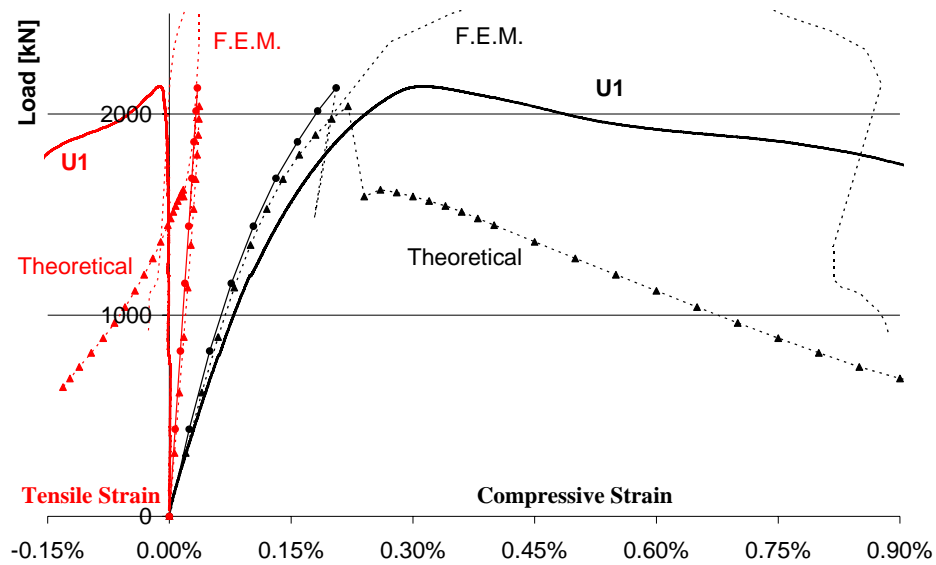


Figure 5.17 – Strains vs. Axial Load Diagram (U1)

A comparison of F.E.M. and proposed refined section modeling moment-curvature diagram with experimental outcomes is plotted in Figure 5.18. A good agreement is found between three available data up to peak, before steel buckling.

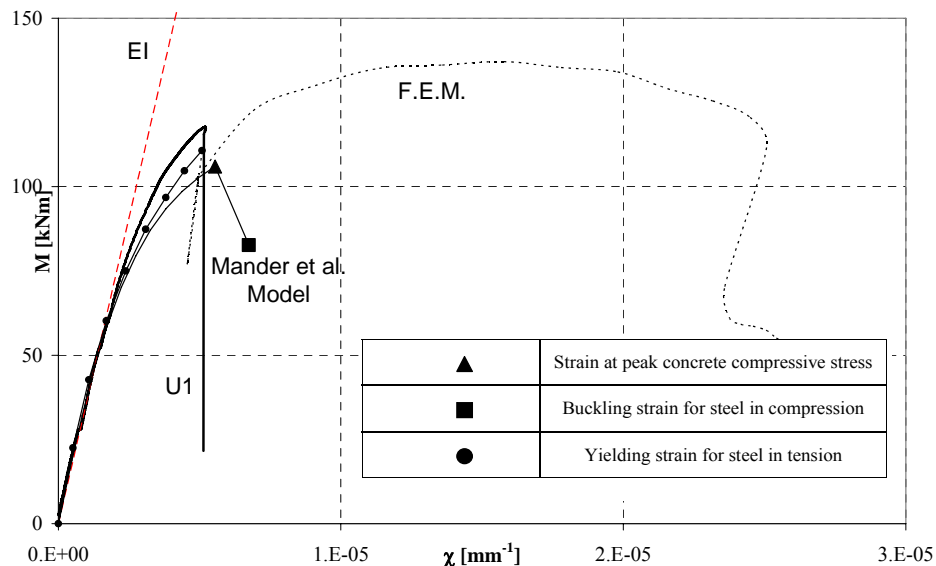


Figure 5.18 – Moment Curvature Diagram (U1)

In Figure 5.19 is the mid span deflection vs. axial load diagram: at peak load deflection was 5.11 mm, this value is very close to the predictions of the proposed refined method (experimental deflection data are not available for this particular test).

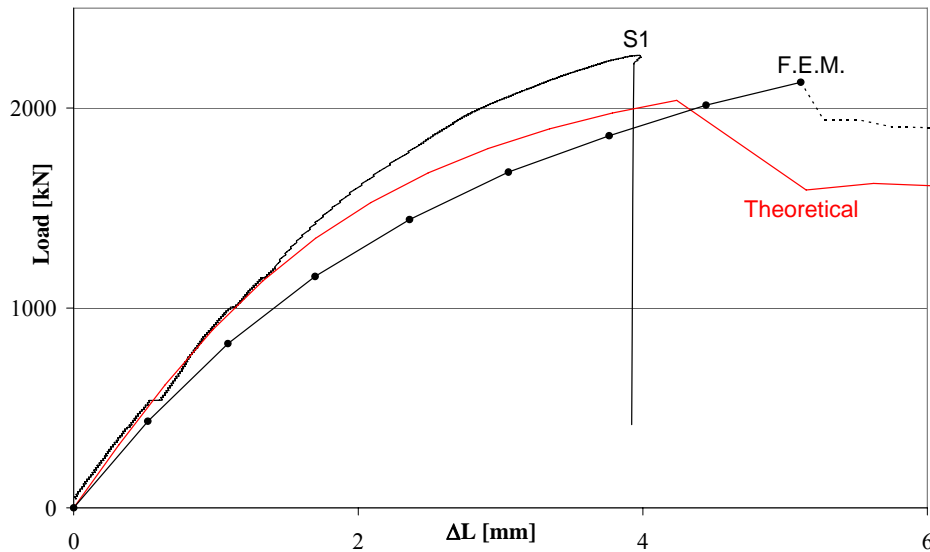


Figure 5.19 – Mid Span Deflection Diagram (U1)

5.2.2 Specimen U2: F.E.M. numerical predictions

The experimental failure of this column was brittle and occurred at the mid span of the hollow column. In figure 5.20 is the F.E.M. smeared crack pattern (external and internal view of the specimen) at an axial load of about 1080 kN, corresponding to steel compressive bars buckling and close to experimental failure. Some tensile cracks are visible on the rear wall in tension. The stress field spreads from the loaded line to the hollow portion in the solid end and neutral axis has the same depth in the hollow portion of the specimen (Figure 5.21).

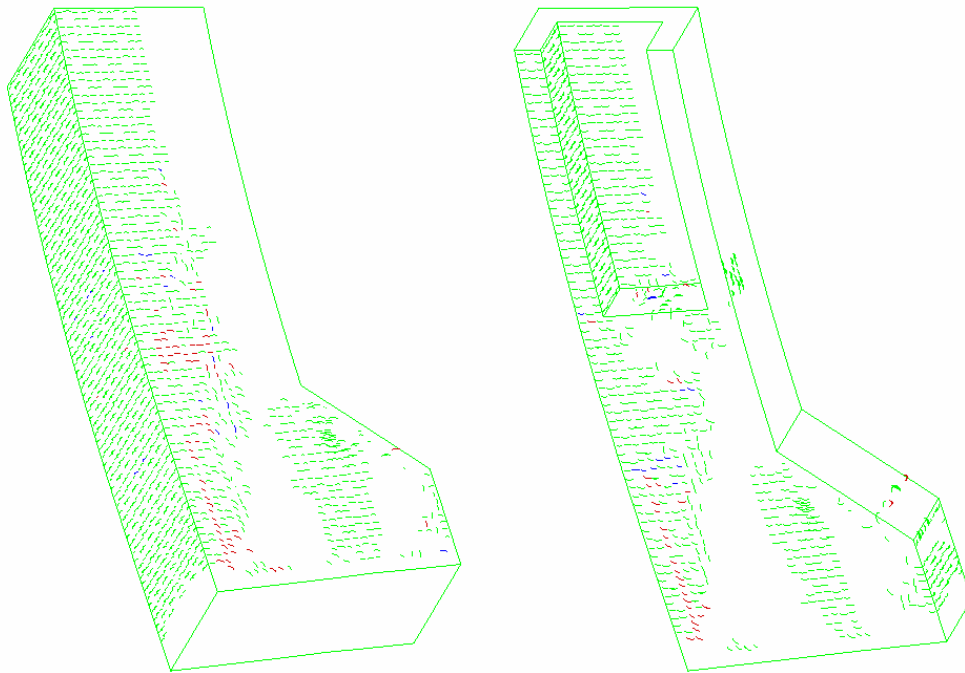


Figure 5.20 –Crack pattern at peak load (U2-F.E.M.)

On the whole tension wall is present a smeared crack pattern and steel reinforcement reaches the buckling stress on the compressed side so that the experimental failure is confirmed by the F.E.M. analysis (steel buckling and some cracks in the tension wall).

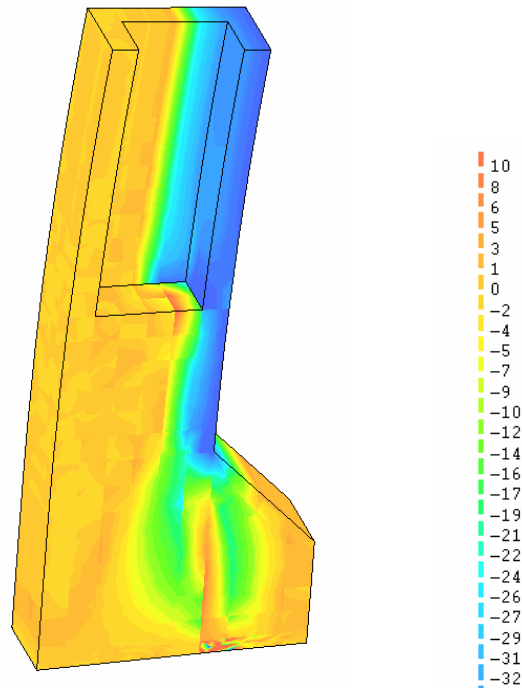


Figure 5.21 – Concrete vertical stresses at peak load (U2-F.E.M.)

In Figure 5.22 is reported the strain versus axial force P diagram. The load carrying capacity after steel reaches buckling stress can be considered a virtual measure of the loss due to the brittle mechanisms occurred during U2 test.

It is clearly shown that up to experimental peak load, the experimental and numerical curves follow the same path, while brittle failure due to steel reinforcement buckling and concrete cover spalling causes the loss of load carrying capacity of the tested specimen. The concrete strain at reinforcement buckling is about 2.8%.

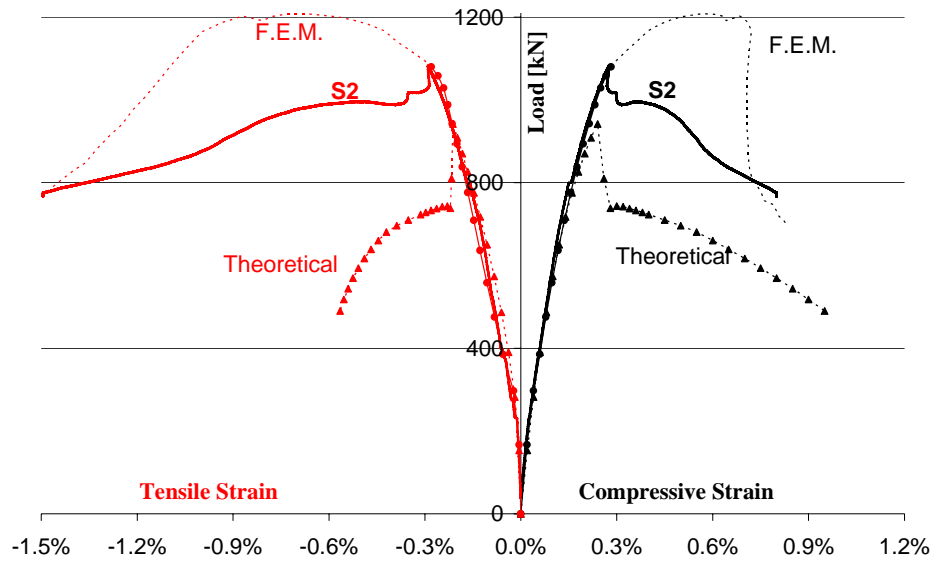


Figure 5.22 –Strains vs. Axial Load Diagram (U2)

A comparison of F.E.M. and proposed refined section modeling moment-curvature diagram with experimental outcomes is plotted in Figure 5.23.

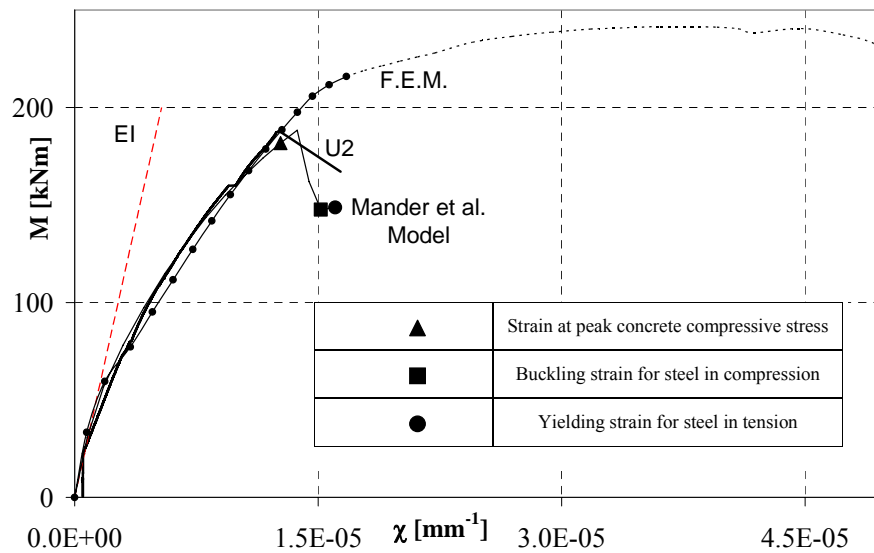


Figure 5.23 –Moment Curvature Diagram (U2)

An excellent agreement is found between three available data up to peak, before steel buckling.

In Figure 5.24 is the mid span deflection vs. axial load diagram: at experimental peak load, deflection is 13.3 mm (this value is very close to the experimental data), while at reinforcement buckling deflection is 17.7 mm.

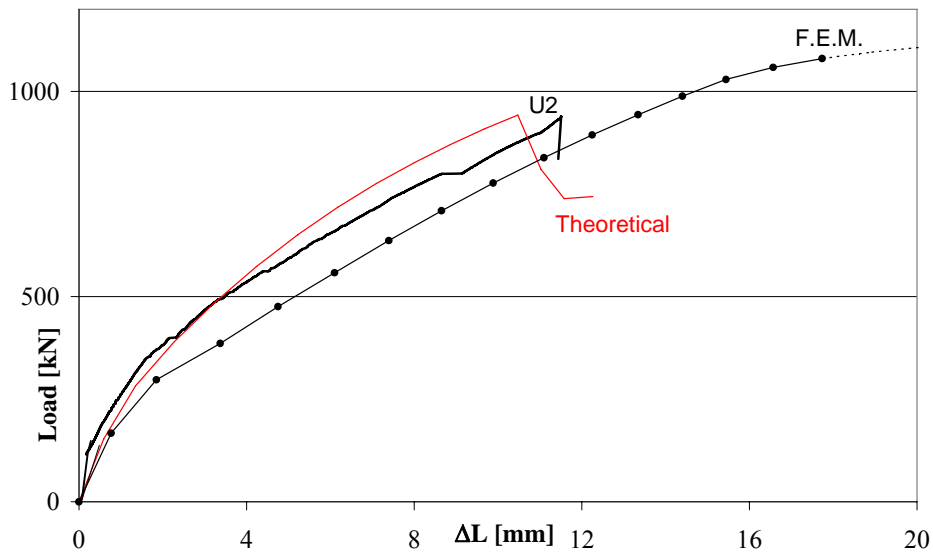


Figure 5.24 – Mid Span Deflection Diagram (U2)

5.2.3 Specimen U3: F.E.M. numerical predictions

The experimental failure of this column was moderately brittle and occurred at the basis of the hollow column. In figure 5.25 is the F.E.M. smeared crack pattern (external and internal view of the specimen) at an axial load of about 633 kN, corresponding to steel compressive bars buckling and close to experimental failure. Many tensile cracks are visible on the rear wall in tension spreading on the lateral walls up to the front wall (as observed in experimental

tests). The neutral axis has almost the same depth in the hollow portion of the specimen, close to the compressed wall (Figure 5.26).

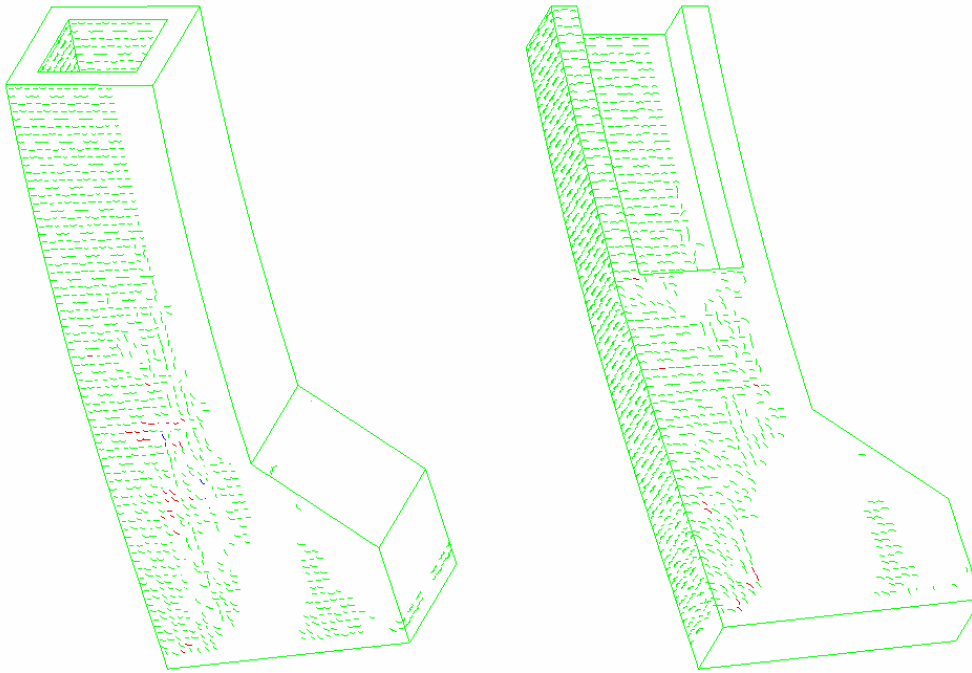


Figure 5.25 –Crack pattern at peak load (U3-F.E.M.)

On the whole tension wall is present a smeared crack pattern and steel reinforcement reaches the buckling stress on the compressed side so that the experimental failure is confirmed by the F.E.M. analysis (steel buckling and wide deep cracks in the tension wall can develop in any section of the hollow portion).

In Figure 5.27 is reported the strain versus axial force P diagram. The load carrying capacity after steel reaches buckling stress can be considered a virtual measure of the loss due to the brittle mechanisms occurred during U3 test.

It is clearly shown that up to experimental peak load, the experimental and numerical curves follow the same path, while brittle failure due to steel reinforcement buckling and concrete cover spalling causes the loss of load

carrying capacity of the tested specimen. The concrete strain at reinforcement buckling is about 3.0‰.

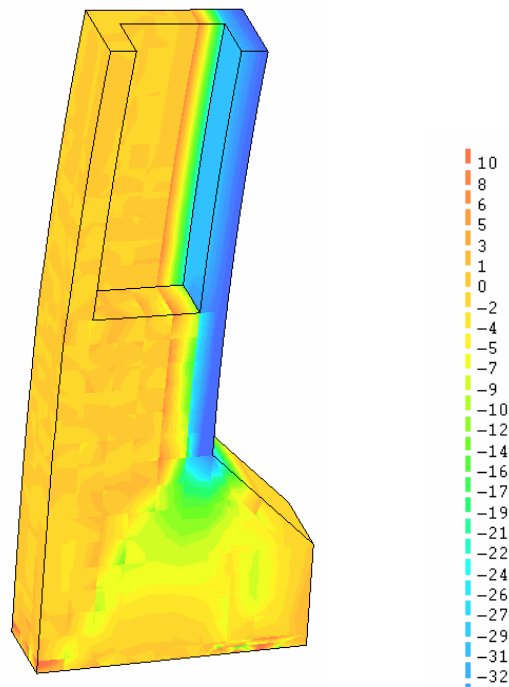


Figure 5.26 – Concrete vertical stresses at peak load (U3-F.E.M.)

Tension Reinforcement reached yielding strains corresponding to a yielding moment of about 150 kNm and some ductility was attained as a consequence of steel yielding.

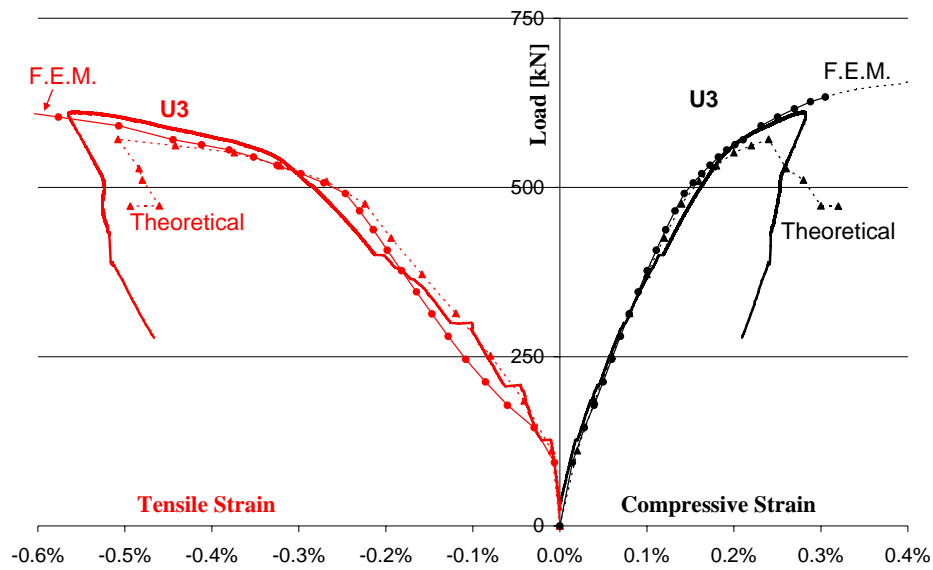


Figure 5.27 – Strains vs. Axial Load Diagram (U3)

A comparison of F.E.M. and proposed refined section modeling moment-curvature diagram with experimental outcomes is plotted in Figure 5.28.

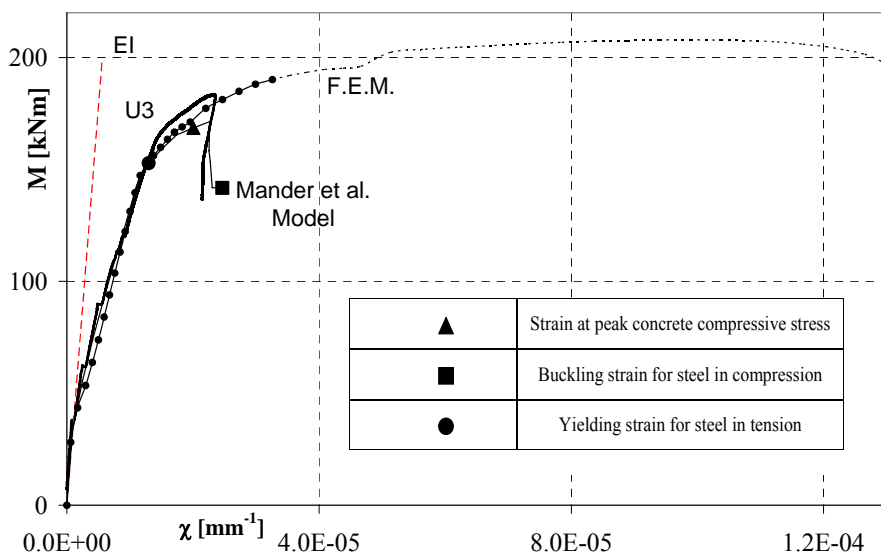


Figure 5.28 – Moment Curvature Diagram (U3)

In Figure 5.29 is the mid span deflection vs. axial load diagram: deflection was 33.3 mm at peak load, this value is higher than the prediction of the proposed refined method (close to experimental outcome).

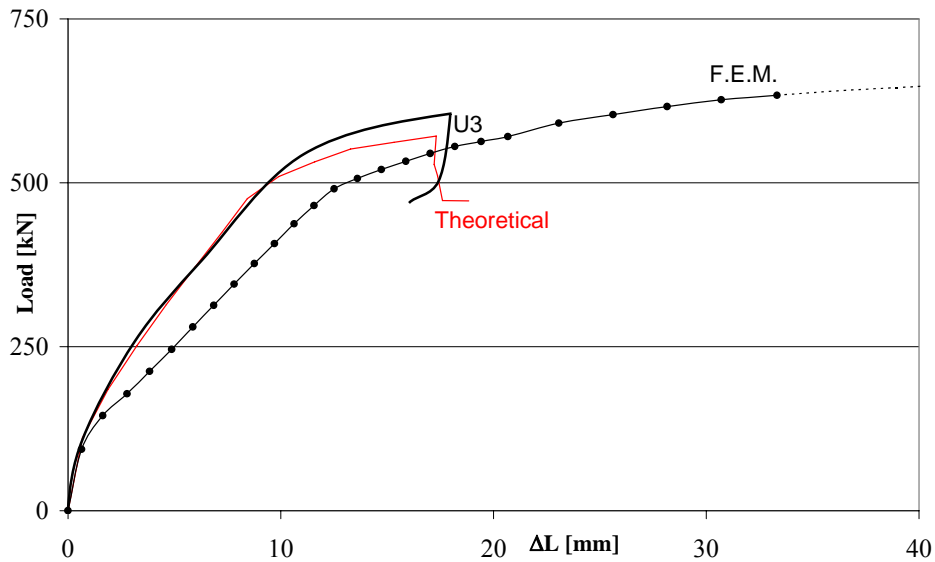


Figure 5.29 – Mid Span Deflection Diagram (U3)

A good agreement is found between three available data up to peak, before steel buckling.

5.2.4 Specimen S1: F.E.M. numerical predictions

In the S series strain predictions are also given for the FRP jacket: the same acquisition point as been chosen in the strain gauges positions on the tested specimens (on the front wall and over the corners).

In figure 5.30 is the F.E.M. smeared crack pattern (external and internal view of the specimen, behind the FRP wraps) at an axial load of about 2197 kN,

corresponding to steel compressive bars buckling and close to experimental failure.

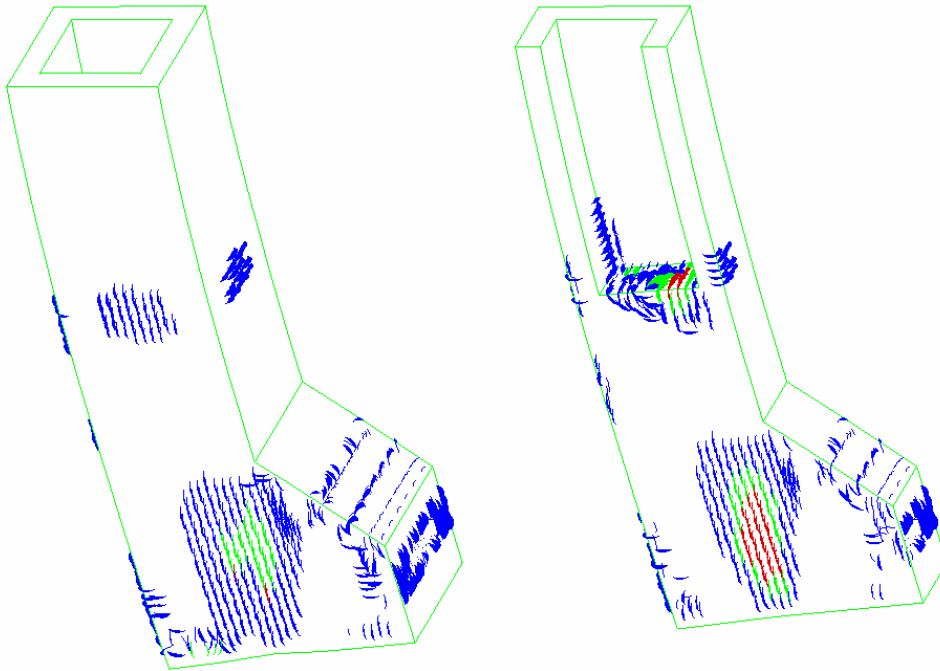


Figure 5.30 –Crack pattern at peak load (S1-F.E.M.)

The stress field spreads from the loaded line to the hollow portion in the solid ends (Figure 5.31) and the neutral axis is inside the wall, in the middle of the rear wall: so strain diagram is almost triangular, with higher strains on the crushed wall and very low strains in the wall in tension.

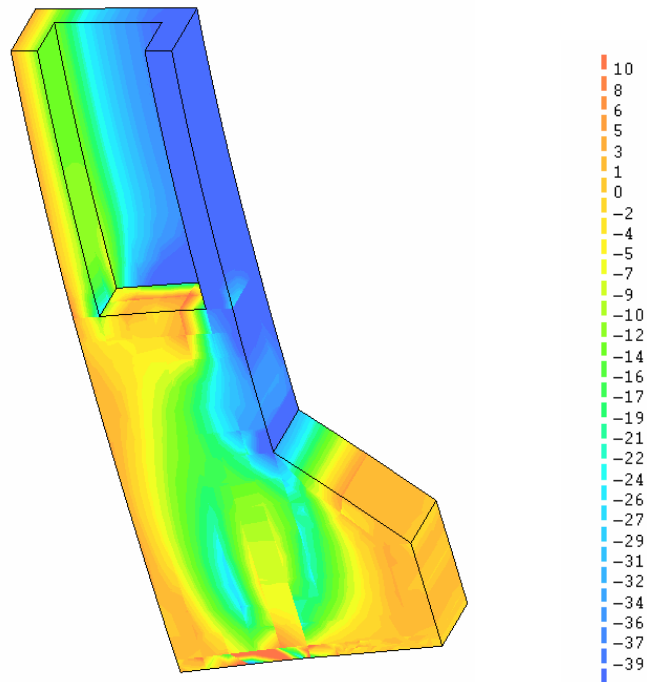


Figure 5.31 – Concrete vertical stresses at peak load (SI-F.E.M.)

In Figure 5.32 is reported the contour plot of the FRP strain in the jacket at steel buckling. FRP strains present a maximum in the middle of the compressed wall and strains decrease on the lateral wall going to the region of lower axial stresses (with reference to the specimen axis).

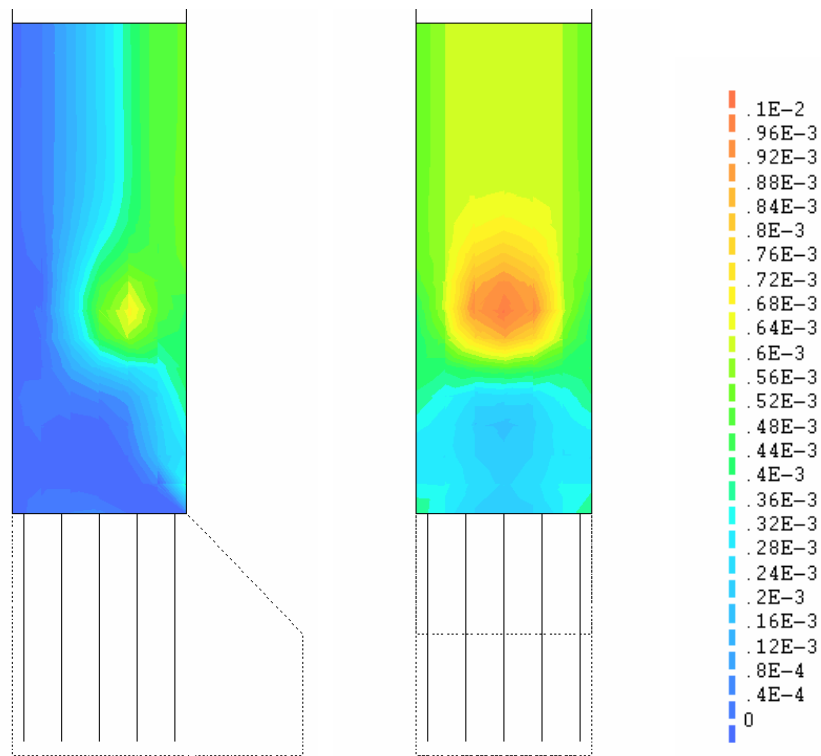


Figure 5.32 – FRP horizontal strains at peak load (S1-F.E.M.)

In Figure 5.33 is reported the strain versus axial force P diagram. The load carrying capacity after steel reaches buckling stress can be considered as a virtual measure of the loss due to the brittle mechanisms due to internal concrete cover spalling.

It is clearly shown that up to experimental peak load, the experimental and numerical curves follow the same path, while brittle failure due to internal concrete cover spalling causes the loss of load carrying capacity of the tested specimen. The concrete strain at reinforcement buckling is about 3.0‰.

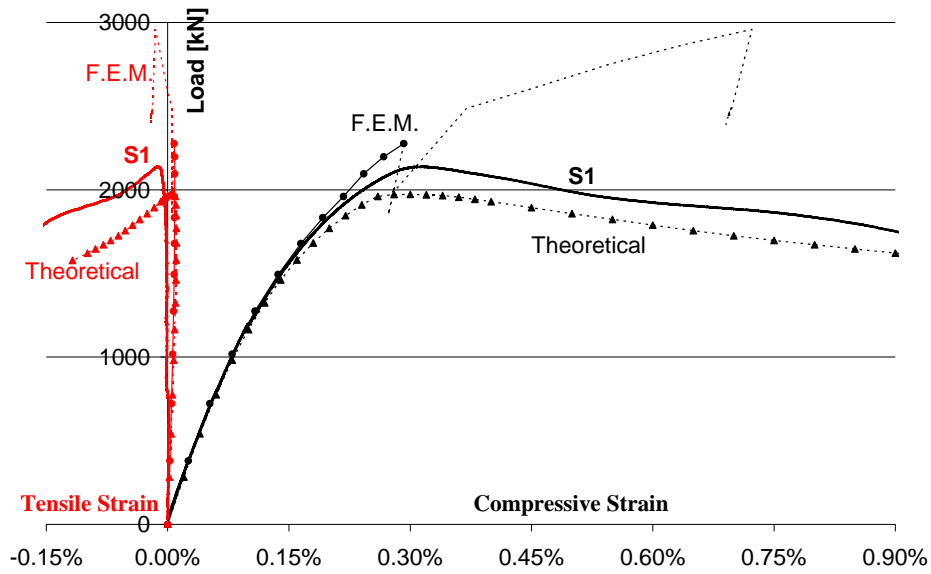


Figure 5.33 – Strains vs. Axial Load Diagram (S1)

A comparison of F.E.M. and proposed refined section modeling moment-curvature diagram with experimental outcomes is plotted in Figure 5.34.

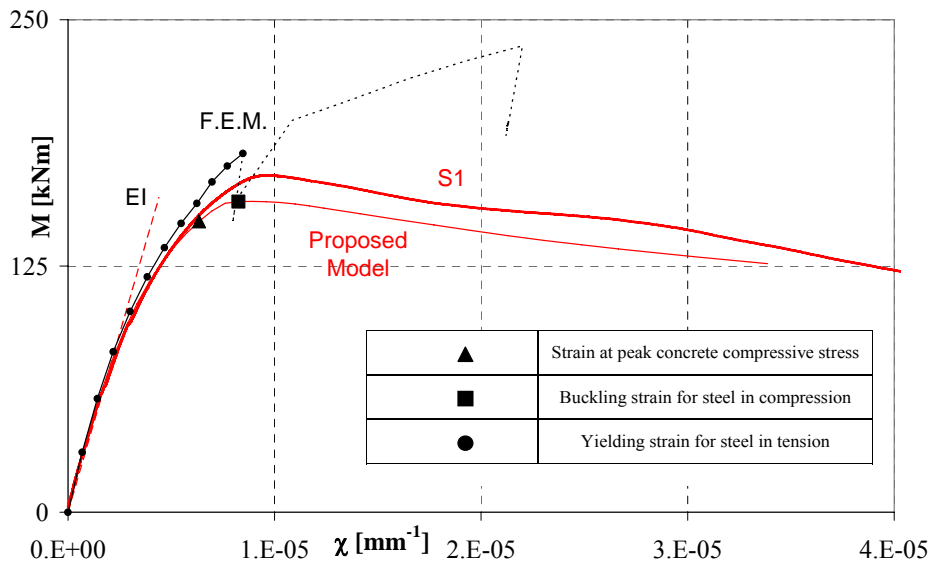


Figure 5.34 – Moment Curvature Diagram (S1)

An excellent agreement is found between three available data up to peak, before steel buckling.

In Figure 5.35 is the mid span deflection vs. axial load diagram: deflection was 7.81 mm at peak load, this value is close to the experimental data.

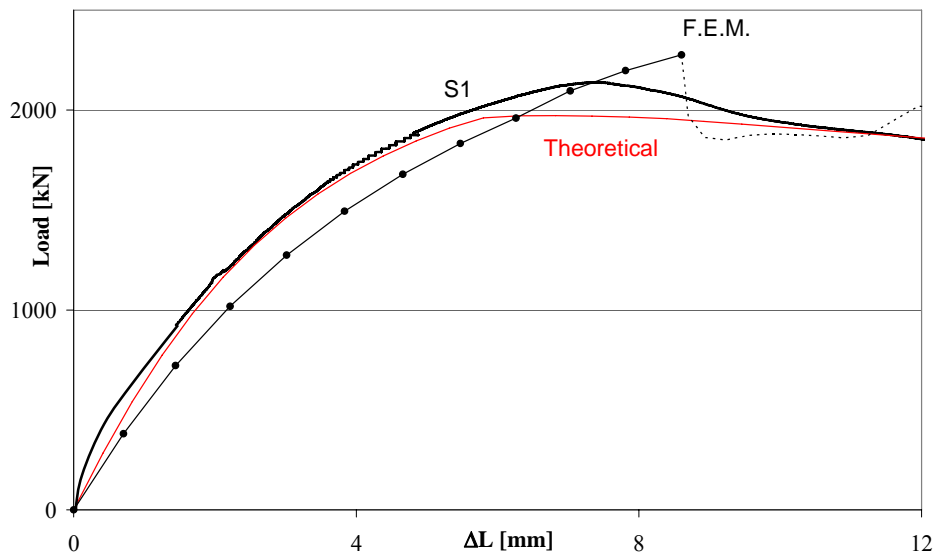


Figure 5.35 – Mid Span Deflection Diagram (S1)

Longitudinal strain distributions into FRP confining wraps have been recorded and analyzed. In Figure 5.36 strain profiles are plotted over the length of the front wall and around corners at the mid span section, at different load levels. Maximum strains in FRP are reached at mid-span in the middle of the compressed wall. At peak load, FRP lateral strains are smaller than 0.06%. After peak, a remarkable strain increment is noticed, the maximum value of 0.2% was recorded. FRP strain experimental data in the middle of the compressed wall are compared with theoretical predictions during the entire load history (Figure 5.37).

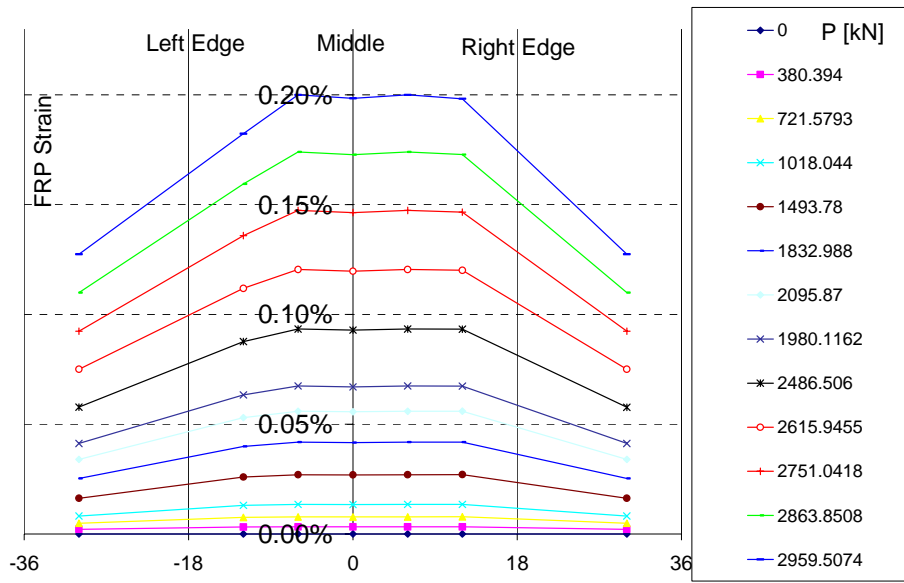


Figure 5.36 –FRP Strain Profiles at different load levels (S1-F.E.M.)

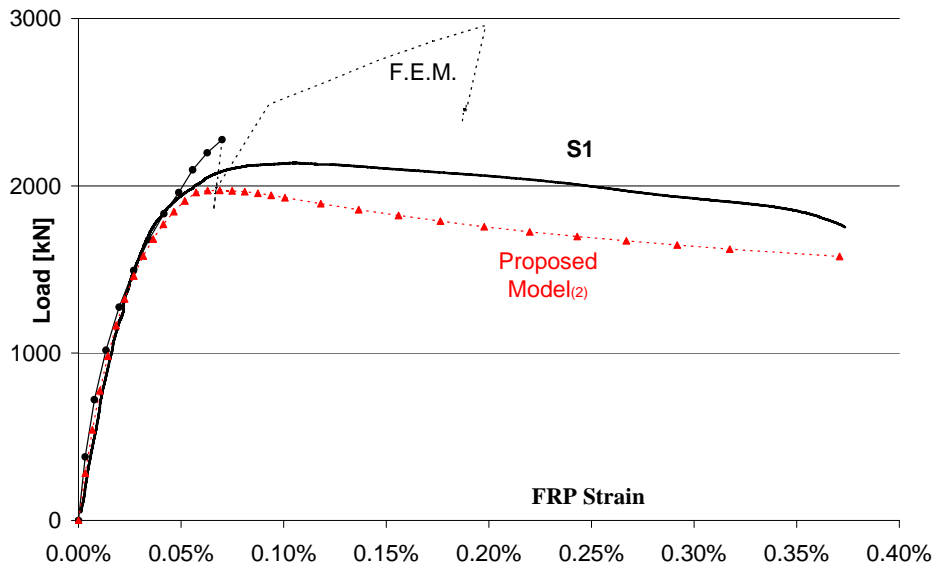


Figure 5.37 –FRP Strain development (S1)

5.2.5 Specimen S2: F.E.M. numerical predictions

In figure 5.38 is the F.E.M. smeared crack pattern (external and internal view of the specimen, behind the FRP wraps) at an axial load of about 1095 kN, corresponding to steel compressive bars buckling and close to experimental failure.

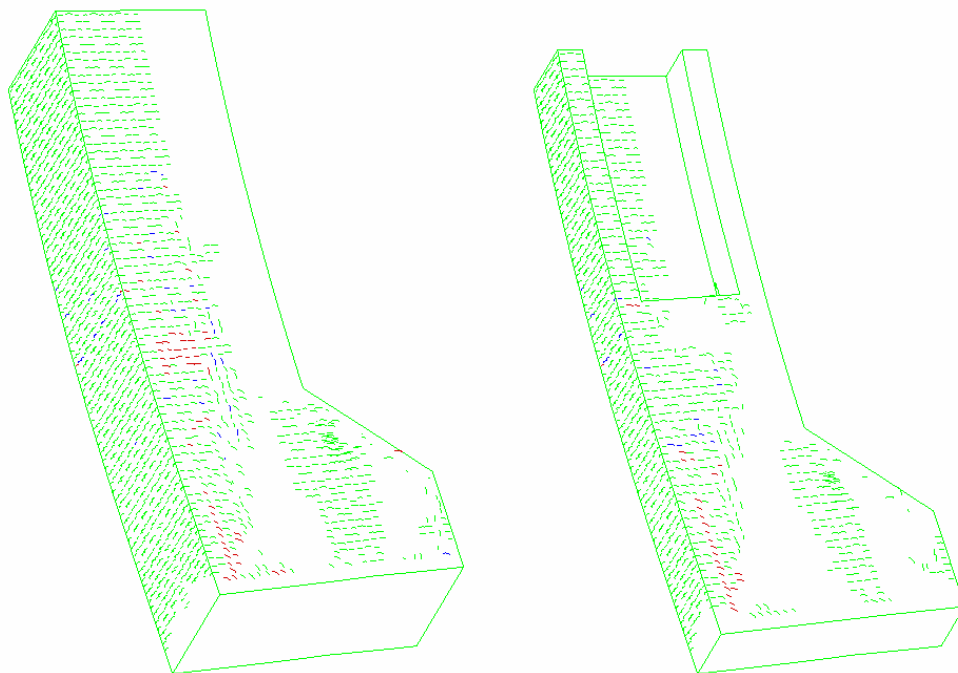


Figure 5.38 –Crack pattern at peak load (S2-F.E.M.)

The stress field spreads from the loaded line to the hollow portion in the solid end (Figure 5.39) and the neutral axis is in the middle of the cross section: so strain diagram is bitriangular, with almost equal strains on the crushed wall and on the wall in tension.

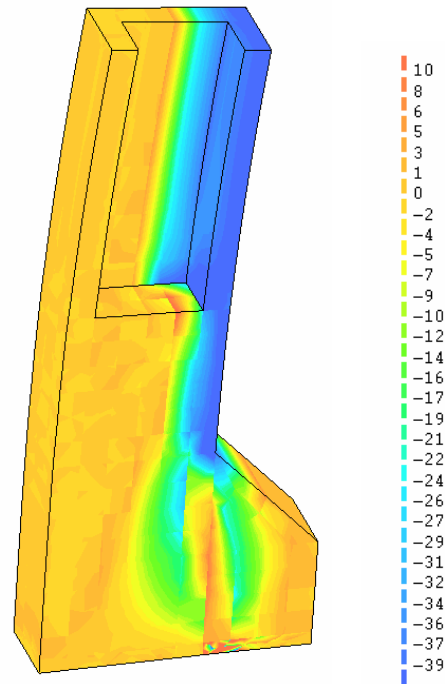


Figure 5.39 – Concrete vertical stresses at peak load (S2-F.E.M.)

In Figure 5.40 is reported the contour plot of the FRP strain in the jacket at steel buckling point. FRP strains present a maximum in the middle of the compressed wall and strains decrease on the lateral walls going to the neutral axis.

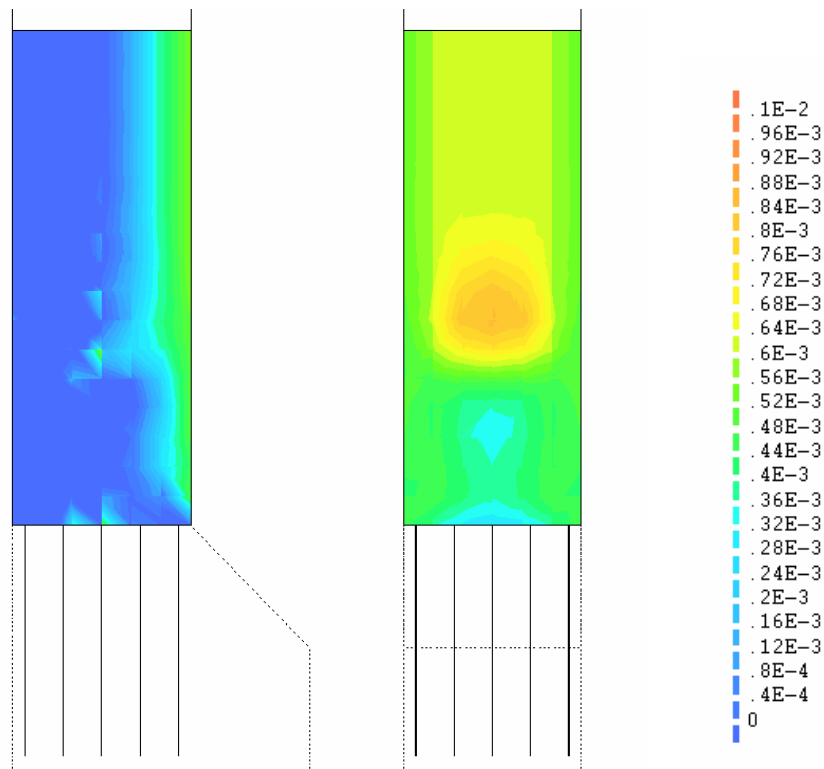


Figure 5.40 – FRP horizontal strains at peak load (S1-F.E.M.)

In Figure 5.41 is reported the strain versus axial force P diagram. The load carrying capacity after steel reaches buckling stress can be considered a virtual measure of the loss due to the brittle mechanisms due to internal concrete cover spalling.

It is clearly shown that up to experimental peak load, the experimental and numerical curves follow the same path, while failure due to internal concrete cover spalling causes the loss of load carrying capacity of the tested specimen. The concrete strain at reinforcement buckling is about 3.0%.

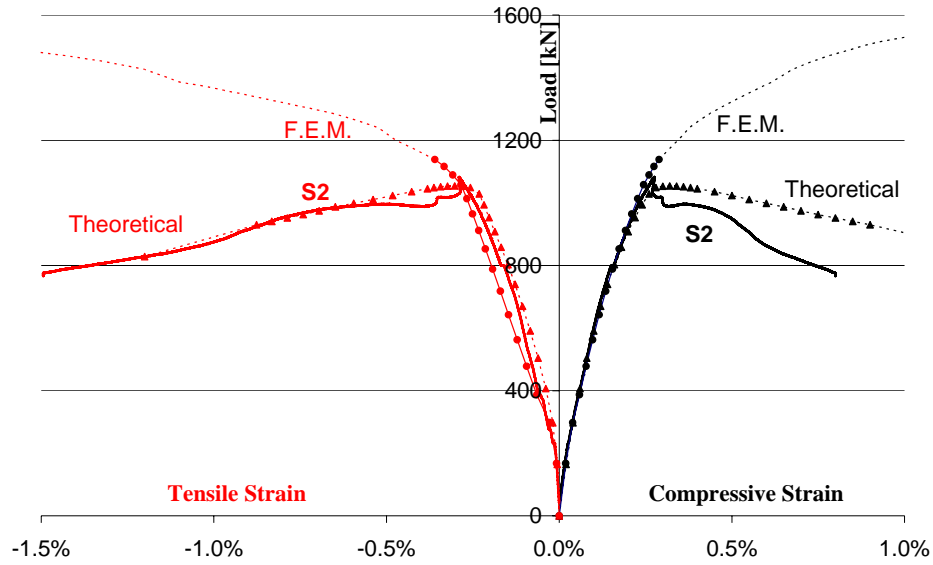


Figure 5.41 –Strains vs. Axial Load Diagram (S2)

A comparison of F.E.M. and proposed refined section modeling moment-curvature diagram with experimental outcomes is plotted in Figure 5.42.

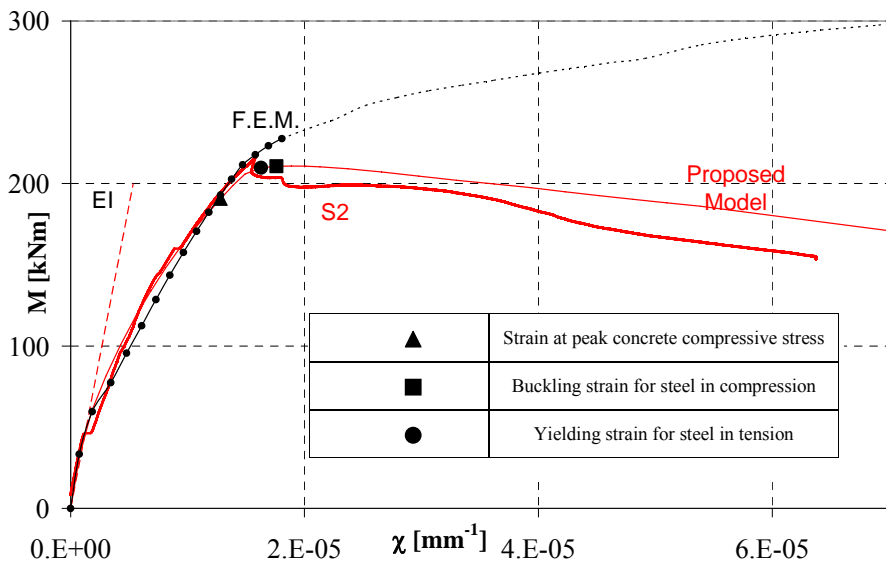


Figure 5.42 –Moment Curvature Diagram (S2)

An excellent agreement is found between three available data up to peak, before steel buckling.

In Figure 5.43 is the mid span deflection vs. axial load diagram: at peak load the deflection was 17.1 mm, this value is close to the experimental data.

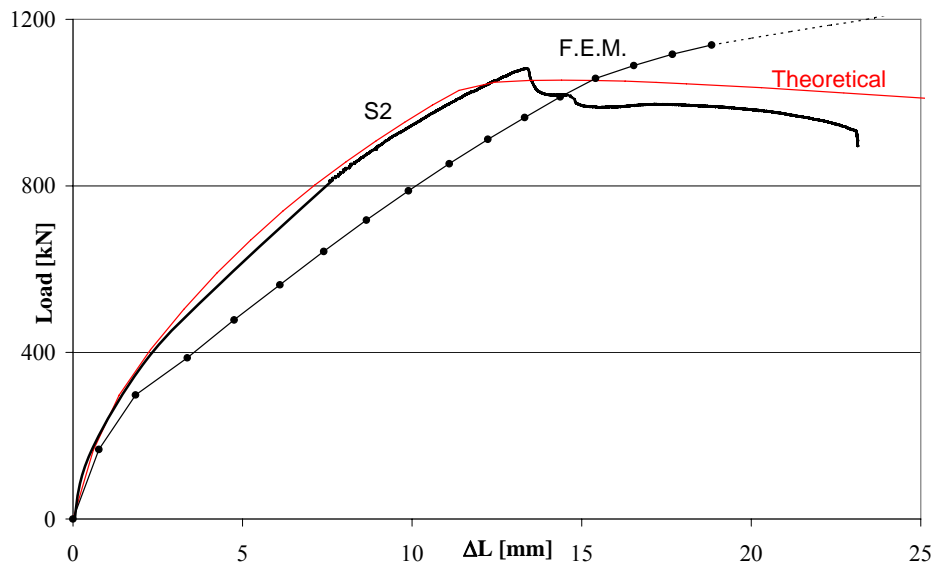


Figure 5.43 – Mid Span Deflection Diagram (S2)

In Figure 5.44 strain profiles are plotted over the length of the front wall and around corners at the mid span section, at different load levels. Maximum strains in FRP are reached at mid-span in the middle of the compressed wall. At peak load, FRP lateral strains are smaller than 0.06%. After peak, a remarkable strain increment was noticed, the maximum value of 0.3% was recorded. FRP strains experimental data in the middle of the compressed wall are compared with theoretical predictions during the entire load history (Figure 5.45).

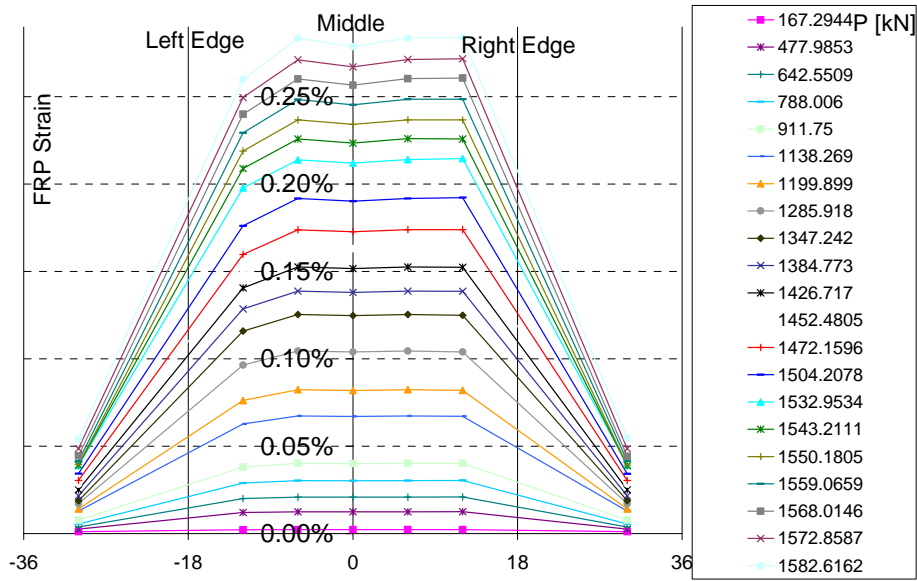


Figure 5.44 –FRP Strain Profiles at different load levels (S2-F.E.M.)

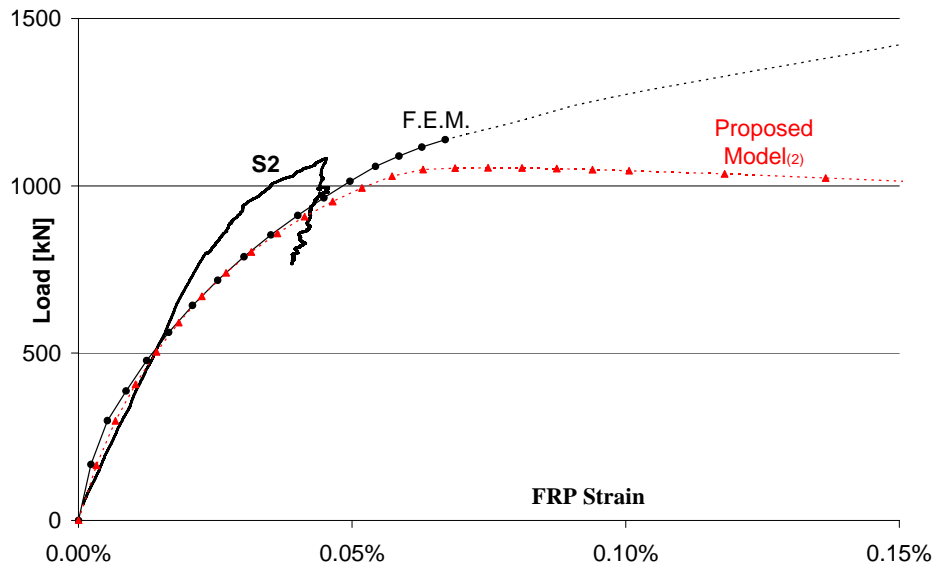


Figure 5.45 –FRP Strain development (S2)

5.2.6 Specimen S3: F.E.M. numerical predictions

In figure 5.46 is the F.E.M. smeared crack pattern (external and internal view of the specimen, behind the FRP wraps) at an axial load of about 678 kN, corresponding to steel compressive bars buckling and close to experimental failure.

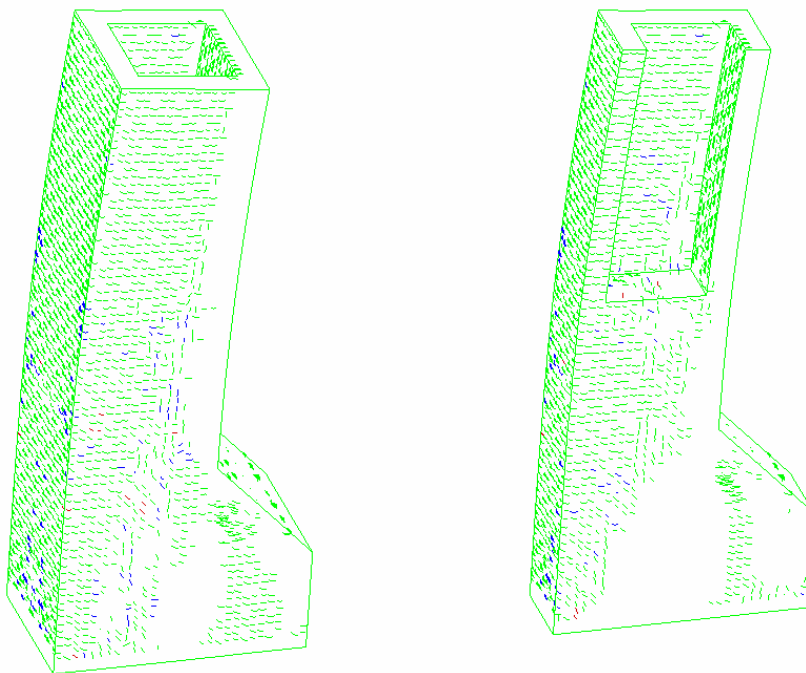


Figure 5.46 –Crack pattern at peak load (S3-F.E.M.)

The stress field spreads from the loaded line to the hollow portion in the solid end (Figure 5.47). The axial load eccentricity (in this case 300 mm) put the hollow section both in tension and compression. The neutral axis is close to the internal side of the compressed wall: strain diagram was bitriangular. Many cracks are expected to open according to the smeared crack pattern with a depth of about 240 mm on the side walls (as found in the laboratory).

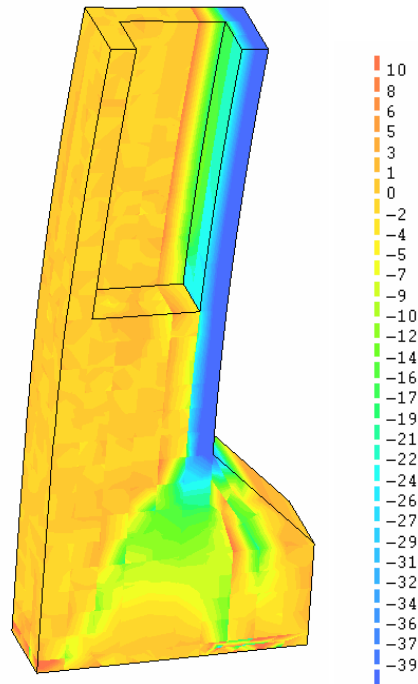


Figure 5.47 – Concrete vertical stresses at peak load (S3-F.E.M.)

In Figure 5.48 is reported the contour plot of the FRP strain in the jacket at steel buckling. FRP strains present a maximum in the middle of the compressed wall and strains are almost zero on the lateral walls.

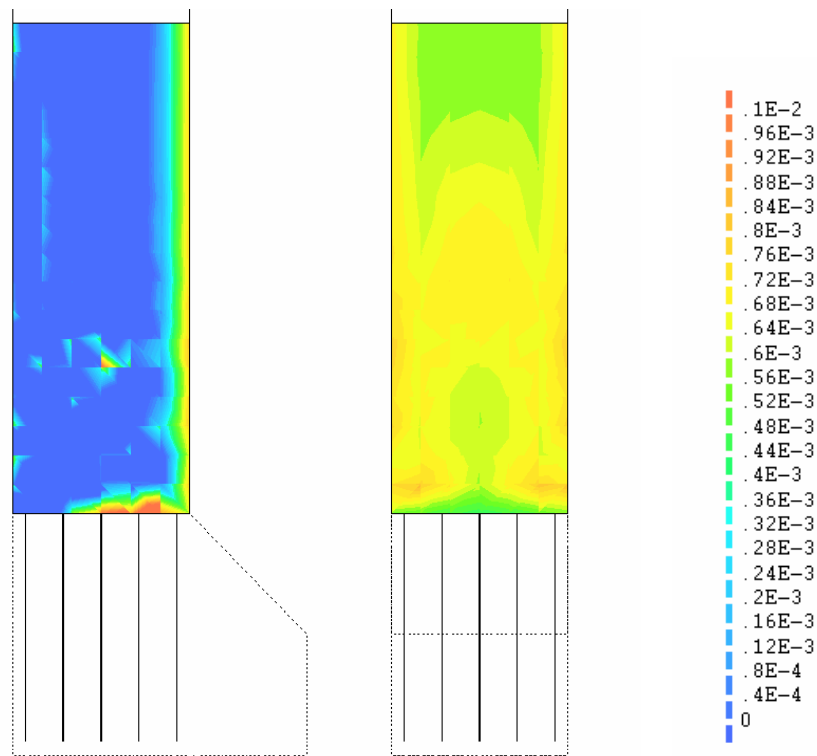


Figure 5.48 – FRP horizontal strains at peak load (S3-F.E.M.)

In Figure 5.49 is reported the strain versus axial force P diagram. The load carrying capacity after steel reaches buckling stress can be considered as a virtual measure of the loss due to the brittle mechanisms due to internal concrete cover spalling.

It is clearly shown that up to experimental peak load, the experimental and numerical curves follow the same path, while failure due to internal concrete cover spalling causes the loss of load carrying capacity of the tested specimen. The concrete strain at reinforcement buckling is about 3.5%.

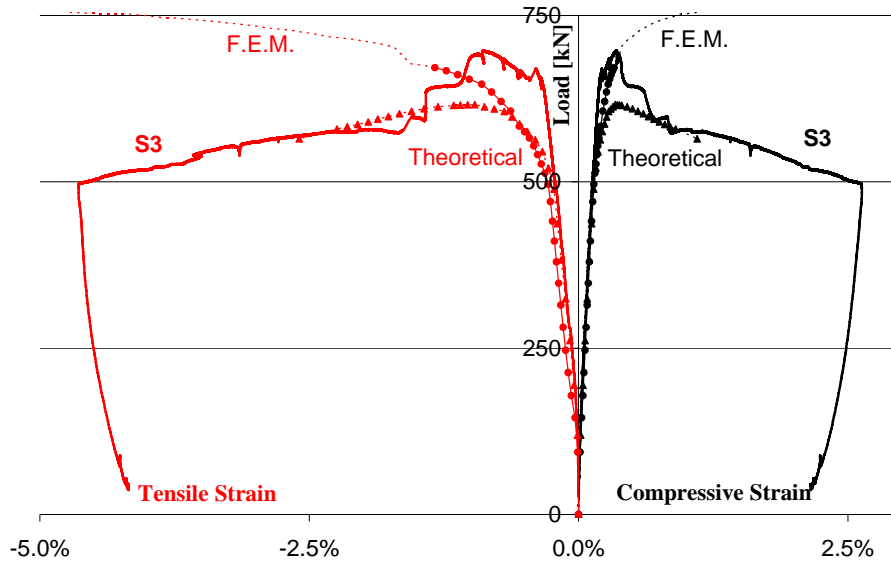


Figure 5.49 – Strains vs. Axial Load Diagram (S3)

A comparison of F.E.M. and proposed refined section modeling moment-curvature diagram with experimental outcomes is plotted in Figure 5.50.

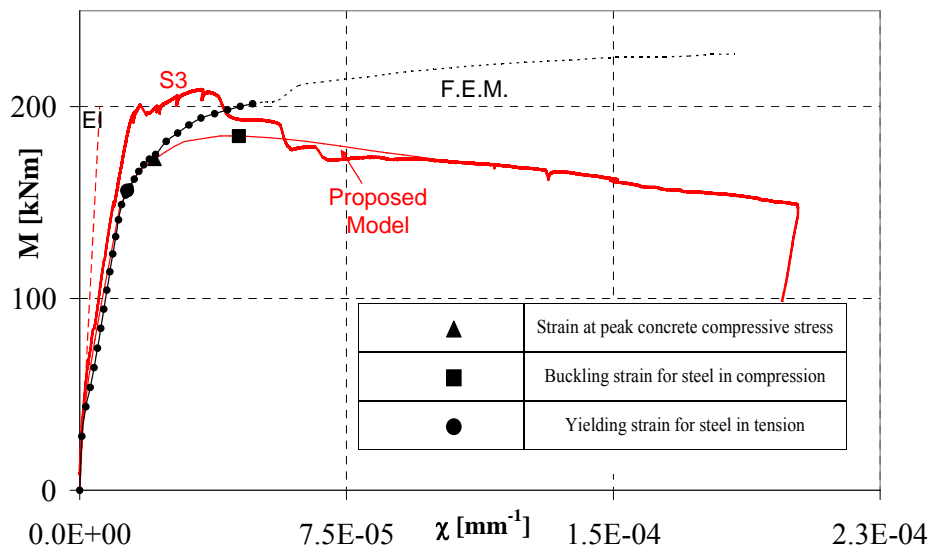


Figure 5.50 – Moment Curvature Diagram (S3)

A good agreement is found between three available data up to peak, before steel buckling.

In Figure 5.51 is the mid span deflection vs. axial load diagram: at peak load the deflection was 45.7 mm, this value is close to the predictions of the proposed refine method (experimental data is lower).

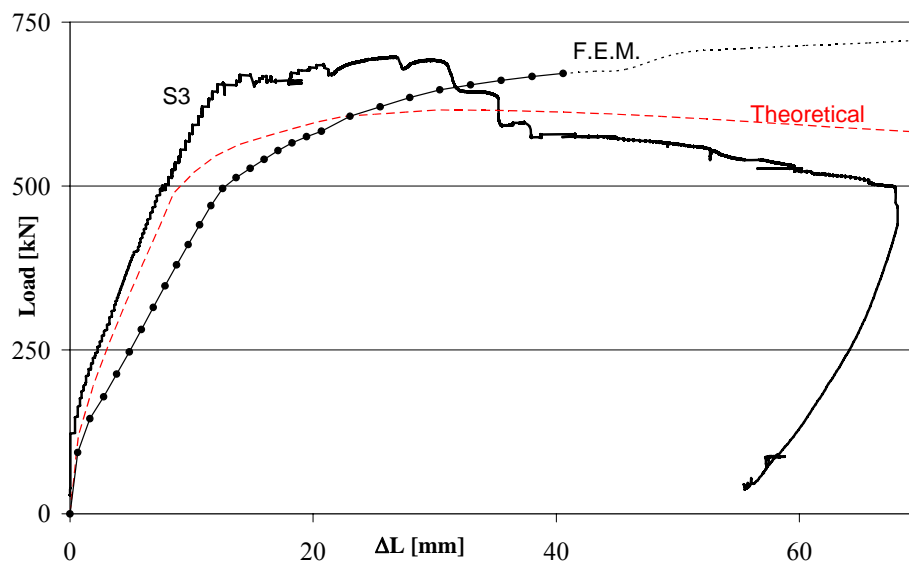


Figure 5.51 – Mid Span Deflection Diagram (S3)

Longitudinal strain distributions into FRP confining wraps have been recorded and analyzed. In Figure 5.52 strain profiles are plotted over the length of the front wall and around corners at the mid span section, at different load levels. Maximum FRP strains are reached at mid-span in the middle of the compressed wall and changes in to compression (ineffective for the confinement of concrete) close to the corners on the lateral walls. At peak load, FRP lateral strains are smaller than 0.06%. After peak, a remarkable strain increment is noticed, the maximum value of less than 0.2% was recorded. FRP strains experimental data in the middle of the compressed wall are compared with theoretical predictions

during the entire load history (Figure 5.53).

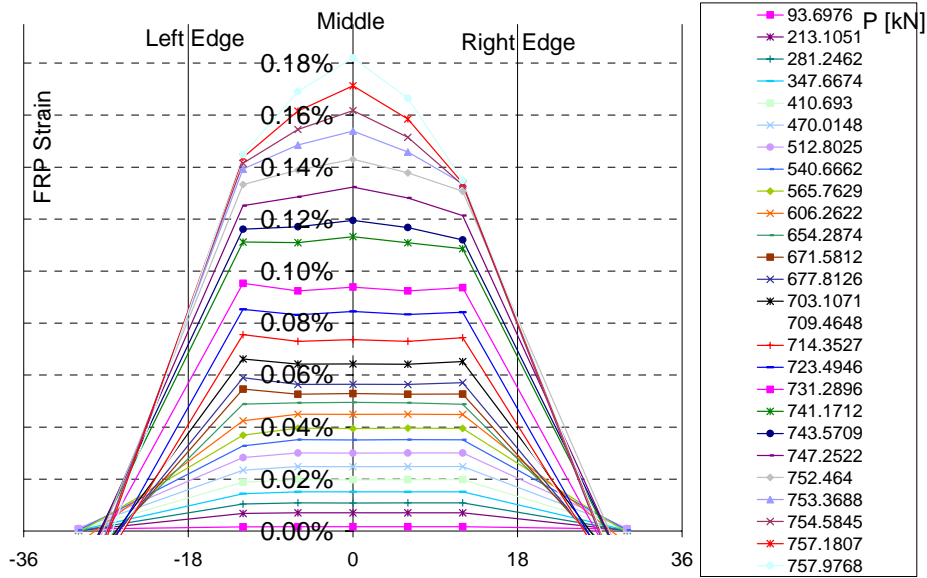


Figure 5.52 –FRP Strain Profiles at different load levels (S3-F.E.M.)

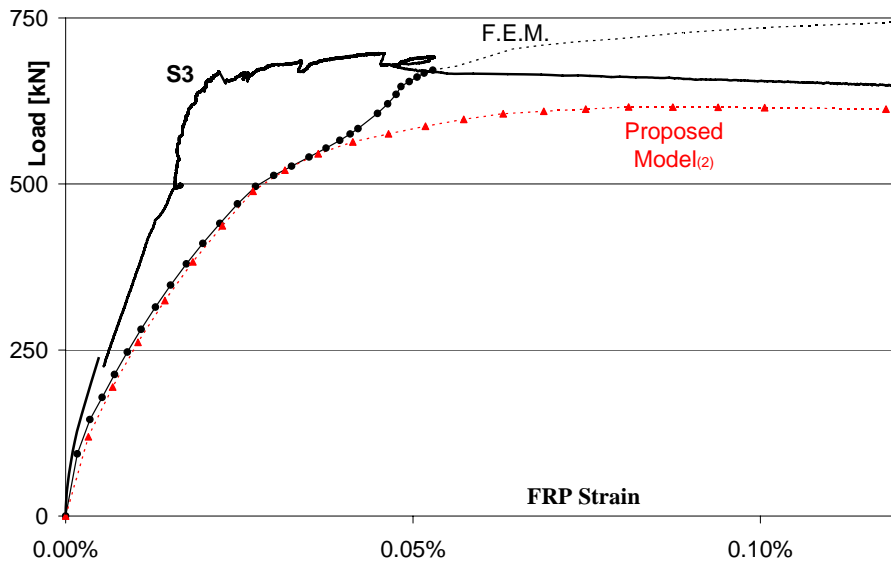


Figure 5.53 –FRP Strain development (S3)

5.2.7 Summary of F.E.M. Predictions.

The F.E.M. analysis of the tested specimens have been performed simulating in great detail concrete nonlinearities in tension (cracking) and compression, steel reinforcement yielding, elastic FRP wrapping, etc. In spite of that numerical outcomes clearly show that to predict hollow column behavior is crucial to consider concrete cover spalling and steel reinforcement buckling. These two brittle mechanisms acting together have a great effect on the load carrying capacity (strength) and ductility of RC hollow members. However good agreement on the ascending (pre peak) branch between F.E.M., proposed method predictions and experimental evidences was found.

In the post peak branch F.E.M. predictions and experimental outcomes diverges, but the difference between the two curves can be considered a virtual measure of the loss due to the brittle mechanisms occurred. FRP confinement is able to delay these mechanisms, thus resulting in both strength and ductility increases of members even under large eccentricities.

In table 5.4 are reported the main F.E.M. predictions at an axial load level corresponding to longitudinal steel compressed reinforcement buckling stress.

Table 5.4– F.E.M. predictions at steel reinforcement buckling

Specimen Code	e (mm)	P_{F.E.M.} (kN)	δ_{F.E.M.} (mm)	ε_{FRP,F.E.M.} (με)	ε_{C,F.E.M.} (με)
U1	52	2129	5.11	N.A.	2055
U2	200	1080	17.7	N.A.	2821
U3	300	633	33.3	N.A.	3052
S1	80	2197	7.81	628	2672
S2	200	1095	17.1	599	2990
S3	300	678	45.7	564	3569

The F.E.M. modeling has been performed to check mainly the crack pattern evolution, the stress/strains concentrations in the FRP wraps and to validate the proposed refined methodology also in the deformability field where F.E.Ms. represent an ideal tool to simulate laboratory tests giving also a detailed view of what happens inside the hollow core of the member.

In figure 5.54 a section of the modeled column is reported. It is subjected to an axial load and the contour lines of vertical stresses clearly show the arching effect.

A sort of ring forms all around the section and a stress concentration is visible close to the four corners of the square hollow section. This numerical result validate also the proposed method to simulate concrete confinement in a square hollow section starting from the proposed confinement model proposed for hollow core circular cross sections.

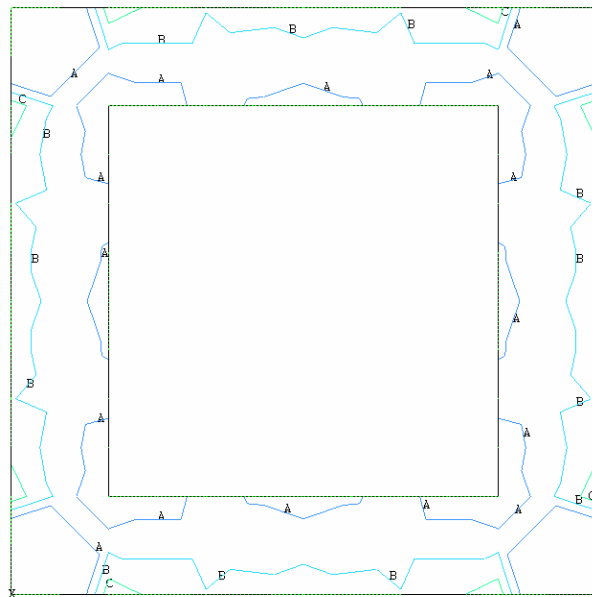


Figure 5.54 – F.E.M. contour lines: vertical stresses under pure axial load

In the following figures 5.55 and 5.56 are shown the same contour lines and contour map of vertical stresses in the case of columns subjected to different axial load eccentricity, close to peak load.

In the first figure (fig. 5.55) is a zoom on the compressed wall of column S1. The section is almost compressed and it is still visible the arching effect in the wall.

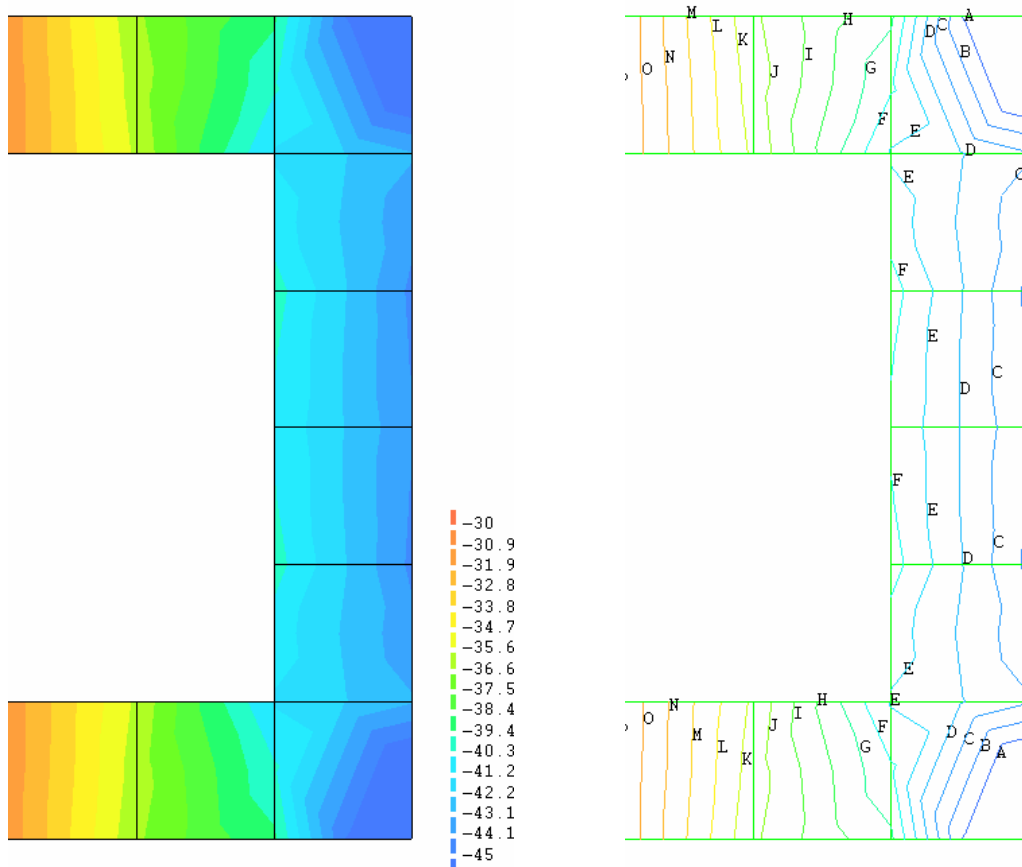


Figure 5.55 – Contour map and lines: vertical stresses (S1-F.E.M.)

In the next figure (fig. 5.56) the compressed wall of column S2 (higher load eccentricity) is shown. The neutral axis is about in the middle of the section and the arching effect in the wall is once more visible.

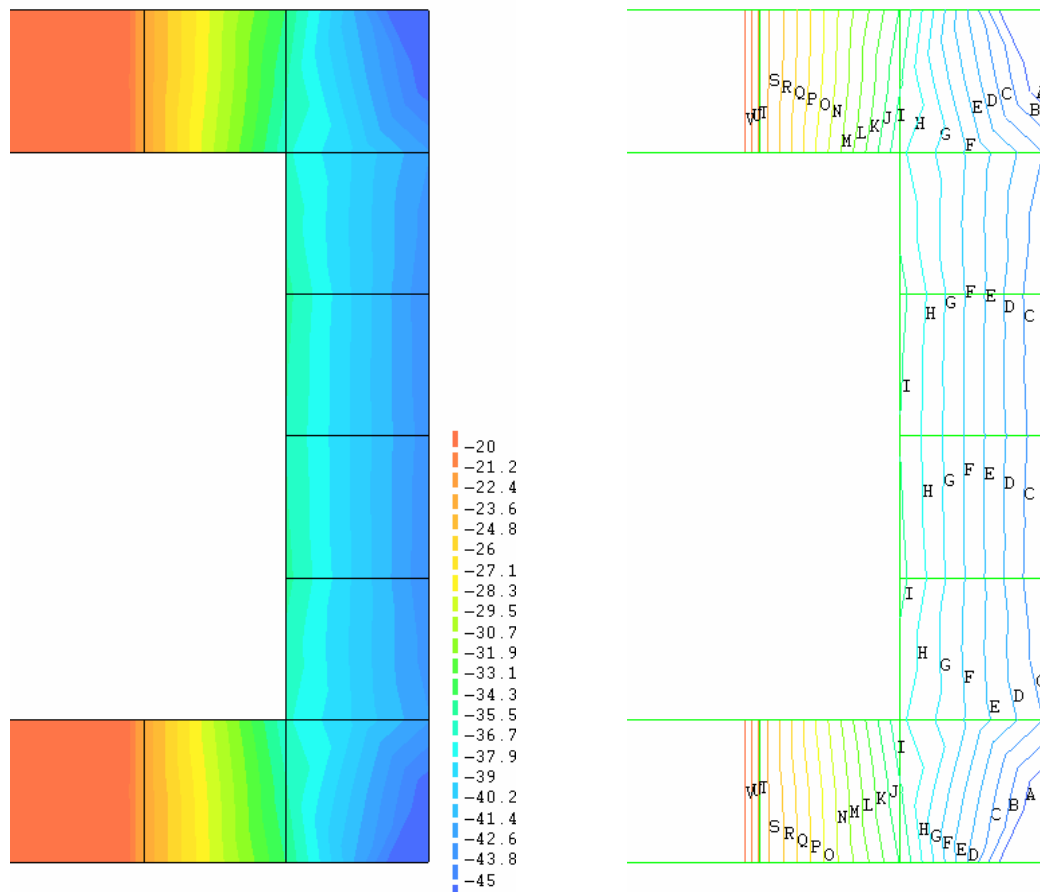


Figure 5.56 – Contour map and lines: vertical stresses (S2-F.E.M.)

5.3 Chapter References

Bazant, Z., J. Planas (1998): Fracture and Size Effect in Concrete and Other Quasibrittle Materials. *CRC Press*, LLC.

de Witte, F.C. and Kikstra, W.P. (2005). DIANA 9. Finite Element Analysis. User's Manual. Analysis Procedures. Delft, The Netherlands. *TNO DIANA bv*.

Desai CS, Zamman MM, Lightner JG, Siriwardane HJ (1984) Thinlayer element for interfaces and joints. *International Journal of Numerical and Analytical Methods in Geomechanics*, 4(8): 19-43.

Goodman RE, Taylor RL, Brekke TL (1968) A model for the mechanics of jointed rock. *Journal of the Soil Mechanics and Foundations Division ASCE*, 94(SM3): 637-659

Hordijk, D. A. (1991) Local Approach to Fatigue of Concrete. PhD thesis, *Delft University of Technology*, Delft, The Netherlands

Rashid Y (1968) Analysis of prestressed concrete pressure vessels. *Nuclear Engrg. and Des.*, 7: 334-344

Rots JG (1988) Computational modeling of concrete fracture. PhD Thesis, *Delft University of Technology*, Delft, The Netherlands

Zienkiewicz OC, Best B, Dullage C, Stagg K (1970) Analysis of nonlinear problems in rock mechanics with particular reference to jointed rock systems. *Proceedings of the Second International Congress on Rock Mechanics*, Belgrade.

Chapter 6

Conclusions

Bridges support important economic lifelines for cities throughout the world. As with other critical components of the infrastructure, they are vulnerable to a variety of threats, including earthquakes. Since many bridges are, or will be, located in areas of moderate or high seismic activity, there is a need to develop new structural systems and innovative strengthening techniques capable of resisting properly under seismic events. There is a lot of interest in protecting large, monumental bridges. However there are many other bridges that are extremely important as lifelines to large cities.

In most cases, the bridge safety is limited and conditioned by piers capacity. Most important elements of concrete bridges resisting to lateral actions are usually the piers. They are responsible for dissipating the energy and their vulnerability needs to be reliably assessed.

Most bridges built today are supported by conventional reinforced concrete columns. These columns likely would fail, leading to bridge collapse in the event of an earthquake. Great attention should be paid in the design of new bridges and future research needs to focus on the development of retrofit alternatives for existing bridges.

Modern codes of practice oriented to new design do not recognize any specific problem related to hollow sections. Hollow reinforced vertical members may be required to dissipate energy by forming ductile plastic hinges when they are subjected to seismic or other lateral forces and the question of their available

ductility has been studied.

The main objectives of the present research project on the analysis of hollow members subjected to flexure combined to compression and strengthened with CFRP wraps can be summarized as follows:

- To evaluate the ductility and post-peak behavior (related to seismic performance) of un-strengthened hollow piers with respect to solid ones.
- To evaluate the performance of hollow piers retrofitted with FRP and quantify the benefits of column wrapping in terms of strength and ductility.
- To provide a refined nonlinear method, coupled to an innovative hollow concrete sections confinement model, to analyze hollow piers both strengthened and unstrengthened and provide design guidelines for hollow members assessment.

6.1 Conclusions

A total of 7 hollow square cross section concrete columns were tested. Unstrengthened and FRP jacketed square hollow piers subjected to combined axial load and bending, therefore slender specimens, whose behavior is dominated by flexure, were investigated. It has been outlined that shear failure occurs only for short rectangular piers; in all other piers the collapse is governed by exhaustion of ductility induced by combined axial load and bending.

The failure of hollow members is strongly affected by the occurrence of premature mechanisms (compressed bars buckling and unrestrained concrete cover spalling). FRP confinement does not change actual failure mode, but it is able to delay bars buckling and to let compressive concrete strains attain higher values, thus resulting in higher load carrying capacity (strength improvement

about 15%) of the column and significantly in ductility enhancement.

The ductility increments have been estimated through the comparison of curvature ductility μ_χ indexes and specific energy. In unstrengthened columns the curvature ductility ranged between 1 (brittle failure of U1 and U2) and 1.54 (specimen U3), while in the case of strengthened columns the curvature ductility increased significantly attaining values ranging between 3.07 and 8.27. This analysis evidenced a remarkable improvement of the seismic response of the wrapped columns: after peak load they kept a good load carrying capability, that is good energy dissipation.

The relationship between the neutral axis position (related to load eccentricity) and the capacity of the section was assessed. The strength improvement was more relevant in the case of specimens loaded with smaller eccentricity, while the ductility improvement was more relevant in the case of bigger eccentricity. At lower levels of axial load also the brittle effect of reinforcement buckling was less noticeable.

The results of the present work suggest that a reliable numerical procedure to predict hollow cross section behavior under combination of flexure and compression should include appropriate models for compressed bars buckling and concrete cover spalling. Besides a reliable stress-strain behavior of concrete, and of course of other structural involved materials, is necessary and concrete parameters affecting the theoretical previsions have been recognized and addressed.

An innovative confinement model for circular hollow sections has been proposed and extended to square hollow ones. The model is able to estimate confinement effectiveness, which is different in the case of solid and hollow sections. The bigger is the hole, the higher is the deformability of the element and the circumferential stresses compared to the radial component: in the case of solid section the dilation of concrete is restrained by the FRP wraps and this interaction

yields a strength improvement, while in the case of thin walls, the larger deformability does not allow to gain such strength improvement, even though a significant ductility development is achieved.

Results of experimental tests and theoretical analyses show that a good agreement was achieved (the same strength increments and curvature ductility increments as experimentally found in performed tests are predicted). The proposed confinement model, coupled with the proposed computation algorithm is able to predict the fundamentals of the behavior of the hollow square members confined with FRP both in terms of strength and ductility giving a clear picture of the mechanisms affecting the response of this kind of elements. The model is able to trace the occurrence of the brittle mechanisms, namely concrete cover spalling and reinforcement buckling, the evolution of stress and strains in the concrete and in the confinement jacket allowing to evaluate at each load step the multiaxial state of stress and eventually the failure of concrete or of external reinforcement. The main output of the proposed model is also the assessment of the member deformability in terms of both curvature and displacement ductility.

The F.E.M. analysis of the tested specimens have been performed simulating in great detail concrete nonlinearities in tension (cracking) and compression, steel reinforcement yielding, elastic FRP wrapping, etc... In spite of that, numerical outcomes clearly show that to predict hollow column behavior it is crucial to consider concrete cover spalling and steel reinforcement buckling. The effect of concrete cover spalling and bars buckling, key aspects of the proposed refined methodology, are not considered in the F.E.M. analyses. These two brittle mechanisms acting together have a great effect on the load carrying capacity (strength) and ductility of RC hollow members. In the post peak branch (after reinforcement buckling) F.E.M. predictions and experimental outcomes diverges, but the difference between the two curves can be considered as a virtual measure of the loss due to the brittle mechanisms occurred. Concrete confinement allows

to gain a big portion of that loss delaying those mechanisms, thus resulting in both strength and ductility increases of RC hollow members even under large eccentricities.

Nevertheless good agreement on the ascending (pre peak) branch between F.E.M., proposed method predictions and experimental evidences was found.

The F.E.M. modeling has been performed to check mainly the crack pattern evolution, the stress/strains concentrations in the FRP wraps and to validate the proposed refined methodology also in the deformability field where F.E.M.s represent an ideal tool (despite of computational requirements) to simulate laboratory tests giving also a detailed view of what happens inside the hollow core of the member.

The present work is included into a wider activity that aims to improve the knowledge and develop a cost and time effective design method for fast FRP strengthening of hollow bridge columns so that bridge function can be quickly restored. The strengthening intends to upgrade seismic capacity in terms of strength and ductility. For this purpose it is required to extend the experimental program. The experimental results and the related database at date have been used for validating CFRP strengthening design methods addressing hollow cross sections. And considering the chance to adopt some current computation method available for solid cross sections for non-circular, hollow cross sections, as well.

Some of the results are well known indeed in the case of solid columns, but have not been confirmed yet for hollow cross section columns. Even though, modern codes of practice do not recognize any specific problem related to hollow sections despite the fact that this kind of cross sections may suffer premature failures that are unusual in solid sections, accordingly “Additional Design Guidelines for hollow members” are proposed.

6.2 Design Guidelines: Add-on proposal

- Hollow sections withstand high moment and shear demands by reducing the self weight and the bearing demand on foundations, maximizing structural efficiency of the strength-mass and stiffness-mass ratios and reducing the mass contribution of the member to seismic response. Usually the piers are the most important elements of concrete bridges resisting to lateral actions. They are responsible for dissipating the seismic input energy by forming ductile plastic hinges and their vulnerability needs to be reliably assessed.

- Rectangular columns, though common in bridge design, are less desirable than circular columns from a seismic viewpoint. Rectangular hoops needs to adequately restrain all longitudinal bars against buckling.

With a single layer of reinforcement, the hollow section becomes extremely economical and besides, the wall thickness should be kept to a minimum, to avoid large volumes of concrete without any reinforcement.

With a two-layer reinforcement pattern, with longitudinal and transverse reinforcement close to both outer and inner surfaces of the hollow section, the inner hoop, if placed in tension by confinement requirements, will tend to induce a radially inward component on the inner concrete cover, providing a negative confining influence, possibly resulting in implosion. To avoid this, cross links must be anchored over the inner spiral or hoops, making for difficult construction.

- At higher extreme fibers strains, external concrete cover spalling can result in a sudden increase in the depth of the neutral axis, increasing the strain at the internal surface of the section to the point that internal spalling, implosion, occurs. Only peripheral hoop reinforcement can be ineffective in confining the concrete core and in providing restraint against longitudinal bar buckling if the spacing is

too coarse.

- The failure of hollow members is strongly affected by the occurrence of premature mechanisms (compressed bars buckling and unrestrained concrete cover spalling).

- Biaxial loading should be considered. When rectangular columns are loaded in the diagonal direction, concrete cover spalling initiates at lower levels of seismic intensity than when loaded in the principal directions. This is because the depth of the compression zone must be larger to provide the required compression force, resulting in lower curvatures corresponding to the extreme-fiber spalling strain.

- Local buckling of the thin compression wall should be checked. If wall buckling occurs, ultimate strength is lower than the value achieved when material failure and/or steel reinforcement bar occur. The wall slenderness ratio is the factor to be checked (at date structural wall threshold is about 15, more experimental data are needed to assess hollow sections).

- Capacity in terms of as-built strength only, can be evaluated by means of a simplified analysis provided extreme fiber compression strains are relatively low (in the order that compressed reinforcement strain should be lower than buckling strain depending on stirrups spacing – i.e. according to Cosenza and Prota (2006) – or, roughly, in the elastic range in poorly detailed piers: more experimental data needed). For piers carrying mainly axial loads it may be questionable to use the post peak part of the stress strain diagram in design, as the descending part is associated with large deformations and stability problems.

- In a ductility based design, detailed capacity analyses should be carried out. The proposed refined algorithm coupled with the confinement model proposed for hollow sections is suggested (Chapters 3.1-3.2-4.2). A reliable numerical procedure to predict hollow cross section behavior under combination of flexure and compression should include appropriate models for compressed bars buckling and concrete cover spalling. A reliable stress-strain behavior of concrete is necessary and concrete post peak behavior should be carefully assessed.

- Modern design code allows to use a behavior factor q (equivalent to displacement ductility index in the case of Single Degree of Freedom systems) for solid sections (i.e. up to 3.5 in the Italian OPCM 3431 for slender piers with pier height to section side ratio higher than 3.5, depending also on axial load ratio) much higher than the experimental outcomes. Hollow piers need to have specific accurate construction details to ensure that level of ductility. All brittle failure mechanisms should be carefully prevented and effective capacity in terms of ductility should be evaluated depending also on axial load ratio η : applied load versus axial capacity (see next design example where, focusing on piers not satisfying transverse reinforcement details given in the next paragraph, η is about 0.10 and displacement ductility index is smaller than 2; experimental data show that $q \approx 1$ if $\eta > 0.35$ and $q \approx 1.5$ if $\eta = 0.20$ while code suggestion for slender piers is q ranging between 3.5 if $\eta < 0.3$ and 1 if $\eta > 0.6$: more experimental data are needed to define a closed formula to correlate behavior factor to axial load ratio in the case of hollow sections).

- Special care should be taken to provide adequate transverse reinforcement. Ductility performances require that concrete is well confined and compressed reinforcement buckling is avoided. Bars' buckling determines a strength reduction

usually higher than 20% and mostly ductility reductions (even leading to very brittle behaviors). In the lack of improved provisions, structural walls details should be used at least, i.e. limiting the stirrup spacing to the smaller between 6 times the longitudinal reinforcement diameter and 1/5 of the wall thickness. Adopt ties to restraint possibly all the longitudinal bars in the plastic hinge length, length at least equal to one section dimension. Avoid lap-splices in the plastic hinges.

- Shear failure has to be checked and avoided taking into account actual ultimate flexural strength, rather than conventional yielding force. Concrete cover contribution cannot be discarded in flexural section evaluation from the very first because this leads to an underestimation of the ultimate strength. Plastic hinge rotations and column displacements can take place at high ductility levels: shear strength deterioration at high ductility levels should be accounted for.

- The structural model of the hollow piers can be regarded as a cantilever carrying a mass on the top because hollow pier has a reduced mass so that the deck mass on top of the pier usually prevails.

- If some of the previous prescriptions are not satisfied and the member is inadequate to meet the stringent requirements imposed as regards both strength and ductility (i.e. stirrups spacing or ductility demand) an FRP retrofit intervention can be designed. Design of FRP wrapping can be performed by means of the proposed methodology. A computer program, running the whole procedure automatically, has been developed to quickly account for capacity enhancement (both in terms of strength and ductility) of hollow section piers when applying different layers numbers and types of FRP wraps.

- FRP Wrapping may increase ductility and in a single bent scheme P- Δ

effects can significantly affect the global response and weaken the retrofitted member.

- FRP Wrapping usually is able to increase slightly the strength of the section and mainly its ductility, nevertheless in a capacity design it is essential to check that brittle mechanisms (i.e. shear failure) are prevented by ductile ones also accounting for over strength.

- FRP pre-cured tubes can be usefully adopted as left-in-place formworks and at the same time as effective confining devices (nowadays this application is also under development to increase the blast resistance of bridge piers and columns in general).

Shear capacity and plastic hinge length enhancement and longitudinal reinforcement buckling control in FRP jacketed members design are strictly related to the capacity design of hollow member, but their detailed evaluation is out of the scope of the present work.

Future developments consist in extending the experimental campaign, mainly on real scale bridge piers, developing a confinement model to account for square hollow sections additional to circular hollow, improving the strain efficiency criterion.

The main outcomes of the present work are summarized in the next concluding paragraph by means of a basic design example.

6.3 Basic Design Example

In this basic design example assume to assess the vulnerability of a bridge designed and constructed in a seismic region in past years without any seismic provision and to check and eventually design an FRP retrofit intervention. The complete assessment of this bridge undoubtedly includes the analysis of many important phenomena affecting the bridge response, topics that can be regarded either from the design or the assessment standpoint. These are issues that significantly affect the overall behavior of bridges, modifying the response and affecting the performance. Namely they are multi-support excitation, soil-structure interaction, vertical oscillations, traffic influence function and girder-line analysis, loss of support of the deck, internal reinforcement lap-splice, etc...

Moreover a bridge should be checked against various loads and load combinations (i.e. gravity, wind, temperature, settlements, braking forces, seismic, water, etc...) and in the design of an FRP retrofit intervention it can be considered the increase of member flexural capacity by using FRP materials with fibers running in the axis direction and shear capacity by using fibers running in the transverse direction, efficiency of lap splices and magnitude of the plastic hinge length by using FRP wraps, etc...

For the simplicity and directness of this basic example, only the increase in ductility and steel longitudinal bars buckling delay by using FRP wrapped around the member cross section and only the gravity and seismic loads will be considered. Great care in the assessment of deformation capacity of the pier must be taken as it is a measure of structural capability to sustain seismic forces.

The RC structure is a multi span, simply supported deck bridge, regular in elevation and the piers have hollow core square cross section and are single-column type so that the mechanical model of the pier consists in all directions of a cantilever carrying a mass on top. One of the piers of this bridge has an height of

6.5 m, cross section of $1800 \times 1800 \text{ mm}^2$ and wall thickness of 300 mm (this section is equivalent to the section considered in the test campaign design). The internal reinforcement consists of 44 D30 steel longitudinal bars equally distributed and D12@300mm stirrups with four legs. The mechanical properties considered in the design example are: the concrete has a strength $f_c = 30 \text{ MPa}$ (and initial Elastic modulus $E_{co} = 34 \text{ GPa}$, initial Poisson ratio $\nu_{co} = 0.12$, tensile strength $f_{ct} = 3 \text{ MPa}$), while the steel has yielding stress $f_y = 500 \text{ MPa}$.

The weight of the deck loading the pier is assumed considering the Italian practice (see Chapter 1.1): the axial load is about 10% of the pier capacity.

The axial capacity of the pier is about $P_{\max} = 67000 \text{ kN}$, so that the mass on top (deck and half pier) gives an axial load $P = 6700 \text{ kN}$.

The bridge is placed in a “zone 1” region and built on a medium soil type B according to Italian Design Code. The analysis is performed at first using the artificial Italian Code OPCM 3431 elastic (5% dumped) response spectrum considering a Peak Ground Acceleration (P.G.A.) $a_g = 0.35g$ (figure 6.1).

According to the proposed refined method, the Moment-Curvature diagram is plotted (figure 6.2) for given hollow section accounting for the concrete cover spalling and reinforcement buckling (in this case the L/D ratio for the D30 bar is 10 if we assume that the stirrups/ties are sufficiently stiff to prevent bars' buckling on a length higher than their spacing $L = 300 \text{ mm}$). The bending capacity is evaluated at constant axial load P equal to 6700 kN.

The outcomes of the available ductility and strength analysis are the following: the maximum, ultimate moment is $M_u = 16715 \text{ kNm}$ corresponding to an horizontal force $F_u = 2571 \text{ kN}$, the yielding moment is $M_y = 14740 \text{ kNm}$ corresponding to an horizontal yielding force $F_y = 2268 \text{ kN}$ and the yielding curvature is $\chi_y = 2.099 \cdot 10^{-6} \text{ mm}^{-1}$. The ultimate curvature is $\chi_u = 5.333 \cdot 10^{-6} \text{ mm}^{-1}$ at peak load due to the brittle capacity drop after peak. Then the curvature ductility index $\mu_\chi = 2.54$ and can be related (see Chapter 1.5.1 eq. 1) to the

displacement ductility index $\mu_{\Delta} = 1.59$. In this computation the plastic hinge length has been considered equal to half the width of the cross section, $\ell_p = 900$ mm.

The stiffness $K_y = 76.72 \text{ kNmm}^{-1}$, yields to a period $T = 2\pi\sqrt{M/K} = 0.587 \text{ s}$, so that the elastic response of the pier is at the beginning of the descending branch of the Acceleration Spectrum after the plateau.

The shear strength is evaluated according to Priestley et al. (1994), where the strength of concrete component is reduced as flexural displacement ductility increases. The shear strength ranges between $V_{\mu_{\Delta}=2} = 4188 \text{ kN}$ if $\mu_{\Delta} < 2$ and $V_{\mu_{\Delta}=4} = 2587 \text{ kN}$ if $\mu_{\Delta} > 4$ and it is in any case higher than the maximum flexural strength of the pier.

The seismic elastic force is higher than the capacity of the pier.

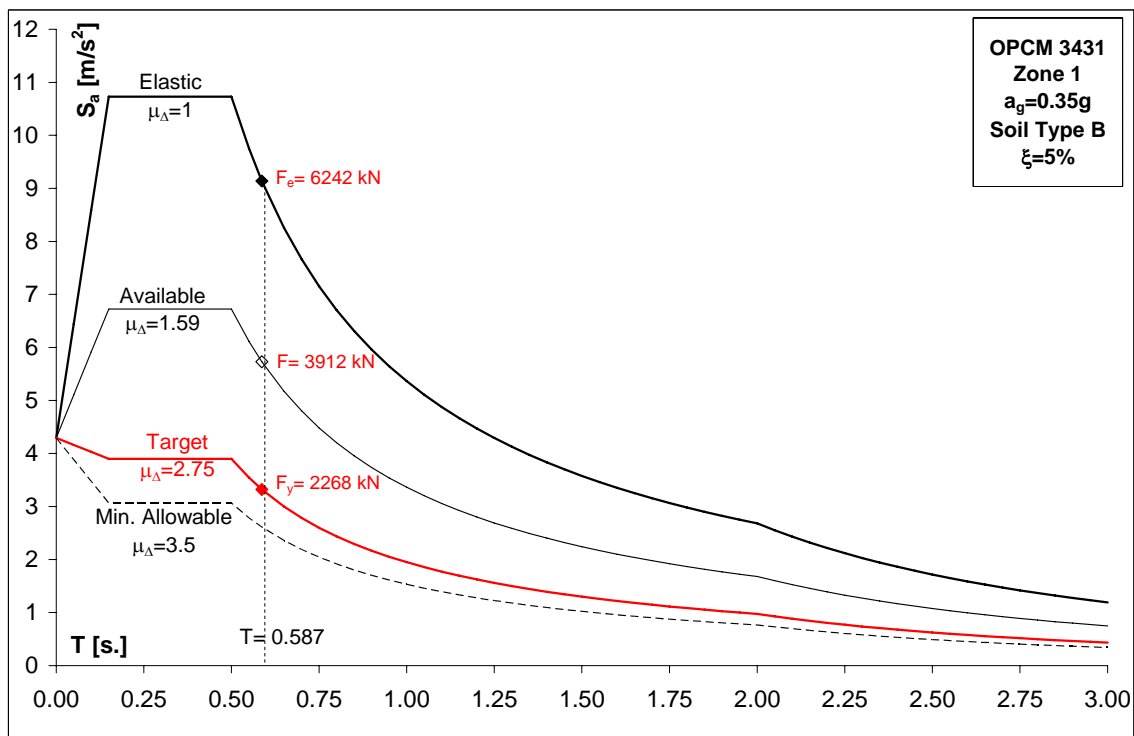


Figure 6.1 – Demand Spectra at different displacement ductility.

In a ductility-based design, the spectral ordinates used for evaluating the forces acting on a structure are related to the amount of available ductility. Considering the available displacement ductility index $\mu_{\Delta}=1.59$, the required strength for the available ductility $F=3912$ kN is still higher than the capacity. It is possible to evaluate the maximum P.G.A. the pier is able to resist to. It is about 0.20g.

It is possible to define a pier upgrading index I_{pier} , (see Chapter 1.5.1 eq. 2).

$$I_{pier} = \frac{\mu}{\mu_{\Delta}} = \frac{M \cdot S_a(T)}{F_y \cdot \mu_{\Delta}} = 1.725 .$$

An upgrade intervention is needed since the pier upgrading index is greater than 1. The Italian Code allows using a displacement ductility $\mu_{\Delta}=3.50$ in the case of slender piers, but this value seems to highly overestimate the available ductility of hollow piers.

To select an appropriate technique and material, it is considered that relevant increases of section ductility and limited or no-increases in flexural strength are needed to resist seismic actions and to avoid shear failure (and eventually shear strengthening). In any case a confinement is needed to avoid brittle reinforcement buckling (i.e. $L/D > 6$) and FRP confinement can be a good choice to avoid mass increases and to gain necessary ductility: target displacement ductility index is $\mu_{\Delta}=2.75$ and the related target curvature ductility index is $\mu_{\chi}=5.53$ (giving a section upgrading index $I_{sec}=2.177$).

Unidirectional fibers wrapping in the transverse direction with respect to the column axis gives relevant increases of section ductility, with limited increases in flexural strength (if the applied axial load is fairly small compared to axial capacity). Carbon fibers are preferred to other types of fibers (i.e. glass) because the retrofit is done in an exposed environment. After section corners have been rounded, the FRP is applied by manual wet lay-up with in situ resin impregnation for the ease of installation.

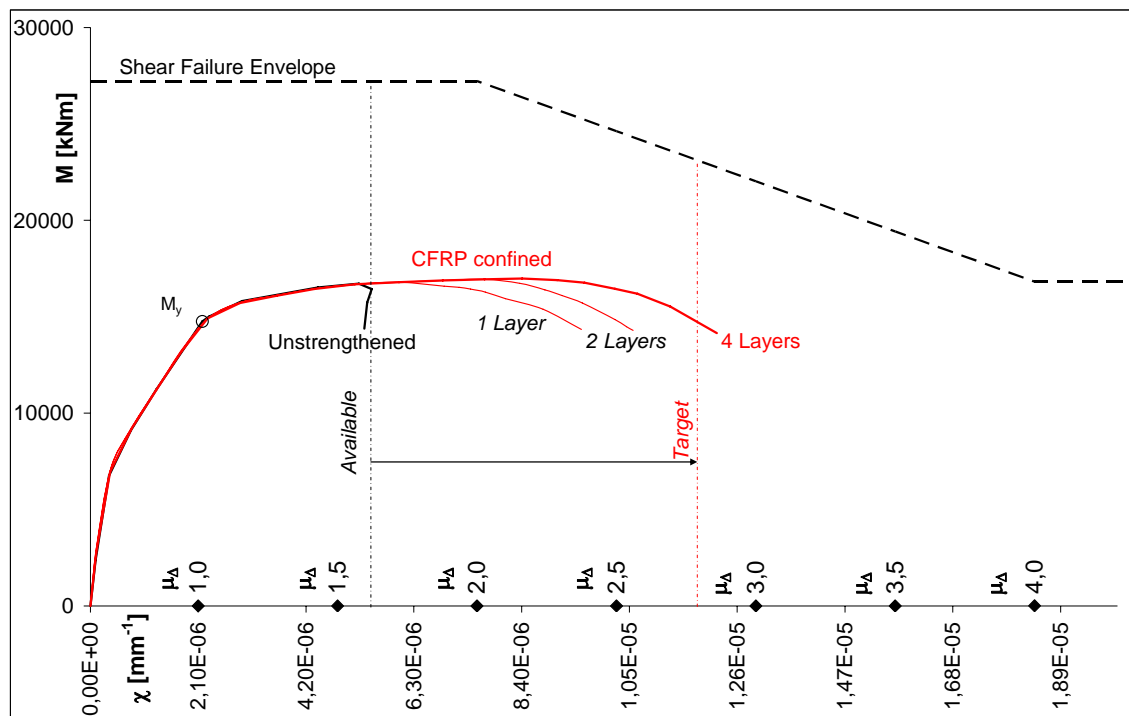


Figure 6.2 – Moment Curvature diagram and Shear strength envelope.

The number of layers of unidirectional CFRP fabrics is now going to be designed. The thickness of the jacket (one layer of dry fibers) is $t = 165 \mu\text{m}$ and the elastic modulus is $E_f = 230 \text{ GPa}$, while design strength is higher than $f_f = 2300 \text{ kN}$ considering also the environmental reduction factor.

Structural analyses taking into account the characteristics of the structure after FRP strengthening are performed (three different number of layers - 1, 2, 4 - are checked until the target curvature ductility is gained). In figure 6.2 is clearly confirmed that increasing the number of FRP layers only a small gain in strength is achieved, while the ductility increments are relevant.

When FRP reinforcement is used to increase the flexural capacity of a member, it is important to verify that the member will be capable of resisting the shear forces associated with the increased flexural strength. In this case this analysis is skipped since the flexural capacity increment is minimal and shear

strengthening due to FRP wrapping is neglected.

The confined concrete stress-strain relationship is evaluated according to proposed confinement model for hollow sections. In figure 6.3 is the confined concrete stress-strain relationship for different layers of CFRP where the β ratio is 0.666. Even if the concrete strength enhancement is negligible, the FRP wrapping is able to delay the brittle mechanisms that cause the brittle failure of unstrengthened piers, increasing the ductility even though only few layers of CFRP are applied.

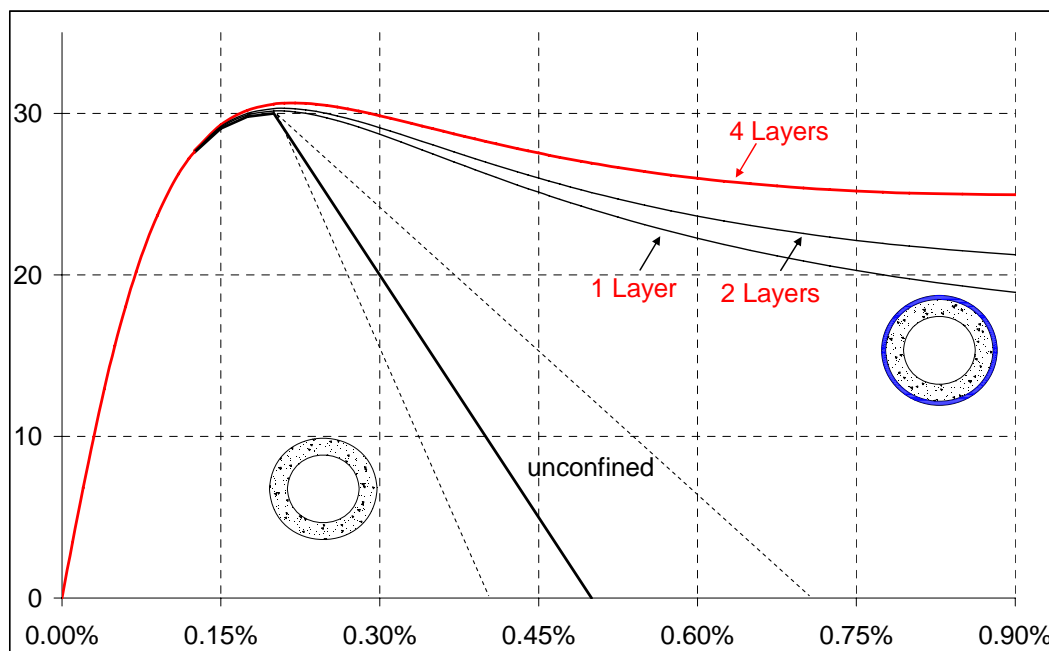


Figure 6.3 – Confined concrete stress strain relationships.

In this example it is clearly shown that the proposed refined method coupled with the innovative hollow concrete sections confinement model allows engineers to recognize bridge piers deficiency (local and global behavior, brittle mechanisms, etc...) and to design a retrofit intervention with FRP materials: an effective engineering tool in the frame of hollow RC bridge piers vulnerability assessment.